METABOLIC MAPPING OF MYC-INDUCED LYMPHOMA MODELS USING ISOTOPICALLY NONSTATIONARY ^{13}C FLUX ANALYSIS

By

Taylor Athanasaw Murphy

Dissertation

Submitted to the Faculty of the

Graduate School of Vanderbilt University

in partial fulfillment of the requirements

for the degree of

DOCTOR OF PHILOSOPHY

in

Chemical Engineering

May, 2013

Nashville, Tennessee

Approved:

Dr. Jamey D. Young

Dr. Scott Guelcher

Dr. Matthew Lang

Dr. Vito Quaranta

To my family

Those given and chosen

ACKNOWLEDGEMENTS

This dissertation is the culmination of over four years of work and there are many people who helped to make it possible. First, I am thankful to my advisor, Jamey Young, for his support, guidance, and patience during my time at Vanderbilt. He has always encouraged me to "Research like a Champion". I am proud to be the first member of his lab and I consider it a privilege to have had such a role in blazing a path for future students. I am especially thankful for the guidance of my committee members: Matthew Lang, Scott Guelcher, and Vito Quaranta. They have helped focus my work into interesting and productive directions.

I am also grateful to all the members of the Young Lab, new and old. Special thanks to Irina without whom I would, quite literally, not be anywhere near finished with my research. Thanks to Neil, Rob, Alex, Lara, Casey, Adeola, Ali, and Young Mi. They have always been a source of fun and strength during frustrating and difficult times. Thanks also goes to the two undergraduates I mentored: Lina Aboulmouna and Jessica Campos. Their efforts were instrumental in my research and I am glad I was able to work with them. I hope they learned something and can look back at their time in the Young Lab as worthwhile and fun.

Thanks also to the many people with whom I worked during my time here. Special thanks to Akshata Udyavar, Shanshan Liu, and Mohamed Hassanein all of whom, especially in the beginning of my research, helped beyond what was necessary. Thanks to Doug Strand for collaborating with us and showing me the other side of campus. Thanks to Christine Eischen and Brian Grieb for their help in pushing the boundaries of what's possible with my research. Thanks also to Qianru Jin for the many conversations we had about life, science, and the future. I am also very grateful for the contributions of Chi Dang, who provided the P493-6 cells used in this work, and Mike Betenbaugh for his support and guidance from Johns Hopkins. I am thankful for the financial support given to this work from numerous sources including a Vanderbilt University Discovery Award, a National Institutes of Health R21 grant, an IBM Graduate Student Fellowship, and several travel awards from the Chemical and Biomolecular Engineering Department and the Graduate School.

Finally, I am beyond thankful for the support of my family and friends. I consider myself lucky to have so many people close to me that I don't have space to thank them all. I am not the same person I was when I entered graduate school and I am grateful to still have the support of so many people. Life is a rollercoaster and I'm glad I can share the journey with all of them. I love you all.

TABLE OF CONTENTS

LIST OF TABLES

LIST OF FIGURES

CHAPTER 1

INTRODUCTION

1.1 Thesis Overview

Altered metabolism inherent to cancer cells has been known since the 1924 publication of Otto Warburg's seminal report on aerobic glycolysis in rat carcinoma cells (Warburg et al., 1924). He found these cells to exhibit dramatically elevated rates of glucose uptake and lactate production in spite of abundant oxygen—a phenotype that is normally exhibited only by hypoxic cells. This phenomenon, dubbed the "Warburg effect", has been observed in multiple tumor types over the subsequent decades and is the basis for clinical FDG-PET imaging of patient tumors (Kim and Dang, 2006). Renewed interest in Warburg's findings has been sparked by numerous studies connecting multiple metabolic pathways with specific cancer phenotypes, such as the connection between isocitrate dehydrogenase 1 and acute myeloid leukemia along with succinate dehydrogenase and fumarate hydratase mutations which are linked to renal carcinoma and ganglioma (Isaacs et al., 2005; Mardis et al., 2009; Selak et al., 2005). A growing number of oncogenes have been shown to profoundly regulate metabolic activity. In particular, the *MYC* oncogene, which has been found to be dysregulated in over 30% of all cancers, was found to exert significant control over cell growth and metabolism (Dang, 2012). This link between oncogenes and metabolism, as typified by *MYC*, has solidified altered cell metabolism as a hallmark trait of cancer and also created a unique opportunity for metabolic engineering to be applied to traditional cancer research (Hanahan and Weinberg, 2011).

Despite its central importance to cancer development, the inherently dynamic nature of cellular metabolism presents unique challenges for its quantification. Traditional procedures employed in cell biology focus on determining transcript, enzyme, and metabolite concentrations. While these data are useful for distinguishing healthy and diseased states, they do not provide functional information about metabolic pathway activation and nutrient utilization. Rate-controlling metabolic enzymes are often regulated at multiple levels—transcriptionally, translationally, post-translationally, and allosterically—emphasizing that mRNA or protein abundance does not equate to pathway activity. The functional end-point of this regulation is the metabolic flux: the kinetic rate of material flow through a biochemical pathway in which metabolites are simultaneously produced and consumed. It is

therefore clear that static metabolite profiling alone will not describe the complete metabolic phenotype of a cell, and that quantitative flux maps provide a unifying framework for unambiguous interpretation of other types of 'omics' data (Sauer, 2006). Although targeted assays exist for quantification of specific metabolic reactions, they are typically limited in scope and would require the investment of substantial time and effort to characterize a large biochemical network. As a result, there is clear need for a widely available, systems-level, dynamic tool for quantitative studies of cellular metabolism. ^{13}C metabolic flux analysis (MFA) provides such a tool, which can be used to map the flow of carbon through entire biochemical networks rather than individual reactions or nodes in isolation. Comparison of flux maps obtained under varying experimental conditions or in the presence of targeted genetic manipulations provides a functional readout on the global impact these perturbations have on cell metabolism. Such information is essential to understanding how metabolic pathways are regulated in working cells—and how they become dysregulated in diseased cells. This dissertation discusses the results of research combining cancer metabolism and metabolic flux analysis in the following chapters:

- **Chapter 2** reviews the literature in several different fields. This dissertation work combines classic cancer biology studies with cutting edge metabolic engineering techniques. As such, it was necessary to review what is and isn't known about cancer metabolism, the *MYC* oncogene, the history of metabolic flux analysis (MFA) and its current state, as well as the application of MFA to cancer.

- **Chapter 3** details the analysis of extracellular fluxes and their errors. Extracellular fluxes such as glucose uptake, lactate secretion, and amino acid transport serve as the basis for intracellular flux analysis techniques such as flux balance analysis (FBA) and MFA. Estimating extracellular fluxes with as much accuracy and precision as possible is critical for increasing the confidence of estimated intracellular flux values. Most previous research does not treat error estimation with as much rigor as is required. The main result of our work in this area is the creation of a simple software package that aids in estimating fluxes from exponential and linear growth cultures.

- **Chapter 4** describes the rigorous validations steps taken to affirm the isotopically nonstationary proteinogenic MFA (INST-MFA) methodology. Due to the slow labeling of protein-bound amino acids,

ribose-bound RNA, and lipids, waiting for steady-state labeling patterns to stabilize is not feasible. Measuring the labeling during the transient period is a novel method to estimate steady-state fluxes from non-steady-state data. We compared several steady-state and non-steady-state methods to confirm that the INST-MFA method was appropriate and accurate. The method was tested on a model of B-cell cancer under High and Low c-Myc conditions.

- **Chapter 5** applies the method detailed in the previous chapter to 4 phenotypes of B-cell cancer: High and Low c-Myc levels in normoxic and hypoxic oxygen tensions. The INST-MFA method allowed for all four phenotypes to be assessed accurately. In normoxia, we confirmed our previous results detailed in Chapter 4 and increased the precision of our results. In hypoxia, we measured highly upregulated glycolytic rates along with a commensurate decrease in oxidative phosphorylation. These flux maps serve as the starting point for rational hypothesis generation geared towards specifically targeting the metabolism of cancer.

- **Chapter 6** details the targeted inhibition studies undertaken using two separate pharmacologic drugs. Based on the flux results discussed in chapters 5 and 6, we decided to target lactate formation and oxidative phosphorylation in our B-cell cancer model. Oxamate, a competitive inhibitor of lactate dehydrogenase (LDH), and phenformin, an antagonist of Complex I of the electron transport chain, were used separately and in combination. High and Low Myc cells were inhibited at multiple concentrations in a normoxic environment. Each phenotype was found to be sensitive to the drugs individually while a synergistic effect was measured when the drugs were used simultaneously.

- **Chapter 7** describes the preliminary work done to extend the INST-MFA technique to an *in vivo* mouse model of Myc-driven cancer. Preliminary analysis on the optimal tracer combination for the experiment is discussed along with the proposed methods for sample extraction and analysis.

- **Chapter 8** concludes the dissertation with a summary of the research and proposals for future work.

1.2 References

Dang CV. 2012. MYC on the Path to Cancer. *Cell* **149**:22–35.

Hanahan D, Weinberg RA. 2011. Hallmarks of cancer: the next generation. *Cell* **144**:646–674.

Isaacs JS, Jung YJ, Mole DR, Lee S, Torres-Cabala C, Chung Y-L, Merino M, Trepel J, Zbar B, Toro J, Ratcliffe PJ, Linehan WM, Neckers L. 2005. HIF overexpression correlates with biallelic loss of fumarate hydratase in renal cancer: novel role of fumarate in regulation of HIF stability. *Cancer Cell* **8**:143–153.

Kim J, Dang CV. 2006. Cancer's molecular sweet tooth and the Warburg effect. *Cancer Res.* **66**:8927.

Mardis ER, Ding L, Dooling DJ, Larson DE, McLellan MD, Chen K, Koboldt DC, Fulton RS, Delehaunty KD, McGrath SD, Fulton LA, Locke DP, Magrini VJ, Abbott RM, Vickery TL, Reed JS, Robinson JS, Wylie T, Smith SM, Carmichael L, Eldred JM, Harris CC, Walker J, Peck JB, Du F, Dukes AF, Sanderson GE, Brummett AM, Clark E, McMichael JF, Meyer RJ, Schindler JK, Pohl CS, Wallis JW, Shi X, Lin L, Schmidt H, Tang Y, Haipek C, Wiechert ME, Ivy JV, Kalicki J, Elliott G, Ries RE, Payton JE, Westervelt P, Tomasson MH, Watson MA, Baty J, Heath S, Shannon WD, Nagarajan R, Link DC, Walter MJ, Graubert TA, DiPersio JF, Wilson RK, Ley TJ. 2009. Recurring mutations found by sequencing an acute myeloid leukemia genome. *N. Engl. J. Med.* **361**:1058–1066.

Sauer U. 2006. Metabolic networks in motion: 13C-based flux analysis. *Mol. Sys. Biol.* **2**:62.

Selak MA, Armour SM, MacKenzie ED, Boulahbel H, Watson DG, Mansfield KD, Pan Y, Simon MC, Thompson CB, Gottlieb E. 2005. Succinate links TCA cycle dysfunction to oncogenesis by inhibiting HIF-alpha prolyl hydroxylase. *Cancer Cell* **7**:77–85.

Warburg O, Posener K, Negelein E. 1924. On the metabolism of carcinoma cells. *Biochem. Zeit.* **152**:309–344.

CHAPTER 2

BACKGROUND AND LITERATURE REVIEW

2.1 Cancer and Metabolism

Cancer is second only to heart disease as the leading cause of adult death in the United States making its treatment and prevention of utmost importance (American Cancer Society, 2012). The pace of cancer research in the past several decades has escalated dramatically leading to new insights and novel therapies (Vander Heiden, 2011). In particular, the metabolism of cancer is in a renaissance of research after having fallen out of vogue. In the late 1920's, Otto Warburg discovered through the study of rat carcinoma that the metabolism of cancer is shifted to fermentation in the presence of oxygen (Warburg et al., 1924). Fermentation typically only occurs when oxygen is a limiting factor as it is in tissues that are far from oxygen-carrying blood vessels. This hypoxic environment stimulates the switch from a primarily oxidative, and thereby energy-efficient behavior, to one that is less efficient and energy poor (Semenza, 2010). Typically, full oxidative phosphorylation (OXPHOS) of 1 mole of glucose in the TCA cycle will yield up to 36 moles of ATP whereas only 2 moles of ATP are generated through glycolytic fermentation of 1 mole of glucose. This means the glycolytic rate is going to be much higher to compensate for the decrease in efficiency. Originally, this switch to glycolytic metabolism in the presence of oxygen, known as the Warburg effect, was thought to occur because of inherent defects in the mitochondria of cancerous cells (Warburg, 1956), but that hypothesis has since been disproven with the discovery of tumors that have fully functional, and even *over*-active, mitochondria (Zu and Guppy, 2004). Tumors do, however, typically have increased glycolytic activity (Fig. 2.1), a feature which has been useful in the imaging of tumors through the use of ^{18}F-deoxyglucose positron emission topography (FDG-PET) (Vander Heiden et al., 2009). Previously, the metabolism was thought to be a curious side effect of the cancerous phenotype: altered only as a byproduct of the other dysregulations occurring in the cell (Hanahan and Weinberg, 2000). Indeed, only in the past few years has altered cell metabolism come to be seen as a *potential* hallmark of cancer (Hanahan and Weinberg, 2011). More evidence, however, has led to the appreciation of the primary role metabolism plays in supporting and influencing the survival of cancer cells with the discovery of oncogenes that directly control metabolism as well as putative "oncometabolites" that may play a significant role in cancer development (Hsu and Sabatini, 2008).

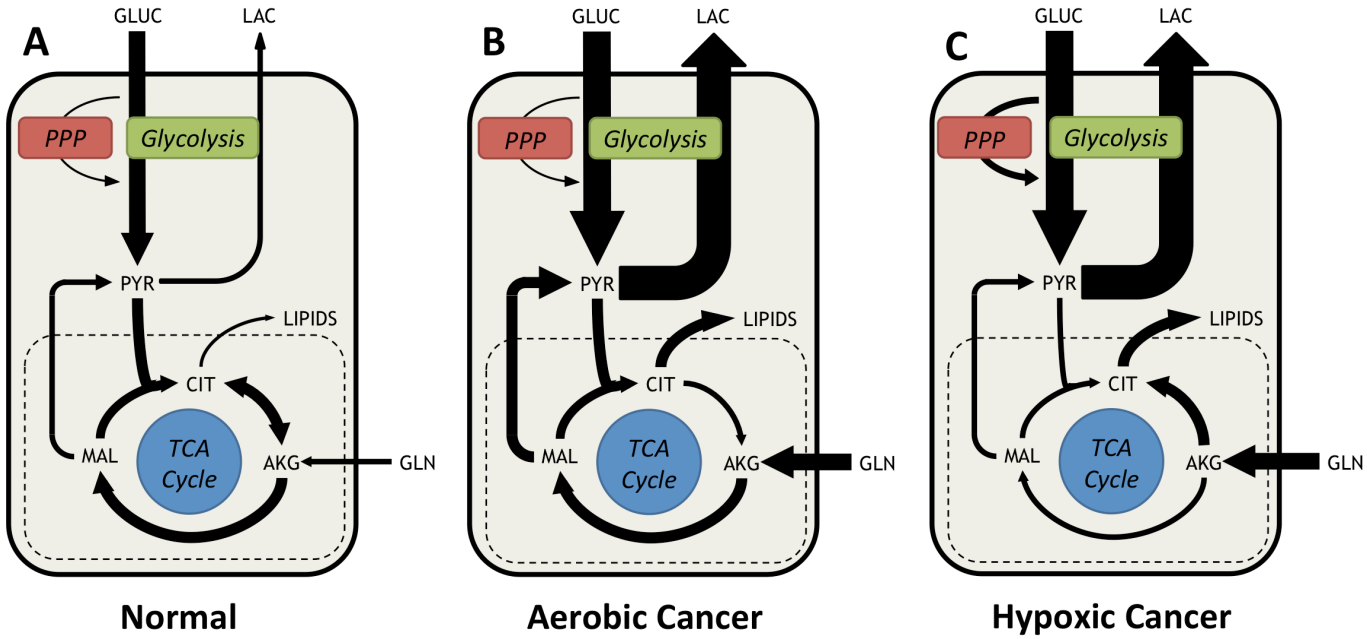

Figure 2.1. Metabolic Phenotypes of Normal Versus Cancer Cells. (A) In normal cells under aerobic conditions, the majority of glucose consumed is fully oxidized in the TCA cycle to generate CO_2 and to supply ATP. Lactate excretion and amino acid catabolism are minimal. **(B)** In cancerous cells, metabolism is rewired depending on oncogenic activation and environmental factors. Cancer cells increase their glycolytic flux by as much as 10-fold relative to normal cells. However, cancer cells grown in abundant oxygen and nutrients will typically maintain active mitochondrial respiration, fueled largely by elevated glutamine consumption. **(C)** *In vivo* tumors are subjected to varying oxygen tensions. In hypoxic environments, tumor cells adapt their energetic metabolism to generate ATP exclusively from glycolysis. However, mitochondria still provide key biosynthetic intermediates such as citrate for lipid synthesis. Glutamine metabolism may be redirected into reductive carboxylation to supply anaplerotic carbon directly to the citrate pool. One key point is that extracellular nutrient uptake and product excretion rates may not appear substantially different between panels **(B)** and **(C)**, but isotope tracers and metabolic flux analysis enable detection of flux rerouting through intracellular metabolic pathways even in cases where extracellular rates are unchanged.

The development of cancer has two interconnected paths: oncogene activation and loss of tumor suppressors (Hsu and Sabatini, 2008). The most well-established tumor suppressor is protein 53 (p53), so named for its characteristic weight of 53-kilodaltons. P53 has a primary role in regulating cell cycle, and patients who have mutated p53 have a higher propensity to form tumors earlier in life (Bensaad and Vousden, 2007). *In vivo*, p53 knockdown or mutation isn't typically enough to induce a cancer-like phenotype, and its knockdown must be coupled with overexpression of tumor promoting genes such as Ras, PI3K, and Myc to initiate spontaneous cancers (Jones and Thompson, 2009). Many of these oncogenes are related in that they phosphorylate each other, target similar aspects of biology, or they engage in cross talk through coregulation of common signaling molecules. Ras, for example, is a part of the mitogen activated protein kinase (MAPK) signaling cascade that affects cell proliferation, growth, and survival (Pylayeva-Gupta et al., 2011). Myc, a major part of this dissertation work, can also be activated by the MAPK signaling pathway.

In addition to oncogenic alterations that lead to tumorigenesis, it is also possible for cells to obtain a proliferative advantage through metabolic adaptations (Ward and Thompson, 2012). One of the most prominent alterations under study right now is the alternative splicing of pyruvate kinase (PK) isoforms. Pyruvate kinase, an enzyme in glycolysis, converts phosphoenolpyruvate (PEP) to pyruvate and has two different isoforms (muscle and liver/erythrocyte) (Fig 2.2). The muscle isozyme can splice into forms 1 and 2 (PKM1 and PKM2) with the M1 isoform having a greater enzymatic activity than M2 (Christofk et al., 2008; Mazurek, 2011). The PKM2 isoform has been shown to be universally expressed in proliferating cells including cancerous and embryonic tissue. It's somewhat paradoxical that the lower activity isoform is expressed, but evidence has been discovered to show that the lower activity supports anabolic synthesis of metabolites in the earlier stages of glycolysis (i.e., nucleotides and possibly glycerol synthesis) (Anastasiou et al., 2012; Dang, 2009; Mazurek et al., 2000). This is further evidence that the preferential expression of the M2 isoform of pyruvate kinase can help a cell select for a more favorable phenotype for tumorigenesis.

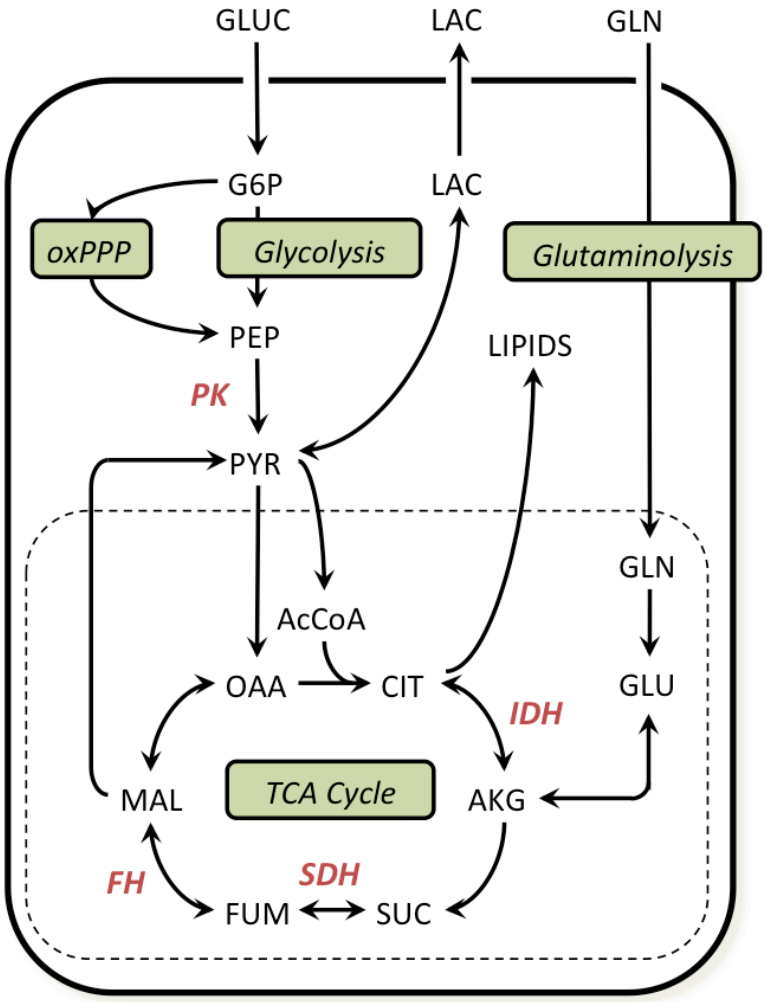

Figure 2.2 A Simplified Description of Central Metabolism. A simplified version of glycolysis, oxidative pentose phosphate pathway (oxPPP), the TCA cycle, and glutaminolysis are shown. Specific enzymes discussed in the text are highlighted in red. Abbreviations: glucose (GLUC), lactate, (LAC), glutamine (GLN), glutamate (GLU), glucose-6-phosphate (G6P), phosphoenolpyruvate (PEP), pyruvate (PYR), oxaloacetate (OAA), Acetyl Coenzyme-A (AcCoA), citrate (CIT), α-ketoglutarate (AKG), succinate (SUC), fumarate (FUM), malate (MAL), pyruvate kinase (PK), isocitrate dehydrogenase (IDH), succinate dehydrogenase (SDH), fumarate hydratase (FH)

Another example of altered metabolism being strongly selected for during tumorigenesis is the discovery of mutations in the isocitrate dehydrogenase 1 gene (*IDH1*) (Dang et al., 2009b). Mutations in this gene are known to be prevalent in glioma as well as acute myeloid leukemia (AML) (Mardis et al., 2009). IDH1 is a cytosolic, $NADP^+$-dependent enzyme that interconverts isocitrate with alpha-ketoglutarate (αKG) (Fig 2.2). When mutations in *IDH1* occur, there is a loss of typical enzyme function. However, it was discovered that the mutation could also cause gain of function through production of the novel metabolite 2-hydroxyglutarate (2HG). It was also discovered that mutations in *IDH2* can lead to the accumulation of 2HG, making the metabolite a possible biomarker for the disease (Reitman and Yan, 2010). Much work has been done lately to determine the exact role of 2HG in tumorigenesis. There is evidence that 2HG can impair normal epigenetic regulation and cell differentiation (Dang et al., 2009b). 2HG has some role to play in these disease states and more work is required to elucidate the specific role of this metabolite in tumorigenesis.

IDH mutations have received much of the attention in the past few years, but it's not the only mutation known to occur in metabolic enzymes. Mutations in succinate dehydrogenase (SDH) (Selak et al., 2005) and fumarate hydratase (FH) (Isaacs et al., 2005), both enzymes in the TCA cycle, have been known to occur in multiple types of cancers including renal carcinoma and ganglioma. These are both loss-of-function mutations that lead to an accumulation of their corresponding substrate (succinate or fumarate) (Fig 2.2). There is evidence suggesting that both metabolites can affect metabolism in additional ways including the inhibition of other enzymes, such as prolyl hydroxylase 2 (PHD2) in the case of succinate, and altering transcription, as in the case of fumarate negatively regulating the Nrf2 transcription factor (Adam et al., 2011). The discoveries made with 2HG and IDH mutations, along with the mutations in SDH and FH, provide strong evidence that metabolism plays a central role in tumorigenesis and has the potential to be targeted for therapeutic intervention.

In the past, metabolism has been successfully targeted, although not in the most rational manner. There have been several accidental discoveries that specific drugs targeting metabolism affect survival rates in cancer patients. Metformin, an inhibitor of Complex I in the electron transport chain (ETC), was shown in a meta-analysis to have pro-survival effects in diabetic patients (Evans et al., 2005). It's not wholly clear whether the effect was due to metformin specifically or rather by a decrease in insulin levels. Folates are another class of drugs that target

enzymes in metabolism and have been used in a wide variety of tumors (Chabner and Roberts, 2005; Scott, 1970). L-asparaginase, an enzyme that limits the availability of asparagine to the cell, has been used successfully in acute lymphoblastic leukemia (ALL) due to the propensity of this cancer type to be auxotrophic with respect to asparagine and glutamine (Neuman and McCoy, 1956). Clearly, there is therapeutic potential in metabolism for many cancers, especially when the specific genetic alterations are known and it's understood how those alterations affect metabolic phenotypes. Rationally determining how to target these alterations and their manifestations in metabolism by understanding the differences between normal and cancer cells is of great importance. Several groups in the past few years have worked to predict drug targets and their effects using large-scale network modeling (Facchetti et al., 2012; Folger et al., 2011; Li et al., 2010). The combined efforts of computational modeling and hypothesis-driven experimental validation using isotope tracers and metabolic flux analysis, under the umbrella of 'metabolomics', has the potential to dramatically increase the pace of drug discovery and understanding in the coming years (Fan et al., 2012).

2.2 *MYC* and Metabolism

Of particular interest to this dissertation work is the *MYC* oncogene. *MYC* encodes the transcription factor c-Myc (herein termed Myc), and it has been found to exhibit altered or deregulated expression in close to 40% of all cancers (Dang, 2012; Gardner et al., 2002). Myc plays a central role in growth and proliferation of normal, cancer, and stem cells with its involvement in many aspects of metabolism and the cell cycle, including transcription, translation, glycolysis, and glutaminolysis (Dang, 1999). It's been shown that Myc can bind to ~30% of all genes but only a small fraction of those will respond to Myc alone (Dang, 2010). Myc can also regulate microRNAs and cooperate with other proteins, such as the hypoxia inducible factor 1 (HIF-1), to regulate and conduct cell metabolism (Dang et al., 2008).

Myc is a helix-loop-helix (two α-helices connected by a loop) leucine zipper (dimer binding domain) transcription factor that requires dimerization with Max to bind to specific consensus sequences (CACGTG) termed E-boxes (Amati et al., 1992). Typically, Myc is regulated by normal cell circuitry such as growth factor signaling, but this ability is lost in many cancer cells (Dang, 2011). If expression of Myc is activated and dissociated from normal signals, proteins such as p53 and p19-ARF (alternate reading frame) will trigger cell cycle arrest, apoptosis, or

senescence. Therefore, loss of function of these proteins is required for Myc-mediated lymphomagenesis (Miller et al., 2012).

Myc has been well-established as a key player in many aspects of cell biology (Dang, 2010) (Fig 2.3). Central to the work presented here is the role of Myc in energy and biosynthetic metabolism (Morrish et al., 2009). It was discovered in the 1990s that Myc directly targets the lactate dehydrogenase A gene (*LDHA*) which encodes an enzyme that converts pyruvate to lactate with NADH as a cofactor (Shim et al., 1997). In subsequent years, Myc was found to target many other glycolytic genes including *GLUT1, HK2, PFKM, TPI1, GAPD,* and *ENO1* (Kim et al., 2004; Osthus et al., 2000). It would stand to reason that Myc would also bind to genes controlling aspects of amino acid metabolism, which directly feeds off glycolysis. However, only one gene involved in amino acid metabolism is known to be under direct Myc control: serine hydroxylmethyltransferase 2 (*SHMT2*) (Nikiforov et al., 2002). This enzyme converts serine to glycine and MEETHF (methylenetetrahydrofolate), which is important for anabolic pathways such as nucleotide synthesis, a pathway also controlled by Myc (Liu et al., 2008).

The direct control Myc has on glycolysis has created an opportunity for targeted inhibition. Many studies have inhibited LDHA either genetically or pharmacologically and have found some success (Fantin et al., 2006; Le et al., 2010; Xie et al., 2009). Indeed, further in this dissertation we will see how targeting the enzyme with oxamic acid affects the growth of Myc-driven cells. But just as important as Myc's control over glycolysis is its influence on the TCA cycle and mitochondrial metabolism. One of two primary carbon sources for the TCA cycle is glutamine (the other being glucose-derived pyruvate) (Vander Heiden et al., 2009). Glutamine is essential for the growth of many Myc-driven tumors, such that the cells are "addicted" to the amino acid, and they will become apoptotic if deprived of it (Dang et al., 2009a). Myc targets glutaminase (GLS), which converts glutamine to glutamate with concurrent production of ammonia, as well as glutamine transporters ASCT2 and SLC7A25 (Fig 2.3) (Gao et al., 2009; Wise et al., 2008). Additionally, Myc has also been shown to stimulate mitochondrial biogenesis through correlation analysis of gene expression in Myc-driven cells (Li et al., 2005). Mitochondrial mass and function have also been shown to correlate with Myc expression through gain- and loss-of-function studies (Dang, 2012).

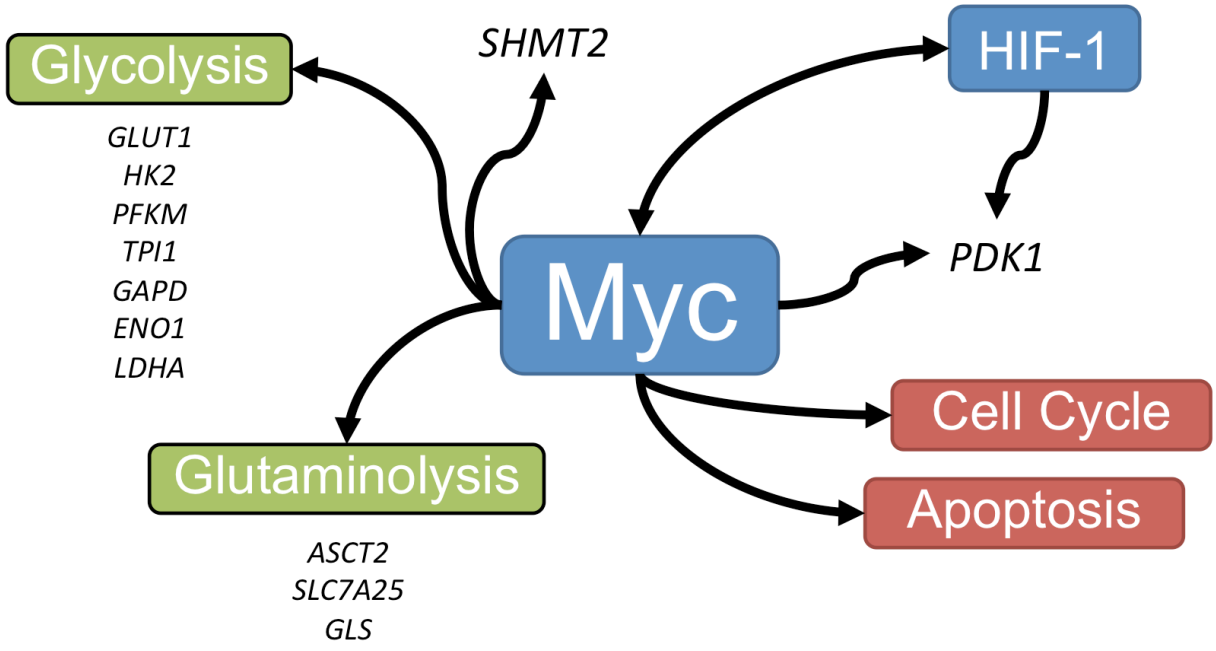

Figure 2.3 Interactions of Myc. Myc has a diverse range of interactions and influences many parts of a cell's phenotype. Boxes highlighted in green indicate metabolic pathways. Blue boxes are transcription factors. Italicized text indicates gene interaction. Red boxes indicate cell programs.

Myc also interacts with HIF-1 to control pyruvate dehydrogenase kinase 1 (PDK1) (Gordan et al., 2007). PDK1 phosphorylates and deactivates pyruvate dehydrogenase (PDH), an enzyme that converts pyruvate to Acetyl-CoA and CO_2 and is the first step in the TCA cycle. Under hypoxic conditions, HIF-1 upregulates PDK1 expression, which is further increased by Myc, to direct cells into a glycolytic phenotype. HIF-1 also targets many of the same genes as Myc, which has led to the examination of the interplay between these two proteins. Under hypoxic conditions, the HIF-1α subunit is stabilized and binds with the constitutively expressed HIF-1β subunit. Together, they form a transcription factor that supports cell growth in low oxygen environments (Semenza, 2010). When a cell is not cancerous, HIF1 blunts the effectiveness of Myc through a complicated, and not fully understood, combination of binding and interaction. However, ectopic Myc expression *in vivo*, along with HIF expression, was shown to increase tumor size, suggesting an interaction between the two transcription factors (Kim et al., 2007). Because hypoxia is a major factor in many tumors due to an increased physical distance from blood supply, understanding how Myc and HIF interact is of critical importance.

It's clear from many of the previous studies that Myc exerts significant control over metabolism. There have been several prominent studies that highlight the effectiveness of targeting metabolism, but a larger picture of the full-scale metabolic network has not yet been realized. Much of the work in this dissertation is spent attempting to understand quantitative measurements of the differences in the metabolism of normal cells and their cancerous, Myc-driven phenotypes, so that we can identify new, rationally chosen therapeutic targets.

2.3 Metabolic Flux Analysis (MFA)

Key to studying metabolism in the past twenty years has been the implementation of a technique called metabolic flux analysis (MFA) (Wiechert, 2001). A flux is defined as the rate of flow of material through a metabolic pathway at steady state (Stephanopoulos, 1999). Fluxes are fundamental determinants of cell physiology because they are the functional endpoint of the cellular phenotype as defined by the genome, transcriptome, proteome, and metabolome (Nielsen, 2003; Sauer, 2006). As such, these quantitative measurements represent important parameters describing of the metabolic state of a cell.

2.3.1 Advances in MFA

A specific application of MFA is the technique called flux balance analysis (FBA) or stoichiometric MFA (Niklas and Heinzle, 2012). In FBA, only stoichiometric constraints are used to estimate intracellular fluxes. This works quite well in simple systems where there are only linear or diverging pathways (Fig 2.4). However, this method fails when there are parallel, cyclic, or bidirectional pathways. Linear programming techniques, thermodynamic constraints, and conserved balances of cofactors such as ATP and NAD(P)H can help, but these additions are still unable to determine bidirectional, also called exchange, fluxes (Bonarius et al., 1997; Stephanopoulos, 1999) and they are inferior compared to the addition of isotopic labeling measurements (Niklas and Heinzle, 2012). It is necessary to add additional constraints to the system in order to estimate the nonlinear pathways and make the system determined, if not overdetermined (Fig 2.4).

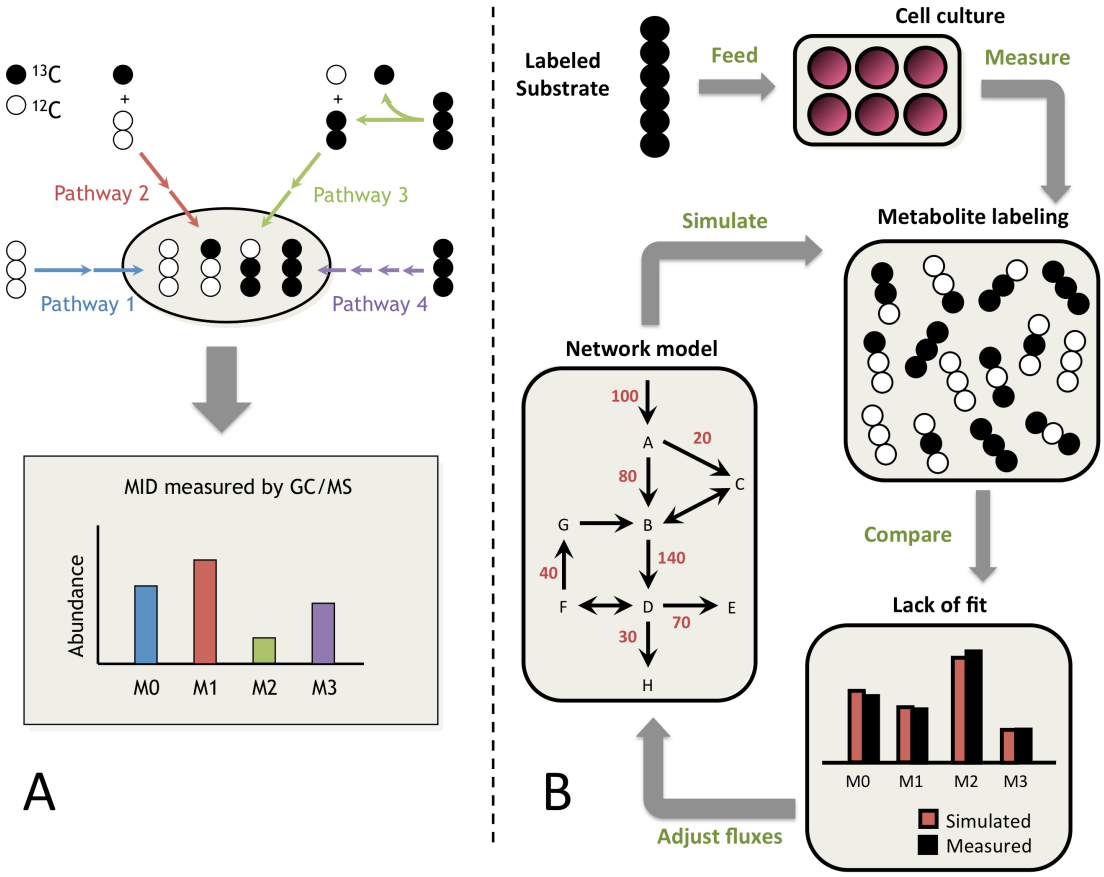

Figure 2.4. Isotope Tracing and ^{13}C-Metabolic Flux Analysis. (A) In simple metabolic networks, each pathway produces a unique labeling pattern in the final product, and the resulting mass isotopomer distribution (MID) provides a direct measure of relative flux in the network. Mass isotopomers are molecules with the same chemical formula but different molecular weights due to varying incorporation of heavy isotopes. They are denoted M0, M1, M2, etc. in order of increasing weight. **(B)** In complex networks, a computational model is applied to determine fluxes by minimizing the lack of fit between simulated and measured labeling patterns at multiple pathway nodes. The flux parameters in the model are iteratively adjusted until the optimization converges.

The best method used to date is the addition of isotopically labeled substrates. Using isotope tracers, such as ^{13}C, allows for additional constraints to be placed upon the estimation after measurement of the steady-state labeling patterns. Other tracers can be used, such as ^{2}H or ^{15}N, but ^{13}C remains the most popular. Carbon-13 tracers are popular because of their lower cost, stability, and they tend to provide very rich data sets (Gomes and Simoes, 2012). When a cell is fed an isotopically labeled substrate, the labeling becomes incorporated into intracellular metabolites as well any macromolecules derived from these metabolites. After some time, the labeling in the cells reaches a steady-state at which point the molecules of interest can be extracted and their labeling patterns measured by nuclear magnetic resonance (NMR) or mass spectrometry (MS) (Fig 2.4).

Much of the work with MFA and labeled tracers has shifted to MS techniques, particularly GC-MS (gas chromatography / mass spectrometry) (Wittmann and Heinzle, 1999). NMR is a powerful technique because it can return information about the specific position of labeled atoms. However, there are drawbacks in that the instruments are typically very expensive compared to MS and the amount of sample required can be prohibitive. MS has emerged as the prominent technique because it has a high signal-to-noise ratio for a lower sample volume (Dauner and Sauer, 2000). The drawback of MS, however, is that it can only describe the mass isotopomer distribution (MID). An isotopomer is an isomer of a molecule that has specific atoms (such as hydrogen, oxygen, nitrogen, or carbon) with additional neutrons and the MID is the abundance distribution of isotopomers that have different weights (M0 fragments have zero labeled atoms, M1 fragments have one of their atoms labeled, etc.) (Wiechert, 2001). This is still very usable data because the distribution of the labeling pattern is unique for each flux distribution and will reach a steady-state once the cell has grown for a sufficient period of time at a metabolic pseudo-steady-state. The MID of each measured metabolite provides additional constraints on the feasible flux space (Zamboni et al., 2009).

The modeling of isotope distributions adds another layer of complexity to the flux estimation. When ^{1}H-NMR is used, the positional abundance of isotopically enriched hydrogens within a molecule can be known and the data is easily analyzed with linear algebra using atom mapping matrices (AMM) (Zupke and Stephanopoulos, 1994). For ^{13}C-NMR or MS data the AMM method is not suitable because both of these methods can return MID data. The isotopomer mapping matrix (IMM) method was developed to extend the AMM method to MID data. This was an

inefficient technique that required massive computing power to solve nonlinear equations. For each molecule, there are 2^N possible isotopomers. So, for a 3-carbon molecule there are 8 possible ways it can be labeled but this number increases more if non-carbon atoms are included, such as oxygen and hydrogen. For large systems, including all possible isotopomers can be cumbersome and unnecessary. Advances were made in simplifying the calculations with the introduction of cumomers which reduce the nonlinear equations generated via IMM to a series of linear equations (Schmidt et al., 1997; Wiechert et al., 1999). Most recently, the elementary metabolite unit (EMU) method was introduced to further simplify the analysis (Antoniewicz et al., 2007). This method identifies the minimum amount of information required to fully describe the data and is considered a bottom-up approach where as IMM and cumomer methods are a top-down approach. For a particular MID, only the EMUs necessary to simulate the data are defined. This significantly reduces computation time by decreased the number of equations to be solved by an order of magnitude and it also allows for multiple tracers to be used in labeling experiments. EMUs are part of the underpinnings for all of the ^{13}C-MFA work presented here.

Another significant advance in MFA is the extension of the technique to isotopically nonstationary systems (Young et al., 2008). Typically, the labeling patterns are allowed to reach a steady-state before extraction and analysis. However, this is either sometimes not feasible, in the case of slow-growing cells, or not useful, in the case of autotrophic systems, which only use CO_2 as their primary carbon source (Schwender, 2008). The development of isotopically nonstationary MFA (INST-MFA) techniques have been created to overcome some of these issues (Wiechert and Nöh, 2005). Mathematically, this adds a time variable to the estimation creating a set of ordinary differential equations as opposed to a set of algebraic balance equations. INST-MFA requires greater sampling and more sophisticated techniques but it has the potential of delivering more information with increased accuracy (Hofmann et al., 2008; Maier et al., 2008; Nöh and Wiechert, 2011; Shastri and Morgan, 2007). Some groups are even utilizing parallel labeling experiments to gain even more accurate information about the metabolism (Ahn and Antoniewicz, 2013; Leighty and Antoniewicz, 2012). The nonstationary technique will be described in more detail and further validated for our application to cancer cells in chapter 4.

2.3.2 Basic Mathematical Principles of MFA

One of the fundamental assumptions of metabolic flux analysis is that the cell is in a pseudo-steady-state condition (Zamboni, 2011). This means that there is no accumulation of intermediate metabolites and that, over the measurement time-span, the metabolism is essentially constant. For quiescent cells this holds true quite well. For growing cells, this assumption can be true if cells are growing exponentially. As long as there is no inhibition of the cell by secreted products, cell-to-cell contact, or nutrient deprivation, this assumption is true. However, this condition does not hold in the times when the cell is transitioning to an alternate growth-phase or when a significant portion of the cell population is undergoing cell death (Niklas et al., 2011). Another basic assumption is the dilution effects on metabolites due to cell growth are minimal and can be ignored. Again, this is a valid assumption in most cases.

Given the previous assumptions, it can be deduced that the sum of fluxes going into a cell must be equal to the sum of fluxes exiting a cell plus the consumption of material for anabolic growth. The same holds true for an internal metabolite. As such, the mass balance equation to solve is:

$$S \cdot v = 0, \tag{2.1}$$

where S is the stoichiometric matrix and v is the flux vector. Each row of S represents the mass balance on an internal metabolite and each column corresponds to a flux in v (Fig 2.5). There are N-M degrees of freedom (F) in the system where N is the number of fluxes and M is the number of balanced metabolites. If we measure exactly F fluxes, then the system is determined and there is a unique solution. If there are fewer than F fluxes to measure then the system is underdetermined and additional constraints, such as linear programming or isotopic labeling data, must be placed on the system to estimate the fluxes. If the number of measured fluxes is greater than F, then the system is overdetermined and it becomes possible to assess the quality of the data and increase the accuracy of the measured values. In all cases discussed in this work, the system becomes overdetermined with the addition of isotope labeling data along with the extracellular flux measurements.

The approach used in this dissertation is INST-MFA with EMUs forming the basis of the estimation. In this case, the math is more complex than the simple example presented in Fig. 2.5. The balances are now ordinary differential

equations, instead of linear algebraic equations, and require more computational effort to solve. At the heart of the flux estimation is the minimization of the difference between measured and simulated data according to the following equation:

$$\min_{\mathbf{u},\mathbf{c}}\phi = [\mathbf{m}(\mathbf{u},\mathbf{c},\mathrm{t}) - \hat{\mathbf{m}}(t)]^T \cdot \sum_m^{-1} \cdot [\mathbf{m}(\mathbf{u},\mathbf{c},\mathrm{t}) - \hat{\mathbf{m}}(t)] \quad (2.2)$$

$$\text{s.t. } \mathbf{N}\cdot\mathbf{u} \geq 0, \mathbf{c} \geq 0$$

where ϕ is the objective function to be minimized, $\mathbf{u}$ is a vector of free fluxes, $\mathbf{c}$ is a vector of metabolite concentrations, t is time, $\mathbf{m}(\mathbf{u},\mathbf{c},\mathrm{t})$ is a vector of simulated measurements, $\hat{\mathbf{m}}$ (t) is a vector of observed measurements, $\Sigma_{\mathbf{m}}$ is the measurement covariance matrix, and $\mathbf{N}$ is the nullspace of the stoichiometric matrix. A reduced gradient method can be implemented to handle the linear constraints of this problem within a Levenberg-Marquardt nonlinear least-squares solver (Jazmin and Young, 2013; Young et al., 2008). Alternatively, gradient-free optimization approaches have been applied by Noh et al (2006).

Simulated metabolite labeling data are generated by solving the forward problem. After the EMUs in a system have been enumerated, they are organized into mutually dependent blocks via a Dulmage-Mendelsohn decomposition (Dulmage and Mendelsohn, 1958; Pothen and Fan, 1990). The decoupled blocks are then arranged into a cascaded system of ODEs with the following form:

$$\mathbf{C}_n \cdot \frac{\mathrm{d}\mathbf{X}_n}{\mathrm{d}t} = \mathbf{A}_n \cdot \mathbf{X}_n + \mathbf{B}_n \cdot \mathbf{Y}_n \quad (2.3)$$

Level n of the cascade represents the network of EMUs within the nth block. The rows of the state matrix $\mathbf{X}_n$ correspond to MIDs of EMUs within the nth block. The input matrix $\mathbf{Y}_n$ is analogous but with rows that are MIDs of EMUs that are previously calculated inputs to the nth block (or MIDs of source EMUs that are unbalanced). The concentration matrix $\mathbf{C}_n$ is a diagonal matrix whose elements are pool sizes corresponding to EMUs represented in $\mathbf{X}_n$. The system matrices $\mathbf{A}_n$ and $\mathbf{B}_n$ describe the network as follows:

$$\mathbf{A}_n(i,j) = \begin{cases} -\text{sum of fluxes consuming } i\text{th EMU in } \mathbf{X}_n & i = j \\ \text{flux to } i\text{th EMU in } \mathbf{X}_n \text{ from } j\text{th EMU in } \mathbf{X}_n & i \neq j \end{cases} \tag{2.4}$$

$$\mathbf{B}_n(i,j) = \{\text{flux to } i\text{th EMU in } \mathbf{X}_n \text{ from } j\text{th EMU in } \mathbf{Y}_n \tag{2.5}$$

After starting estimates of the fluxes and pool sizes are provided, equation 2.3 can then be integrated using standard ODE numerical solvers or more specialized algorithms detailed in Young et al. (2008). Solving the inverse problems requires, as previously mentioned, a gradient method to inform the optimization algorithms about the best search direction. The most accurate method of doing this by integrating a system of sensitivity equations whose solution describes how the calculated MIDs vary in response to changes in the model parameters. The following sensitivity equation comes via implicit differentiation of equation 2.3:

$$\frac{\mathrm{d}}{\mathrm{d}t}\frac{\partial \mathbf{X}_n}{\partial \mathbf{p}} = \mathbf{C}_n^{-1} \cdot \mathbf{A}_n \cdot \frac{\partial \mathbf{X}_n}{\partial \mathbf{p}} + \frac{\partial\left(\mathbf{C}_n^{-1} \cdot \mathbf{A}_n\right)}{\partial \mathbf{p}} \cdot \mathbf{X}_n + \mathbf{C}_n^{-1} \cdot \mathbf{B}_n \cdot \frac{\partial \mathbf{Y}_n}{\partial \mathbf{p}} + \frac{\partial\left(\mathbf{C}_n^{-1} \cdot \mathbf{B}_n\right)}{\partial \mathbf{p}} \cdot \mathbf{Y}_n \tag{2.6}$$

where **p** is the vector of adjustable flux and pool size parameters.

The end result of this estimation, assuming the inputs fluxes and labeling measurements are accurately estimated and the model correctly describes the biologic phenotype, is a map that details the rates of intracellular reactions. From this data, the overall fit of the estimation can be assessed along with the goodness-of-fit of each measurement and the overall contribution of each measurement to the precision of the estimated fluxes (Jazmin and Young, 2013).

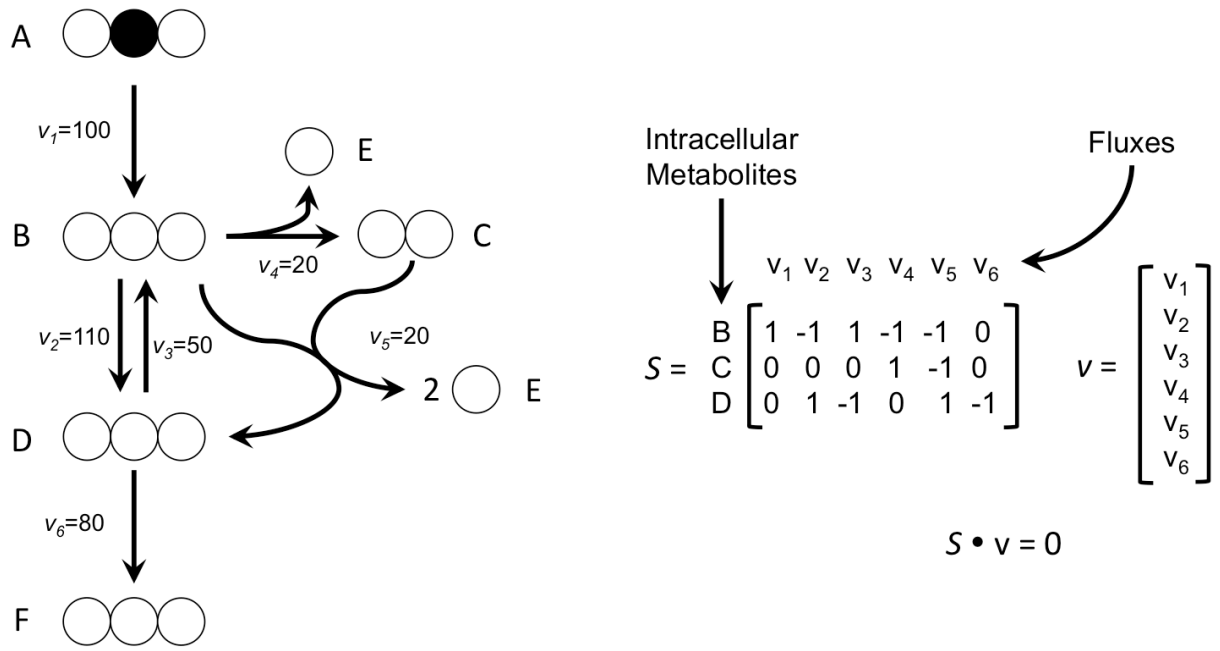

Figure 2.5. Simple Example Network Detailing the Stoichiometric Matrix and Flux Vector. The above simple metabolic network is given to demonstrate the construction of the stoichiometric matrix (S) and the flux vector (v).

2.3.3 Applications of MFA

Prior to the past decade, MFA, and metabolic engineering in general, was applied mainly to prokaryotic cells (Stephanopoulos, 1999). Prokaryotes are simpler systems that lend themselves to less complicated network models, growth mediums, assumptions, and experiments. The transition to eukaryotic cells has been challenging because mammalian cells grow on a variety of substrates, are subject to internal compartmentation, have slower growth rates, and require assumptions that are more stringent and oftentimes less true (Niklas et al., 2010; Quek et al., 2010; Zamboni, 2011).

Typical application of MFA in mammalian systems has been limited to the study of the production of vaccines and complex proteins like monoclonal antibodies (MAbs) (Genzel and Reichl, 2009; Seth et al., 2006; Wurm, 2004). This work has historically been done in CHO or hybridoma cell lines. Production of these proteins in mammalian systems is preferred primarily because of post-translational modifications that occur only in eukaryotic cells, and MFA is usually used in these cases for process optimization purposes. Of particular interest to this dissertation work

is the application of MFA to medical research. MFA has been applied to the study of diabetes, brain metabolism, as well as cancer with interesting results discovered in all cases (Niklas and Heinzle, 2012).

2.4 MFA and Cancer

The application of flux analysis to cancer metabolism has emerged only in the past ten years with the advances in modeling techniques detailed previously (Keibler et al., 2012). Even though Warburg detailed the metabolic phenomenon known as aerobic glycolysis in tumors in 1924 in rat tumors (Warburg et al., 1924), and with the exception of a few studies done in the following decades, it wasn't until the early 21st century that the post-genomic era truly started to take hold and other 'omics, such as transcriptomics, proteomics, and in particular, metabolomics were appreciated and accepted within the scope of cancer (Griffin and Shockcor, 2004). Many studies over the years used radioactive isotope labels to elucidate alterations in metabolism (Bier et al., 1977; Lorber et al., 1945), but it wasn't until the 80s and 90s that the tracers were applied to cancer metabolism in earnest (Kelleher et al., 1987). It was around that same era that the use of *stable* isotopic tracers (namely carbon-13) came into prominence (Hellerstein et al., 1991; Hellerstein, 2004).

2.4.1 Metabolic Pathway Discovery

In the past five years alone, several studies have used stable isotopic tracers along with MFA (See Figure 2.3). Hunnewell et. al. (2010) analyzed *ras*-transormed fibroblast spheroids to determine the activity of specific metabolic pathways. They used 1-^{13}C glucose and GC-MS techniques to measure the labeling of intracellular metabolites, such as PEP and 3PG, and intracellular amino acids. The MIDs of each metabolite is indicative of the active (or inactive) pathways in the cell. Some of their major conclusions were that glutamine is used primarily for biosynthetic purposes, rather than energy creation, and gluconeogenic pathways were inactive. Also of interest was the lack of malic enzyme (ME) activity. ME is important for creating reducing equivalents in the form of NAD(P)H (Chang and Tong, 2003). This study did not use true MFA even though extracellular measurements were gathered along with labeling data. (MFA is the combination of these data to estimate intracellular fluxes).

Akin to the previous study, several independent groups have discovered an alternate use for glutamine in cells that are grown in hypoxic conditions or have their electron transport chain inhibited in some manner (Metallo et al.,

2012; Mullen et al., 2012; Wise et al., 2011). Without the use of tracers, the changes that occurred in these cells would not have been evident based on the extracellular measurements alone. It was only through the measurement of MIDs derived from differently labeled substrates (^{13}C-labeled glutamine and glucose) that these cells were found to use reductive carboxylation to meet the biosynthetic requirements of the cell. Reductive carboxylation is the shuttling of glutamine-derived alpha-ketoglutarate to citrate via isocitrate dehydrogenase and aconitase enzymes working in reverse of their typical behavior (See Figure 2.6). This physiology was discovered by measuring labeling patterns in citrate and lipids that could not be derived from the typical oxidative behavior of the TCA cycle. This clearly indicates the power of using isotopic tracers in cancer metabolism.

The use of serine biosynthetic pathways in cancer was also discovered through the use of isotope tracers. While it has been known that cancer cells use serine biosynthetic pathways, how it was linked to promoting cancer growth was not fully understood (Kit, 1955). Two separate groups discovered that phosphoglycerate dehydrogenase (PHDGH) was essential in the growth of breast cancer and melanoma (Locasale et al., 2011; Possemato et al., 2011). PHDGH directs 3-phosphoglycerate from glycolysis towards serine biosynthesis (See Figure 2.3). Through the use of isotopically labeled glucose and glutamine, the groups discovered that, even in the presence of excess serine, carbon is still shunted from glycolysis towards serine synthesis. It was also found that alterations in TCA cycle activity (namely through a decrease in αKG metabolite levels) occurred when PHDGH activity was inhibited via shRNA. This non-intuitive linking evidences the complex nature of metabolism; a discovery that could only be done through the use of isotopically labeled tracers.

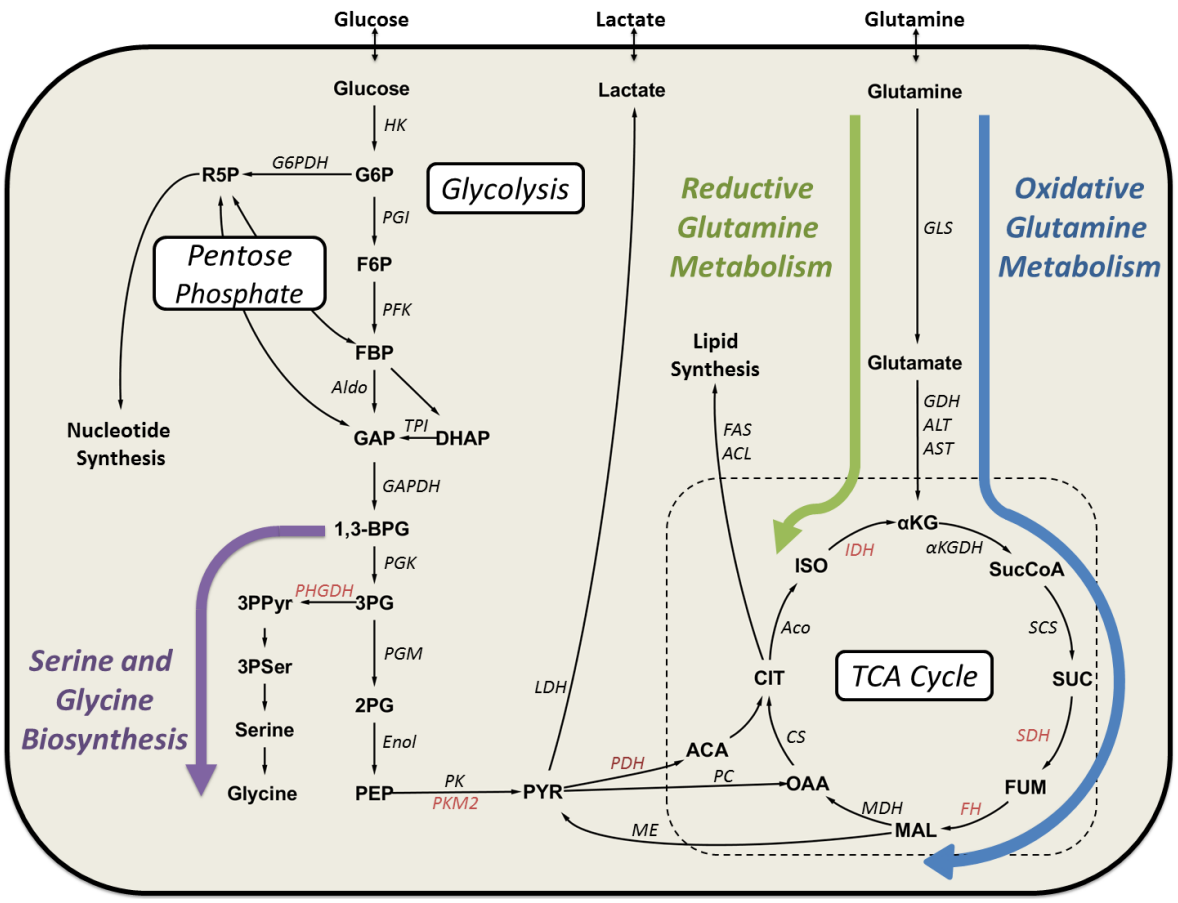

Figure 2.6. Major Pathways of Central Carbon Metabolism and Key Enzymes Commonly Dysregulated in Cancer Cells. Important pathways implicated in cancer cell proliferation are indicated: serine metabolism is highlighted with a purple arrow, oxidative glutamine metabolism with a blue arrow, and reductive glutamine metabolism with a green arrow. Enzymes known to be dysregulated in some cancers are shown in red text. Abbreviations: ACL, ATP citrate lyase; Aco, aconitase; αKGDH, α-ketoglutarate dehydrogenase; Aldo, aldolase; ALT, alanine transaminase; AST, aspartate transaminase; CS, citrate synthase; Enol, enolase; FAS, fatty acid synthase; FH, fumarate hydratase; G6PDH, glucose-6-phosphate dehydrogenase; GAPDH, glyceraldehyde-3-phosphate dehydrogenase; GDH, glutamate dehydrogenase; GLS, glutaminase; HK, hexokinase; IDH, isocitrate dehydrogenase; LDH, lactate dehydrogenase; MDH, malate dehydrogenase; ME, malic enzyme; PC, pyruvate carboxylase; PDH, pyruvate dehydrogenase; PFK, phosphofructokinase; PGI, phosphoglucose isomerase; PGK, phosphoglycerate kinase; PGM, phosphoglycerate mutase; PHGDH, phosphoglycerate dehydrogenase; PK, pyruvate kinase; PKM2, pyruvate kinase M2; SCS, succinyl-CoA synthetase; SDH, succinate dehydrogenase; TPI, triose phosphate isomerase.

2.4.2 Metabolic Alterations Due to Oncogenic Changes

MFA and the use of isotope labeling can be a powerful tool in studying cancer. However, analysis of a single cell phenotype is not very useful (Vander Heiden et al., 2009). The real power of flux analysis comes in the comparison between different cell states (Vander Heiden, 2011). Of particular interest to cancer researchers are the differences between normal cells and oncogenically-transformed cells. Understanding the fundamental differences in the functional endpoint of a host of cell processes can aid in the discovery of new and useful therapeutics.

The first study that applied comprehensive ^{13}C-MFA to map cancer cell metabolism was published in 2006 by researchers investigating ER-positive, breast carcinoma cells (Forbes et al., 2006). The response of MCF-7 cells to estradiol stimulation and two metabolic inhibitors—cerulinin, a fatty acid synthase inhibitor, and oxamate, an inhibitor of lactate dehydrogenase—was characterized using MFA. The goal of this study was the identification of targets whose inhibition could be useful as adjuvant treatment in ER-antagonist therapies. The authors report elevated rates of glucose and glutamine consumption upon estradiol-stimulation. Surprisingly, however, they also report a dramatically elevated flux into the pentose phosphate pathway (PPP). It was hypothesized that the NADPH generated by this pathway was critical for the elevated fatty acid synthesis required for proliferation; however, treatment with cerulinin did not reduce PPP flux.

Another group compared regular mouse embryonic fibroblasts and *K-Ras*-transformed MEFs (Gaglio et al., 2011). They used ^{13}C-MFA along with non-targeted tracer fate detection (NTFD) of ^{15}N-glutamine and transcriptomic profiling to understand what the differences are between cancerous and non-cancerous cell lines. Through MFA, they discovered that the *K-Ras* transformed cell lines increase flux through glycolysis and decrease flux through the TCA Cycle. Transcriptional profiling supported the flux data with the result that multiple metabolic genes had upregulated expression. NTFD is used to examine how isotopic tracers, in this case ^{15}N-glutamine, are used throughout the cell, not just in central metabolism. By measuring where the labeling appears inside the cell, it's possible to gain a better understanding about how glutamine is utilized. In this study, it was found that *K-Ras*-transformed cells utilized glutamine for greater biosynthetic purposes even though there was a decrease in the flux from the non-transformed state. However, the decrease in overall TCA cycle metabolism was greater than the decrease in glutamine uptake which indicated a decoupling between glycolysis, TCA cycle, and glutamine

metabolism. They further used chemical inhibition of specific enzymes (namely aminotransferase and glutamate dehydrogenase) to show that transformed cells were reliant upon glutamine to support proliferation and growth. This study shows the power of combining metabolic flux analysis with genomic profiling of cells to elucidate specific alterations between cancerous and non-cancerous cells.

Other researchers are attempting to link morphological changes with metabolism using the techniques of metabolic engineering. Using the cancerous cell line, MCF-10A, Grassian et al. (2011) examined how extracellular matrix (ECM) detachment affects metabolism. Using [1,2-$^{13}C_2$]glucose, they compared the metabolism of attached and detached cells along with normal and over-expression of HER2, an epidermal growth factor receptor. ECM detachment resulted in a decrease through all major central metabolic pathways (glycolysis, pentose phosphate, and TCA cycle), but they did find a disproportionate decrease in pyruvate dehydrogenase (PDH) flux. However, in the presence of HER2, they found that the PDH flux was maintained through the suppression of pyruvate dehydrogenase kinase 4 (PDK4) in an Erk-dependent manner. The focus on PDH was driven by the labeling alterations of TCA cycle intermediates caused by ECM detachment and subsequent reversal of this effect through HER2 overexpression. These changes were brought to light specifically by using isotope tracers, again revealing the power they bring to a traditional biologist's toolset.

Another group, with whom we've collaborated for different studies, have used isotopic labeling in a Myc-driven model of Burkitt's lymphoma (Liu et al., 2012). (This is the same cell line used in this dissertation work and is discussed in detail in chapters 3, 4, 5, and 6.) Le et al. (2012) examined the growth of P493-6 B-cells with and without Myc overexpression, normoxic and hypoxic oxygen tensions, and glucose abundant and deprived states. They grew cells with two separate tracers, [U-$^{13}C_6$]glucose and [U-$^{13}C_5$, U-$^{15}N_2$]glutamine, to examine the effects of the different metabolic perturbations. Using MID analysis, and not strict MFA, they were able to compare the labeling patterns in many different metabolic fragments such as citrate, succinate, fumarate, alanine and several others. The data gave strong evidence that these cells, and possibly most Myc-driven tumors, are highly dependent on glutamine and are capable of redirecting metabolism to a glucose-independent form of the TCA cycle when necessary. Evidence was also found, via labeling patterns in glutathione and other metabolites, that the glutamine contributed to ATP as well as antioxidant production, which is a key method of protecting the cell against reactive

oxygen species (ROS) produced by elevated OXPHOS. While this work had only a small amount of truly quantitative flux measurements, the labeling data revealed hidden details not evidenced by extracellular measurements alone. Further analysis of these cells and conditions using full-scale MFA is detailed in later chapters and expands upon the work briefly mentioned here.

2.4.3 Translational Uses of MFA in Cancer Research

Clearly, the use of isotope tracers and metabolic flux analysis are powerful tools in cancer research. This nascent application of MFA is the cutting edge in the field and it holds great promise for the future. However, while there have been many advances in the use of metabolic engineering techniques in studying diseases, much of the work to date has been *ex vivo*, i.e., in cell cultures or *in vitro* disease models (Vander Heiden, 2011). Many great discoveries have been made using *in vitro* methods, but there is a fundamental disconnect between the environment in a laboratory and inside of a patient. Drugs and techniques that show great promise in culture have been ineffective in clinics (American Cancer Society, 2012; Ledford, 2011). This begs the question, how can we improve the quality and applicability of data gained from the lab?

Ideally, *in vitro* research would translate to *in vivo* models in a one-to-one fashion. This is almost never the case, although steps are being taken to bring the two together (Johnson, 2012). Extension of techniques to mice and other animals is not as easy as changing a few lines in a protocol. Entirely new methods are necessary to generate similar information as obtained from cell cultures. In the study of cancer, it would be of great benefit to generate metabolic flux maps of the *in vivo* tumor physiology. The way a cancer cell behaves inside a body can be very different than in a culture dish (Hanahan and Weinberg, 2011). Understanding exactly how the environment impacts the metabolism, and subsequently the growth and formation, of tumors inside a person is of critical importance to discovering how to best treat said patients.

Part of this dissertation work was focused on extending the MFA techniques optimized *in vitro* into mice models: the first step on the path to doing MFA with actual tumors. Indeed, our choice of proteinogenic MFA was chosen specifically because of the impracticality of using intracellular metabolite labeling from whole tumors. Due to the physical limitations of extracting a whole tumor and freezing it, coupled with the sub-second changes that can occur

in the labeling patterns of intracellular metabolites, extracting the protein, RNA, and lipids of whole tumors is the preferred method due to their longer-term stability outside of the host (Goudar et al., 2010; Sriram et al., 2008). However, there are groups who have made the intracellular metabolite method work with some interesting results (Niklas and Heinzle, 2012).

Yuneva et. al. (2012) used isotopic tracers to measure the differences in Myc- and Met-induced liver tumors in mice. By using ^{13}C-labeled glucose and glutamine they were able to see the distribution of labeling in these tumors. They found that Myc-driven tumors increased rates of glucose and glutamine catabolism while Met tumors increased the conversion of glucose to glutamine. This difference underscores the metabolic differences that occur with different oncogenic drivers and the importance of understanding how these cells behave in an *in vivo* environment. Akin to this study, Marin-Valencia et al. (2012) applied MID analysis to study the effects of plasma infusions of ^{13}C-glucose on mice bearing human glioblastoma orthotopic tumors. They found that all tumors studied exhibited active mitochondrial glucose oxidation as well as conversion of glucose carbon into glutamine and other biosynthetic intermediates. Building upon these studies will enable better MFA techniques to be applied to more *in vivo* cancer models. Fan et al. (2011) examined the differences between mice that have no lung cancer and mice that were injected with human lung adenocarcinoma cells. They used ^{13}C-glucose as the tracer and found significant increases in the level of labeling in the tumor tissue in both glycolytic and TCA cycle metabolites, suggesting an enhanced flux through these pathways. While no true flux analysis was done, this experiment gives us a tantalizing glimpse of the kinds of data *in vivo* MFA can potentially return. These studies are the cutting edge of isotope labeling studies *in vivo,* and it's clear there is still much work to be done to generate better results and conclusions from this data.

2.5 References

Adam J, Hatipoglu E, O'Flaherty L, Ternette N, Sahgal N, Lockstone H, Baban D, Nye E, Stamp GW, Wolhuter K, Stevens M, Fischer R, Carmeliet P, Maxwell PH, Pugh CW, Frizzell N, Soga T, Kessler BM, El-Bahrawy M, Ratcliffe PJ, Pollard PJ. 2011. Renal cyst formation in Fh1-deficient mice is independent of the Hif/Phd pathway: roles for fumarate in KEAP1 succination and Nrf2 signaling. *Cancer Cell* **20**:524–537.

Ahn WS, Antoniewicz MR. 2013. Parallel labeling experiments with [1,2-(13)C]glucose and [U-(13)C]glutamine provide new insights into CHO cell metabolism. *Metab. Eng.* **15**:34–47.

Amati B, Dalton S, Brooks MW, Littlewood TD, Evan GI, Land H. 1992. Transcriptional activation by the human c-Myc oncoprotein in yeast requires interaction with Max. *Nature* **359**:423–426.

American Cancer Society. 2012. Cancer Facts & Figures 2012. *American Cancer Society*:1–68.

Anastasiou D, Yu Y, Israelsen WJ, Jiang J-K, Boxer MB, Hong BS, Tempel W, Dimov S, Shen M, Jha A, Yang H, Mattaini KR, Metallo CM, Fiske BP, Courtney KD, Malstrom S, Khan TM, Kung C, Skoumbourdis AP, Veith H, Southall N, Walsh MJ, Brimacombe KR, Leister W, Lunt SY, Johnson ZR, Yen KE, Kunii K, Davidson SM, Christofk HR, Austin CP, Inglese J, Harris MH, Asara JM, Stephanopoulos G, Salituro FG, Jin S, Dang L, Auld DS, Park H-W, Cantley LC, Thomas CJ, Vander Heiden MG. 2012. Pyruvate kinase M2 activators promote tetramer formation and suppress tumorigenesis. *Nat. Chem. Biol.* **8**:839–847.

Antoniewicz MR, Kelleher JK, Stephanopoulos G. 2007. Elementary metabolite units (EMU): a novel framework for modeling isotopic distributions. *Metab. Eng.* **9**:68–86.

Bensaad K, Vousden KH. 2007. p53: new roles in metabolism. *Trends Cell Biol.* **17**:286–291.

Bier DM, Arnold KJ, Sherman WR, Holland WH, Holmes WF, Kipnis DM. 1977. In-vivo measurement of glucose and alanine metabolism with stable isotopic tracers. *Diabetes* **26**:1005–1015.

Bonarius HPJ, Schmid G, Tramper J. 1997. Flux analysis of underdetermined metabolic networks: the quest for the missing constraints. *Trends Biotechnol.* **15**:308–314.

Chabner BA, Roberts TG. 2005. Timeline: Chemotherapy and the war on cancer. *Nat. Rev. Cancer* **5**:65–72.

Chang G, Tong L. 2003. Structure and Function of Malic Enzymes, A New Class of Oxidative Decarboxylases†. *Biochemistry* **42**:12721–12733.

Christofk H, Vander Heiden MG, Wu N, Asara J, Cantley L. 2008. Pyruvate kinase M2 is a phosphotyrosine-binding protein. *Nature* **452**:181–186.

Dang CV. 2011. Therapeutic targeting of Myc-reprogrammed cancer cell metabolism. *Cold Spring Harb. Symp. Quant. Biol.* **76**:369–374.

Dang CV. 1999. c-Myc target genes involved in cell growth, apoptosis, and metabolism. *Mol. Cell. Biol.* **19**:1.

Dang CV. 2009. PKM2 tyrosine phosphorylation and glutamine metabolism signal a different view of the Warburg effect. *Sci. Signal* **2**:pe75.

Dang CV. 2010. Enigmatic MYC Conducts an Unfolding Systems Biology Symphony. *Genes Cancer* **1**:526–531.

Dang CV. 2012. MYC on the Path to Cancer. *Cell* **149**:22–35.

Dang CV, Kim J, Gao P, Yustein J. 2008. The interplay between MYC and HIF in cancer. *Nat. Rev. Cancer* **8**:51–56.

Dang CV, Le A, Gao P. 2009a. MYC-induced cancer cell energy metabolism and therapeutic opportunities. *Clin. Cancer Res.* **15**:6479–6483.

Dang L, White DW, Gross S, Bennett BD, Bittinger MA, Driggers EM, Fantin VR, Jang HG, Jin S, Keenan MC, Marks KM, Prins RM, Ward PS, Yen KE, Liau LM, Rabinowitz JD, Cantley LC, Thompson CB, Vander Heiden MG, Su SM. 2009b. Cancer-associated IDH1 mutations produce 2-hydroxyglutarate. *Nature* **462**:739–744.

Dauner M, Sauer U. 2000. GC-MS analysis of amino acids rapidly provides rich information for isotopomer balancing. *Biotechnol. Prog.* **16**:642–649.

Dulmage AL, Mendelsohn NS. 1958. Coverings of bipartite graphs. *Canad. J. Math.* **10**:517–534.

Evans JMM, Donnelly LA, Emslie-Smith AM, Alessi DR, Morris AD. 2005. Metformin and reduced risk of cancer in diabetic patients. *BMJ* **330**:1304–1305.

Facchetti G, Zampieri M, Altafini C. 2012. Predicting and characterizing selective multiple drug treatments for metabolic diseases and cancer. *BMC Sys. Biol.* **6**:115.

Fan TWM, Lane AN, Higashi RM, Yan J. 2011. Stable isotope resolved metabolomics of lung cancer in a SCID mouse model. *Metabolomics* **7**:257–269.

Fan TWM, Lorkiewicz PK, Sellers K, Moseley HNB, Higashi RM, Lane AN. 2012. Stable isotope-resolved metabolomics and applications for drug development. *Pharmacol. Ther.* **133**:366–391.

Fantin V, St-Pierre J, Leder P. 2006. Attenuation of LDH-A expression uncovers a link between glycolysis, mitochondrial physiology, and tumor maintenance. *Cancer Cell* **9**:425–434.

Folger O, Jerby L, Frezza C, Gottlieb E, Ruppin E, Shlomi T. 2011. Predicting selective drug targets in cancer through metabolic networks. *Mol. Sys. Biol.* **7**:501.

Forbes NS, Meadows AL, Clark DS, Blanch HW. 2006. Estradiol stimulates the biosynthetic pathways of breast cancer cells: detection by metabolic flux analysis. *Metab. Eng.* **8**:639–652.

Gaglio D, Metallo CM, Gameiro PA, Hiller K, Danna LS, Balestrieri C, Alberghina L, Stephanopoulos G, Chiaradonna F. 2011. Oncogenic K-Ras decouples glucose and glutamine metabolism to support cancer cell growth. *Mol. Sys. Biol.* **7**:523.

Gao P, Tchernyshyov I, Chang T, Lee Y, Kita K, Ochi T, Zeller K, de Marzo A, van Eyk J, Mendell J. 2009. c-Myc suppression of miR-23a/b enhances mitochondrial glutaminase expression and glutamine metabolism. *Nature* **458**:762–765.

Gardner L, Lee L, Dang C. 2002. The c-Myc oncogenic transcription factor. *The Encyclopedia of Cancer*.

Genzel Y, Reichl U. 2009. Continuous cell lines as a production system for influenza vaccines. *Expert Rev Vaccines* **8**:1681–1692.

Gomes LC, Simoes M. 2012. 13C Metabolic Flux Analysis: From the Principle to Recent Applications. *Current Bioinformatics* **7**:77–86.

Gordan JD, Thompson CB, Simon MC. 2007. HIF and c-Myc: sibling rivals for control of cancer cell metabolism and proliferation. *Cancer Cell* **12**:108–113.

Goudar C, Biener R, Boisart C, Heidemann R, Piret J, de Graaf A, Konstantinov K. 2010. Metabolic flux analysis of CHO cells in perfusion culture by metabolite balancing and 2D [13C, 1H] COSY NMR spectroscopy. *Metab. Eng.* **12**:138–149.

Grassian AR, Metallo CM, Coloff JL, Stephanopoulos G, Brugge JS. 2011. Erk regulation of pyruvate dehydrogenase flux through PDK4 modulates cell proliferation. *Genes Devel.* **25**:1716–1733.

Griffin JL, Shockcor JP. 2004. Metabolic profiles of cancer cells. *Nat. Rev. Cancer* **4**:551–561.

Hanahan D, Weinberg RA. 2000. The hallmarks of cancer. *Cell* **100**:57–70.

Hanahan D, Weinberg RA. 2011. Hallmarks of cancer: the next generation. *Cell* **144**:646–674.

Hellerstein MK, Christiansen M, Kaempfer S, Kletke C, Wu K, Reid JS, Mulligan K, Hellerstein NS, Shackleton CH. 1991. Measurement of de novo hepatic lipogenesis in humans using stable isotopes. *J. Clin. Invest.* **87**:1841–1852.

Hellerstein MK. 2004. New stable isotope-mass spectrometric techniques for measuring fluxes through intact metabolic pathways in mammalian systems: introduction of moving pictures into functional genomics and biochemical phenotyping. *Metab. Eng.* **6**:85–100.

Hofmann U, Maier K, Niebel A, Vacun G, Reuss M, Mauch K. 2008. Identification of metabolic fluxes in hepatic cells from transient 13C-labeling experiments: Part I. Experimental observations. *Biotechnol. Bioeng.* **100**:344–354.

Hsu PP, Sabatini DM. 2008. Cancer cell metabolism: Warburg and beyond. *Cell* **134**:703–707.

Hunnewell MG, Forbes NS. 2010. Active and inactive metabolic pathways in tumor spheroids: determination by GC-MS. *Biotechnol. Prog.* **26**:789–796.

Isaacs JS, Jung YJ, Mole DR, Lee S, Torres-Cabala C, Chung Y-L, Merino M, Trepel J, Zbar B, Toro J, Ratcliffe PJ, Linehan WM, Neckers L. 2005. HIF overexpression correlates with biallelic loss of fumarate hydratase in renal cancer: novel role of fumarate in regulation of HIF stability. *Cancer Cell* **8**:143–153.

Jazmin LJ, Young JD. 2013. Isotopically nonstationary (13)c metabolic flux analysis. *Meth. Mol. Biol.* **985**:367–390.

Johnson L. 2012. Cancer: Clinical trials unite mice and humans. *Nature* **483**:546–548.

Jones RG, Thompson CB. 2009. Tumor suppressors and cell metabolism: a recipe for cancer growth. *Genes Devel.* **23**:537–548.

Keibler MA, Fendt S-M, Stephanopoulos G. 2012. Expanding the concepts and tools of metabolic engineering to elucidate cancer metabolism. *Biotechnol. Prog.* **28**:1409–1418.

Kelleher JK, Bryan BM, Mallet RT, Holleran AL, Murphy AN, Fiskum G. 1987. Analysis of tricarboxylic acid-cycle metabolism of hepatoma cells by comparison of 14CO2 ratios. *Biochem. J.* **246**:633–639.

Kim J-W, Gao P, Liu Y-C, Semenza GL, Dang CV. 2007. Hypoxia-inducible factor 1 and dysregulated c-Myc cooperatively induce vascular endothelial growth factor and metabolic switches hexokinase 2 and pyruvate dehydrogenase kinase 1. *Mol. Cell. Biol.* **27**:7381–7393.

Kim J-W, Zeller KI, Wang Y, Jegga AG, Aronow BJ, O'Donnell KA, Dang CV. 2004. Evaluation of myc E-box phylogenetic footprints in glycolytic genes by chromatin immunoprecipitation assays. *Mol. Cell. Biol.* **24**:5923–5936.

Kit S. 1955. The biosynthesis of free glycine and serine by tumors. *Cancer Res.* **15**:715–718.

Le A, Cooper CR, Gouw AM, Dinavahi R, Maitra A, Deck LM, Royer RE, Vander Jagt DL, Semenza GL, Dang CV. 2010. Inhibition of lactate dehydrogenase A induces oxidative stress and inhibits tumor progression. *Proc. Nat. Acad. Sci.* **107**:2037–2042.

Le A, Lane AN, Hamaker M, Bose S, Gouw A, Barbi J, Tsukamoto T, Rojas CJ, Slusher BS, Zhang H, Zimmerman LJ, Liebler DC, Slebos RJC, Lorkiewicz PK, Higashi RM, Fan TWM, Dang CV. 2012. Glucose-Independent Glutamine Metabolism via TCA Cycling for Proliferation and Survival in B Cells. *Cell Metab.* **15**:110–121.

Ledford H. 2011. Translational research: 4 ways to fix the clinical trial. *Nature*, September 29.

Leighty RW, Antoniewicz MR. 2012. Parallel labeling experiments with [U-(13)C]glucose validate E. coli metabolic network model for (13)C metabolic flux analysis. *Metab. Eng.* **14**:533–541.

Li F, Wang Y, Zeller KI, Potter JJ, Wonsey DR, O'Donnell KA, Kim J-W, Yustein JT, Lee LA, Dang CV. 2005. Myc stimulates nuclearly encoded mitochondrial genes and mitochondrial biogenesis. *Mol. Cell. Biol.* **25**:6225–6234.

Li L, Zhou X, Ching W-K, Wang P. 2010. Predicting enzyme targets for cancer drugs by profiling human Metabolic reactions in NCI-60 cell lines. *BMC Bioinformatics* **11**:501.

Liu W, Le A, Hancock C, Lane AN, Dang CV, Fan TWM, Phang JM. 2012. Reprogramming of proline and glutamine metabolism contributes to the proliferative and metabolic responses regulated by oncogenic transcription factor c-MYC. *Proc. Nat. Acad. Sci.* **109**:8983–8988.

Liu Y-C, Li F, Handler J, Huang CRL, Xiang Y, Neretti N, Sedivy JM, Zeller KI, Dang CV. 2008. Global regulation of nucleotide biosynthetic genes by c-Myc. *PLoS One* **3**:e2722.

Locasale JW, Grassian AR, Melman T, Lyssiotis CA, Mattaini KR, Bass AJ, Heffron G, Metallo CM, Muranen T, Sharfi H, Sasaki AT, Anastasiou D, Mullarky E, Vokes NI, Sasaki M, Beroukhim R, Stephanopoulos G, Ligon AH, Meyerson M, Richardson AL, Chin L, Wagner G, Asara JM, Brugge JS, Cantley LC, Vander Heiden MG. 2011. Phosphoglycerate dehydrogenase diverts glycolytic flux and contributes to oncogenesis. *Nat. Genet.* **43**:869–874.

Lorber V, Lifson N, Wood HG. 1945. Incorporation of acetate carbon into rat liver glycogen by pathways other than carbon dioxide fixation. *J. Biol. Chem.* **161**:411–412.

Maier K, Hofmann U, Reuss M, Mauch K. 2008. Identification of metabolic fluxes in hepatic cells from transient 13C-labeling experiments: Part II. Flux estimation. *Biotechnol. Bioeng.* **100**:355–370.

Mardis ER, Ding L, Dooling DJ, Larson DE, McLellan MD, Chen K, Koboldt DC, Fulton RS, Delehaunty KD, McGrath SD, Fulton LA, Locke DP, Magrini VJ, Abbott RM, Vickery TL, Reed JS, Robinson JS, Wylie T, Smith SM, Carmichael L, Eldred JM, Harris CC, Walker J, Peck JB, Du F, Dukes AF, Sanderson GE, Brummett AM, Clark E, McMichael JF, Meyer RJ, Schindler JK, Pohl CS, Wallis JW, Shi X, Lin L, Schmidt H, Tang Y, Haipek C, Wiechert ME, Ivy JV, Kalicki J, Elliott G, Ries RE, Payton JE, Westervelt P, Tomasson MH, Watson MA, Baty J, Heath S, Shannon WD, Nagarajan R, Link DC, Walter MJ, Graubert TA, DiPersio JF, Wilson RK, Ley TJ. 2009. Recurring mutations found by sequencing an acute myeloid leukemia genome. *N. Engl. J. Med.* **361**:1058–1066.

Marin-Valencia I, Yang C, Mashimo T, Cho S, Baek H, Yang X-L, Rajagopalan KN, Maddie M, Vemireddy V, Zhao Z, Cai L, Good L, Tu BP, Hatanpaa KJ, Mickey BE, Matés JM, Pascual JM, Maher EA, Malloy CR, DeBerardinis RJ, Bachoo RM. 2012. Analysis of tumor metabolism reveals mitochondrial glucose oxidation in genetically diverse human glioblastomas in the mouse brain in vivo. *Cell Metab.* **15**:827–837.

Mazurek S, Grimm H, Oehmke M, Weisse G, Teigelkamp S, Eigenbrodt E. 2000. Tumor M2-PK and glutaminolytic enzymes in the metabolic shift of tumor cells. *Anticancer Res.* **20**:5151–5154.

Mazurek S. 2011. Pyruvate kinase type M2: a key regulator of the metabolic budget system in tumor cells. *Int. J. Biochem. Cell Biol.* **43**:969–980.

Metallo CM, Gameiro PA, Bell EL, Mattaini KR, Yang J, Hiller K, Jewell CM, Johnson ZR, Irvine DJ, Guarente L, Kelleher JK, Vander Heiden MG, Iliopoulos O, Stephanopoulos G. 2012. Reductive glutamine metabolism by IDH1 mediates lipogenesis under hypoxia. *Nature* **481**:380–384.

Miller DM, Thomas SD, Islam A, Muench D, Sedoris K. 2012. c-Myc and cancer metabolism. *Clin. Cancer Res.* **18**:5546–5553.

Morrish F, Isern N, Sadilek M, Jeffrey M, Hockenbery DM. 2009. c-Myc activates multiple metabolic networks to generate substrates for cell-cycle entry. *Oncogene* **28**:2485–2491.

Mullen AR, Wheaton WW, Jin ES, Chen P-H, Sullivan LB, Cheng T, Yang Y, Linehan WM, Chandel NS, DeBerardinis RJ. 2012. Reductive carboxylation supports growth in tumour cells with defective mitochondria. *Nature* **481**:385–388.

Neuman RE, McCoy TA. 1956. Dual requirement of Walker carcinosarcoma 256 in vitro for asparagine and glutamine. *Science* **124**:124–125.

Nielsen J. 2003. It is all about metabolic fluxes. *J. Bacteriol.* **185**:7031.

Nikiforov MA, Chandriani S, O'Connell B, Petrenko O, Kotenko I, Beavis A, Sedivy JM, Cole MD. 2002. A functional screen for Myc-responsive genes reveals serine hydroxymethyltransferase, a major source of the one-carbon unit for cell metabolism. *Mol. Cell. Biol.* **22**:5793.

Niklas J, Heinzle E. 2012. Metabolic flux analysis in systems biology of Mammalian cells. *Adv. Biochem. Eng. Biotechnol.* **127**:109–132.

Niklas J, Schneider K, Heinzle E. 2010. Metabolic flux analysis in eukaryotes. *Curr. Opin. Biotechnol.* **21**:63–69.

Niklas J, Schräder E, Sandig V, Noll T, Heinzle E. 2011. Quantitative characterization of metabolism and metabolic shifts during growth of the new human cell line AGE1.HN using time resolved metabolic flux analysis. *Bioproc. Biosys. Eng.* **34**:533–545.

Nöh K, Wahl A, Wiechert W. 2006. Computational tools for isotopically instationary 13C labeling experiments under metabolic steady state conditions. *Metab. Eng.* **8**:554–577.

Nöh K, Wiechert W. 2011. The benefits of being transient: isotope-based metabolic flux analysis at the short time scale. *Appl Microbiol Biotechnol* **91**:1247–1265.

Osthus RC, Shim H, Kim S, Li Q, Reddy R, Mukherjee M, Xu Y, Wonsey D, Lee LA, Dang CV. 2000. Deregulation of glucose transporter 1 and glycolytic gene expression by c-Myc. *J. Biol. Chem.* **275**:21797–21800.

Possemato R, Marks KM, Shaul YD, Pacold ME, Kim D, Birsoy K, Sethumadhavan S, Woo H-K, Jang HG, Jha AK, Chen WW, Barrett FG, Stransky N, Tsun Z-Y, Cowley GS, Barretina J, Kalaany NY, Hsu PP, Ottina K, Chan AM, Yuan B, Garraway LA, Root DE, Mino-Kenudson M, Brachtel EF, Driggers EM, Sabatini DM. 2011. Functional genomics reveal that the serine synthesis pathway is essential in breast cancer. *Nature* **476**:346–350.

Pothen A, Fan C-J. 1990. Computing the block triangular form of a sparse matrix. *ACM Trans. Math. Softw.* **16**:303–324.

Pylayeva-Gupta Y, Grabocka E, Bar-Sagi D. 2011. RAS oncogenes: weaving a tumorigenic web. *Nat. Rev. Cancer* **11**:761–774.

Quek L-E, Dietmair S, Krömer JO, Nielsen LK. 2010. Metabolic flux analysis in mammalian cell culture. *Metab. Eng.* **12**:161–171.

Reitman ZJ, Yan H. 2010. Isocitrate dehydrogenase 1 and 2 mutations in cancer: alterations at a crossroads of cellular metabolism. *J. Natl. Cancer Inst.* **102**:932–941.

Sauer U. 2006. Metabolic networks in motion: 13C-based flux analysis. *Mol. Sys. Biol.* **2**:62.

Schmidt K, Carlsen M, Nielsen J, Villadsen J. 1997. Modeling isotopomer distributions in biochemical networks using isotopomer mapping matrices. *Biotechnol. Bioeng.* **55**:831–840.

Schwender J. 2008. Metabolic flux analysis as a tool in metabolic engineering of plants. *Curr. Opin. Biotechnol.* **19**:131–137.

Scott RB. 1970. Cancer chemotherapy--the first twenty-five years. *BMJ* **4**:259–265.

Selak MA, Armour SM, MacKenzie ED, Boulahbel H, Watson DG, Mansfield KD, Pan Y, Simon MC, Thompson CB, Gottlieb E. 2005. Succinate links TCA cycle dysfunction to oncogenesis by inhibiting HIF-alpha prolyl hydroxylase. *Cancer Cell* **7**:77–85.

Semenza GL. 2010. Defining the role of hypoxia-inducible factor 1 in cancer biology and therapeutics. *Oncogene* **29**:625–634.

Seth G, Hossler P, Yee J, Hu WS. 2006. Engineering cells for cell culture bioprocessing–physiological fundamentals. *Cell. Cult. Eng.* **101**:119–164.

Shastri AA, Morgan JA. 2007. A transient isotopic labeling methodology for 13C metabolic flux analysis of photoautotrophic microorganisms. *Phytochemistry* **68**:2302–2312.

Shim H, Dolde C, Lewis B, Wu C, Dang CV, Jungmann R, Dalla-Favera R. 1997. c-Myc transactivation of LDH-A: implications for tumor metabolism and growth. *Proc. Nat. Acad. Sci.* **94**:6658.

Sriram G, Rahib L, He J, Campos A, Parr L, Liao J, Dipple K. 2008. Global metabolic effects of glycerol kinase overexpression in rat hepatoma cells. *Mol. Genet. Metab.* **93**:145–159.

Stephanopoulos G. 1999. Metabolic Fluxes and Metabolic Engineering. *Metab. Eng.* **1**:1–11.

Vander Heiden MG. 2011. Targeting cancer metabolism: a therapeutic window opens. *Nat. Rev. Drug Discov.* **10**:671–684.

Vander Heiden MG, Cantley LC, Thompson CB. 2009. Understanding the Warburg effect: the metabolic requirements of cell proliferation. *Science* **324**:1029–1033.

Warburg O. 1956. On the origin of cancer cells. *Science* **123**:309–314.

Warburg O, Posener K, Negelein E. 1924. On the metabolism of carcinoma cells. *Biochem. Zeit.* **152**:309–344.

Ward PS, Thompson CB. 2012. Metabolic Reprogramming: A Cancer Hallmark Even Warburg Did Not Anticipate. *Cancer Cell* **21**:297–308.

Wiechert W. 2001. 13C metabolic flux analysis. *Metab. Eng.* **3**:195–206.

Wiechert W, Möllney M, Isermann N, Wurzel M, de Graaf AA. 1999. Bidirectional reaction steps in metabolic networks: III. Explicit solution and analysis of isotopomer labeling systems. *Biotechnol. Bioeng.* **66**:69–85.

Wiechert W, Nöh K. 2005. From stationary to instationary metabolic flux analysis. *Adv. Biochem. Eng. Biotechnol.* **92**:145–172.

Wise DR, Ward PS, Shay JES, Cross JR, Gruber JJ, Sachdeva UM, Platt JM, Dematteo RG, Simon MC, Thompson CB. 2011. Hypoxia promotes isocitrate dehydrogenase-dependent carboxylation of α-ketoglutarate to citrate to support cell growth and viability. *Proc. Nat. Acad. Sci.* **108**:19611–19616.

Wise D, DeBerardinis RJ, Mancuso A, Sayed N, Zhang X, Pfeiffer H, Nissim I, Daikhin E, Yudkoff M, McMahon S. 2008. Myc regulates a transcriptional program that stimulates mitochondrial glutaminolysis and leads to glutamine addiction. *Proc. Nat. Acad. Sci.* **105**:18782.

Wittmann C, Heinzle E. 1999. Mass spectrometry for metabolic flux analysis. *Biotechnol. Bioeng.* **62**:739–750.

Wurm FM. 2004. Production of recombinant protein therapeutics in cultivated mammalian cells. *Nature Biotech.*

Xie H, Valera VA, Merino MJ, Amato AM, Signoretti S, Linehan WM, Sukhatme VP, Seth P. 2009. LDH-A inhibition, a therapeutic strategy for treatment of hereditary leiomyomatosis and renal cell cancer. *Mol. Cancer Therap.* **8**:626–635.

Young JD, Walther JL, Antoniewicz MR, Yoo H, Stephanopoulos G. 2008. An elementary metabolite unit (EMU) based method of isotopically nonstationary flux analysis. *Biotechnol. Bioeng.* **99**:686–699.

Yuneva MO, Fan TWM, Allen TD, Higashi RM, Ferraris DV, Tsukamoto T, Matés JM, Alonso FJ, Wang C, Seo Y, Chen X, Bishop JM. 2012. The metabolic profile of tumors depends on both the responsible genetic lesion and tissue type. *Cell Metab.* **15**:157–170.

Zamboni N, Fendt SM, Rühl M, Sauer U. 2009. 13C-based metabolic flux analysis. *Nat. Protoc.* **4**:878–892.

Zamboni N. 2011. 13C metabolic flux analysis in complex systems. *Curr. Opin. Biotechnol.* **22**:103–108.

Zu X, Guppy M. 2004. Cancer metabolism: facts, fantasy, and fiction. *Biochem. Biophys. Res. Comm.* **313**:459–465.

Zupke C, Stephanopoulos G. 1994. Modeling of isotope distributions and intracellular fluxes in metabolic networks using atom mapping matrices. *Biotechnol. Prog.* **10**:489–498.

CHAPTER 3

DEVELOPMENT AND VALIDATION OF ETA SOFTWARE PACKAGE FOR DETERMINATION OF CELL SPECIFIC RATES FROM EXTRACELLULAR TIME COURSES

3.1 Introduction

Metabolic fluxes represent quantitative measures of material flow within a biochemical network and are thus considered fundamental determinants of *in vivo* cell physiology (Nielsen, 2003; Sauer, 2006; Stephanopoulos, 1999; Wiechert, 2001). Measurements of cell specific rates of nutrient uptake and product formation (i.e., normalized to cell density) provide the basis for intracellular flux calculations using flux balance analysis (FBA) or metabolic flux analysis (MFA) (Quek et al., 2010). The measured extracellular rates are critical inputs to these methods because they constrain the solution space of feasible intracellular fluxes. Therefore, accurate estimation of cell specific extracellular rates, and their associated uncertainties, is an essential task in the construction of accurate metabolic flux maps. In addition, cell specific rates are intensive properties that do not depend on the size of the system under investigation, which facilitates comparisons between different experimental platforms.

Under balanced growth conditions, where the culture attains an internal metabolic steady state, all cell specific metabolic rates are considered constant and the extracellular rates can be determined by measuring changes in medium composition over time. This is not as trivial as it may seem since the observed rates of change are proportional to the mathematical product of specific rate (v) and cell density (X), with the latter continuously increasing as the culture grows. Therefore, the calculation procedure must account for the combined effects of both variables on the measured time courses, as well as random errors introduced by the various measurements of extracellular metabolite and cell concentrations. The preferred method involves regression analysis to estimate the specific growth rate of the culture (m) and specific production rate (v) of each measured extracellular metabolite, using integrated balance equations that describe the rates of concentration change over time.

Several prior articles have applied regression analysis to determine metabolic rates from extracellular time courses of substrate depletion or product accumulation (Glacken et al., 1988; Goudar, 2012; Kim and Forbes, 2007; Zupke et

al., 1995). However, these articles did not undertake a detailed error analysis of their regression approach and did not attempt to validate their approach using simulated data sets. Accurate assessment of uncertainty is critical for MFA because it provides the proper weighting of each measured rate in the sum-of-squares objective function that defines the best-fit solution. Furthermore, quantifying the uncertainty in each measurement enables rigorous statistical comparisons to be made between experiments. Recently, Goudar et al. (2009) assessed the propagation of uncertainty from prime variables into specific rates using both a Gaussian error propagation approach and Monte Carlo analysis. Their analysis, however, was limited to perfusion culture where cell concentrations are largely time invariant, and they did not provide a comparison to the more traditional approach of simply averaging the regressed rate parameters derived from replicate experiments. Furthermore, none of these prior studies have led to the development of publically available software tools that automate the estimation of metabolic rates and their uncertainties based on experimental time course measurements.

Here, we compare two methods of error analysis applied to the problem of estimating metabolic rates from extracellular time-course measurements: (i) "Gaussian" error propagation from prime variables and (ii) "Sampling" the regressed parameters from multiple replicate experiments to estimate their standard deviation. Uncertainties obtained from the Gaussian and Sampling approaches were compared to the "true" Monte Carlo error estimate, which provides an asymptotically correct value but is more expensive to compute. We found that the Gaussian approach was the best choice for estimating uncertainty when using a small number of experimental replicates (n=3), which is typical of cell culture experiments. To automate the determination of specific rates and their uncertainties, we developed a MATLAB software package called Extracellular Time-Course Analysis (ETA). This software facilitates the import and selection of data points for regression, calculation of cell specific metabolic rates (or yields) and their uncertainties using either Gaussian error propagation or Monte Carlo analysis, and assessment of the goodness-of-fit of the exponential (or linear) growth model. The model can also account for first-order degradation of metabolites due to non-biological effects. The software provides an intuitive graphical user interface and documentation so that non-experts can readily implement these statistical features to analyze their own experimental data sets.

Using our newly developed ETA software package and a B-cell model of c-Myc-driven cancer, we assessed metabolic phenotypes under both High and Low Myc expression based solely upon extracellular metabolite and cell density measurements. We conducted time-course growth experiments and used ETA to estimate the specific uptake or excretion rate of glucose, lactate, and 18 different amino acids based on the exponential growth model. We found that the faster-growing High Myc cells globally upregulated their consumption of amino acids relative to glucose. In particular, specific uptake rates of glutamine, arginine, serine, lysine, and branched-chain amino acids were substantially increased in High Myc cells relative to Low Myc cells. Rates of glucose uptake and lactate excretion were also increased in High Myc cells, but the relative changes were modest in comparison to growth rate and amino acid fluxes. This study provides an example of how ETA can be applied to assess metabolic phenotypes of mammalian cells as a prelude to flux balance analysis, metabolic flux analysis, or more comprehensive metabolic profiling studies.

3.2 Methods

3.2.1 Balance Equation for Cell Growth

Balanced exponential growth in batch culture is a key underlying assumption of these calculations. This assumption is generally valid for cells that are not experiencing nutrient or spatial growth limitations. The exponential growth equation is

$$X = X_0 e^{\mu t}, \tag{3.1}$$

where μ is the specific growth rate, X is the cell density (i.e., cell mass or number per unit volume of culture medium), t is time, and X_0 is the initial cell density at the onset of exponential growth. Transformation of the equation into a form suitable for linear regression results in

$$\ln(X) = \ln(X_0) + \mu t. \tag{3.2}$$

This equation can be used to determine the specific growth rate from linear regression of cell density measurements over time.

3.2.2 Balance Equations for Substrate Uptake and Product Secretion

The general balance equation that relates changes in medium composition to extracellular metabolic fluxes under batch growth conditions is

$$\frac{dC}{dt} = -kC + vX, \tag{3.3}$$

where C is metabolite concentration, k is the first-order degradation rate constant, v is the specific metabolite production rate, and X is the cell density determined from Equation (3.1). The sign of the specific rate is defined to be negative for substrates and positive for products. The decay term is necessary to account for spontaneous first-order degradation or accumulation of metabolites. Glutamine is the best example of a metabolite that is subject to degradation, since it is known to spontaneously degrade to ammonia and pyrrolidonecarboxylic acid under typical culture conditions (Ozturk and Palsson, 1990). The degradation rate constant is assumed to be independent of cellular metabolism and can be determined empirically by measuring the disappearance rate of glutamine in the absence of cells.

Substituting for X in Equation (3.3) using Equation (3.1) and integrating with respect to t gives

$$\underbrace{Ce^{kt}}_{y} = \underbrace{\frac{vX_0}{\mu+k}}_{a}\underbrace{\left(e^{(\mu+k)t} - 1\right)}_{x} + \underbrace{C_0}_{b}. \tag{3.4}$$

When the decay rate constant k is zero, this equation reduces to

$$\underbrace{C}_{y} = \underbrace{\frac{vX_0}{\mu}}_{a}\underbrace{\left(e^{\mu t} - 1\right)}_{x} + \underbrace{C_0}_{b}. \tag{3.5}$$

Equations (3.4) and (3.5) are both in a linear form $y = ax + b$ that can be used to determine the slope parameter a by regression analysis, which can be subsequently used to calculate the specific rate v.

3.2.3 Data Simulation

Noise-free time courses for cell density and glucose and lactate concentrations were simulated using the rate parameters in Table 3.1. Equations (3.2) and (3.5) were used to simulate 8 measurement time points separated by 12-hour intervals. Normally distributed random errors were introduced to the noise-free data using MATLAB's *normrnd* random number generator to simulate 9999 replicate data sets. The data sets were separated into 3333 groups with $n = 3$ replicates.

Table 3.1 Parameters Used to Generate Simulated Data Sets. The values are representative of those found in our prior experiments and in the literature. Equations (3.2) and (3.5) were used to simulate noise-free time courses for cell density (X), glucose concentration (S), and lactate (P). Normally distributed random errors with zero mean and standard deviation (SD) of $\sigma_{\ln(X)}$, σ_s, or σ_p were added to the noise-free time courses of $\ln(X)$, S, or P, respectively.

Parameter	*Variable*	*Value*	*Units*
Initial Log Cell Density	$\ln(X_0)$	$\ln(2\times10^5)$	
Log Cell Density Measurement SD	$\sigma_{\ln(X)}$	0.1	
Growth Rate	M	0.02888	h^{-1}
Initial Glucose Concentration	S	20	mM
Glucose Measurement SD	σ_s	2	mM
Glucose Uptake Flux	v_s	150	nmol/10^6 cells/h
Initial Lactate Concentration	P	2	mM
Lactate Measurement SD	σ_p	2	mM
Lactate Excretion Flux	v_p	300	nmol/10^6 cells/h
Time step	Δt	12	h

3.2.4 Least-Squares Regression and Error Analysis

Two separate methods were used for least-squares regression and error analysis (Fig. 3.1). The Gaussian approach averaged the n replicate measurements at each time point and performed a single regression using the mean time-course data [m_1, m_2, …, m_N]. The sample variance s_i^2 of each data point was calculated and used to determine a pooled sample variance, s_p^2, over the entire time course according to the equation

$$s_p^2 = \frac{\sum_{i=1}^{N} s_i^2}{N}, \tag{3.6}$$

where N is the total number of time points included in the regression. The standard error of the mean (SEM) was used to represent the uncertainty of each prime variable measurement, given by

$$\delta m_i = \sqrt{\frac{s_p^2}{n}}. \tag{3.7}$$

Errors were propagated from directly measured prime variables, such as cell density or metabolite concentration, to each calculated variable $q = f(m_1, m_2, \ldots)$ using the equation (Taylor, 1997)

$$\delta q^2 = \sum_i \left(\frac{\partial f}{\partial m_i}\right)^2 \delta m_i^2, \tag{3.8}$$

where the sum is over all prime variables that influence the calculated value of q. Numerical finite differencing was applied to estimate the partial derivatives with respect to prime variables (Gardenier et al., 2011). Least-squares linear regression was performed based on Equations (3.2) and (3.5), using the propagated uncertainties dx_i and dy_i associated with x- and y-axis variables, respectively, to determine the weight w_i of each data point in the sum-of-squared residuals (SSR) objective function

$$\text{SSR} = \sum_{i=1}^{N} w_i (y_i - ax_i - b)^2, \tag{3.9}$$

Where,

$$w_{\mathrm{i}} = \frac{1}{(\delta y_i^2 + a\delta x_i^2)}. \quad (3.10)$$

MATLAB's *lscov* command was used to obtain the weighted least-squares estimate of the best-fit line. The iterative re-weighting method of York et al. (2004) was applied to regressions where errors were simultaneously present in both the *x*- and *y*-axis variables.

Alternatively, the Sampling approach did not average the raw data prior to regression. Each replicate time course was regresssed in an unweighted manner and rates were calculated based on Equations (3.2) and (3.5) without estimating the uncertainties of prime variables. The average and SEM of specific rates were then determined within each group of *n* replicates. Because uncertainties were calculated directly from sampling replicate rate estimates, this method required no error propagation.

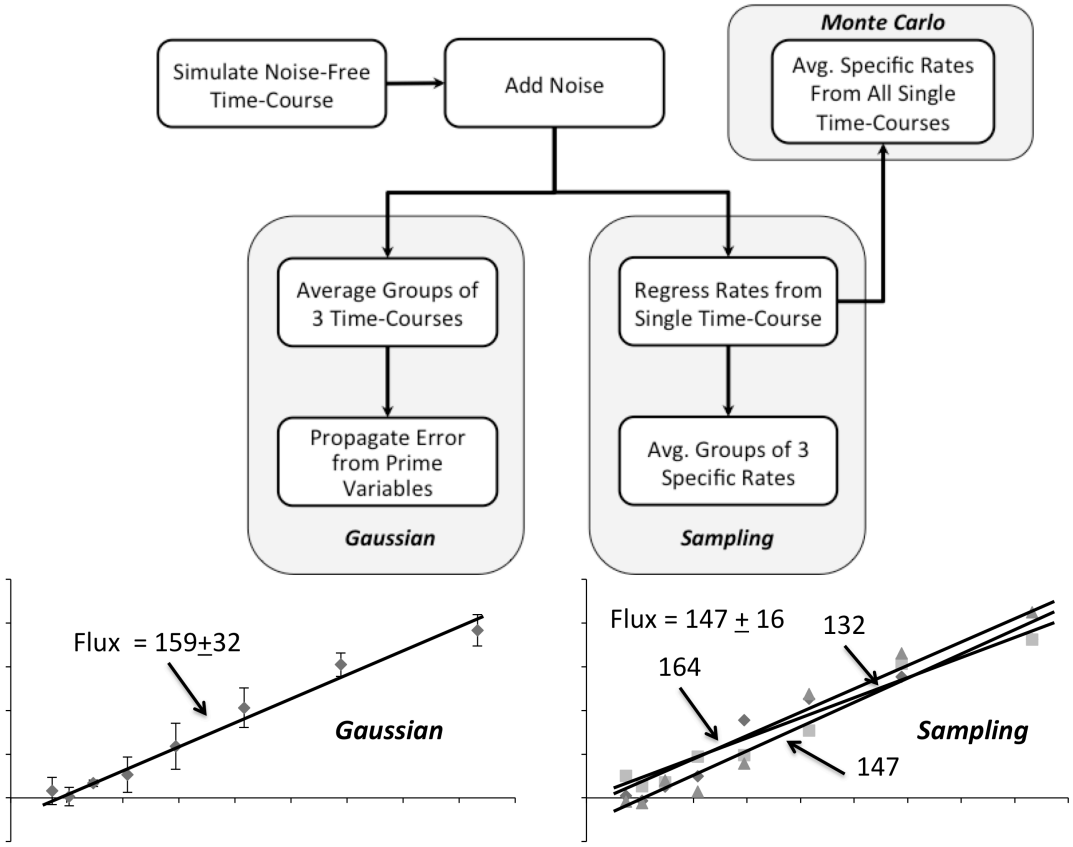

Figure 3.1 Overview of Study Design. A noise-free time course was simulated using the parameter values listed in Table 3.1. Normally distributed random errors were added to the noise-free time course to generate 9999 replicates. The replicates were grouped into 3333 simulated experiments, each with n=3. The simulated experiments were analyzed using either the Gaussian or Sampling approach to estimate specific rates and uncertainties. Monte Carlo estimates of the true parameter values and uncertainties were determined by computing the average and standard deviation of specific rates regressed from all 9999 time courses. An example is provided to illustrate how the Gaussian approach applies a single regression based on the average measurements from each simulated experiment, whereas the Sampling approach averages the rate parameters from n replicate regressions to estimate the final specific rate and its associated uncertainty.

3.2.5 Monte-Carlo Estimation

Monte Carlo (MC) parameter estimates provided "true" values to which the Gaussian and Sampling methods were compared. MC estimates were determined by averaging the specific rates derived from unweighted regression of all 9999 replicate time courses. The standard deviation *s* of all 9999 replicates was used to estimate the true uncertainty of each rate parameter.

3.2.6 Goodness-of-Fit Assessment

We applied an F-test to assess the goodness-of-fit of our mathematical model to each experimental data set. This test is appropriate when the measurement variances are estimated from sample replicates (Bevington et al., 1993; Nielsen, 2003; Sauer, 2006; Stephanopoulos, 1999; Wiechert, 2001). The null hypothesis (H_0) is that the model provides an adequate description of the data and that any lack-of-fit can be attributed to normally distributed random errors in the measurements. The F-test uses the degrees of freedom due to lack of fit (DOF_{LOF}), the degrees of freedom due to pure error (DOF_{PE}), and the sum-of-squared residuals (SSR) to determine a p-value. The DOF_{LOF} is $N–M$, where N is the number of regressed data points and M is the number of fitted parameters (e.g., M=2 in the case of a linear model). The DOF_{PE} is given by $N(n–1)$. The p-value of the F-test is defined as

$$p = \Pr[\mathrm{SSR} > F(DOF_{LOF}, DOF_{PE})], \tag{3.11}$$

or the probability that the SSR exceeds a particular value of the F distribution with corresponding values of DOF_{LOF} and DOF_{PE}.

3.2.7 Cell Culture

The human P493-6 B-cell line expresses an EBNA2-estrogen receptor fusion protein and contains a tetracycline (Tet)-repressible human *MYC* construct (Quek et al., 2010; Schuhmacher et al., 1999). Addition of 1 μg/mL Tet completely represses *MYC* expression, while the co-addition of 1 μM beta-estradiol (BES, MP Biomedicals, Solon, OH) induces a low level of endogenous *MYC* expression driven by the EBNA2 viral protein (Glacken et al., 1988;

Goudar, 2012; Kim and Forbes, 2007; Yustein et al., 2010; Zupke et al., 1995). This allows for three distinct levels of Myc expression: High (no addition), Low (Tet + BES), and None (Tet alone). Only High and Low Myc expression levels were examined in this study. Cells were cultured in RPMI 1640 medium (2 g/L glucose and 2 mM glutamine) supplemented with 10% fetal bovine serum (FBS) and 1% penicillin and streptomycin (PS) at 37°C and 5% CO_2. All cell culture supplies were purchased from Invitrogen (Carlsbad, CA).

3.2.8 Cell Density and Metabolite Concentration Measurements

Extracellular uptake and excretion rates of P493-6 cells were determined in triplicate growth experiments. Three separate T-75 tissue culture flasks were seeded at a density of 150,000 cells/mL. Every 12–16 hours, 300 μL of cell suspension was removed from each flask after gentle mixing with a pipettor. 50 μL were used for counting on a hemacytometer while the remainder was centrifuged to remove cells, and the conditioned cell-free medium was frozen at −80°C. Concentrations of medium glucose and lactate were determined using a YSI 2300 Stat Plus Glucose and Lactate Analyzer (YSI, Yellow Springs, OH). Medium amino acid concentrations were determined using high-performance liquid chromatography (HPLC, Agilent 1200 series) with a gradient elution method on a reverse-phase column (2009; Greene et al., 2009). Briefly, samples were derivatized immediately prior to injection with orthophthalaldehyde (OPA) and injected onto a ZORBAX Eclipse PLUS C18 column (Agilent Technologies, 4.6 × 150 mm, 3.5 μm). Mobile phase A was composed of 10 mM Na_2HPO_4, 10 mM $Na_2B_4O_7$, and 8 ppm NaN_3. Mobile phase B was a 9:9:2 mixture of methanol:acetonitrile:water. The gradient profile was as follows: 2% B for 0.5 minutes, ramp linearly to 47% for 15.5 minutes, ramp linearly to 100% B in 0.1 minutes, hold at 100% B for 3.4 minutes, ramp linearly to 2% B in 0.1 minutes, and hold for 1.4 minutes for a total time of 21 minutes. The flow rate was 1.5 mL/min, and the column was held at 40°C for the duration of the run.

The spontaneous degradation of glutamine to ammonia and pyrrolidonecarboxylic acid was included in the specific rate calculations (Ozturk and Palsson, 1990). The degradation rate was determined to be 0.0031 h^{-1} by measuring glutamine disappearance in control experiments performed in the absence of cells. Evaporation rates determined in control T-75 flasks without cells were found to be negligible in comparison to cell specific metabolic rates.

3.2.9 T-test for Comparison of Flux Estimates

A two tailed t-test was applied to compare specific rate estimates between two experimental groups. The t-statistic is calculated as

$$t = \frac{(v_1 - v_2)}{\sqrt{s^2_{v_1 - v_2}}}, \tag{3.12}$$

where

$$s^2_{v_1 - v_2} = s_p^2 \left(\frac{1}{n_1} + \frac{1}{n_2}\right) \tag{3.13}$$

and

$$s_p^2 = \frac{d_1 s_1^2 + d_2 s_2^2}{d_1 + d_2}. \tag{3.14}$$

Here, $s_p{}^2$ is the pooled sample variance, d_i is the degrees of freedom defined as (N_i – 2), and N_1 and N_2 are the total number of data points used in each regression.

3.2.10 MATLAB Program – Extracellular Time-Course Analysis (ETA)

Using the MATLAB programming environment, custom m-files were coded to perform all calculations required to implement the Gaussian, Sampling, and Monte Carlo methods of rate and uncertainty estimation. A user interface was implemented to facilitate data input and analysis. Documentation included with the software details program usage and functionality. Briefly, cell density and metabolite concentration data can be imported from Microsoft Excel or manually entered by the user. Individual time points can be selected interactively to achieve an acceptable fit to the exponential growth model, based on both graphical displays and the p-value of the F-statistic. A first-order decay rate can be entered to correct for spontaneous metabolite degradation. Calculated specific rates (or yields) and

their uncertainties are tabulated automatically and plotted in an accompanying figure window. The software is freely available at http://mfa.vueinnovations.com/.

In addition to proliferating cell cultures, the exponential growth model can be readily applied to cultures in stationary or decline phase, in which case the specific growth rate will be estimated as near zero or negative, respectively. Furthermore, specifying the dead cell density (X_d) as an accumulating product formed from first-order death of viable cells can then be used to estimate the death rate constant (k_d) of the culture if measurements of cell viability are available (i.e., replace C with X_d and v with k_d in Equation 3.3). ETA is also capable of applying a linear growth model, which is known to occur in some instances of diffusion-limited or contact-inhibited growth of cultures (Freshney, 2000; Rizzi et al., 1989; Taylor, 1997). Although advanced growth models involving logistic or Gompertz equations have been previously used to describe more complicated growth curves, these models are explicitly intended to describe unbalanced growth conditions where growth rate and metabolism are changing over time. Therefore, we have chosen to include only two growth models in ETA (i.e., exponential and linear), because they are applicable to the vast majority of typical cell cultures undergoing balanced growth. Since balanced growth is also a key underlying assumption of FBA and MFA, we do not expect that this limitation will severely restrict the applicability of the program for the purposes it is intended.

3.3 Results

3.3.1 Comparison of Simulated Data Sets

We applied the Gaussian, Sampling, and Monte Carlo approaches to determine specific growth and metabolite production rates by regressing 9999 simulated time courses generated using the parameter values in Table 3.1. We hypothesized that Gaussian error propagation from prime variables would provide more precise rate and uncertainty estimates in comparison to the Sampling approach, which involves simply averaging the regressed rate parameters derived from replicate experiments, when the number of replicates is small. To test this hypothesis we compared 3333 rate estimates derived from the Gaussian and Sampling approaches (each with n=3) to the "true" Monte Carlo estimates determined by averaging rate estimates from all 9999 simulated data sets. The calculated growth, glucose uptake, and lactate excretion rates returned by the Gaussian and Sampling methods exhibited normal distributions over the 3333 simulated experiments (data not shown). The mean of each distribution was nearly identical to the

Monte Carlo estimate (Table 3.2), and approximately 68% of the calculated rates fell within one standard error of the MC estimate in each case. As a result, we concluded that averaging experimental replicates either before or after regression analysis provides an equally valid approach to estimate the value of each specific rate parameter.

In contrast to the rate values, the two methods did not produce equally accurate estimates of parameter uncertainties. When comparing the distribution of uncertainties returned by each method, we found that Gaussian error propagation resulted in an approximately normal distribution that was centered on the true value while the uncertainties determined by the Sampling approach had a non-normal distribution that was not centered around the true value (Fig. 3.2). In order to assess the accuracy of the two methods quantitatively, we calculated root-mean-square (RMS) errors based on the residuals between estimated uncertainties returned by the Gaussian or Sampling approach and the true values determined by Monte Carlo analysis. The RMS errors for Gaussian error propagation were nearly 3-fold lower than the Sampling approach, indicating less variability and greater accuracy (Table 3.3). As a result, we concluded that the Gaussian approach provides more accurate and precise uncertainty estimates when the number of experimental replicates is small (e.g., n=3) and is therefore the preferred method.

Table 3.2 Rate Estimations Based on Simulated Data Sets. Values for both Gaussian and Sampling approaches are shown as $M \pm SEM$, where M is the population mean over all 3333 simulated experiments (each with n=3) and SEM is the standard error of the population mean. The Monte Carlo estimates represent the means over all 9999 replicates.

	Growth (h^{-1})	***Glucose nmol/10^6 cells/h***	***Lactate nmol/10^6 cells/h***
Gaussian	0.028878 ± 0.000013	150.1 ± 0.3	299.9 ± 0.3
Sampling	0.028878 ± 0.000013	150.1 ± 0.3	300.0 ± 0.3
Monte Carlo	0.028878 ± 0.000013	150.1 ± 0.3	300.0 ± 0.3

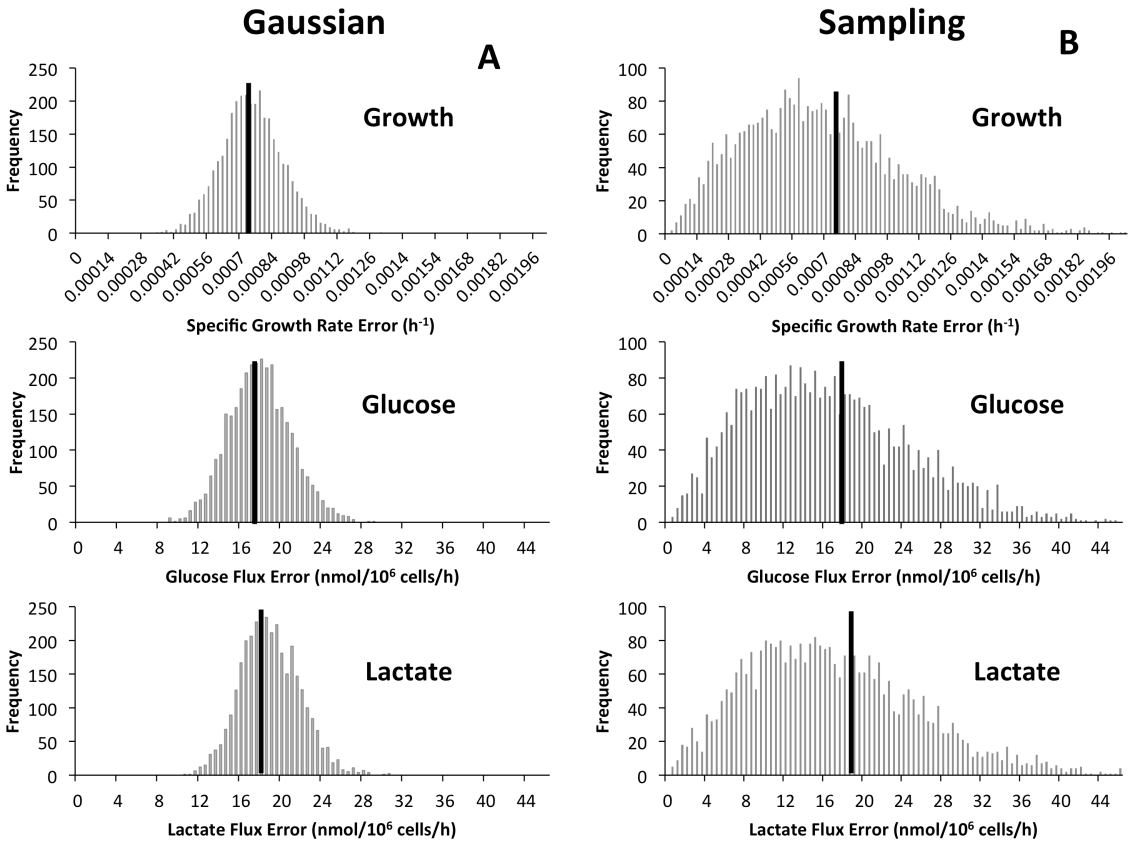

Figure 3.2 Distribution of Estimated Uncertainties Determined from Simulated Data Sets. Histograms describing the distribution of uncertainties for specific growth, glucose uptake, and lactate excretion rates are shown for both (A) Gaussian error propagation and (B) Sampling rate estimates from replicate experiments. The solid black lines represent the Monte Carlo estimate of the true uncertainty of the estimated rates, which is given by $\sigma_i/\sqrt{n}$.

Table 3.3 Root-Mean-Square (RMS) Errors of Estimated Uncertainties. RMS errors were calculated for both the Gaussian and Sampling approaches by first computing the residuals between estimated uncertainties and the true values determined by Monte Carlo analysis. The residuals for all simulated experiments were then combined by taking the square root of the sum of squared residuals divided by the total number of simulated experiments (3333).

	Growth (h^{-1})	*Glucose* (*nmol/10*^{6} *cells/h*)	*Lactate* (*nmol/10*^{6} *cells/h*)
Gaussian	1.3×10^{-4}	3.1	2.9
Sampling	3.5×10^{-4}	8.6	9.0

3.3.2 P493-6 Rate Estimation with ETA

Using our custom ETA software, we estimated specific metabolic rates for High and Low Myc P493-6 cell cultures. We estimated specific growth rate as well as uptake and excretion rates of glucose, lactate, and 18 of 20 amino acids (Table 3.4). ETA enabled us to select the most appropriate points for analysis based on the goodness-of-fit F-test and visual inspection (Fig. 3.3). For glutamine, we included an empirically determined degradation rate constant of 0.0031 h^{-1}, which significantly improved the p-value of the model fit from 0.0044 to 0.9329. As shown in Fig. 3.4, the data fall along a straight line when corrected for degradation effects using Equation (3.4), but have a curved profile when uncorrected.

Growth of Low Myc cells was 40% slower than High Myc cells, while glucose uptake was reduced by only 21%. Both High and Low Myc cells exhibited a highly glycolytic phenotype, with the majority of incoming carbon excreted as lactate. This was most clearly indicated by the high lactate-to-glucose (L/G) ratios of 1.9 ± 0.2 and 2.1 ± 0.3 for High and Low Myc cells, respectively. Besides glucose, glutamine is the other major carbon substrate for mammalian cell cultures (Gardenier et al., 2011; Vander Heiden et al., 2009). Glutamine uptake was elevated nearly 2-fold in High Myc cells relative to Low Myc cells, supplying 9% of total carbon to High Myc cells and 7% to Low Myc cells. The uptake rates of most other amino acids were similarly elevated in High Myc cells (Table 3.4).

Table 3.4 Metabolic Rates for High and Low Myc P493-6 Cell Cultures. Rates have units of nmol/10^6 cells/h except for cell growth, which has units of h^{-1}. P-values based on the goodness-of-fit F-test are listed for each rate parameter. Significance is indicated for the comparison between Low and High Myc conditions based on a two-tailed Student's t-test with $p < 0.05$.

	High Myc		***Low Myc***		
Metabolite	***Specific Rate (nmol/10^6 cells/h)***	***Fit p-value***	***Specific Rate (nmol/10^6 cells/h)***	***Fit p-value***	***Sig. Diff. ($p < 0.05$)***
Biomass (h^{-1})	0.0290 ± 0.0010	0.1477	0.0176 ± 0.0010	0.7419	✔
			Uptake Fluxes		
Glucose	73 ± 7	0.9177	58 ± 7	0.5981	✖
Arginine	4.6 ± 0.6	0.4751	1.9 ± 0.3	0.0387	✔
Asparagine	0.9 ± 0.4	0.2923	0.9 ± 0.3	0.1637	✖
Cystine	0.73 ± 0.13	0.7364	0.88 ± 0.09	0.3990	✖
Glutamine	11.5 ± 0.7	0.9329	5.9 ± 0.40	0.2089	✔
Histidine	0.78 ± 0.12	0.903	0.17 ± 0.05	0.5644	✔
Isoleucine	2.5 ± 0.2	0.9694	1.3 ± 0.30	0.7093	✔
Leucine	3.3 ± 0.3	0.8483	1.02 ± 0.14	0.2334	✔
Lysine	2.1 ± 0.2	0.9233	0.26 ± 0.08	0.3271	✔
Methionine	0.7 ± 0.1	0.9807	0.11 ± 0.04	0.6590	✔
Phenylalanine	0.1 ± 0.3	0.9951	0.3 ± 0.11	0.9754	✖
Serine	4.1 ± 0.2	0.8515	1.34 ± 0.10	0.3054	✔
Threonine	0.27 ± 0.06	0.8198	0.57 ± 0.09	0.0520	✔
Tyrosine	0.57 ± 0.09	0.9797	0.14 ± 0.05	0.5471	✔
Valine	1.41 ± 0.12	0.9193	0.54 ± 0.07	0.4526	✔
			Excretion Fluxes		
Lactate	138 ± 9	0.2805	119 ± 7	0.9953	✖
Alanine	1.63 ± 0.14	0.8557	0.44 ± 0.09	0.1483	✔
Aspartate	0.36 ± 0.14	0.8772	-0.38 ± 0.05	0.0072	✔
Glutamate	2.7 ± 0.4	0.6521	2.9 ± 0.2	0.4787	✖
Glycine	0.8 ± 0.2	0.3028	0.01 ± 0.08	0.3727	✔

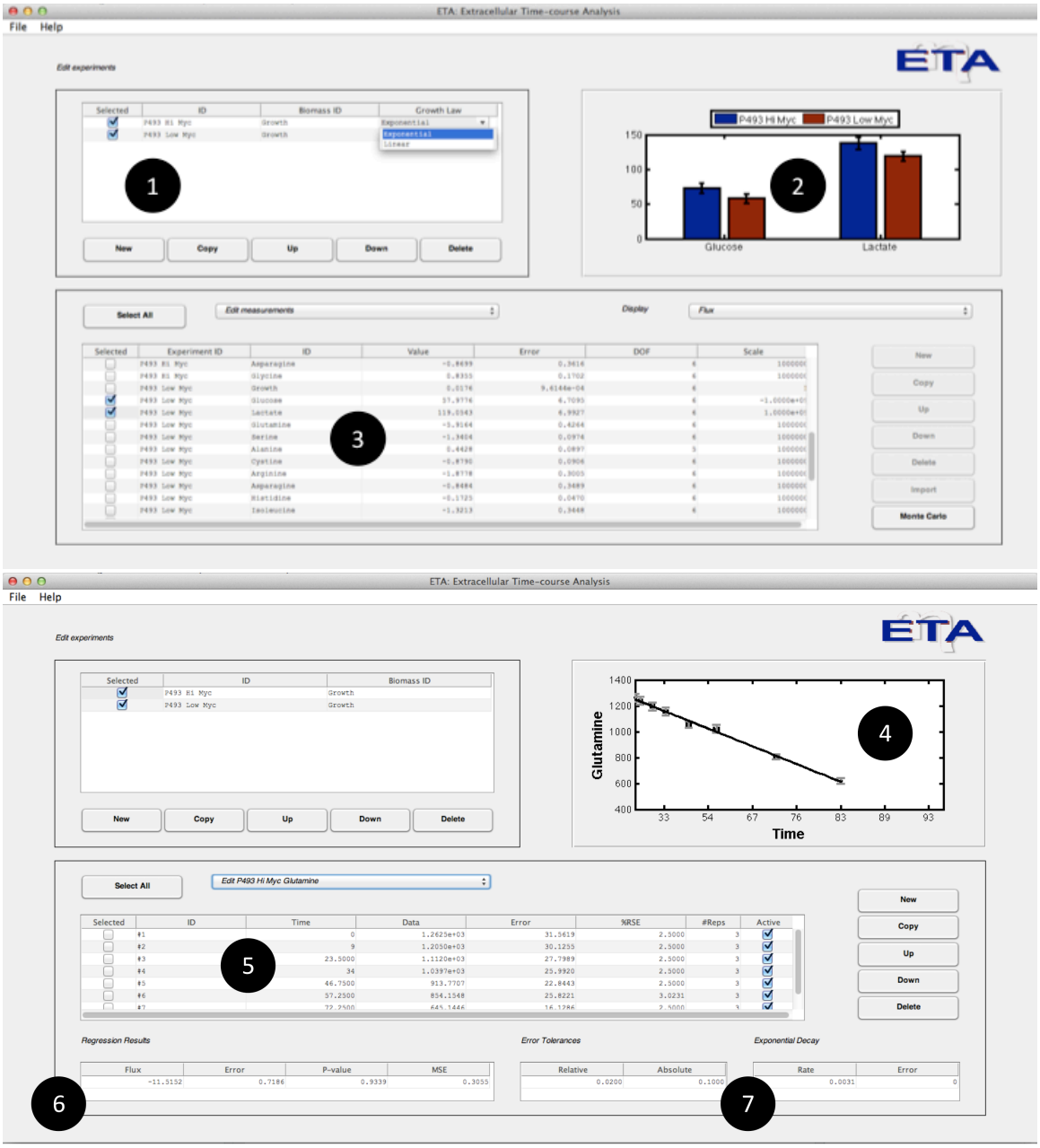

Figure 3.3 Features of the ETA Software Package. (A) Users are able to (1) create new experimental time courses and view the calculated rate (or yield) estimates and associated uncertainties in both (2) graphical and (3) tabular formats for either exponential or linear growth models. (B) When a single measurement is selected, the program allows the user to (4) graphically assess the goodness-of-fit, (5) enter and select raw data for regression, and (6) view the calculated rates along with the p-value and mean-square error of the fit. Adjustable error tolerances and first-order degradation parameters can also be supplied by the user (7).

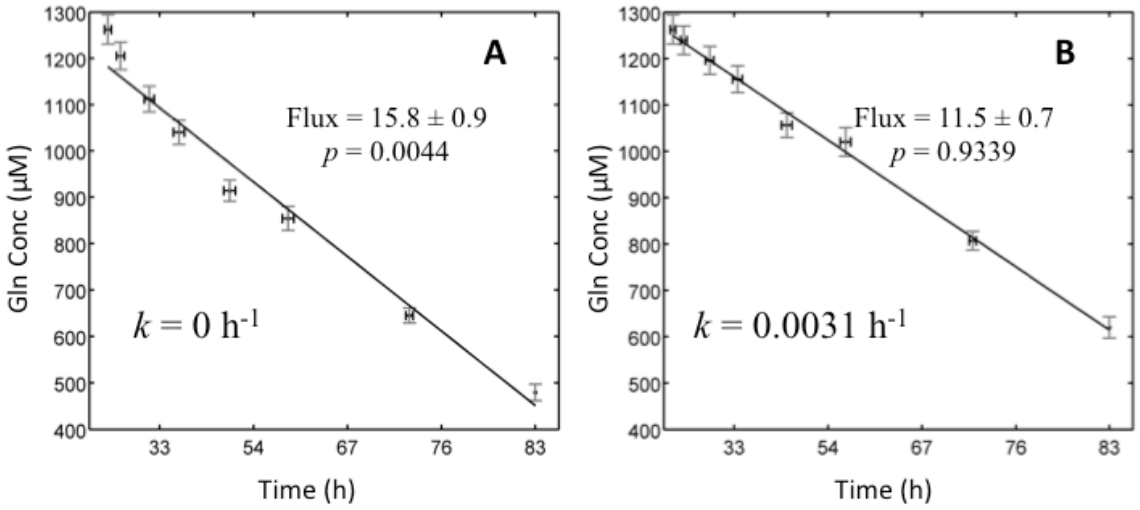

Figure 3.4 Effects of Spontaneous Degradation on Glutamine Rate Estimation. (A) When first-order degradation of glutamine is not accounted for, the data do not fit the exponential growth model. (B) When the correct degradation constant is included, Equation (3.4) provides an acceptable fit to the raw concentration measurements. Flux is measured in units of nmol/10^6 cells/hour.

3.4 Discussion

Accurate quantification of cell specific metabolic rates and their uncertainties is of critical importance for assessing metabolic phenotypes of cultured cells. Using rigorous parameter regression approaches, we have shown that Gaussian error propagation is the most accurate and precise method for estimating the uncertainty of specific rates when the number of experimental replicates is small. This analysis uses finite differencing to compute the derivatives in Equation (3.8), which allows the uncertainties in all prime variables to be propagated into calculated variables. The Sampling approach, however, attempts to estimate uncertainties based solely on the standard deviation of estimated rates determined from replicate experiments. When n is sufficiently large, this is an acceptable method that asymptotically approaches the accuracy of the Monte Carlo result. However, when n is small, uncertainty estimates become less reliable than those determined by Gaussian error propagation. A further practical consideration is that some experiments do not allow for repeated sampling of the same cell culture, which means that each time point must be derived from a separate culture plate or flask. Because there is no logical way to group these data points into individual time courses without first averaging the data from separate experimental replicates, the Sampling approach is not applicable to this scenario and Gaussian error propagation is the only approach that can be used to obtain meaningful uncertainty estimates.

We applied the Gaussian approach coded within our custom ETA software to analyze time-course experiments conducted on High Myc and Low Myc P493-6 B-cells. These cells contain a tetracycline-repressible Myc construct, which enables different levels of Myc expression to be studied on an isogenic background (Pajic et al., 2000; Pajic et al., 2001; 2004). High Myc cells are tumorigenic and resemble human Burkitt lymphoma cells, whereas Low Myc cells are nontumorigenic (Yustein et al., 2010). Therefore, comparison of metabolic phenotypes between High and Low Myc cells is expected to reveal differences between cancerous cells and normal proliferating cells.

Measurements of cell density and extracellular nutrient concentrations were obtained throughout exponential phase and biological replicates were averaged. This was followed by regression analysis to estimate specific rates of growth, substrate consumption, and product excretion. Based on these specific rates, we observed that High Myc cells significantly increased their growth rate and the magnitude of most nutrient uptake and excretion rates in comparison to Low Myc cells. These results are consistent with previous reports of the general stimulating effect of

Myc on cell growth and metabolism (Fan et al., 2010; Morrish et al., 2009; Morrish et al., 2008). Studies in Rat1a fibroblasts and P493-6 cells have shown that Myc enhances flux through the glycolytic pathway by direct transactivation of several glycolytic genes (Kim et al., 2004; Osthus et al., 2000; Shim et al., 1997). However, ectopic Myc expression only modestly increased glucose consumption and lactate production in our system, and the relative changes in these rates were sub-proportional to the change in specific growth rate we observed. In contrast, most amino acid uptake fluxes were increased 2- to 3-fold in High Myc cells relative to Low Myc cells, which exceeded the 1.6-fold change in specific growth rate. Therefore, ectopic Myc expression impacted amino acid fluxes more strongly than glycolytic fluxes in P493-6 cells.

It has been previously shown that Myc exerts direct control over glutamine metabolism and that Myc-overexpressing cells are acutely sensitive to glutamine withdrawal or inhibition of anaplerotic glutamine flux entering the TCA cycle (Fan et al., 2010; Wise et al., 2008; Yuneva et al., 2007). Our data support these findings, as we observed a significant increase in glutamine uptake in High Myc cells as compared to Low Myc cells. However, our results also indicate that High Myc cells simultaneously increased most other amino acid fluxes in addition to glutamine. Nearly half of the incoming amino acids were consumed in excess of their biosynthetic requirements, which indicates that they were partially catabolized to meet the energetic or redox demands of P493-6 cells. Aside from one study that identified serine hydroxymethyltransferase (*SHMT2*) as a direct Myc target gene (Nikiforov et al., 2002), little is known about how Myc stimulates metabolism of other amino acids besides glutamine. Based on these results, further work to elucidate the mechanisms by which Myc influences global patterns of amino acid utilization in tumor cells could have significant therapeutic or diagnostic implications.

One distinct advantage of using Gaussian error propagation for specific rate determination is the ability to rigorously assess the goodness-of-fit of the exponential growth model to the experimental data. In addition to accurate uncertainty estimation, the ETA software enables the user to interactively include or exclude individual data points based on the p-values of the goodness-of-fit F-test and graphical displays. This would not be possible without measurement of full time-course data, which enables confirmation of the underlying assumptions implying balanced growth and constant metabolic rates. Several recent articles have appeared in the biotechnology literature that rely on rate estimates computed from only two measurement time points (Jain et al., 2012; Mullen et al., 2012). While

this may be suitable for initial screening experiments, it does not lend itself to the type of rigorous error analysis and statistical treatment that is necessary for quantitative flux studies. Therefore, collection of multiple sample time points under balanced growth conditions followed by regression analysis and Gaussian error propagation are prerequisite for precise determination of metabolic fluxes.

We determined p-values for the P493-6 data set which describe the confidence level in each fitted parameter based on an F-test. The goodness-of-fit p-value reflects the probability that any disagreements between the model and the experimental measurements are due to random errors rather than systematic errors. Based on this test, we should conclude that the fit is inadequate if the calculated p-value is unreasonably low. A low p-value can result from a few possible causes. First, it can indicate that the model is inadequate (e.g., balanced exponential growth assumption does not hold) or there are gross measurement errors in the data. Second, it can indicate that the true measurement errors are larger than what was specified in the regression analysis. If both of these can be excluded, the final possibility is that the measurement errors are not normally distributed. This can lead to p-values that seem small (e.g., 0.001) but may still be justifiable in practical cases where the errors have some non-Gaussian component. Fits that are grossly incorrect will often give very small p-values (e.g., 10^{-18}) and should be summarily rejected (Press et al., 1992). In all cases, the p-values of the P493-6 rate estimates were greater than 0.001, indicating that the exponential model was acceptable.

One limitation of our approach is that it assumes balanced exponential growth with constant specific rates of nutrient uptake or product excretion. If the culture exhibits multiple distinct growth phases (e.g., exponential, stationary, decline, etc.) or metabolic shifts during the experiment, the full time course can be divided into separate subintervals in which growth and metabolism are approximately constant. This will allow for each subinterval to be separately analyzed and subsequently compared. Obviously, this is not possible if growth and metabolism are changing continuously over time or if distinct transition points cannot be readily identified within the overall time course. Both Leighty and Antoniewicz (2011) and Niklas et al. (2011) have developed sophisticated approaches for addressing such fully time-dependent scenarios by combining extracellular measurements with stoichiometric balance constraints that enable dynamic MFA calculations. Leighty and Antoniewicz used piece-wise linear functions to approximate the time-dependence of extracellular concentration measurements, whereas Niklas et al.

applied polynomial splines to smooth and differentiate the extracellular measurements. Although these methods provide powerful alternative approaches that can be applied more generally to either metabolically transient or steady-state conditions, the underlying growth equations do not reduce to the canonical exponential growth model under steady-state growth conditions and therefore do not lend themselves readily to the analysis of standard growth experiments. Furthermore, the increased parameterization of these models can lead to elevated flux uncertainties in situations where the additional complexity is not warranted. This is especially evident during the initial period of batch or fed-batch growth when extracellular concentrations change slowly and therefore signal-to-noise ratios are small, as noted by Niklas et al. (2011).

In summary, the application of regression analysis and Gaussian error propagation provides a rigorous approach to compare the metabolic phenotypes of different cell lines and growth conditions. While many types of experimental assays have been developed to facilitate the rapid collection of metabolic measurements, software tools that automate the analysis and statistical assessment of these data have been lacking. Therefore, ETA has been developed to streamline the analysis workflow required to (i) compute cell specific metabolic rates and their uncertainties based on an exponential or linear growth assumption, (ii) test the goodness-of-fit of the experimental data to the regression model, and (iii) rapidly compare the results across multiple experiments. Although our approach does not involve the complexity of some recently introduced dynamic MFA algorithms, we expect that it will be applicable to most typical batch or intermittent fed-batch experiments where metabolic steady state is achieved for extended intervals punctuated by infrequent metabolic transitions caused by the onset of nutrient depletion, oxygen limitation, or accumulation of some inhibitory factor (Deshpande et al., 2009). The rates calculated by ETA can then serve as inputs for a wide range of more advanced stoichiometric or kinetic modeling approaches, including FBA or MFA.

3.5 References

Bevington PR, Robinson DK, Bunce G. 1993. Data reduction and error analysis for the physical sciences. *Am. J. Physics* **61**:766.

Deshpande R, Yang TH, Heinzle E. 2009. Towards a metabolic and isotopic steady state in CHO batch cultures for reliable isotope-based metabolic profiling. *Biotechnol. J.* **4**:247–263.

Fan Y, Dickman KG, Zong WX. 2010. Akt and c-Myc Differentially Activate Cellular Metabolic Programs and Prime Cells to Bioenergetic Inhibition. *J. Biol. Chem.* **285**:7324–7333.

Freshney RI. 2000. Culture of Animal Cells: A Manual of Basic Technique. 4 ed. New York: Wiley-Liss. Vol. xxvi 577 pp.

Gardenier GH, Gui F, Demas JN. 2011. Error Propagation Made Easy Or at Least Easier. *J. Chem. Educ.* **88**:916–920.

Glacken MW, Adema E, Sinskey AJ. 1988. Mathematical descriptions of hybridoma culture kinetics: I. Initial metabolic rates. *Biotechnol. Bioeng.* **32**:491–506.

Goudar CT. 2012. Computer programs for modeling mammalian cell batch and fed-batch cultures using logistic equations. *Cytotechnology* **64**:465–475.

Goudar CT, Biener R, Konstantinov KB, Piret JM. 2009. Error propagation from prime variables into specific rates and metabolic fluxes for mammalian cells in perfusion culture. *Biotechnol. Prog.* **25**:986–998.

Greene J, Henderson JW Jr, Wikswo JP. 2009. Rapid and Precise Determination of Cellular Amino Acid Flux Rates Using HPLC with Automated Derivatization with Absorbance Detection. *Agilent Technologies*:1–8.

Jain M, Nilsson R, Sharma S, Madhusudhan N, Kitami T, Souza AL, Kafri R, Kirschner MW, Clish CB, Mootha VK. 2012. Metabolite profiling identifies a key role for glycine in rapid cancer cell proliferation. *Science* **336**:1040–1044.

Kim B-J, Forbes NS. 2007. Flux analysis shows that hypoxia-inducible-factor-1-alpha minimally affects intracellular metabolism in tumor spheroids. *Biotechnol. Bioeng.* **96**:1167–1182.

Kim J-W, Zeller KI, Wang Y, Jegga AG, Aronow BJ, O'Donnell KA, Dang CV. 2004. Evaluation of myc E-box phylogenetic footprints in glycolytic genes by chromatin immunoprecipitation assays. *Mol. Cell. Biol.* **24**:5923–5936.

Leighty RW, Antoniewicz MR. 2011. Dynamic metabolic flux analysis (DMFA) A framework for determining

fluxes at metabolic non-steady state. *Metab. Eng.* **13**:745–755.

Morrish F, Isern N, Sadilek M, Jeffrey M, Hockenbery DM. 2009. c-Myc activates multiple metabolic networks to generate substrates for cell-cycle entry. *Oncogene* **28**:2485–2491.

Morrish F, Neretti N, Sedivy JM, Hockenbery DM. 2008. The oncogene c-Myc coordinates regulation of metabolic networks to enable rapid cell cycle entry. *Cell Cycle* **7**:1054–1066.

Mullen AR, Wheaton WW, Jin ES, Chen P-H, Sullivan LB, Cheng T, Yang Y, Linehan WM, Chandel NS, DeBerardinis RJ. 2012. Reductive carboxylation supports growth in tumour cells with defective mitochondria. *Nature* **481**:385–388.

Nielsen J. 2003. It is all about metabolic fluxes. *J. Bacteriol.* **185**:7031.

Nikiforov MA, Chandriani S, O'Connell B, Petrenko O, Kotenko I, Beavis A, Sedivy JM, Cole MD. 2002. A functional screen for Myc-responsive genes reveals serine hydroxymethyltransferase, a major source of the one-carbon unit for cell metabolism. *Mol. Cell. Biol.* **22**:5793.

Niklas J, Schräder E, Sandig V, Noll T, Heinzle E. 2011. Quantitative characterization of metabolism and metabolic shifts during growth of the new human cell line AGE1.HN using time resolved metabolic flux analysis. *Bioproc. Biosys. Eng.* **34**:533–545.

Osthus RC, Shim H, Kim S, Li Q, Reddy R, Mukherjee M, Xu Y, Wonsey D, Lee LA, Dang CV. 2000. Deregulation of glucose transporter 1 and glycolytic gene expression by c-Myc. *J. Biol. Chem.* **275**:21797–21800.

Ozturk SS, Palsson BO. 1990. Chemical decomposition of glutamine in cell culture media: effect of media type, pH, and serum concentration. *Biotechnol. Prog.* **6**:121–128.

Pajic A, Spitkovsky D, Christoph B, Kempkes B, Schuhmacher M, Staege MS, Brielmeier M, Ellwart J, Kohlhuber F, Bornkamm GW. 2000. Cell cycle activation by c-myc in a Burkitt lymphoma model cell line. *Int. J. Cancer* **87**:787–793.

Pajic A, Staege MS, Dudziak D, Schuhmacher M, Spitkovsky D, Eissner G, Brielmeier M, Polack A, Bornkamm GW. 2001. Antagonistic effects of c-myc and Epstein-Barr virus latent genes on the phenotype of human B cells. *Int. J. Cancer* **93**:810–816.

Press WH, Teukolsky SA, Vetterling WT, Flannery BP. 1992. Numerical Recipes in C: The Art of Scientific Computing. *Cambridge University Press*.

Quek L-E, Dietmair S, Krömer JO, Nielsen LK. 2010. Metabolic flux analysis in mammalian cell culture. *Metab. Eng.* **12**:161–171.

Rizzi M, Klein C, Schulze C, Bui-Thanh N-A, Dellweg H. 1989. Xylose fermentation by yeasts. 5. Use of ATP balances for modeling oxygen-limited growth and fermentation of yeastPichia stipitis with xylose as carbon source. *Biotechnol. Bioeng.* **34**:509–514.

Sauer U. 2006. Metabolic networks in motion: 13C-based flux analysis. *Mol. Sys. Biol.* **2**:62.

Schuhmacher M, Staege M, Pajic A, Polack A, Weidle U, Bornkamm G, Eick D, Kohlhuber F. 1999. Control of cell growth by c-Myc in the absence of cell division. *Curr. Bio.* **9**:1255–1258.

Shim H, Dolde C, Lewis B, Wu C, Dang CV, Jungmann R, Dalla-Favera R. 1997. c-Myc transactivation of LDH-A: implications for tumor metabolism and growth. *Proc. Nat. Acad. Sci.* **94**:6658.

Stephanopoulos G. 1999. Metabolic Fluxes and Metabolic Engineering. *Metab. Eng.* **1**:1–11.

Taylor JR. 1997. An Introduction to Error Analysis: The Study of Uncertainties in Physical Measurements 17(null) ed. Sausalito, CA: University Science Books 327 pp.

Vander Heiden MG, Cantley LC, Thompson CB. 2009. Understanding the Warburg effect: the metabolic requirements of cell proliferation. *Science* **324**:1029–1033.

Wiechert W. 2001. 13C metabolic flux analysis. *Metab. Eng.* **3**:195–206.

Wise D, DeBerardinis RJ, Mancuso A, Sayed N, Zhang X, Pfeiffer H, Nissim I, Daikhin E, Yudkoff M, McMahon S. 2008. Myc regulates a transcriptional program that stimulates mitochondrial glutaminolysis and leads to glutamine addiction. *Proc. Nat. Acad. Sci.* **105**:18782.

York D, Evensen NM, Martínez ML, De Basabe Delgado J. 2004. Unified equations for the slope, intercept, and standard errors of the best straight line. *Am. J. Physics* **72**:367.

Yuneva M, Zamboni N, Oefner P, Sachidanandam R, Lazebnik Y. 2007. Deficiency in glutamine but not glucose induces MYC-dependent apoptosis in human cells. *J. Cell Biol.* **178**:93.

Yustein JT, Liu Y-C, Gao P, Jie C, Le A, Vuica-Ross M, Chng WJ, Eberhart CG, Bergsagel PL, Dang CV. 2010. Induction of ectopic Myc target gene JAG2 augments hypoxic growth and tumorigenesis in a human B-cell model. *Proc. Nat. Acad. Sci.* **107**:3534–3539.

Zupke C, Sinskey AJ, Stephanopoulos G. 1995. Intracellular flux analysis applied to the effect of dissolved oxygen on hybridomas. *Appl Microbiol Biotechnol* **44**:27–36.

CHAPTER 4

^{13}C METABOLIC FLUX ANALYSIS METHOD VALIDATION AND APPLICATION TO MYC-OVEREXPRESSING B-CELLS

4.1 Introduction

The reprogramming of energy metabolism is emerging as an important molecular hallmark of cancer cells (Hanahan and Weinberg, 2011). In particular, understanding the so-called Warburg effect, described as the avid conversion of glucose to lactate by tumor cells under aerobic conditions, has become a high priority in cancer research (Hsu and Sabatini, 2008; Koppenol et al., 2011; Vander Heiden et al., 2009). Recent discoveries linking specific metabolic alterations to cancer development have strengthened the idea that deregulated metabolism is more than a side effect of malignant transformation, but may in fact be a functional driver of tumor growth and progression in some cancers (Dang et al., 2009; DeBerardinis et al., 2008; Vander Heiden et al., 2010). Furthermore, prior studies have demonstrated that the Warburg effect can be reversed by either inhibiting lactate production (Fantin et al., 2006; Le et al., 2010) or altering the expression of specific glycolytic enzymes (Christofk et al., 2008), which correlates with a reduction in the ability of isogenic cancer cells to form tumors in nude mouse xenografts. Because of these and other discoveries, deregulated metabolic pathways have become attractive targets for cancer therapeutics (Evans et al., 2005; Kroemer and Pouyssegur, 2008; Michelakis et al., 2008).

To guide the search for new therapeutic targets and to better understand the mechanisms of metabolic reprogramming in tumor cells, integrative approaches are needed to fully characterize the metabolic phenotypes of cancer cells and to determine how they are influenced by specific molecular alterations. In particular, the ability to map intracellular carbon flows using ^{13}C metabolic flux analysis (MFA) provides an attractive platform to elucidate the functional behavior of entire biochemical networks, rather than individual reactions or nodes in isolation (Sauer, 2006). By feeding cells a ^{13}C-labeled substrate, and subsequently measuring the patterns of isotope incorporation in downstream metabolic products, extensive information about the intracellular distribution of carbon flux can be obtained. This enables system-wide quantification of reversible, parallel, and cyclic metabolic pathways that would

be otherwise unidentifiable based solely upon measurements of extracellular nutrient uptake and product excretion (Zamboni et al., 2009).

While ^{13}C MFA provides a rich source of phenotypic information, the application of this technique to mammalian systems presents unique challenges. In particular, the presence of subcellular compartmentation, complex media formulations, and slow labeling dynamics can lead to significant difficulties in experimental design and data interpretation (Zamboni, 2011). As a result, most mammalian MFA studies have relied on direct extraction and isotopomer analysis of free intracellular metabolites, rather than more slowly labeled—but highly abundant and stable—macromolecular species (Zamboni et al., 2009). Isotopically non-stationary MFA (INST-MFA) provides one approach to circumvent these limitations through computational analysis of metabolite labeling patterns obtained during the transient labeling period prior to isotopic steady state (Wiechert and Nöh, 2005). This approach offers several advantages over steady-state MFA, including shorter experimental times and the ability to determine fluxes with increased precision (Nöh and Wiechert, 2011; Young et al., 2008).

Here, we investigated the metabolic alterations caused by differential expression of the *MYC* oncogene in a human B-cell line. *MYC* encodes the transcription factor c-Myc (herein termed Myc), which is a global regulator of cell growth, metabolism, and apoptosis (Dang, 1999). Myc exhibits deregulated expression in approximately 30% of human cancers (Dang et al., 2008) and is one of four transcription factors that collectively can reprogram differentiated adult cells back to a pluripotent stem cell state (Takahashi and Yamanaka, 2006). Although a few prior studies have applied isotopomer analysis to investigate the metabolic fates of ^{13}C-labeled glucose and glutamine tracers in Myc-expressing cells, these approaches were not capable of integrating numerous isotopic measurements into a comprehensive flux map that encompasses all major pathways of central carbon metabolism (Le et al., 2012; Morrish et al., 2008; Wise et al., 2008). Furthermore, these studies were focused on discovering metabolic differences between Myc-expressing and non-expressing cells, rather than between cells with oncogenic (High) and endogenous (Low) Myc expression levels. Our study, on the other hand, applied rigorous ^{13}C flux analysis to quantify metabolic phenotypes of P493-6 B-cells, which have been engineered to provide three distinct levels of Myc expression (No, Low, or High) depending on culture conditions.

We compared several steady-state and isotopically nonstationary MFA approaches to identify the best approach for analysis of P493-6 cells based on isotopomer measurements of protein-bound amino acids and ribose-bound RNA. We concluded that ^{13}C INST-MFA was the most effective strategy for flux determination in these cells, and that ribose isotopomer measurements were important for maximizing flux identifiability. We then applied this approach to quantify fluxes in both High and Low Myc P493-6 cells (Fig. 4.1) and found significant reprogramming of central metabolism in response to ectopic Myc expression. High Myc cells relied more heavily on mitochondrial metabolism than Low Myc cells and globally upregulated their consumption of amino acids relative to glucose. The oxidative pentose phosphate (PP) pathway exhibited minimal activity under both High and Low Myc conditions, with negligible flux through the non-oxidative PP branch. Based on these results, we expect that ^{13}C INST-MFA will become a powerful tool for analysis of tumor cell physiology and for identification of critical metabolic nodes that can be targeted to inhibit cancer growth.

4.2 Methods

4.2.1 Cell Culture

P493-6 B-cells were cultured according to the method detailed in section 3.2.7 of Chapter 3 with the following exception. For tracer experiments, glucose-free medium was supplemented with the following mixture of ^{13}C-labeled substrates: 28% [U-$^{13}C_6$]glucose, 20% [1-^{13}C]glucose, and 52% [1,2-$^{13}C_2$]glucose. All tracers were purchased from Cambridge Isotope Laboratories (Andover, MA).

4.2.2 Oxygen Uptake Rates

High-resolution O_2 consumption measurements were conducted at 37°C in RPMI 1640 medium using the OROBOROS O_2K Oxygraph (Oroboros Instruments, Innsbruck, Austria). Cells were adjusted to a density of one million cells/mL and allowed to equilibrate in the instrument for a minimum of ten minutes. Cells were stirred at 750 rpm in atmospheric conditions without CO_2 control. To confirm that oxygen uptake was dependent on cellular respiration, we treated cells with the Complex I inhibitor rotenone at a concentration of 100 nM (Kim et al., 2006). Higher rotenone concentrations produced erratic measurements and did not result in further reductions in the O_2 uptake rate.

4.2.3 Specific Rate Determination

Cell specific rates were determined according to the methods detailed in section 3.2 of Chapter 3.

4.2.4 Steady-State Labeling Experiment

In order to achieve steady-state labeling, it was necessary to culture cells continuously in the presence of tracers throughout multiple platings. Cells were seeded at an initial density of 150,000 cells/mL in a T-25 flask. Every two days, cells were counted and replated at the same initial density in fresh tracer-containing medium. After 4 platings (approximately 8 cell doublings), the cells were harvested by centrifugation at 1500 RPM, washed with PBS, and extracted to isolate total cellular protein and RNA. Each experiment was performed in triplicate.

4.2.5 Isotopically Nonstationary Labeling Experiment

INST-MFA requires the measurement of isotopic enrichment at multiple time points during the transient labeling period. For High Myc cells, samples were taken at 6, 12, 24, 36, 48, and 72 hours. For Low Myc cells, which exhibited a slower growth rate, samples were taken at 12, 24, 36, 48, 72, and 96 hours. For each time point, three separate T-75 flasks were seeded at the appropriate density to achieve a final cell number of approximately ten million cells per flask at the time of sampling. Prior to seeding, the growth medium was removed by centrifugation and the cells were resuspended in glucose labeled medium. At the sample times indicated previously, cells were harvested by centrifugation at 1500 RPM, washed with phosphate buffered saline (PBS), and extracted to isolate total cellular protein and RNA.

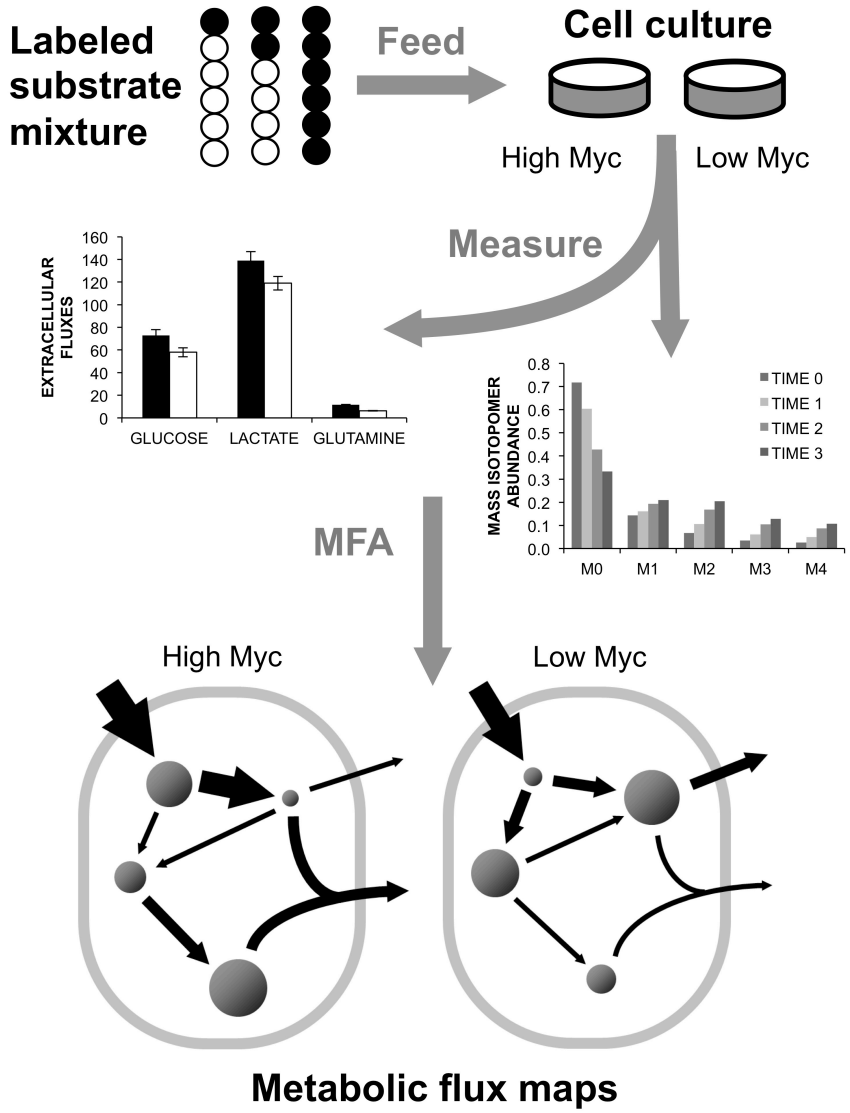

Figure 4.1 Overview of MFA Study Design. A mixture of ^{13}C-labeled glucose tracers was fed to P493-6 cells growing under High or Low Myc conditions. Extracellular medium concentrations and intracellular metabolite labeling were measured at various time points throughout exponential phase. A computational model was applied to map fluxes by minimizing the lack of fit between simulated and measured labeling data and extracellular flux measurements.

4.2.6 Extraction, Hydrolysis, and Derivatization of Total Cellular Protein and RNA

Extraction of protein and RNA was achieved using the TRIzol method, with the exception that proteins were precipitated using acetone instead of isopropanol (Simms et al., 1993). Protein samples were hydrolyzed to their constituent amino acids by incubating in 6N HCl for 20 hours at 110°C in a vacuum hydrolysis tube (Pierce). Similarly, RNA samples were hydrolyzed to ribose by incubating in 2N HCl at 100°C for 2 hours under vacuum. Protein hydrolysate samples were evaporated to dryness at 60°C under air flow. These dried samples were redissolved in 200 μL of ddH_2O, filtered through a 0.2 μm filter, and re-dried prior to derivatization. RNA hydrolysate samples were evaporated to dryness at 60°C under air flow prior to derivatization.

To enable GC-MS analysis, amino acids were converted to their *tert*-butyl dimethylsilyl (TBDMS) derivatives by dissolving in 50 μL pyridine and 70 μL MTBSTFA + 1% TBDMCS (Pierce), followed by incubation at 60°C for 30 minutes. Ribose was converted to its aldonitrile pentapropionate derivative to enable GC-MS analysis (Antoniewicz et al., 2011; Lee et al., 1998). Briefly, dried samples were dissolved in 50 μL of 2 wt. % hydroxylamine hydrochloride in pyridine (Sigma) and incubated for 60 minutes at 90°C. Next, 100 μL of propionic anhydride (Sigma) was added, and the samples were incubated at 60°C for an additional 30 minutes. Samples were then centrifuged and evaporated at 60°C. The dried samples were dissolved in 100 μL of ethyl acetate prior to GC-MS analysis.

4.2.7 Medium Glucose Derivatization

Medium glucose labeling was assessed by GC-MS analysis. 100 μL of medium was washed with three volumes of cold acetone and centrifuged to remove protein. Samples were then evaporated to dryness at 60°C under air flow. Glucose was then converted to its aldonitrile pentapropionate derivative using the same procedure described in the previous section for ribose analysis.

4.2.8 Gas Chromatography Mass Spectrometry (GC-MS) Analysis

Derivatized sugar and amino acid samples were analyzed by GC-MS using a HP5-MS capillary column (30 m × 0.25 mm i.d. × 0.25 μm; Agilent J&W Scientific) installed in an Agilent 7890A gas chromatograph (GC). The injection volume was 1 μL, and all samples were run in split mode with an inlet temperature of 270°C and a split

ratio of 10:1. Helium flow was controlled electronically at 0.73 mL/min for amino acid analysis and 1.65 ml/min for ribose and glucose analysis. The GC was interfaced to an Agilent 5975C mass spectrometer (MS) operated in electron impact mode with temperatures of 230°C for the ion source and 150°C for the quadrupole. The GC temperature program for amino acid analysis was: 150°C for 2 minutes, ramp at 5°C/min to 280°C, hold for 2 minutes. Mass spectra were obtained in scan mode over the range 100–500 m/z. The GC temperature program for glucose and ribose analysis was: 80°C for 1 minute, ramp at 20°C/min to 280°C, hold for 4 minutes. Mass spectra were obtained in scan mode over the range 100–700 m/z. Raw ion chromatograms were integrated using a custom MATLAB M-file that applies consistent integration bounds and baseline correction to each ion (Antoniewicz et al., 2007b).

4.2.9 Isotopomer Network Model

A detailed isotopomer model for mammalian B-cell metabolism was constructed. The metabolic network contains reactions for glycolysis, pentose phosphate pathway, TCA cycle, amphibolic pathways, amino acid catabolism, and biomass synthesis (Table 4.F.2 in Appendix 4.F). The network comprises 54 reactions with carbon atom transitions specified for all reactions. The network includes 8 extracellular substrates (glucose, arginine, asparagine, cysteine, glutamine, isoleucine, leucine, and serine), 6 metabolic products (biomass, lactate, alanine, glutamate, glycine, and lipids) and 35 balanced intracellular metabolites. Constraints from cofactor metabolites such as ATP and NAD(P)H were excluded because these balances have been shown to produce unreliable results in mammalian systems (Bonarius et al., 1998). Refer to Appendix 4.A for a detailed description of the model formulation and assumptions.

4.2.10 Flux Determination and Statistical Analysis

The elementary metabolite unit (EMU) framework was applied to efficiently simulate the labeling state of measurable metabolites represented in the isotopomer model (Antoniewicz et al., 2007a; Young et al., 2008). Both steady-state MFA and INST-MFA approaches involve solving an inverse problem whereby metabolic fluxes are determined by least-squares regression of measured extracellular fluxes and metabolite labeling patterns. The flux parameters of the isotopomer model were iteratively adjusted using a Levenberg-Marquardt algorithm until optimal agreement with experimental data was obtained. Flux estimation was repeated a minimum of 50 times from random initial values to ensure a global minimum was achieved. All results were subjected to a chi-square statistical test to

assess goodness-of-fit, and accurate 95% confidence intervals were computed for all estimated parameters by evaluating the sensitivity of the sum-of-squared residuals (SSRES) to parameter variations (Antoniewicz et al., 2006).

4.2.11 Isotopomer Spectral Analysis (ISA)

Isotopomer spectral analysis (ISA) is an alternative method to determine fluxes from nonstationary isotopomer measurements. It assumes that any deviations from steady state are due to the presence of unlabeled material that has not yet washed out of the system, and adjustable parameters are introduced that represent the fraction of unlabeled material that persists in both precursor and product pools; these parameters are denoted as D and G, respectively. The ISA framework was originally developed by Kelleher and Masterson (1992) and has been applied by Antoniewicz et al. (2007c) to determine fluxes in a nonstationary model of *E. coli* metabolism.

As an alternative to INST-MFA, we developed an ISA-based nonstationary model by including two G dilution parameters, G_1 and G_2, into our steady-state isotopomer model. G_1 represents the fraction of labeled protein in biomass and G_2 represents the fraction of labeled RNA. Hence, $(1\text{-}G_1)$ and $(1\text{-}G_2)$ represent the amount of unlabeled protein and RNA, respectively, that remain at a given time point. Theoretical values for G_1 and G_2 were determined based on the doubling time of the cells as described in Antoniewicz et al. (2007c). Fluxes were determined at each sample time point of the nonstationary labeling experiment using the ISA-based model. Further details of the ISA procedure and its underlying assumptions are provided in Appendix 4.A.

4.2.12 Biomass Equation

The dry weight of each cell was determined to be approximately 150 pg. This value was estimated by drying $70–150\times10^6$ cells in triplicate at 80°C overnight. The composition of the dry cell mass was estimated from the literature (Quek et al., 2010; Sheikh et al., 2005). Non-protein components included in the equation were nucleotides, lipids, and glycogen. The composition used for each purine was assumed to be: one R5P, one GLY, one CO_2, and two MEETHF. The pyrimidine composition was assumed to be: one R5P, one CO_2, and 1 ASP, except for thymine, which has one additional MEETHF. One G6P was assumed to make one glycogen monomer. The phospholipid fraction was assumed to be composed of the following lipids: phosphatidylcholine,

phosphatidylethanolamine, phosphatidylserine, phosphatidylinositol, phosphatidylglycerol, and cardiolipin. In each case, these molecules were modeled as having 17.43 AcCoA molecules and one DHAP with the following additional requirements: phosphatidylserine requires one SER, phosphatidylinositol requires one G6P, phosphatidylglycerol requires an additional DHAP, and cardiolipin requires an additional 17.43 AcCoA and 2 DHAP. (17.43 is the AcCoA requirement for each pair of fatty acid side-chains based on the average lipid composition reported by Sheikh et al. (2005).) Glycolipids were assumed to be represented wholly by sphingomyelin, which was modeled as requiring 17.43 AcCoA, and 1 SER. Sterols were modeled as cholesterol, which was assumed to require 18 AcCoA molecules for biosynthesis. Stoichiometric coefficients were determined by multiplying the estimated fraction of each biomass component by the cell dry weight and converting to units of nmol/million cells (Zamorano et al., 2010).

4.3 Results

4.3.1 Cell Metabolic Phenotypes

The calculated growth rates and extracellular fluxes for both High and Low Myc cells are shown in Table 4.1. Specific uptake and excretion rates were determined for 18 of 20 amino acids, but only 10 of those were consumed (or produced) in stoichiometric excess of the amounts required for biomass synthesis. Growth of Low Myc cells was 40% slower than High Myc cells, while glucose uptake was reduced by only 21%. Both High and Low Myc cells exhibited a highly glycolytic phenotype, with the majority of incoming carbon excreted as lactate. This was most clearly indicated by the lactate-to-glucose (L/G) ratios of 1.9 ± 0.2 and 2.1 ± 0.3 for High and Low Myc cells, respectively. Besides glucose, glutamine is the other major carbon substrate for mammalian cell cultures (Vander Heiden et al., 2009). Glutamine uptake supplied 9% of total carbon to High Myc cells and 7% to Low Myc cells. The uptake of most other amino acids was similarly elevated in High Myc cells. The total amount of carbon contributed by amino acids decreased from 28% in High Myc cells to 20% in Low Myc cells, with uptake fluxes of arginine, glutamine, histidine, isoleucine, leucine, lysine, methionine, serine, tyrosine, and valine all significantly elevated in the High Myc cells. Excretion fluxes of alanine, aspartate, and glycine were also significantly increased in High Myc cells.

4.3.2 Isotopic Steady-State MFA – High Myc Cells

Because the extracellular flux measurements do not provide sufficient constraints to estimate intracellular fluxes involved in cyclic or parallel pathways (See Appendix 4.B), we sought to apply isotope labeling experiments and ^{13}C MFA to generate a comprehensive flux map of High Myc P493-6 cells. At least 6 doublings of the cell population are required for the protein fraction to approach steady-state labeling. We estimated fluxes based on the steady-state labeling experiment both with and without ribose labeling data. After adding the ribose measurements to the model, the SSRES increased slightly above the acceptable 95% confidence threshold of the associated chi-square distribution (from SSRES = 11.7 with 8 degrees of freedom (DOF) to SSRES = 36.1 with 20 DOF). Despite this marginal lack of fit, we hypothesized that the addition of ribose labeling measurements would improve the precision of the flux estimates, especially within the PP pathway where ribose precursors are generated. This hypothesis was tested by computing the root-mean-square (RMS) error of net flux estimates within glycolysis, PP pathway, and TCA cycle (Table 4.2). We found that the addition of ribose labeling data decreased the RMS error of net PP pathway reactions from 57% to 34% and resulted in an overall improvement in RMS error from 27% to 21%. These findings confirm our hypothesis that the addition of ribose labeling measurements has a substantial impact on the precision of flux estimates within the PP pathway.

Table 4.1 Extracellular Fluxes for High and Low Myc Conditions. Fluxes have units of nmol/10^6 cells/h except for biomass, which has units of h^{-1}. Fluxes that were included in the MFA flux estimations are marked with a ✔. The uptake rates of other amino acids (marked with a ✖) were stoichiometrically matched to the growth rate, indicating that they were solely used for biomass synthesis. These amino acids were not included in the MFA flux estimations because their catabolism was assumed to be negligible. Significance is indicated for the comparison between Low and High Myc conditions based on a two-tailed Student's t-test with $p < 0.05$.

	High Myc	***Low Myc***		
Metabolite	***Flux (nmol/10^6 cells/h)***	***Flux (nmol/10^6 cells/h)***	***Included in MFA***	***p < 0.05***
Biomass (h^{-1})	0.0293 ± 0.0008	0.0176 ± 0.0006	✔	✔
		Uptake Fluxes		
Glucose	73 ± 5	58 ± 4	✔	✔
Arginine	4.7 ± 0.4	2.03 ± 0.15	✔	✔
Asparagine	0.9 ± 0.2	1 ± 0.2	✔	✖
Cystine	0.73 ± 0.11	0.94 ± 0.15	✔	✖
Glutamine	11.5 ± 0.3	6.3 ± 0.2	✔	✔
Histidine	0.78 ± 0.08	0.19 ± 0.03	✖	✔
Isoleucine	2.5 ± 0.2	1.4 ± 0.2	✔	✔
Leucine	3.3 ± 0.2	1.1 ± 0.1	✔	✔
Lysine	2.09 ± 0.15	0.61 ± 0.05	✖	✔
Methionine	0.67 ± 0.07	0.13 ± 0.03	✖	✔
Phenylalanine	0.13 ± 0.17	0.32 ± 0.07	✖	✖
Serine	4.1 ± 0.2	1.44 ± 0.01	✔	✔
Threonine	0.27 ± 0.04	0.61 ± 0.06	✖	✔
Tyrosine	0.58 ± 0.06	0.15 ± 0.03	✖	✔
Valine	1.42 ± 0.09	0.58 ± 0.05	✖	✔
		Excretion Fluxes		
Lactate	139 ± 8	119 ± 6	✔	✖
Alanine	1.65 ± 0.11	0.76 ± 0.12	✔	✔
Aspartate	0.36 ± 0.08	-0.57 ± 0.12	✖	✔
Glutamate	2.8 ± 0.3	3.11 ± 0.03	✔	✖
Glycine	0.84 ± 0.11	0.02 ± 0.06	✔	✔

Table 4.2 Root-Mean-Square (RMS) Percentage Errors for Selected Net Flux Estimations. RMS errors were calculated by first computing the percentage relative standard error of each net flux (i.e., $s_i/\max(v_i,1)\times 100\%$, where s_i is standard error and v_i is the net flux value). The resulting relative errors were combined by taking the square root of the sum of squared errors divided by the number of fluxes in each pathway. Reactions included in glycolysis, PP pathway, and TCA cycle are listed in Appendix 4.F Table 4.F.2. (SS w/w/o Ribose = steady-state with/without ribose measurements included.)

	Pathway			
Method	**Glycolysis**	**PPP**	**TCA Cycle**	**Overall**
SS w/ Ribose	5.5	34	32	21
SS w/o Ribose	5.7	57	31	27
ISA 24 Hour	5.5	54	42	29
ISA 36 Hour	5.5	54	30	26
ISA 48 Hour	5.0	62	27	27
ISA 72 Hour	4.9	60	22	26
INST-MFA	4.8	32	18	19

4.3.3 Isotopically Nonstationary MFA – High Myc Cells

Because of the long experimental times required to reach isotopic steady state, we performed a transient labeling experiment on High Myc cells and analyzed the data using INST-MFA. Metabolic fluxes were estimated using isotopomer data collected at six time points: 6, 12, 24, 36, 48, and 72 hours after tracer introduction. This resulted in 376 independent mass isotopomer measurements, which were combined with the 13 extracellular fluxes indicated in Table 4.1 to estimate metabolic fluxes and their 95% confidence intervals. Each time point included proteinogenic amino acid and RNA-ribose isotopomer measurements, except for 48 and 72 hours, which only included amino acid measurements. Fig. 4.2A shows the dynamic labeling trajectories of several selected GC-MS fragment ions along with the INST-MFA model fits. (Fits for the remaining isotopomer measurements are shown in Appendix 4.F, Fig. 4.F.2A.) The model was overdetermined by 240 measurements, and the fit was accepted based on a chi-square test with SSRES = 91.7.

The High Myc flux map determined by INST-MFA is shown in Fig. 4.3A. (Refer to Appendix 4.F Tables 4.F.3 and 4.F.4 for a full listing of flux values and 95% confidence intervals. Pool sizes were completely unidentifiable or exhibited large 95% confidence intervals for most metabolites except for those where labeling was directly measured. Identifiable pool sizes and their 95% confidence intervals are shown in Appendix 4.F Table 4.F.5. Model reduction assumptions are discussed in Appendix 4.C). The oxidative PP pathway exhibited negligible activity, with only 2% of the incoming glucose diverted into this branch. Approximately 19% of the pyruvate synthesized from glucose entered the TCA cycle, 79% was excreted as lactate, and the remainder was converted to alanine. The majority (~73%) of glutamine consumed by the cell was metabolized to α-ketoglutarate, with the remainder excreted as glutamate. Both ATP-citrate lyase and mitochondrial malic enzyme were highly active, consuming more than 35% of the citrate and 25% of the malate produced by the cell, respectively. These enzymes are hypothesized to play an important role in supplying carbon for lipid biosynthesis in tumor cells (Moreadith and Lehninger, 1984).

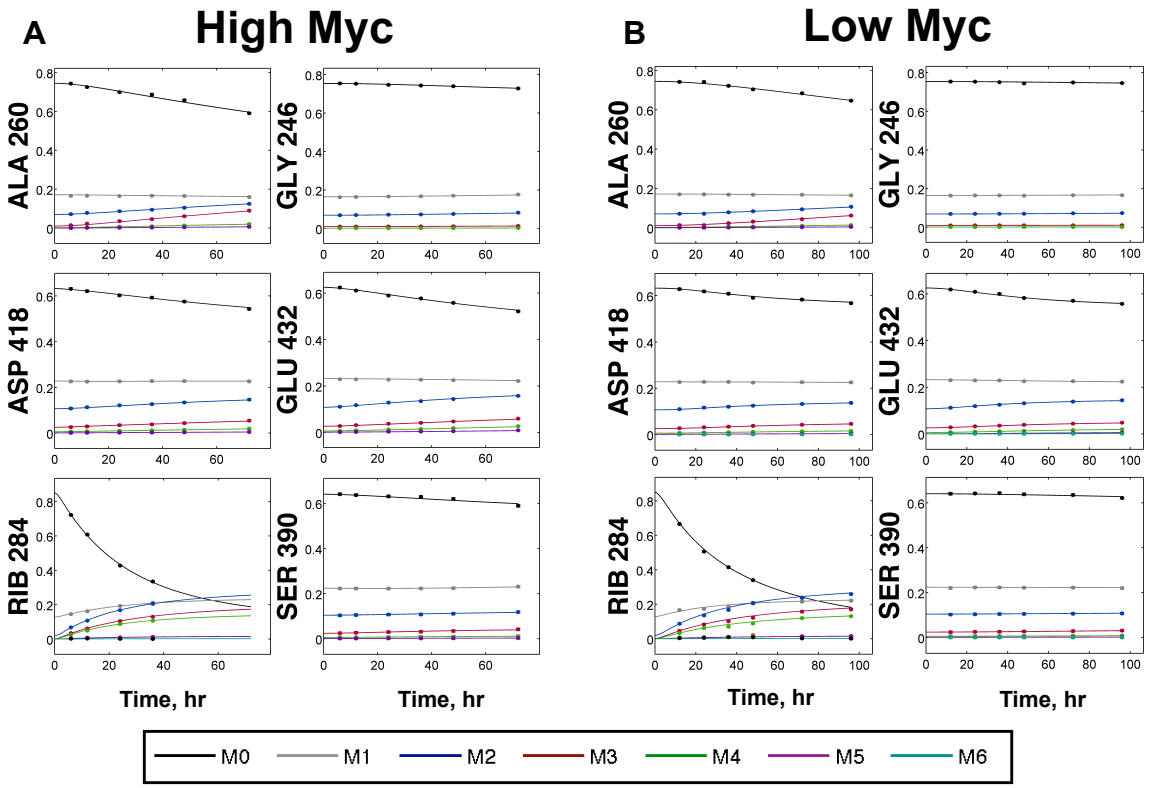

Figure 4.2 Labeling Dynamics of Selected GC-MS Fragment Ions. GC-MS ions shown are for alanine (ALA), glycine (GLY), serine (SER), aspartate (ASP), glutamate (GLU), and ribose (RIB). Each panel shows the experimentally measured mass isotopomer abundances (data points) and INST-MFA model fits (solid lines) for a single fragment ion measured under the **(A)** High or **(B)** Low Myc condition. Raw mass isotopomer data are shown without correction for natural isotope abundance.

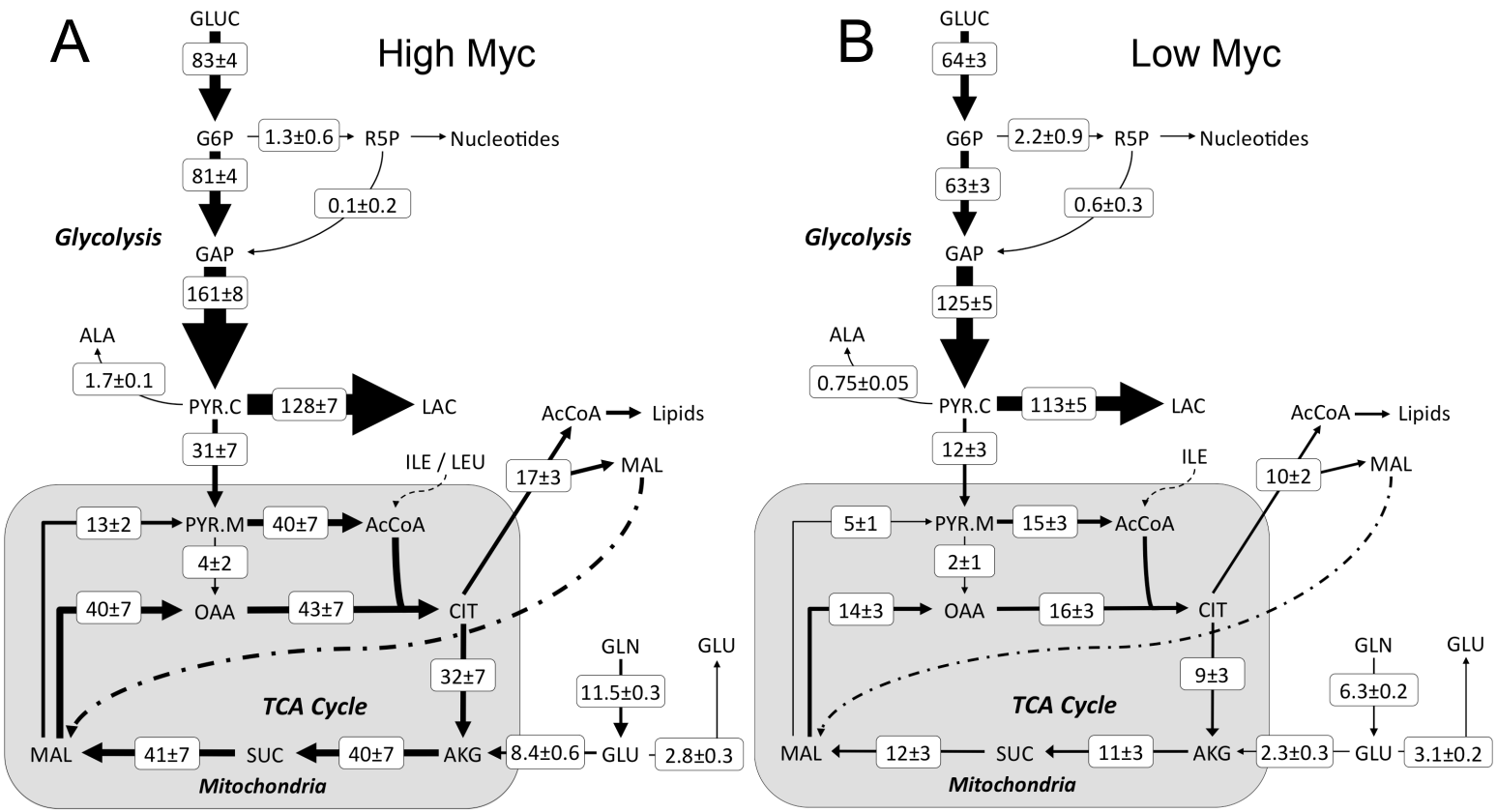

Figure 4.3 P493-6 B-cell Flux Maps Determined Under (A) High and (B) Low Myc Conditions. Net fluxes are shown in units of nmol/10^6 cells/hour. Fluxes are represented as $M \pm SE$, where M is the median of the 95% flux confidence interval and SE is the estimated standard error of M calculated as (UB95 – LB95)/3.92. (UB95 and LB95 are the upper and lower bounds of the 95% confidence interval, respectively.) Arrow thickness is scaled proportional to net flux. Some fluxes included in the isotopomer model are not shown in the figure to enhance clarity.

4.3.4 Isotopomer Spectral Analysis (ISA)-based Flux Estimation – High Myc Cells

As an alternative to INST-MFA, we applied an ISA-based approach to estimate fluxes from nonstationary labeling data collected at 24, 36, 48, and 72 hours after tracer introduction. The 24- and 36-hour time points were overdetermined by 19 measurements while those at 48 and 72 hours were overdetermined by 6 measurements due to the lack of ribose labeling information. All estimates returned SSRES values that were within the expected 95% confidence range of the appropriate chi-square distribution. As shown in Table 4.3, the G_1 parameter, which represents the fraction of newly synthesized protein estimated from isotope labeling measurements, was unidentifiable at time points prior to 48h. This is due to the low ^{13}C enrichment of amino acids at these time points and the inability of the ISA model to distinguish between internal and external sources of isotope dilution. At later times, the estimated G_1 values differed significantly from theoretical values derived from a simple dilution calculation (Antoniewicz et al., 2007c). Because Antoniewicz et al. (2007c) provided a simple bacterial growth medium that contained glucose as the sole carbon substrate, they observed close agreement between experimentally determined and theoretically predicted G parameter values. However, our mammalian culture medium contained high concentrations of amino acids and other unlabeled carbon sources. This additional source of isotope dilution resulted in a large mismatch between the experimental and theoretical G_1 parameters. In contrast, the ribose portion of RNA was apparently derived exclusively from glucose carbon, and therefore the trajectory of G_2 values matched closely with the theoretically predicted values in Table 4.3.

Table 4.3 Experimentally Determined and Theoretically Predicted G_1 and G_2 Dilution Parameters. Theoretical values are the same for both the G_1 and G_2 parameters and were determined based on the High Myc condition growth rate of 0.0293 h^{-1}. RNA samples were not available for the 48 and 72 hour time points, which prevents the calculation of the G_2 parameter at these times. Optimized parameter values and their standard errors are shown.

Time Point (Hours)	***Dilution Parameters***		***Theory***
	G_1	***G_2***	
6	3.3 ± 25.3	16.3 ± 0.7	16.1
12	22.8 ± 24	30.7 ± 1.1	29.6
24	34.4 ± 21.3	54.5 ± 0.9	50.5
36	35.3 ± 19.7	66.9 ± 1.1	65.1
48	40.7 ± 8.7	*N/A*	75.4
72	51.1 ± 5.5	*N/A*	87.9

4.3.5 Comparison of MFA Approaches

In order to select the most appropriate method for further MFA studies, we compared the precision and accuracy of each flux estimation approach. We compared steady-state MFA, 24-, 36-, 48-, and 72-hour ISA, and INST-MFA based on the 95% confidence intervals of net flux estimates. INST-MFA provided noticeably tighter confidence intervals for PP pathway and TCA cycle fluxes (Fig. 4.4 and Table 4.2). We attribute this increase in precision primarily to the transient labeling measurements of alanine and ribose ion fragments, which are particularly sensitive to changes in G6PDH flux (Appendix 4.F, Fig. 4.F.3). Furthermore, the overall RMS errors of INST-MFA flux estimates were lower than those obtained from any other method (Table 4.2). These comparisons reveal that the INST-MFA method is the most robust approach to determine fluxes in our system because of its enhanced flux precision as well as its ability to integrate labeling data obtained at multiple time points during the isotopically nonstationary period. Despite these noticeable differences in precision, the methods produced overlapping 95% confidence intervals for the majority of flux estimates. All but 8 of the 56 net fluxes exhibited overlap of their 95% confidence intervals when compared across all methods. The only disagreements were between the steady-state and INST-MFA experiments, which exhibited nonoverlapping confidence intervals in the PP pathway (Fig. 4.4). This could be attributable to biological variation between the experiments or disturbances introduced by periodic replating of cells in the steady-state labeling experiment. Furthermore, the SSRES of the steady-state experiment was slightly outside the acceptable range, which suggests that isotope labeling may not have been fully equilibrated at the time of sampling. All other pair-wise comparisons (steady-state vs. ISA or ISA vs. INST-MFA) exhibited overlapping confidence intervals across all fluxes, indicating statistical agreement. Overall, the methods were remarkably consistent in light of the different labeling strategies (single vs. multiple platings), seed densities, and modeling assumptions applied in each case. In addition to providing superior flux resolution, INST-MFA also imposes the least restrictive modeling assumptions (e.g., no isotopic steady-state assumption) and is therefore expected to be free from potential biases introduced by the other methods.

We also sought to determine whether the increased precision we observed in the INST-MFA flux estimates was due to the increased total number of labeling measurements or to an inherent increase in sensitivity associated with the transient labeling measurements. We copied the steady-state labeling data five times to simulate six replicate measurement sets. This produced the same total number of isotopomer measurements as in the INST-MFA data set. We re-estimated fluxes based on the replicated steady-state measurements and found that there was

significant improvement in net flux precision over the original steady-state dataset, but that INST-MFA still provided superior identifiability of net fluxes in glycolysis and TCA cycle (Appendix 4.F, Table 4.F.9). INST-MFA was also able to resolve a greater number of exchange fluxes in comparison to steady-state MFA, and the number of identifiable exchange fluxes was not impacted by replicating the steady-state isotopomer measurements. Taken together, these results indicate that the increase in total number of labeling measurements can partially explain the improved precision of INST-MFA, but that the transient isotopomer measurements contain some inherent flux information that is not obtainable from the steady-state isotopomer measurements

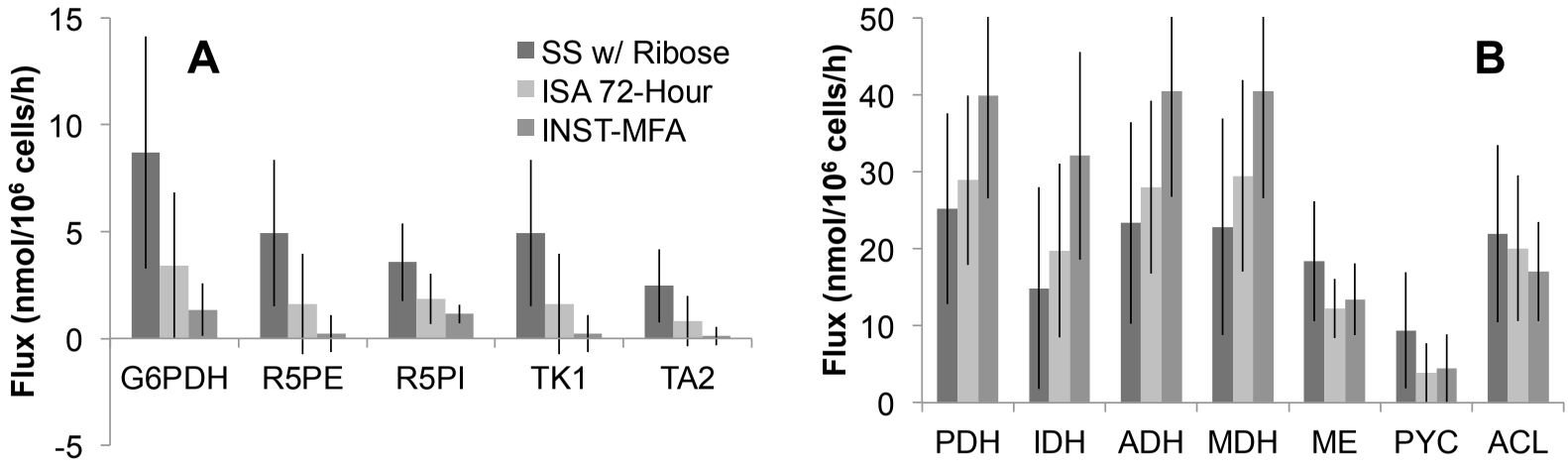

Figure 4.4 Intracellular Fluxes in the High Myc Condition as Determined by Alternative MFA Methods. A comparison of three flux estimation methods is shown based on 12 fluxes of central metabolism obtained under the High Myc condition (SS w/ Ribose = steady-state with ribose measurements included). Error bars represent 95% confidence intervals on the flux estimates, and the plotted values represent the medians of the confidence intervals. The fluxes shown were chosen because their confidence intervals exhibited the most variability across the three methods. **(A)** PP pathway net fluxes: glucose-6-phosphate dehydrogenase (G6PDH), ribulose-5-phosphate epimerase (R5PE), ribulose-5-phosphate isomerase (R5PI), transketolase 1 (TK1), and transaldolase 2 (TA2). **(B)** TCA cycle and amphibolic net fluxes: pyruvate dehydrogenase (PDH), isocitrate dehydrogenase (IDH), α-ketoglutarate dehydrogenase (ADH), malate dehydrogenase (MDH), malic enzyme (ME), pyruvate carboxylase (PYC), and ATP citrate lyase (ACL).

4.3.6 Isotopically Nonstationary MFA – Low Myc cells

We next applied INST-MFA to estimate fluxes in Low Myc cells because of its superior precision in determining fluxes of High Myc cells. Furthermore, the short labeling time required for INST-MFA is especially important in experiments with the more slowly growing Low Myc cells, because it would require nearly two weeks to achieve isotopic steady state in the protein fraction of these cells. Fluxes were estimated from labeling data obtained at six time points: 12, 24, 36, 48, 72, and 96 hours after tracer introduction. We fit the isotopomer model to 402 independent mass isotopomer abundances and 12 external flux measurements. Figure 4.2B shows the dynamic labeling measurements of several selected GC-MS fragment ions along with model simulations based on the best-fit parameters. (Fits for the remaining isotopomer measurements are shown in Appendix 4.F, Fig. 4.F.2B.) The system was overdetermined by 263 measurements, and the fit was accepted based on a chi-square test with SSRES = 89.0. (Refer to Appendix 4.F Tables 4.F.6, 4.F.7, and 4.F.8 for a full listing of estimated flux and pool size values and 95% confidence intervals.) The data clearly indicate slower labeling in the Low Myc cells when compared to the High Myc cells, which agrees with the lower rates of growth and substrate uptake shown in Table 4.1.

A comparison of the flux maps of the High and Low Myc cells in Fig. 4.3 shows several noticeable differences in nutrient utilization, as well as some unexpected similarities. Overall, the distribution of glycolytic and PP pathway fluxes was quite similar in High and Low Myc cells, which was surprising in light of the 42% reduction in growth rate exhibited by the Low Myc cells. Despite a reduced rate of glucose uptake, the Low Myc cells exhibited a slightly higher L/G ratio and a non-significant reduction in lactate excretion rate. Small oxidative PP pathway fluxes were observed in both conditions, which was just sufficient to meet the biosynthetic demand for ribose-5-phosphate (R5P). On the other hand, the most striking differences were found in mitochondrial metabolic pathways, where the Low Myc cells exhibited 2- to 4-fold reductions in all TCA cycle and amphibolic fluxes. Furthermore, the Low Myc cells channeled a significantly lower percentage of pyruvate into the TCA cycle (10% versus 19%). Glutamine uptake was halved in Low Myc cells, but glutamate secretion remained the same, resulting in a near 4-fold reduction in anaplerotic flux from glutamine to alpha-ketoglutarate. This directly correlated with a near 3-fold reduction in mitochondrial malic enzyme flux, which functions to balance the flow of carbon leading to citrate synthesis. The extrusion of citrate into the cytosol and its subsequent degradation to AcCoA, a process that supplies carbon for fatty acid synthesis and protein acetylation, did not change as drastically as other mitochondrial fluxes and was closely matched to growth rate. This fate accounted for 53% of the citrate produced in Low Myc

cells, but only 35% of the citrate produced in High Myc cells, indicating a clear shift toward increased oxidative metabolism in High Myc cells.

4.3.7 Oxygen Uptake Rates

The flux maps in Fig. 4.3 indicate a decrease in overall mitochondrial metabolism as a result of reduced Myc expression. We hypothesized that this change would correlate with a decrease in oxygen uptake rate (OUR) for respiratory processes. This hypothesis was tested by direct measurement of OUR, which confirmed that the Low Myc cells consumed oxygen at a rate of approximately 60% that of High Myc cells (Fig. 4.5). Oxygen uptake was strongly dependent on mitochondrial Complex I, as it was almost completely abolished in the presence of the Complex I inhibitor rotenone in both High and Low Myc cells.

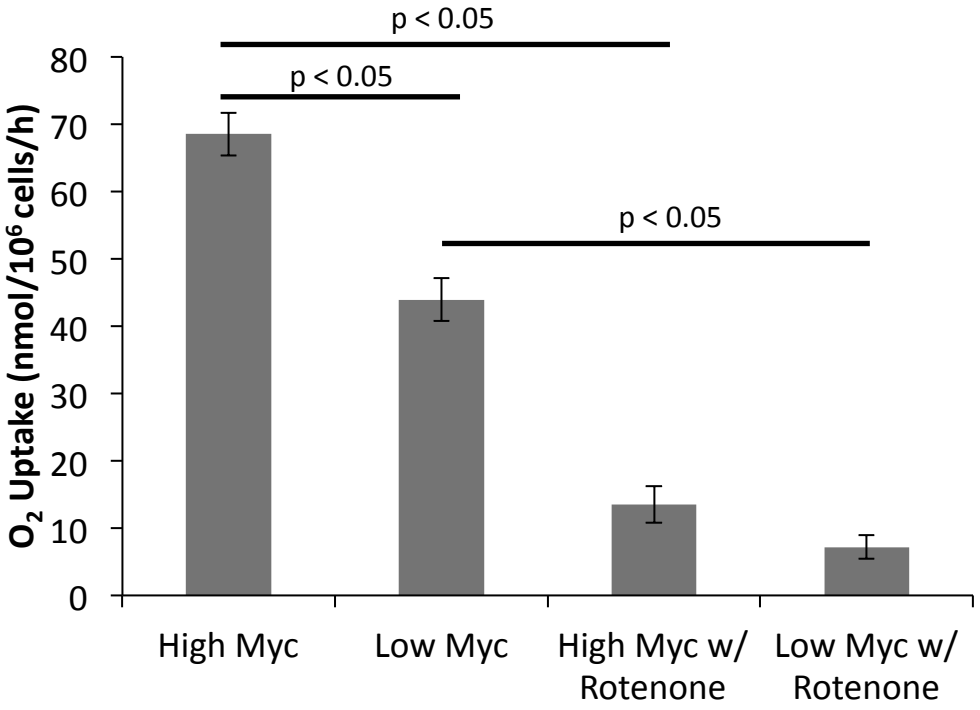

Figure 4.5 Oxygen Uptake Rate of P493-6 Cells Under High and Low Myc Conditions. Oxygen uptake rates were measured in units of nmol/10^6 cells/hour. Rates were determined either in untreated cells (n=11) or cells treated with 100 nM rotenone (n=2). Error bars indicate standard error of the mean values. Significance was determined using a two-tailed Student's t-test with $p<0.05$.

4.4 Discussion

The ability to quantitatively map intracellular carbon fluxes using isotope tracers and metabolic flux analysis (MFA) provides a powerful approach to identify functional network states and regulatory mechanisms that characterize cell metabolism. Although a handful of prior studies have used ^{13}C MFA to examine the role of specific oncoproteins (Gaglio et al., 2011; Kim and Forbes, 2007) or cell signaling pathways (Forbes et al., 2006; Grassian et al., 2011) in promoting global metabolic adaptations of tumor cells, we postulated that applying ^{13}C MFA to map fluxes in P493-6 B-cells would allow us to quantify the direct metabolic consequences of oncogenic Myc expression while minimizing the confounding effects of clonal variability. The P493-6 B-cell line is an EBV-immortalized line with a tetracycline-repressible Myc expression construct (Pajic et al., 2000; Pajic et al., 2001). This cell system therefore provides a unique platform to investigate the effects of varying Myc expression within an isogenic background, and it has been used successfully by other groups to assess the role of Myc in regulating cell growth, metabolism, and apoptosis (Gao et al., 2009; Kim et al., 2004; Kim et al., 2007; Le et al., 2012; Li et al., 2005; Liu et al., 2008; Schlosser et al., 2004). Furthermore, because Low Myc cells are nontumorigenic while High Myc cells resemble human Burkitt lymphoma cells, comparison of metabolic phenotypes between Low and High Myc cells is expected to reveal specific differences between normal proliferating cells and cancerous cells (Yustein et al., 2010).

Using this B-cell model system, we proceeded to quantify metabolic phenotypes under both Low and High Myc conditions. We measured time courses of cell density and extracellular metabolite concentrations throughout exponential phase, followed by regression analysis to estimate specific rates of growth, substrate consumption, and product excretion. Based on these specific rates, we observed that High Myc cells significantly increased their growth rate and the magnitude of most nutrient uptake and excretion fluxes in comparison to Low Myc cells. This is consistent with previous reports of the general stimulating effect of Myc on cell growth and metabolism (Fan et al., 2010; Morrish et al., 2009; Morrish et al., 2008). In particular, Myc has been shown to enhance flux through the glycolytic pathway by direct transactivation of *GLUT1*, *HK2*, *PFKM*, *TPI1*, *GAPD*, *ENO1* and *LDHA* genes in studies of Rat1a fibroblasts and P493-6 cells (Kim et al., 2004; Osthus et al., 2000; Shim et al., 1997). Although our results show a modest increase in glucose consumption and lactate production as a result of ectopic Myc expression, the relative changes in these glycolytic fluxes were sub-proportional to the change in specific growth rate we observed. On the other hand, most amino acid uptake fluxes were increased 2- to 3-fold in High Myc cells relative to

Low Myc cells, which exceeded the 1.7-fold change in specific growth rate. Therefore, ectopic Myc expression impacted amino acid fluxes more strongly than glycolytic fluxes in P493-6 cells.

Prior work has shown that glutamine metabolism is under direct control of Myc (Gao et al., 2009; Wise et al., 2008) and that Myc-overexpressing cells are particularly sensitive to glutamine withdrawal or inhibition of anaplerotic glutamine flux entering the TCA cycle (Fan et al., 2010; Wise et al., 2008; Yuneva et al., 2007). Our results show that, in addition to strongly upregulating their glutamine consumption, High Myc cells exhibited significant increases in most other incoming and outgoing amino acid fluxes. Furthermore, nearly half of the incoming amino acids were consumed in excess of their biosynthetic requirements, which indicates that they were partially catabolized to meet the energetic or redox demands of P493-6 cells. Aside from one study that identified serine hydroxymethyltransferase (*SHMT2*) as a direct Myc target gene (Nikiforov et al., 2002), little is known about how Myc stimulates metabolism of other amino acids besides glutamine. Based on our results, elucidating the mechanisms by which Myc influences global patterns of amino acid utilization in tumor cells represents a promising area of further investigation.

Despite much prior work to investigate the altered nutrient requirements of Myc-overexpressing cells, quantitative information about flux through intracellular metabolic pathways is not obtainable based on analysis of extracellular measurements alone. Therefore, we applied isotope labeling and ^{13}C MFA to further elucidate the intracellular flux distributions of P493-6 cells under Low and High Myc conditions. After considering several alternative approaches, we concluded that a transient isotope labeling experiment followed by INST-MFA would provide the best overall accuracy and precision for flux determination in our system. A comparison of flux maps generated under High and Low Myc conditions not only confirmed the previously described global increases in glucose and amino acid metabolism exhibited by High Myc cells, but also revealed dramatic alterations in mitochondrial metabolism. In contrast to the small relative shift in glycolytic flux, we observed near 4-fold enhancements in most TCA cycle and amphibolic fluxes in response to ectopic Myc expression. We also observed a significantly higher rate of oxygen consumption by High Myc cells in comparison to Low Myc cells, although the relative increase in oxygen consumption was less dramatic than the increase in TCA cycle flux determined by MFA. This could be attributable to increased utilization of NAD(P)H for anabolic metabolism in High Myc cells or to unavoidable differences in

culture conditions that were required to determine oxygen uptake rate (OUR). Despite these differences, however, both the MFA and OUR measurements are qualitatively consistent with an overall upregulation of mitochondrial metabolism in High Myc cells. This increase in mitochondrial activity is likely necessary to meet the increased ATP demands of High Myc cells, since the observed increase in glycolytic flux is insufficient to support the change in growth rate. Assuming a biosynthetic ATP requirement of 43 mmol/gDW (Sheikh et al., 2005) and our measured cell dry weight of 150 pg/cell, the difference in ATP demand for growth between High and Low Myc cells is approximately 75 nmol/10^6 cells/h. However, the difference in glycolytic flux accounts for only half of this ATP production, the remainder of which must be supplied by oxidative phosphorylation. The increase in TCA cycle flux and oxygen uptake exhibited by High Myc cells would more than compensate for the ATP deficit attributable to glycolysis.

In addition to providing ATP to support enhanced growth of High Myc cells, increased mitochondrial metabolism likely also plays a role in promoting availability of biosynthetic precursors, such as AcCoA that is needed for lipid biosynthesis and post-translational modification of proteins (Morrish et al., 2009; Morrish et al., 2010). Several recent studies have reported that tumor cells growing under hypoxic conditions or with mitochondrial defects shift to a reductive carboxylation pathway to supply carbon for lipid biosynthesis (Metallo et al., 2012; Mullen et al., 2012; Wise et al., 2011). This involves conversion of glutamine to citrate by reversal of the isocitrate dehydrogenase (IDH) reaction, which normally functions to oxidize citrate in the TCA cycle. Although we could not precisely assess the reversibility of IDH based on our measurements, the net TCA cycle flux was determined to operate strictly in the forward direction in both Low and High Myc cells. This does not preclude the possibility of glutamine carbons becoming incorporated into citrate or fatty acids through reversible or cyclic action of IDH1/2 isoforms, even in the presence of a net forward TCA cycle flux. However, Le et al. (2012) have recently shown that when P493-6 cells were grown in the presence of [U-$^{13}C_5$]glutamine under either aerobic or hypoxic conditions, the labeling patterns of citrate reflect a predominantly oxidative mode of glutamine metabolism rather than reductive carboxylation or its conversion to lactate.

One surprising finding of our study was the overall low level of oxidative PP pathway flux in both High and Low Myc cells. This could be due to the previously reported effects of Myc to enhance mitochondrial capacity and

thereby decrease production of reactive oxygen species (ROS) in Myc-overexpressing cells (Morrish et al., 2008). Oxidative stress is a key regulator of oxidative PP pathway flux, which has been shown to decrease dose-dependently in response to treatments that reduce ROS levels (Tuttle et al., 2007). It is also possible that NADP-dependent isoforms of isocitrate dehydrogenase (IDH1 or IDH2) or malic enzyme (ME1 or ME3) provide the dominant source of NADPH required for biosynthesis and redox homeostasis in P493-6 cells, and thereby diminish the cellular demand for oxidative PP pathway activity.

To assess isotope labeling in our system, we relied exclusively on GC-MS measurements of RNA-bound ribose and protein-bound amino acids, following extraction and hydrolysis of total cellular protein and RNA. The labeling patterns of these macromolecular building blocks serve as proxies of the precursor metabolites from which they were biosynthetically derived. This "retrobiosynthetic" approach is commonly used in microbial and plant systems; however, the vast majority of recent ^{13}C MFA studies performed on mammalian cells have relied exclusively upon direct extraction and isotopomer analysis of free intracellular metabolites (Niklas and Heinzle, 2012). Lee et al. (1998) previously applied mass isotopomer measurements of RNA-derived ribose and lipid-derived palmitate to investigate PP pathway fluxes in HepG2 cells but did not attempt to integrate these labeling data within a comprehensive flux model of central metabolism. Furthermore, we could identify only two previous examples where ^{13}C MFA has been applied to a mammalian system based on isotopomer measurements of protein-bound amino acids rather than free metabolites (Goudar et al., 2010; Sriram et al., 2008). Although there are advantages and disadvantages to both approaches, and the preferred method will clearly depend upon the biological system and questions to be addressed, the most important benefits of the retrobiosynthetic approach are (i) the high signal-to-noise ratio that is obtained due to the abundance of protein and RNA within the cell and (ii) the long-term stability of the macromolecule pools, which obviates the need for sophisticated sample quenching and extraction methods that are required to preserve the *in vivo* labeling state of labile intracellular metabolites. The latter consideration is particularly germane to the possible future extension of ^{13}C MFA to 3D culture systems or other cellular environments where rapid sample collection is not practical. For example, harvesting cells from semi-solid substrates such as collagen or Matrigel typically requires incubation at altered temperatures, possibly in the presence of proteolytic enzymes, in order to depolymerize the matrix. These procedures are not compatible with current metabolite extraction methods that have been developed for 2D adherent cultures or suspension cultures where cells

can be readily recovered after quenching. One potential drawback of the retrobiosynthetic approach is that it is only applicable to actively proliferating cells; however, this would still encompass the vast majority of cancer biology studies that are aimed at identifying potential drug targets or biomarkers that are specifically upregulated in growing tumors. We anticipate that further development of MFA approaches based on isotopomer analysis of protein, nucleotide, and lipid building blocks will open the door to novel investigations of tumor cell metabolism in non-traditional culture systems, and perhaps eventually to *in vivo* tumors.

Prior to initiating MFA studies under both Low and High Myc conditions, we compared several different approaches for collecting and analyzing isotope labeling data as a function of time. To date, most MFA studies have relied upon steady-state isotope labeling measurements as inputs for flux estimation, rather than transient isotopomer measurements (Niklas and Heinzle, 2012). This simplifies the sampling procedure and furthermore reduces the isotopomer model to a system of algebraic equations, which can be solved more efficiently in comparison to the ODE-based models that are required for INST-MFA (Quek et al., 2010). A major drawback of the retrobiosynthetic approach, however, is the slow labeling that occurs in protein and RNA fractions. Because the turnover of these pools is linked to cell growth, at least 6 cell doublings must be achieved under balanced growth conditions and in the presence of tracer to achieve isotopic steady state. Therefore, we examined the possibility of using a transient isotope labeling approach to circumvent the practical difficulties associated with prolonged tracer experiments.

We analyzed isotope labeling data collected at multiple time points during exponential growth of P493-6 cells in simple flask cultures using steady-state MFA, INST-MFA, and an ISA-based pseudo-steady-state method. Comparison of all approaches revealed that their net flux estimates were largely in agreement, at least within the errors of the respective methods. The precision of INST-MFA flux estimates was best overall and was dramatically superior to other methods in resolving PP pathway fluxes. We attribute this to enhanced sensitivity of the SSRES to transient measurements of ribose and alanine labeling, particularly the Ala232 and Rib284 fragment ions, which constrained the nonoxidative branch of the PP pathway and indicated low net flux through the pathway as a whole. INST-MFA has the further advantage that it integrates the entire transient labeling data into a single flux map, and it does not depend on isotopic steady-state or pseudo-steady-state assumptions. Although INST-MFA has been previously applied to other mammalian systems (Ahn and Antoniewicz, 2011; Maier et al., 2008; Maier et al., 2009;

Munger et al., 2008; Young et al., 2008) and bacterial systems (Nöh et al., 2007; Schaub et al., 2008; Young et al., 2011), this is the first time that it has been used to analyze transient labeling of macromolecular components such as proteinogenic amino acids or RNA-ribose. Furthermore, only one prior study has presented a systematic comparison between steady-state and INST-MFA methods in the same system, and this work was restricted to bacterial cultures (Noack et al., 2011).

Overall, ^{13}C INST-MFA was the most effective strategy for flux determination in P493-6 cells based on isotopic measurements of protein-bound amino acids and RNA-bound ribose. This approach has the advantage of relying exclusively on isotopomer measurements derived from highly stable and abundant macromolecular pools, while avoiding the long experimental times that would be required to achieve isotopic steady state. We were able to precisely quantify the rates of all major glycolytic, PP pathway, TCA cycle, and amphibolic fluxes in P493-6 cells under both High and Low Myc expression levels. High Myc cells relied more heavily on mitochondrial metabolism than Low Myc cells and globally upregulated their consumption of amino acids relative to glucose. Most TCA cycle and amphibolic mitochondrial pathways exhibited near 4-fold flux increases in High Myc cells, in contrast to modest increases in glucose uptake and lactate excretion. The oxidative pentose phosphate pathway exhibited minimal activity under both High and Low Myc conditions. This approach can be readily extended to investigate the metabolic adaptations of tumor cells and other proliferating mammalian cells, as well as their response to specific pharmacologic or genetic interventions.

4.5 References

Ahn WS, Antoniewicz MR. 2011. Metabolic flux analysis of CHO cells at growth and non-growth phases using isotopic tracers and mass spectrometry. *Metab. Eng.* **13**:598–609.

Antoniewicz MR, Kelleher JK, Stephanopoulos G. 2006. Determination of confidence intervals of metabolic fluxes estimated from stable isotope measurements. *Metab. Eng.* **8**:324–337.

Antoniewicz MR, Kelleher JK, Stephanopoulos G. 2007a. Elementary metabolite units (EMU): a novel framework for modeling isotopic distributions. *Metab. Eng.* **9**:68–86.

Antoniewicz MR, Kelleher JK, Stephanopoulos G. 2007b. Accurate assessment of amino acid mass isotopomer distributions for metabolic flux analysis. *Anal. Chem* **79**:7554–7559.

Antoniewicz MR, Kelleher JK, Stephanopoulos G. 2011. Measuring deuterium enrichment of glucose hydrogen atoms by gas chromatography/mass spectrometry. *Anal. Chem* **83**:3211–3216.

Antoniewicz MR, Kraynie DF, Laffend LA, González-Lergier J, Kelleher JK, Stephanopoulos G. 2007c. Metabolic flux analysis in a nonstationary system: fed-batch fermentation of a high yielding strain of E. coli producing 1,3-propanediol. *Metab. Eng.* **9**:277–292.

Bonarius HP, Timmerarends B, de Gooijer CD, Tramper J. 1998. Metabolite-balancing techniques vs. 13C tracer experiments to determine metabolic fluxes in hybridoma cells. *Biotechnol. Bioeng.* **58**:258–262.

Christofk H, Vander Heiden MG, Harris M, Ramanathan A, Gerszten R, Wei R, Fleming M, Schreiber S, Cantley L. 2008. The M2 splice isoform of pyruvate kinase is important for cancer metabolism and tumour growth. *Nature* **452**:230–233.

Dang CV. 1999. c-Myc target genes involved in cell growth, apoptosis, and metabolism. *Mol. Cell. Biol.* **19**:1.

Dang CV, Kim J, Gao P, Yustein J. 2008. The interplay between MYC and HIF in cancer. *Nat. Rev. Cancer* **8**:51–56.

Dang L, White DW, Gross S, Bennett BD, Bittinger MA, Driggers EM, Fantin VR, Jang HG, Jin S, Keenan MC, Marks KM, Prins RM, Ward PS, Yen KE, Liau LM, Rabinowitz JD, Cantley LC, Thompson CB, Vander Heiden MG, Su SM. 2009. Cancer-associated IDH1 mutations produce 2-hydroxyglutarate. *Nature* **462**:739–744.

DeBerardinis RJ, Lum JJ, Hatzivassiliou G, Thompson CB. 2008. The biology of cancer: metabolic reprogramming fuels cell growth and proliferation. *Cell Metab.* **7**:11–20.

Evans JMM, Donnelly LA, Emslie-Smith AM, Alessi DR, Morris AD. 2005. Metformin and reduced risk of cancer in diabetic patients. *BMJ* **330**:1304–1305.

Fan Y, Dickman KG, Zong WX. 2010. Akt and c-Myc Differentially Activate Cellular Metabolic Programs and Prime Cells to Bioenergetic Inhibition. *J. Biol. Chem.* **285**:7324–7333.

Fantin V, St-Pierre J, Leder P. 2006. Attenuation of LDH-A expression uncovers a link between glycolysis, mitochondrial physiology, and tumor maintenance. *Cancer Cell* **9**:425–434.

Forbes NS, Meadows AL, Clark DS, Blanch HW. 2006. Estradiol stimulates the biosynthetic pathways of breast cancer cells: detection by metabolic flux analysis. *Metab. Eng.* **8**:639–652.

Gaglio D, Metallo CM, Gameiro PA, Hiller K, Danna LS, Balestrieri C, Alberghina L, Stephanopoulos G, Chiaradonna F. 2011. Oncogenic K-Ras decouples glucose and glutamine metabolism to support cancer cell growth. *Mol. Sys. Biol.* **7**:523.

Gao P, Tchernyshyov I, Chang T, Lee Y, Kita K, Ochi T, Zeller K, de Marzo A, van Eyk J, Mendell J. 2009. c-Myc suppression of miR-23a/b enhances mitochondrial glutaminase expression and glutamine metabolism. *Nature* **458**:762–765.

Goudar C, Biener R, Boisart C, Heidemann R, Piret J, de Graaf A, Konstantinov K. 2010. Metabolic flux analysis of CHO cells in perfusion culture by metabolite balancing and 2D [13C, 1H] COSY NMR spectroscopy. *Metab. Eng.* **12**:138–149.

Grassian AR, Metallo CM, Coloff JL, Stephanopoulos G, Brugge JS. 2011. Erk regulation of pyruvate dehydrogenase flux through PDK4 modulates cell proliferation. *Genes Devel.* **25**:1716–1733.

Hanahan D, Weinberg RA. 2011. Hallmarks of cancer: the next generation. *Cell* **144**:646–674.

Hsu PP, Sabatini DM. 2008. Cancer cell metabolism: Warburg and beyond. *Cell* **134**:703–707.

Kelleher JK, Masterson TM. 1992. Model equations for condensation biosynthesis using stable isotopes and radioisotopes. *Am. J. Physiol.* **262**:E118–25.

Kim B-J, Forbes NS. 2007. Flux analysis shows that hypoxia-inducible-factor-1-alpha minimally affects intracellular metabolism in tumor spheroids. *Biotechnol. Bioeng.* **96**:1167–1182.

Kim J, Tchernyshyov I, Semenza G, Dang CV. 2006. HIF-1-mediated expression of pyruvate dehydrogenase kinase: a metabolic switch required for cellular adaptation to hypoxia. *Cell Metab.* **3**:177–185.

Kim J-W, Gao P, Liu Y-C, Semenza GL, Dang CV. 2007. Hypoxia-inducible factor 1 and dysregulated c-Myc

cooperatively induce vascular endothelial growth factor and metabolic switches hexokinase 2 and pyruvate dehydrogenase kinase 1. *Mol. Cell. Biol.* **27**:7381–7393.

Kim J-W, Zeller KI, Wang Y, Jegga AG, Aronow BJ, O'Donnell KA, Dang CV. 2004. Evaluation of myc E-box phylogenetic footprints in glycolytic genes by chromatin immunoprecipitation assays. *Mol. Cell. Biol.* **24**:5923–5936.

Koppenol WH, Bounds PL, Dang CV. 2011. Otto Warburg's contributions to current concepts of cancer metabolism. *Nat. Rev. Cancer* **11**:325–337.

Kroemer G, Pouyssegur J. 2008. Tumor cell metabolism: cancer"s Achilles" heel. *Cancer Cell* **13**:472–482.

Le A, Cooper CR, Gouw AM, Dinavahi R, Maitra A, Deck LM, Royer RE, Vander Jagt DL, Semenza GL, Dang CV. 2010. Inhibition of lactate dehydrogenase A induces oxidative stress and inhibits tumor progression. *Proc. Nat. Acad. Sci.* **107**:2037–2042.

Le A, Lane AN, Hamaker M, Bose S, Gouw A, Barbi J, Tsukamoto T, Rojas CJ, Slusher BS, Zhang H, Zimmerman LJ, Liebler DC, Slebos RJC, Lorkiewicz PK, Higashi RM, Fan TWM, Dang CV. 2012. Glucose-Independent Glutamine Metabolism via TCA Cycling for Proliferation and Survival in B Cells. *Cell Metab.* **15**:110–121.

Lee WN, Boros LG, Puigjaner J, Bassilian S, Lim S, Cascante M. 1998. Mass isotopomer study of the nonoxidative pathways of the pentose cycle with [1,2-13C2]glucose. *Am. J. Physiol.* **274**:E843–51.

Li F, Wang Y, Zeller KI, Potter JJ, Wonsey DR, O'Donnell KA, Kim J-W, Yustein JT, Lee LA, Dang CV. 2005. Myc stimulates nuclearly encoded mitochondrial genes and mitochondrial biogenesis. *Mol. Cell. Biol.* **25**:6225–6234.

Liu Y-C, Li F, Handler J, Huang CRL, Xiang Y, Neretti N, Sedivy JM, Zeller KI, Dang CV. 2008. Global regulation of nucleotide biosynthetic genes by c-Myc. *PLoS One* **3**:e2722.

Maier K, Hofmann U, Reuss M, Mauch K. 2008. Identification of metabolic fluxes in hepatic cells from transient 13C-labeling experiments: Part II. Flux estimation. *Biotechnol. Bioeng.* **100**:355–370.

Maier K, Hofmann U, Bauer A, Niebel A, Vacun G, Reuss M, Mauch K. 2009. Quantification of statin effects on hepatic cholesterol synthesis by transient (13)C-flux analysis. *Metab. Eng.* **11**:292–309.

Metallo CM, Gameiro PA, Bell EL, Mattaini KR, Yang J, Hiller K, Jewell CM, Johnson ZR, Irvine DJ, Guarente L, Kelleher JK, Vander Heiden MG, Iliopoulos O, Stephanopoulos G. 2012. Reductive glutamine metabolism by IDH1 mediates lipogenesis under hypoxia. *Nature* **481**:380–384.

Michelakis ED, Webster L, Mackey JR. 2008. Dichloroacetate (DCA) as a potential metabolic-targeting therapy for cancer. *Br. J. Cancer* **99**:989–994.

Moreadith RW, Lehninger AL. 1984. Purification, kinetic behavior, and regulation of NAD(P)+ malic enzyme of tumor mitochondria. *J. Biol. Chem.* **259**:6222–6227.

Morrish F, Isern N, Sadilek M, Jeffrey M, Hockenbery DM. 2009. c-Myc activates multiple metabolic networks to generate substrates for cell-cycle entry. *Oncogene* **28**:2485–2491.

Morrish F, Neretti N, Sedivy JM, Hockenbery DM. 2008. The oncogene c-Myc coordinates regulation of metabolic networks to enable rapid cell cycle entry. *Cell Cycle* **7**:1054–1066.

Morrish F, Noonan J, Perez-Olsen C, Gafken PR, Fitzgibbon M, Kelleher J, VanGilst M, Hockenbery D. 2010. Myc-dependent mitochondrial generation of acetyl-CoA contributes to fatty acid biosynthesis and histone acetylation during cell cycle entry. *J. Biol. Chem.* **285**:36267–36274.

Möllney M, Wiechert W, Kownatzki D, de Graaf AA. 1999. Bidirectional reaction steps in metabolic networks: IV. Optimal design of isotopomer labeling experiments. *Biotechnol. Bioeng.* **66**:86–103.

Mullen AR, Wheaton WW, Jin ES, Chen P-H, Sullivan LB, Cheng T, Yang Y, Linehan WM, Chandel NS, DeBerardinis RJ. 2012. Reductive carboxylation supports growth in tumour cells with defective mitochondria. *Nature* **481**:385–388.

Munger J, Bennett BD, Parikh A, Feng X-J, McArdle J, Rabitz HA, Shenk T, Rabinowitz JD. 2008. Systems-level metabolic flux profiling identifies fatty acid synthesis as a target for antiviral therapy. *Nature Biotech.* **26**:1179–1186.

Nikiforov MA, Chandriani S, O'Connell B, Petrenko O, Kotenko I, Beavis A, Sedivy JM, Cole MD. 2002. A functional screen for Myc-responsive genes reveals serine hydroxymethyltransferase, a major source of the one-carbon unit for cell metabolism. *Mol. Cell. Biol.* **22**:5793.

Niklas J, Heinzle E. 2012. Metabolic flux analysis in systems biology of Mammalian cells. *Adv. Biochem. Eng. Biotechnol.* **127**:109–132.

Noack S, Nöh K, Moch M, Oldiges M, Wiechert W. 2011. Stationary versus non-stationary (13)C-MFA: a comparison using a consistent dataset. *J. Biotech.* **154**:179–190.

Nöh K, Grönke K, Luo B, Takors R, Oldiges M, Wiechert W. 2007. Metabolic flux analysis at ultra short time scale: Isotopically non-stationary 13C labeling experiments. *J. Biotech.* **129**:249–267.

Nöh K, Wiechert W. 2011. The benefits of being transient: isotope-based metabolic flux analysis at the short time scale. *Appl Microbiol Biotechnol* **91**:1247–1265.

Osthus RC, Shim H, Kim S, Li Q, Reddy R, Mukherjee M, Xu Y, Wonsey D, Lee LA, Dang CV. 2000. Deregulation of glucose transporter 1 and glycolytic gene expression by c-Myc. *J. Biol. Chem.* **275**:21797–21800.

Pajic A, Spitkovsky D, Christoph B, Kempkes B, Schuhmacher M, Staege MS, Brielmeier M, Ellwart J, Kohlhuber F, Bornkamm GW. 2000. Cell cycle activation by c-myc in a Burkitt lymphoma model cell line. *Int. J. Cancer* **87**:787–793.

Pajic A, Staege MS, Dudziak D, Schuhmacher M, Spitkovsky D, Eissner G, Brielmeier M, Polack A, Bornkamm GW. 2001. Antagonistic effects of c-myc and Epstein-Barr virus latent genes on the phenotype of human B cells. *Int. J. Cancer* **93**:810–816.

Quek L-E, Dietmair S, Krömer JO, Nielsen LK. 2010. Metabolic flux analysis in mammalian cell culture. *Metab. Eng.* **12**:161–171.

Sauer U. 2006. Metabolic networks in motion: 13C-based flux analysis. *Mol. Sys. Biol.* **2**:62.

Schaub J, Mauch K, Reuss M. 2008. Metabolic flux analysis in Escherichia coli by integrating isotopic dynamic and isotopic stationary 13C labeling data. *Biotechnol. Bioeng.* **99**:1170–1185.

Schlosser I, Hölzel M, Hoffmann R, Burtscher H, Kohlhuber F, Schuhmacher M, Chapman R, Weidle UH, Eick D. 2004. Dissection of transcriptional programmes in response to serum and c-Myc in a human B-cell line. *Oncogene* **24**:520–524.

Sheikh K, Förster J, Nielsen LK. 2005. Modeling hybridoma cell metabolism using a generic genome-scale metabolic model of Mus musculus. *Biotechnol. Prog.* **21**:112–121.

Shim H, Dolde C, Lewis B, Wu C, Dang CV, Jungmann R, Dalla-Favera R. 1997. c-Myc transactivation of LDH-A: implications for tumor metabolism and growth. *Proc. Nat. Acad. Sci.* **94**:6658.

Simms D, Cizdziel PE, Chomczynski P. 1993. TRIzol: A new reagent for optimal single-step isolation of RNA. *Focus* **15**:99–102.

Sriram G, Rahib L, He J, Campos A, Parr L, Liao J, Dipple K. 2008. Global metabolic effects of glycerol kinase overexpression in rat hepatoma cells. *Mol. Genet. Metab.* **93**:145–159.

Takahashi K, Yamanaka S. 2006. Induction of Pluripotent Stem Cells from Mouse Embryonic and Adult Fibroblast

Cultures by Defined Factors. *Cell* **126**:663–676.

Tuttle SW, Maity A, Oprysko PR, Kachur AV, Ayene IS, Biaglow JE, Koch CJ. 2007. Detection of reactive oxygen species via endogenous oxidative pentose phosphate cycle activity in response to oxygen concentration: implications for the mechanism of HIF-1alpha stabilization under moderate hypoxia. *J. Biol. Chem.* **282**:36790–36796.

Vander Heiden MG, Cantley LC, Thompson CB. 2009. Understanding the Warburg effect: the metabolic requirements of cell proliferation. *Science* **324**:1029–1033.

Vander Heiden MG, Locasale JW, Swanson KD, Sharfi H, Heffron GJ, Amador-Noguez D, Christofk HR, Wagner G, Rabinowitz JD, Asara JM, Cantley LC. 2010. Evidence for an alternative glycolytic pathway in rapidly proliferating cells. *Science* **329**:1492–1499.

Wiechert W, Nöh K. 2005. From stationary to instationary metabolic flux analysis. *Adv. Biochem. Eng. Biotechnol.* **92**:145–172.

Wise DR, Ward PS, Shay JES, Cross JR, Gruber JJ, Sachdeva UM, Platt JM, Dematteo RG, Simon MC, Thompson CB. 2011. Hypoxia promotes isocitrate dehydrogenase-dependent carboxylation of α-ketoglutarate to citrate to support cell growth and viability. *Proc. Nat. Acad. Sci.* **108**:19611–19616.

Wise D, DeBerardinis RJ, Mancuso A, Sayed N, Zhang X, Pfeiffer H, Nissim I, Daikhin E, Yudkoff M, McMahon S. 2008. Myc regulates a transcriptional program that stimulates mitochondrial glutaminolysis and leads to glutamine addiction. *Proc. Nat. Acad. Sci.* **105**:18782.

Young JD, Shastri AA, Stephanopoulos G, Morgan JA. 2011. Mapping photoautotrophic metabolism with isotopically nonstationary (13)C flux analysis. *Metab. Eng.* **13**:656–665.

Young JD, Walther JL, Antoniewicz MR, Yoo H, Stephanopoulos G. 2008. An elementary metabolite unit (EMU) based method of isotopically nonstationary flux analysis. *Biotechnol. Bioeng.* **99**:686–699.

Yuneva M, Zamboni N, Oefner P, Sachidanandam R, Lazebnik Y. 2007. Deficiency in glutamine but not glucose induces MYC-dependent apoptosis in human cells. *J. Cell Biol.* **178**:93.

Yustein JT, Liu Y-C, Gao P, Jie C, Le A, Vuica-Ross M, Chng WJ, Eberhart CG, Bergsagel PL, Dang CV. 2010. Induction of ectopic Myc target gene JAG2 augments hypoxic growth and tumorigenesis in a human B-cell model. *Proc. Nat. Acad. Sci.* **107**:3534–3539.

Zamboni N, Fendt SM, Rühl M, Sauer U. 2009. 13C-based metabolic flux analysis. *Nat. Protoc.* **4**:878–892.

Zamboni N. 2011. 13C metabolic flux analysis in complex systems. *Curr. Opin. Biotechnol.* **22**:103–108.

Zamorano F, Wouwer AV, Bastin G. 2010. A detailed metabolic flux analysis of an underdetermined network of CHO cells. *J. Biotech.* **150**:497–508.

APPENDIX 4.A - MFA Model Formulation

The metabolic network model includes the reactions listed in Table 4.F.2 and is based on the following assumptions:

- Intracellular metabolite levels and metabolic fluxes remained constant throughout the duration of the labeling experiment. Extracellular fluxes were confirmed to be constant throughout the experiment based on a long-term growth experiment from which the extracellular time courses were determined.
- Differing seeding densities did not affect the metabolic phenotype. The 36, 48, and 72 hour plates were seeded with a lower density compared to the 6, 12, and 24 hour plates, but it was assumed that balanced growth was maintained throughout the experiment.
- Cytosolic malic enzyme (ME1) and PEP carboxylase (PEPCK) were not detectable based on the [U-$^{13}C_5$]glutamine labeling study discussed below under Model Reduction. Also, separate pools of malate, oxaloacetate, and isocitrate were not modeled to simplify the reaction network.
- All essential amino acids except arginine, isoleucine, and leucine were assumed to be utilized solely for biomass synthesis in the High Myc condition. Isoleucine was also assumed to be utilized solely for biomass synthesis in the Low Myc condition. Catabolism of these amino acids was not modeled.
- For the steady-state, ISA, and INST-MFA flux estimates, dilution of amino acid labeling was allowed to occur through reversible exchange with unlabeled substrates in the medium. Dilution of alanine was not allowed because it was not present in the medium prior to the labeling period. Lactate was allowed to be diluted from the medium because it was present in serum.
- Succinate and fumarate are symmetric molecules that have interchangeable orientations when metabolized by enzymes of the TCA cycle.
- There was no re-incorporation of labeled CO_2.

APPENDIX 4.B - Stoichiometric Balancing Alone is Insufficient to Determine All Net Fluxes

Prior to conducting isotope labeling experiments, we sought to determine whether our extracellular measurements were feasible by applying stoichiometric balancing alone to estimate fluxes in the High Myc condition. To do so, we fit our metabolic network model to the measured extracellular fluxes shown in Table 4.1. We obtained an acceptable fit (SSRES = 0) but were unable to determine several net fluxes and all exchange fluxes with uncertainties less than ±100%. The net fluxes of PYC, MDH, and ME were completely unidentifiable, while several net fluxes in the pentose phosphate (PP) pathway and TCA cycle were estimated with 95% confidence intervals that spanned zero. This indicated that the fluxes balanced stoichiometrically, but that there was not enough information in the extracellular measurements to estimate fluxes involved in cyclic or parallel pathways. Therefore, we sought to apply isotope labeling experiments and ^{13}C MFA to resolve the flux distribution within these important intracellular pathways.

APPENDIX 4.C - Model Reduction

Isotopomer models used for ^{13}C MFA must be tailored to the relevant metabolic reaction network and available measurements of the experimental system. While developing a model to describe the High Myc labeling experiment, we identified two network redundancies that could not be fully resolved by feeding glucose tracers alone. These were (i) presence of serine dehydratase activity, which deaminates serine directly to pyruvate and thus provides a route to bypass the pyruvate kinase (PK) enzyme and (ii) presence of cytosolic malic enzyme, which converts malate into pyruvate inside the cytosolic compartment. Both redundancies impact the precision with which fluxes surrounding the pyruvate node can be determined. Therefore, we sought to determine whether these enzymes were indeed active in our system and should be included in the isotopomer model.

To determine whether serine could be converted to pyruvate by serine dehydratase in High Myc cells, we fed [U-$^{13}C_3$]serine for 8 days and subsequently measured isotope labeling in proteinogenic amino acids (Appendix F, Fig. 4.F.1). Based on the absence of ^{13}C-labeling in alanine, aspartate and glutamate, we concluded that serine dehydratase was inactive in P493-6 cells under the conditions of our experiment. This was further confirmed by absence of serine dehydratase expression as assessed by Western blot (data not shown). To determine whether carbon could be recycled back to pyruvate through cytosolic malic enzyme or PEP carboxykinase (PEPCK), we fed [U-$^{13}C_5$]glutamine to High Myc cells for 8 days but found no significant labeling in proteinogenic alanine, glycine, or serine (Appendix F, Fig. 4.F.1). (The detection limit on our GC-MS is approximately 0.2 to 0.5 mol% enrichment for these fragments.) Based on this finding and to preserve parsimony in our isotopomer model, we concluded that cytosolic malic enzyme and PEPCK activities were not detectable and should be excluded from the model. A recent publication from CV Dang's group also shows minimal activity of cytosolic malic enzyme based on a similar $^{13}C_5$-glutamine labeling experiment using measurements of free alanine isotopomers (Le et al., 2012). However, these data do not exclude the possibility of mitochondrial malic enzyme activity, which has been previously observed in tumor cells and was therefore retained in the model (Moreadith and Lehninger, 1984).

APPENDIX 4.D - Optimal Design of Isotope Labeling Experiments

Since the optimal tracer combination for ^{13}C MFA can depend strongly on the network topology and the available measurements, we adapted the approach of Möllney et al. (1999) to identify a mixture of ^{13}C-labeled glucose tracers that would maximize the precision of net fluxes estimated from the steady-state isotope labeling measurements in Table 4.F.1. By applying the Nelder-Mead simplex algorithm (MATLAB *fminsearch* routine), we adjusted the relative amounts of five readily available glucose tracers—[1-^{13}C], [2-^{13}C], [6-^{13}C], [1,2-$^{13}C_2$], and [U-$^{13}C_6$]—until D-optimality was obtained. (The D-optimality criterion minimizes the determinant of the parameter covariance matrix.) This resulted in an optimal tracer combination of 20% [1-^{13}C]glucose, 28% [U-$^{13}C_6$]glucose, and 52% [1,2-$^{13}C_2$]glucose. This tracer combination was applied in all subsequent labeling experiments.

APPENDIX 4.E - Abbreviations

3PG, 3-phosphoglycerate; **AcCoA**, Acetyl-Coenzyme A; **AcCoA.C**, cytosolic Acetyl-Coenzyme A; **ACL**, ATP-citrate lyase; **ADH**, α-ketoglutarate dehydrogenase; **AKG**, α-ketoglutarate; **ALA**, alanine; **ALA.E**, extracellular alanine; **ALAR**, alanine excretion rate; **ALDO**, aldolase; **ALT**, alanine transaminase; **ARG**, arginine; **ARG.E**, extracellular arginine; **ARGR**, arginine uptake rate; **ARGS**, arginase; **ASN.E**, extracellular asparagine; **ASNR**, asparagine uptake rate; **ASNS**, asparaginase; **ASP**, asparate; **AST**, aspartate transaminase; **BIOM**, biomass; **CIT**, citratre; **CO2,** carbon dioxide; **CS**, citrate synthase; **CYS**, cysteine; **CYS.E**, extracellular cysteine; **CYSR**, cysteine uptake rate; **CYST**, cystathionine synthase; **DHAP**, dihydroxyacetone phosphate; **E4P**, erythrose-4-phosphate; **EC2**, 2 enzyme-bound carbons; **EC3**, 3 enzyme-bound carbons; **ENO**, enolase; **F6P**, fructose-6-phosphate; **FBP**, fructose-1,6-bisphosphate; **FUM**, fumarate; **FUMS**, fumarase; **G6P**, glucose-6-phosphate; **G6PDH**, glucose-6-phosphate dehydrogenase;**GAP**, glyceraldehyde-3-phosphate; **GAPDH**, glyceraldehyde-3-phosphate dehydrogenase; **GDH**, glutamate dehydrogenase; **GLC.C**, cytosolic glucose; **GLC.E**, extracellular glucose; **GLN**, glutamine; **GLN.E**, extracellular glutamine; **GLNR**, glutamine uptake rate; **GLS**, glutaminase; **GLU**, glutamate; **GLU.E**, extracellular glutamate; **GLUR**, glutamate excretion rate; **GLUT**, glucose transport; **GLY**, glycine; **GLY.E**, extracellular glycine; **GLYR**, glycine excretion rate; **GLYS**, glycine synthase; **HK,** hexokinase; **IDH**, isocitrate dehydrogenase; **ILE**, isoleucine; LABG, labeled glucose; **LAC**, lactate; **LAC.E**, extracellular lactate; **LEU**, leucine; **LDH**, lactate dehydrogenase; **LIPS**, lipid sink; **MAL**, malate; **MCT**, monocarboxylate transporter; **MDH**, malate dehydrogenase; **ME**, malic enzyme; **MEETHF**, methylene tetrahydrofuran; **OAA**, oxaloacetate; **PDH**, pyruvate dehydrogenase; **PEP**, phosphoenolpyruvate; **PFK**, phosphofructokinase; **PGI**, phosphoglucose isomerase; **PK**, pyruvate kinase;**PST**, serine transaminase;**PYC**, pyruvate carboxylase; **PYR.C**, cytosolic pyruvate; **PYR.M**, mitochondrial pyruvate; **PYRT**, pyruvate transport; **R5P**, ribose-5-phosphate; **R5PE**, ribulose-5-phosphate epimerase; **R5PI**, ribulose-5-phosphate isomerase; **RU5P**, ribulose-5-phosphate; **S7P**, sedoheptulose-7-phosphate; **SER**, serine; **SER.E**, extracellular serine; **SERR**, serine uptake rate; **SHT**, serine hydroxymethyl transferase; **SUC**, succinate; **SUDH**, succinate dehydrogenase; **TA1**, transaldolase 1; **TA2**, transaldolase 2; **TK1**, transketolase 1; **TK2**, transketolase 2; **TK3**, transketolase 3; **TPI**, triose phosphate isomerase; **UNLG**, unlabeled glucose; **X5P**, xylulose-5-phosphate.

APPENDIX 4.F - Supplementary Tables and Figures

Table 4.F.1 Isotope Labeling Measurements Used for Metabolic Flux Determination. GC-MS ions used to assess metabolite labeling. Standard errors of measurement (SEM) were determined based on the lack of agreement between measured and theoretically computed mass isotopomer distributions obtained from unlabeled cell extracts.

Metabolite	*Mass*	*Carbons*	*Composition*	*SEM (mol%)*
ALA	260	1-2-3	$C_{11}H_{26}O_2NSi_2$	0.4
ALA	232	2-3	$C_{10}H_{26}ONSi_2$	0.2
GLY	246	1-2	$C_{10}H_{24}O_2NSi_2$	0.2
GLY	218	2	$C_9H_{24}ONSi_2$	0.3
SER	390	1-2-3	$C_{17}H_{40}O_3NSi_3$	0.5
ASP	418	1-2-3-4	$C_{18}H_{40}O_4NSi_3$	0.4
ASP	390	2-3-4	$C_{17}H_{40}O_3NSi_3$	0.4
GLU	432	1-2-3-4-5	$C_{19}H_{42}O_4NSi_3$	0.2
GLU	330	2-3-4-5	$C_{16}H_{36}O_2NSi_2$	0.2
RIB	284	1-2-3-4	$C_{13}H_{18}O_6N_1$	0.4
RIB	259	3-4-5	$C_{12}H_{19}O_6$	0.4

Table 4.F.2 Complete List of Reactions and Atom Transitions for the B-cell Metabolic Network. Refer to *Nomenclature* for a list of metabolite abbreviations.

Glycolysis			
HK	GLC.C (abcdef)	→	G6P (abcdef)
PGI	G6P (abcdef)	↔	F6P (abcdef)
PFK	F6P (abcdef)	→	FBP (abcdef)
ALDO	FBP (abcdef)	↔	DHAP (cba) + GAP (def)
TPI	DHAP (abc)	↔	GAP (abc)
GAPDH	GAP (abc)	↔	3PG (abc)
ENO	3PG (abc)	↔	PEP (abc)
PK	PEP (abc)	→	PYR.C (abc)
LDH	PYR.C (abc)	↔	LAC (abc)
Pentose Phosphate Pathway			
G6PDH	G6P (abcdef)	→	RU5P (bcdef) + CO2 (a)
R5PE	RU5P (abcde)	↔	R5P (abcde)
R5PI	RU5P (abcde)	↔	X5P (abcde)
TK1	X5P (abcde)	↔	GAP (cde) + EC2 (ab)
TK2	F6P (abcdef)	↔	E4P (cdef) + EC2 (ab)
TK3	S7P (abcdefg)	↔	R5P (cdefg) + EC2 (ab)
TA1	F6P (abcdef)	↔	GAP (def) + EC3 (abc)
TA2	S7P (abcdefg)	↔	E4P (defg) + EC3 (abc)
TCA Cycle			
PYRT	PYR.C (abc)	↔	PYR.M (abc)
PDH	PYR.M (abc)	→	AcCoA (bc) + CO2 (a)
CS	OAA (abcd) + AcCoA (ef)	→	CIT (dcbfea)
IDH	CIT (abcdef)	↔	AKG (abcde) + CO2 (f)
ADH	AKG (abcde)	→	SUC (bcde) + CO2 (a)
SUDH	SUC (½ abcd + ½ dcba)	↔	FUM (½ abcd + ½ dcba)
FUMS	FUM (½ abcd + ½ dcba)	↔	MAL (abcd)
MDH	MAL (abcd)	↔	OAA (abcd)
Amphibolic reactions			
ME	MAL (abcd)	→	PYR.M (abc) + CO2 (d)
PYC	PYR.M (abc) + CO2 (d)	→	OAA (abcd)
ACL	CIT (abcdef)	→	AcCoA.C (ed) + MAL (fcba)

Table 4.F.2 Continued

Amino Acid Metabolism			
GDH	AKG (abcde)	↔	GLU (abcde)
ARGS	ARG (abcde)	→	GLU (abcde)
GLS	GLN (abcde)	↔	GLU (abcde)
AST	OAA (abcd)	↔	ASP (abcd)
ASNS	ASP (abcd)	↔	ASN (abcd)
PST	3PG (abc)	→	SER (abc)
SHT	SER (abc)	↔	GLY (ab) + MEETHF (c)
CYST	SER (abc)	↔	CYS (abc)
GLYS	CO2 (a) + MEETHF (b)	→	Gly (ab)
ALT	PYR.C (abc)	↔	ALA (abc)
BAA1	ILE (abcdef) + CO2 (g)	→	SUC (bcdg) +AcCoA (ef) + CO2 (a)
BAA2	LEU (abcdef) + CO2 (g)	→	AcCoA (bc) + AcCoA (de) + AcCoA (gf) + CO2 (a)
ALAR	ALA (abc)	→	ALA.E (abc)
ARGR	ARG.E (abcde)	→	ARG (abcde)
ASNR	ASN.E (abcd)	→	ASN (abcd)
CYSR	CYS.E (abcde)	→	CYS (abcde)
GLUR	GLU (abcde)	→	GLU.E (abcde)
GLNR	GLN.E (abcde)	→	GLN (abcde)
GLYR	GLY (ab)	→	GLY.E (ab)
ILER	ILE.E (abcdef)	→	ILE (abcdef)
LEUR	LEU.E (abcdef)	→	LEU (abcdef)
SERR	SER.E (abc)	→	SER (abc)
Transport			
GLUT	GLC.E (abcdef)	→	GLC.C (abcdef)
LIPS	AcCoA.C	→	LIPID
MCT	LAC (abc)	→	LAC.E (abc)
Biosynthesis			
BIOM	90 ALA + 56.55 ARG + 43.2 ASN + 21.75 CYS + 18.12 CYS + 52.5 GLN + 48.3 GLN + 57.9 GLU + 98.7 GLY + 48.6 ILE + 84.6 LEU + 64.5 SER + 34.95 R5P + 38.25 MEETHF + 34.95 CO2 + 17.25 DHAP + 368.5 AcCoA.C	→	BIOMASS

Table 4.F.3 Net Fluxes Determined by ^{13}C INST-MFA for High Myc Cells. Values have units of nmol/10^6 cells/h. Estimated flux values and 95% confidence bounds are shown.

Reaction		*Value*	*LB95*	*UB95*
Glycolysis				
HK	GLC.C → G6P	83.32	75.80	91.09
PGI	G6P ↔ F6P	81.70	74.14	89.47
PFK	F6P → FBP	81.22	73.70	88.60
ALDO	FBP ↔ DHAP + GAP	81.22	73.70	88.60
TPI	DHAP ↔ GAP	80.67	73.16	88.45
GAPDH	GAP ↔ 3PG	161.64	146.59	177.17
ENO	3PG ↔ PEP	160.95	145.96	176.35
PK	PEP → PYR.C	160.95	145.96	176.35
LDH	PYR.C ↔ LAC	128.11	114.37	141.01
Pentose Phosphate Pathway				
G6PDH	G6P → RU5P + CO2	0.32	0.11	2.57
R5PE	RU5P ↔ R5P	-0.49	-0.64	1.08
R5PI	RU5P ↔ X5P	0.80	0.71	1.58
TK1	X5P ↔ GAP + EC2	-0.49	-0.64	1.08
TK2	F6P ↔ E4P + EC2	0.24	-0.54	0.32
TK3	S7P ↔ R5P + EC2	0.24	-0.54	0.32
TA1	F6P ↔ GAP + EC3	0.24	-0.54	0.32
TA2	S7P ↔ E4P + EC3	-0.24	-0.32	0.54
TCA Cycle				
PYRT	PYR.C ↔ PYR.M	28.49	17.46	44.19
PDH	PYR.M → AcCoA + CO2	37.56	26.53	53.23
CS	OAA + AcCoA → CIT	40.94	29.77	56.74
IDH	CIT ↔ AKG + CO2	29.82	18.60	45.62
ADH	AKG → SUC + CO2	38.25	26.76	54.20
SUDH	SUC ↔ FUM	39.33	27.86	55.28
FUMS	FUM ↔ MAL	39.33	27.86	55.28
MDH	MAL ↔ OAA	38.14	26.57	54.31
Amphibolic reactions				
ME	MAL → PYR.M + CO2	12.30	8.75	18.14
PYC	PYR.M + CO2 → OAA	3.23	0.00	8.86
ACL	CIT → AcCoA.C + MAL	11.12	10.61	23.44

Table 4.F.3 Continued

Reaction		*Value*	*LB95*	*UB95*
Amino Acid Metabolism				
GDH	AKG ↔ GLU	-8.44	-9.60	-7.28
ARGS	ARG → GLU	2.91	2.12	3.71
GLS	GLN ↔ GLU	10.04	9.47	10.62
AST	OAA ↔ ASP	0.44	0.01	0.87
ASNS	ASP ↔ ASN	0.44	0.01	0.87
PST	3PG → SER	0.69	0.45	1.04
SHT	SER ↔ GLY + MEETHF	2.49	2.35	2.63
CYST	SER ↔ CYS	-0.03	-0.18	0.12
GLYS	CO2 + MEETHF → GLY	1.34	1.23	1.45
ALT	PYR.C ↔ ALA	4.35	4.08	4.61
BAA1	ILE + CO2 → SUC + AcCoA + CO2	1.07	0.72	1.43
BAA2	LEU + CO2 → 3AcCoA + CO2	0.77	0.30	1.23
ALAR	ALA → ALA.E	1.65	1.43	1.87
ARGR	ARG.E → ARG	4.61	3.82	5.40
ASNR	ASN.E → ASN	0.86	0.44	1.28
CYSR	CYS.E → CYS	0.68	0.53	0.84
GLUR	GLU → GLU.E	2.78	2.21	3.34
GLNR	GLN.E → GLN	11.49	10.92	12.06
GLYR	GLY → GLY.E	0.88	0.67	1.08
ILER	ILE.E → ILE	2.53	2.18	2.88
LEUR	LEU.E → LEU	3.30	2.86	3.74
SERR	SER.E → SER	3.75	3.44	4.05
Transport				
GLUT	GLC.E → GLC.C	83.32	75.80	91.09
LIPS	AcCoA.C → Sink	0.00	0.00	12.51
MCT	LAC → LAC.E	128.11	114.37	141.01
Biosynthesis				
BIOM	Biomass Synthesis	0.0300	0.0284	0.0315

Table 4.F.4 Exchange Fluxes Determined by ^{13}C INST-MFA for High Myc Cells. Values have units of nmol/10^6 cells/h. Estimated flux values and 95% confidence bounds are shown.

Reaction		*Value*	*LB95*	*UB95*
Glycolysis				
PGI	G6P ↔ F6P	158.98	0.00	Inf
ALDO	FBP ↔ DHAP + GAP	0.00	0.00	Inf
TPI	DHAP ↔ GAP	0.39	0.00	Inf
GAPDH	GAP ↔ 3PG	0.00	0.00	Inf
ENO	3PG ↔ PEP	45250.00	0.00	Inf
LDH	PYR.C ↔ LAC	285.65	140.29	575.42
Pentose Phosphate Pathway				
R5PE	RU5P ↔ R5P	213.81	0.00	Inf
R5PI	RU5P ↔ X5P	3.34	0.00	Inf
TK1	X5P ↔ GAP + EC2	0.00	0.00	Inf
TK2	F6P ↔ E4P + EC2	2.21	0.31	14.28
TK3	S7P ↔ R5P + EC2	0.22	0.00	1.26
TA1	F6P ↔ GAP + EC3	273.48	2.95	Inf
TA2	S7P ↔ E4P + EC3	3.02	0.00	8.63
TCA Cycle				
PYRT	PYR.C ↔ PYR.M	86.56	2.93	Inf
IDH	CIT ↔ AKG + CO2	44.62	0.00	Inf
SUDH	SUC ↔ FUM	0.00	0.00	Inf
FUMS	FUM ↔ MAL	861.67	0.00	Inf
MDH	MAL ↔ OAA	3337.70	0.00	Inf
Amino Acid Metabolism				
GDH	AKG ↔ GLU	27.18	14.34	52.40
GLS	GLN ↔ GLU	133.35	23.70	349.61
AST	OAA ↔ ASP	1.46	0.00	17.64
ASNS	ASP ↔ ASN	9.89	0.32	133.35
SHT	SER ↔ GLY + MEETHF	5.87	1.92	14.60
CYST	SER ↔ CYS	0.00	0.00	Inf
ALT	PYR.C ↔ ALA	0.00	0.00	46.26

Table 4.F.5 Pool Sizes Determined by ^{13}C INST-MFA for High Myc Cells. Values shown have units of nmol/10^6 cells. Estimated pool size and 95% confidence interval are shown. Only identifiable pool sizes are shown.

	High Myc Pool Sizes		
Pool	***Value***	***LB95***	***UB95***
3PG	0.00	0.00	539.14
AcCoA	73.00	0.00	468.59
Ala	436.72	292.67	4109.20
Asn	181.18	0.00	1864.90
Asp	1.39	0.00	379.95
Cit	67.95	0.00	716.84
DHAP	0.00	0.00	144.74
EC2	0.00	0.00	7.76
EC3	0.00	0.00	72.78
F6P	0.02	0.00	69.81
FBP	1.36	0.00	72.08
Fum	45.01	0.00	793.62
G6P	0.00	0.00	98.37
GAP	3.50	0.00	143.73
Glc.C	0.00	0.00	106.30
Gln	1680.70	332.86	3889.10
Glu	217.58	0.00	1495.10
Gly	189.04	97.93	328.55
Lac	8211.20	4290.30	13495.00
MEETHF	50.11	0.00	332.38
Mal	2.78	0.00	780.14
OAA	22.21	0.00	785.68
PEP	150.27	0.00	547.95
Pyr.C	1.03	0.00	1062.70
Pyr.m	124.40	0.00	1499.40
R5P	17.02	0.45	66.49
Ru5P	4.01	0.00	70.27
Ser	356.30	177.32	651.35
Suc	99.89	0.00	791.51
X5P	1.48	0.00	67.99
aKG	82.87	0.00	714.72

Table 4.F.6 Net Fluxes Determined by ^{13}C INST-MFA for Low Myc Cells. Values have units of nmol/10^6 cells/h. Estimated flux values and 95% confidence bounds are shown.

Reaction		*Value*	*LB95*	*UB95*
Glycolysis				
HK	GLC → G6P	64.30	59.30	69.45
PGI	G6P ↔ F6P	61.61	56.43	67.00
PFK	F6P → FBP	62.49	57.52	67.60
ALDO	FBP ↔ DHAP + GAP	62.49	57.52	67.60
TPI	DHAP ↔ GAP	62.17	57.20	67.27
GAPDH	GAP ↔ 3PG	125.10	115.25	135.30
ENO	3PG ↔ PEP	124.73	114.71	134.90
PK	PEP → PYR.C	124.73	114.71	134.90
LDH	PYR.C ↔ LAC	114.04	104.32	122.67
Pentose Phosphate Pathway				
G6PDH	G6P → RU5P + CO2	1.94	0.47	3.86
R5PE	RU5P ↔ R5P	0.88	-0.09	2.54
R5PI	RU5P ↔ X5P	1.05	0.56	1.89
TK1	X5P ↔ GAP + EC2	0.88	-0.09	2.54
TK2	F6P ↔ E4P + EC2	-0.44	-1.27	0.05
TK3	S7P ↔ R5P + EC2	-0.44	-1.27	0.05
TA1	F6P ↔ GAP + EC3	-0.44	-1.27	0.05
TA2	S7P ↔ E4P + EC3	0.44	-0.05	1.27
TCA Cycle				
PYRT	PYR.C ↔ PYR.M	8.36	5.91	18.03
PDH	PYR.M → AcCoA + CO2	11.52	9.20	21.15
CS	OAA + AcCoA → CIT	12.11	9.85	21.80
IDH	CIT ↔ AKG + CO2	5.60	3.47	15.12
ADH	AKG → SUC + CO2	7.93	5.13	17.58
SUDH	SUC ↔ FUM	8.52	5.60	18.12
FUMS	FUM ↔ MAL	8.52	5.60	18.12
MDH	MAL ↔ OAA	11.12	8.66	20.24
Amphibolic reactions				
ME	MAL → PYR.M + CO2	3.92	2.74	7.22
PYC	PYR.M + CO2 → OAA	0.76	0.00	3.95
ACL	CIT → AcCoA.C + MAL	6.51	6.11	13.75

Table 4.F.6 Continued

Reaction		*Value*	*LB95*	*UB95*
Amino Acid Metabolism				
GDH	AKG ⇔ GLU	-2.3323	-2.9044	-1.7411
ARGS	ARG → GLU	1.0425	0.6515	1.4326
GLS	GLN ⇔ GLU	5.4145	5.1167	5.7098
AST	OAA ⇔ ASP	-0.2355	-0.6637	0.1886
ASNS	ASP ⇔ ASN	-0.2355	-0.6637	0.1886
PST	3PG → SER	0.3739	0.1158	0.6359
SHT	SER ⇔ GLY + MEETHF	1.2125	1.1293	1.2989
CYST	SER ⇔ CYS	-0.5598	-0.6878	-0.4322
GLYS	CO2 + MEETHF → GLY	0.5418	0.4983	0.599
ALT	PYR.C ⇔ ALA	2.3328	2.1941	2.4705
BAA1	ILE + CO2 → SUC + AcCoA + CO2	0.5918	0.1597	1.0246
ALAR	ALA → ALA.E	0.7547	0.6567	0.853
ARGR	ARG.E → ARG	2.0341	1.6577	2.4189
ASNR	ASN.E → ASN	0.993	0.5883	1.4289
CYSR	CYS.E → CYS	0.9412	0.8155	1.067
GLUR	GLU → GLU.E	3.1095	2.8151	3.3994
GLNR	GLN.E → GLN	6.2615	5.9684	6.5557
GLYR	GLY → GLY.E	0.0232	0.0000	0.1183
ILER	ILE.E → ILE	1.444	1.0244	1.8756
SERR	SER.E → SER	1.44	1.29	1.59
Transport				
GLUT	GLC.E → GLC.C	64.30	59.30	69.45
LIPS	AcCoA.C → Sink	0.00	0.00	8.59
MCT	LAC → LAC.E	114.04	104.32	122.67
Biosynthesis				
BIOM	Biomass Synthesis	0.0175	0.0165	0.0186

Table 4.F.7 Exchange Fluxes Determined by ^{13}C INST-MFA for Low Myc Cells. Values have units of nmol/10^6 cells/h. Estimated flux values and 95% confidence bounds are shown.

Reaction		*Value*	*LB95*	*UB95*
Glycolysis				
PGI	G6P ↔ F6P	0.00	0.00	Inf
ALDO	FBP ↔ DHAP + GAP	0.00	0.00	Inf
TPI	DHAP ↔ GAP	134550.00	0.00	Inf
GAPDH	GAP ↔ 3PG	0.00	0.00	4.41
ENO	3PG ↔ PEP	2826.90	0.00	Inf
LDH	PYR.C ↔ LAC	0.00	0.00	Inf
Pentose Phosphate Pathway				
R5PE	RU5P ↔ R5P	12.73	6.83	28.95
R5PI	RU5P ↔ X5P	0.78	0.06	2.28
TK1	X5P ↔ GAP + EC2	233.51	39.04	Inf
TK2	F6P ↔ E4P + EC2	1.70	0.34	4.38
TK3	S7P ↔ R5P + EC2	0.40	0.04	1.78
TA1	F6P ↔ GAP + EC3	0.00	0.00	44.04
TA2	S7P ↔ E4P + EC3	0.38	0.02	Inf
TCA Cycle				
PYRT	PYR.C ↔ PYR.M	9239.30	0.00	Inf
IDH	CIT ↔ AKG + CO2	2.84	0.00	Inf
SUDH	SUC ↔ FUM	0.00	0.00	Inf
FUMS	FUM ↔ MAL	3384.70	0.00	Inf
MDH	MAL ↔ OAA	4328.80	0.00	Inf
Amino Acid Metabolism				
GDH	AKG ↔ GLU	4.43	3.22	19.32
GLS	GLN ↔ GLU	24.91	2.20	96.54
AST	OAA ↔ ASP	0.67	0.00	7.42
ASNS	ASP ↔ ASN	2.06	0.00	15.15
SHT	SER ↔ GLY + MEETHF	0.49	0.00	Inf
CYST	SER ↔ CYS	0.00	0.00	Inf
ALT	PYR.C ↔ ALA	75.41	0.00	166.77

Table 4.F.8 Pool Sizes Determined by ^{13}C INST-MFA for Low Myc Dells. Values shown have units of nmol/10^6 cells. Estimated pool size and 95% confidence interval are shown. Only identifiable pool sizes are shown.

	Low Myc Pool Sizes		
Pool	***Value***	***LB95***	***UB95***
3PG	2873.30	0.00	5040.60
AcCoA	0.16	0.00	193.03
Ala	14159.00	310.85	22100.00
Asn	109.81	2.42	604.52
Asp	0.00	0.00	369.09
Cit	8.00	0.00	276.33
DHAP	34.30	0.00	338.22
EC2	0.24	0.00	13.98
EC3	0.00	0.00	99.33
F6P	61.17	0.00	178.27
FBP	12.22	0.00	173.87
Fum	4.09	0.00	383.67
G6P	16.84	0.00	141.03
GAP	11.63	0.00	348.37
Glc.C	9.42	0.00	141.00
Gln	334.57	69.80	3650.10
Glu	0.30	0.00	461.73
Gly	21.51	0.00	2337.20
Mal	1.76	0.00	383.71
OAA	1.22	0.00	384.69
PEP	1.82	0.00	5074.60
Pyr.C	0.21	0.00	1043.40
Pyr.m	0.20	0.00	1087.20
R5P	64.25	22.75	141.07
Ru5P	0.01	0.00	14.02
S7P	23.17	1.73	83.90
Ser	837.83	0.00	2479.90
Suc	60.48	0.00	357.46
X5P	0.13	0.00	13.75
aKG	10.34	0.00	279.56

Table 4.F.9 Root-Mean-Square (RMS) Errors for Selected Flux Estimations. RMS errors were calculated as described in the caption to Table 4.2. Reactions included in glycolysis, PP pathway, and TCA cycle are listed in Appendix F, Table 4.F.2. (SS w/ Ribose = steady-state with ribose measurements included, 6× SS w/ Ribose = 6 identical replicates of SS w/ Ribose labeling data.)

	Pathway			
Method	***Glycolysis***	***PPP***	***TCA Cycle***	***Overall***
SS w/ Ribose	5.5	34	32	21
6x SS w/ Ribose	5.4	19	26	17
INST-MFA	4.8	32	18	19

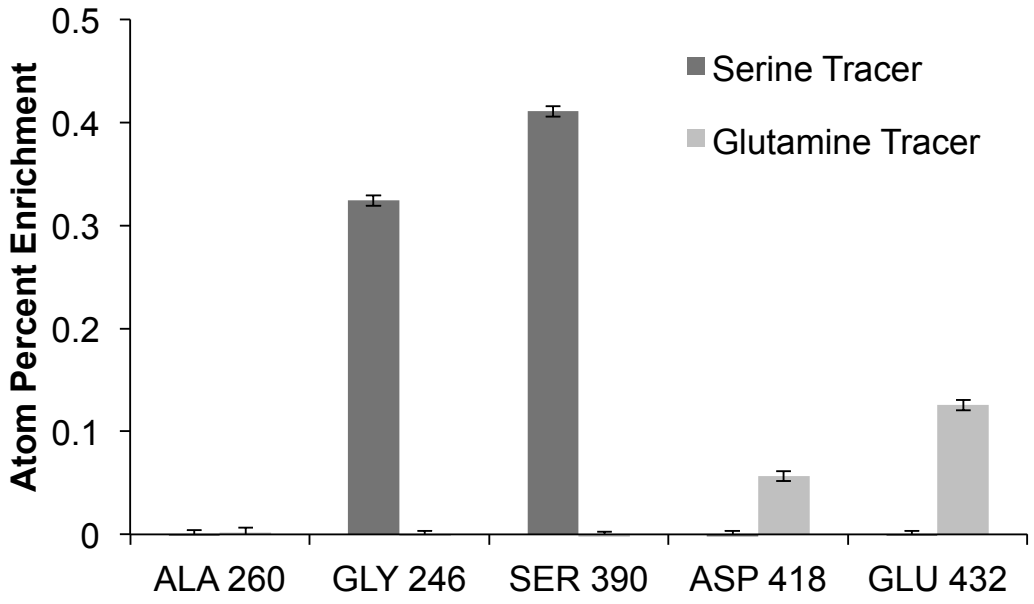

Figure 4.F.1 Atom Percent Enrichment (APE) of Proteinogenic Amino Acid Fragments Sampled from [U-$^{13}C_3$]serine and [U-$^{13}C_5$]glutamine Tracer Experiments. Fragments shown are for alanine (Ala), glycine (Gly), serine (Ser), aspartate (Asp), and glutamate (Glu). The atom percent enrichment represents the percentage of isotopically labeled carbons. The [U-$^{13}C_3$]serine tracer experiments showed no labeling in alanine, aspartate, and glutamate fragments, while significant labeling was obtained in serine and glycine fragments. The [U-$^{13}C_5$]glutamine tracer experiments showed no labeling in serine, glycine, and alanine, while significant labeling was found in aspartate and glutamate fragments. This is evidence that serine dehydratase, cytosolic malic enzyme, and PEP carboxykinase are not detectable in our system.

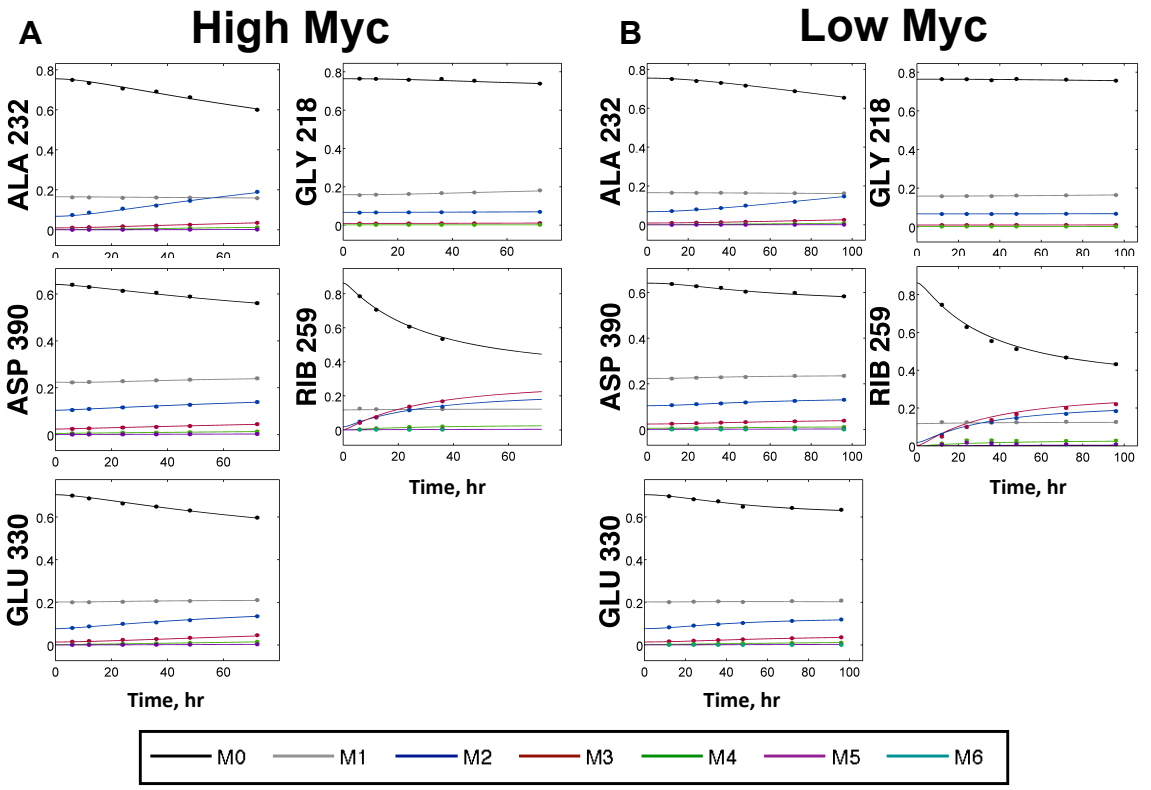

Figure 4.F.2 Dynamic Isotope Labeling Trajectories of Measured Metabolites in the High and Low Myc Conditions. Experimentally determined (•) and INST-MFA fitted (−) mass isotopomer distributions for the **(A)** High Myc and **(B)** Low Myc conditions. Nominal masses of M0 mass isotopomers are shown next to the fragment abbreviation. Error bars represent standard measurement errors. Raw mass isotopomer data are shown without correction for natural isotope abundance.

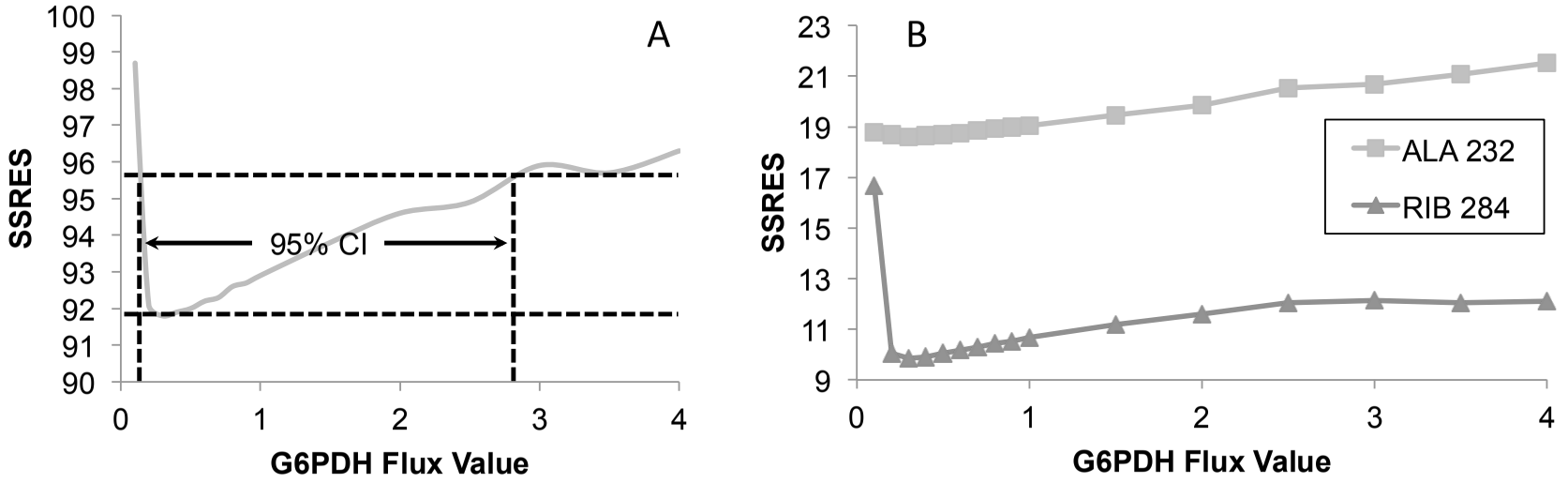

Figure 4.F.3 Impact of G6PDH Flux on SSRES of High Myc INST-MFA Isotopomer Model. The G6PDH flux was varied in a step-wise manner from 0 to 4 nmol/million cells/h and fluxes were re-estimated using INST-MFA while holding the G6PDH flux fixed. At each increment, flux estimation was repeated 50 times starting from random initial values to approximate the global minimum. A) Impact of G6PDH flux on the total SSRES. The dotted lines indicate the SSRES cutoff for determining the 95% confidence interval on the G6PDH flux. B) Impact of G6PDH flux on the squared residuals of selected alanine and ribose ion fragments.

CHAPTER 5

COMPARISON OF HIGH AND LOW MYC B-CELLS IN NORMOXIC AND HYPOXIC CONDITIONS USING ISOTOPICALLY NONSTATIONARY MFA

5.1 Introduction

In chapter 4, we saw that the isotopically nonstationary metabolic flux analysis (INST-MFA) method can be a more powerful way to estimate the intracellular fluxes of a mammalian cell than other methods (e.g., stationary MFA or ISA). The model system used, a P493-6 B-cell with varying levels of Myc expression, served as a solid proof-of-concept cell model that verified the validity of the new techniques as well as revealed specific alterations between the normal and tumorigenic phenotypes (Murphy et al., 2013). While this is a complete and insightful study, there was an opportunity for improvements in many aspects of the work.

Key to understanding how cancer survives and grows is placing the disease in its proper context. When a tumor grows *in vivo*, the cancerous cells typically outgrow the surrounding vasculature (Vander Heiden, 2011). When the cells become physically distant from the oxygen-carrying veins and arteries, a burden is created where the availability of oxygen is limited (Semenza, 2010b). This hypoxic environment, as discussed in the background in Chapter 2, causes a host of changes within the cell, namely the stabilization of the hypoxia inducible factors (HIF). These transcription factors then activate a host of processes that adapts the cell to the low oxygen environment (Semenza, 2010a). If the cells contain Myc alterations, as do the P493-6 cells used in this work, then it's possible that the two proteins work together to support the altered phenotype (Dang et al., 2008).

The previous MFA study of these cells (Chapter 4) lacked an analysis of how these cells adjust their metabolism in a hypoxic environment. Understanding how the carbon flux changes when tumors are unable to fully utilize the TCA cycle is critical to selecting new methods to specifically target cancerous cells (Vander Heiden, 2011). We have addressed this knowledge gap by repeating the INST-MFA studies from Chapter 4, adding the hypoxic condition as a variable. To address the limitations of the previous study, we have added measurements of lipid labeling to our analysis as well as improving how we collect and analyze samples.

Here, we show comparisons between a complete set of metabolic flux maps for the combination of High and Low Myc expression levels along with Normoxic and Hypoxic growth environments. We detail in the methods section the addition of lipid labeling measurements as well as new findings that build upon the previous MFA studies in Chapter 4.

5.2 Methods

5.2.1 Cell Culture

Cells were maintained according to the method in section 3.2.7 of Chapter 3 with the following exceptions. Hypoxic cells were cultured in 5% CO_2 and 1% O_2. For tracer experiments, glucose-free medium was supplemented with a 1:1 mixture of [U-$^{13}C_6$]glucose and [1,2-$^{13}C_2$]glucose. All tracers were purchased from Cambridge Isotope Laboratories.

5.2.2 Specific Rate Determination

Specific rates were determined according to the methods detailed in section 3.2 of Chapter 3 with the following exceptions. The degradation rate of glutamine in culture medium without cells was found to be slightly different for each experiment. Also, evaporation led to non-negligible increases in the concentration of certain metabolites over time. These cell-independent effects were modeled by inclusion of a non-zero exponential decay rate in the regression equation (Equation 3.3 in chapter 3). Table 5.B.1 lists the decay rates incorporated into the specific rate determination.

5.2.3 Isotopically Nonstationary Labeling Experiment

INST-MFA requires the measurement of isotopic enrichment at multiple time points during the transient labeling period. For each condition, the time points were chosen based on the doubling-time of the cell such that approximately three doubling periods will have occurred at the last point and the more intermediate samples will give the highest level of labeling possible based on the expected growth rate. For High Myc cells in normoxia (HN), samples were taken at 6, 12, 24, 36, 48, and 72 hours. For High Myc cells in hypoxia (HH), samples were taken at 12, 24, 36, 48, 71, and 96 hours. For Low Myc cells in normoxia (LN), samples were taken at 18, 36, 54, 72, 90, and 108 hours. For Low Myc cells in hypoxia (LH), samples were taken at 18, 36, 54, 72, 96, 120, and 144 hours. For

each time point, three separate T-75 flasks were seeded at the appropriate density to achieve a final cell number of approximately ten million cells per flask at the time of sampling. Prior to seeding, the growth medium was removed by centrifugation and the cells were resuspended in glucose-labeled medium. At the sample times indicated previously, cells were harvested by centrifugation at 1500 RPM, washed with phosphate buffered saline (PBS), and split into two microcentrifuge tubes. Each tube was centrifuged at 1500 RPM to pelletize cells. One tube was flash frozen in liquid nitrogen for future lipid analysis. TRIzol was added to the other tube, and the sample was homogenized and then frozen at -80°C for future protein and RNA extraction and analysis.

5.2.4 Extraction, Hydrolysis, and Derivation of Total Cellular Protein and RNA

Refer to section 4.2.6 in Chapter 4 for details on this methodology.

5.2.5 Medium Glucose Derivatization

Refer to section 4.2.7 in Chapter 4 for details on this methodology.

5.2.6 Extraction and Derivatization of Total Cellular Lipids

Samples were removed from the -80°C freezer and thawed at room temperature for ten minutes. A solution of 5% sulfuric acid in methanol was made fresh and 1 mL was added to the cell pellet. The pellet was homogenized with a glass Pasteur pipet and transferred to a 6 mL glass tube. An additional 1 mL of 5% sulfuric acid in methanol was added. Then, 0.5 mL of toluene and 25 μL of a 0.2% BHT in methanol solution were added. The sample was heated at 95°C for 2 hours with occasional vortexing. After heating, 3 mL of DI water was added, and the solution was vortexed vigorously to quench. 2 mL of hexane was added; the sample was shaken and then centrifuged at 2500 RPM to separate layers. The hexane layer (top portion) was removed and dried under nitrogen flow at room temperature. Dried samples were resuspended in 200 μL of hexane and transferred to a glass GC/MS vial.

5.2.7 Gas chromatography Mass Spectrometry (GC-MS) Analysis

Derivatized sugar and amino acid samples were analyzed according to the method in section 4.2.8 of chapter 4. Derivatized lipid samples were analyzed by GC-MS using a DB-23 capillary column (30 m × 0.25 mm i.d. × 0.25 μm; Agilent J&W Scientific) installed in an Agilent 7890A gas chromatograph (GC). The injection volume was 1

μL, and all samples were run in split mode with an inlet temperature of 270°C and a split ratio of 10:1. Helium flow was controlled electronically at 1 mL/min. The GC was interfaced to an Agilent 5975C mass spectrometer (MS) operated in electron impact mode with temperatures of 230°C for the ion source and 150°C for the quadrupole. The GC temperature program for lipid analysis was: inject sample at 100°C, ramp at 40°C/min to 150°C, ramp at 10°C/min to 190°C, ramp at 40°C to 250°C, hold for 3 minutes. Because the primary lipid of interest was palmitate, mass spectra were obtained in scan mode over the range 269-290 m/z (Yoo et al., 2004). Raw ion chromatograms were integrated using a custom MATLAB M-file that applies consistent integration bounds and baseline correction to each ion (Antoniewicz et al., 2007).

5.2.8 Isotopomer Network Model

A detailed isotopomer model for mammalian B-cell metabolism was constructed. The metabolic network contains reactions for glycolysis, pentose phosphate pathway, TCA cycle, amphibolic pathways, amino acid catabolism, and biomass synthesis (Table 5.B.3 in Appendix B). The network comprises 59 reactions with carbon atom transitions specified for all reactions. The network includes 10 extracellular substrates (glucose, aspartate, arginine, asparagine, cystine, glutamine, isoleucine, leucine, serine, and valine), 5 metabolic products (biomass, lactate, alanine, glutamate, and glycine) and 41 balanced intracellular metabolites with the following exceptions: HN did not include aspartate or arginine fluxes, HH did not include aspartate or valine, and LN did not include aspartate. These amino acids were left out based on the biomass requirement and the growth rate. If the incoming amino acid flux was less that what was required by the biomass equation then catabolism of that amino acid was not included. Constraints from cofactor metabolites such as ATP and NAD(P)H were excluded because these balances have been shown to produce unreliable results in mammalian systems (Bonarius et al., 1998). Refer to the Appendix of Chapter 4 for a detailed description of the model formulation and assumptions.

5.2.9 Flux Determination and Statistical Analysis

Refer to section 4.2.10 of chapter 4 for details on this analysis.

5.2.10 Biomass Equation

The biomass equation is the same as described in chapter 4, section 4.2.12 with the following exceptions. Palmitate is included in the biomass and is assumed to come from the AcCoA.c pool. As such, the coefficients for these metabolites are 40.26 for palmitate and 49.14 for AcCoA.c.

5.3 Results

5.3.1 Cell Metabolic Phenotypes in a Normoxic Environment

Under normal cell-culture oxygen tension (21%) we measured qualitatively similar results to those discussed in the previous chapter (see Table 5.1). A 28% decrease in growth rate was measured between High and Low Myc cells. Both conditions exhibited the high glycolytic phenotype measured previously with lactate to glucose ratios of 1.9 ± 0.2 and 2.0 ± 0.2, respectively. Glutamine, the other primary source of carbon aside from glucose, represented 8.4% of the incoming carbon in the High Myc condition and 8.0% in Low Myc. Most fluxes are decreased when comparing from High Myc to Low Myc, but most are not significantly different with a p-value greater than 0.05. Serine uptake and lactate and asparagine efflux were the only significantly different extracellular fluxes. In both conditions, amino acids contributed 30% of the incoming carbon.

5.3.2 Cell Metabolic Phenotypes in a Hypoxic Environment

When High and Low Myc cells were placed in a low oxygen environment (1% oxygen), their metabolism adjusted to enable growth under hypoxia (Table 5.2). High Myc cell growth rate was decreased by 37% while Low Myc was decreased by 59%. Compared to each other, the shift from High Myc to Low Myc was marked by a 53% decrease in growth rate under hypoxia. As expected, both conditions exhibited very high glycolytic activity with L/G ratios of 1.92 ± 0.15 (High) and 1.94 ± 0.15 (Low). Surprisingly, the Low Myc condition had a larger glucose and lactate flux in the hypoxic environment than High Myc. This difference potentially highlights some of the interaction between ectopic and regulated levels of Myc and the induction of HIF by low oxygen. In low oxygen environments, we would expect a decrease in TCA cycle activity, a notion supported by the low consumption of glutamine in both conditions (Semenza, 2010a). Glutamine only represented 1.7% and 0.7% of the incoming carbon for High and Low Myc, respectively. Amino acids in general decreased their relative contribution to the incoming carbon flux to 9% (High) and 6% (Low), indicating a shift towards reliance on glucose as the major source of carbon.

Table 5.1 Extracellular Fluxes for High and Low Myc Phenotypes in a Normoxic Environment.

Fluxes have units of nmol/10^6 cells/h except for biomass, which has units of h^{-1}. Fluxes that were included in the MFA flux estimations are marked with a ✔. The uptake rates of other amino acids (marked with an ✖) were stoichiometrically matched to the growth rate, indicating that they were solely used for biomass synthesis. These amino acids were not included in the MFA flux estimation because their catabolism was assumed to be negligible. Significance is indicated for the comparison between Low and High Myc conditions based on a two-tailed Student's *t*-test with $p<0.05$.

	High Myc	***Low Myc***		
Metabolite	***Flux (nmol/10^6 cells/h)***	***Flux (nmol/10^6 cells/h)***	***Included in MFA***	***p < 0.05***
Biomass (h^{-1})	0.0363 ± 0.0016	0.0261 ± 0.0013	✔	✔
		Uptake Fluxes		
Glucose	124 ± 12	95 ± 7	✔	✖
Aspartate	0.85 ± 0.97	1.23 ± 0.69	✔	✖
Serine	6.1 ± 0.7	3.3 ± 0.5	✔	✔
Glutamine	16.3 ± 4.4	11.9 ± 2.1	✔	✖
Histidine	0.58 ± 0.27	0.2 ± 0.18	✖	✖
Threonine	1.35 ± 0.49	0.84 ± 0.47	✖	✖
Arginine	0.11 ± 3.31	2.2 ± 1.9	✖	✖
Tyrosine	0.82 ± 0.25	0.06 ± 0.26	✖	✖
Cystine	1.27 ± 0.42	1.91 ± 0.2	✔	✖
Valine	3.33 ± 0.43	1.96 ± 0.35	✔	✖
Methionine	0.91 ± 0.34	0.41 ± 0.17	✖	✖
Tryptophan	0.18 ± 0.13	0.54 ± 0.31	✖	✖
Phenylalanine	1.16 ± 0.22	0.77 ± 0.2	✖	✖
Isoleucine	4.82 ± 0.94	3.05 ± 0.66	✔	✖
Leucine	4.44 ± 0.97	3.15 ± 0.72	✔	✖
Lysine	2.12 ± 0.24	1.79 ± 0.56	✖	✖
		Secretion Fluxes		
Lactate	233 ± 12	186 ± 9.6	✔	✔
Glutamate	5 ± 0.8	5.1 ± 1.1	✔	✖
Asparagine	8.3 ± 2	-0.91 ± 1.87	✔	✔
Glycine	1.21 ± 0.66	-0.09 ± 0.35	✔	✖
Alanine	2.45 ± 0.73	0.75 ± 0.35	✔	✖

Table 5.2 Extracellular Fluxes for High and Low Myc Phenotypes in a Hypoxic Environment.

Fluxes have units of nmol/10^6 cells/h except for biomass, which has units of h^{-1}. Fluxes that were included in the MFA flux estimations are marked with a ✔. The uptake rates of other amino acids (marked with an ✖) were stoichiometrically matched to the growth rate, indicating that they were solely used for biomass synthesis. These amino acids were not included in the MFA flux estimation because their catabolism was assumed to be negligible. Significance is indicated for the comparison between Low and High Myc conditions based on a two-tailed Student's *t*-test with $p<0.05$.

	High Myc	***Low Myc***		
Metabolite	***Flux (nmol/10^6 cells/h)***	***Flux (nmol/10^6 cells/h)***	***Included in MFA***	***p < 0.05***
Biomass (h^{-1})	0.0229 ± 0.0017	0.0107 ± 0.0009	✔	✔
	Uptake Fluxes			
Glucose	173 ± 11	217 ± 13	✔	✔
Aspartate	0.47 ± 0.49	2.53 ± 1.18	✔	✖
Serine	2.56 ± 0.39	2.86 ± 0.54	✔	✔
Glutamine	3.96 ± 2.18	2.1 ± 2.65	✔	✖
Histidine	0.08 ± 0.22	-0.14 ± 0.28	✖	✖
Threonine	0.36 ± 0.32	0.3 ± 0.34	✖	✖
Arginine	3.57 ± 1.26	2.41 ± 2.32	✖	✖
Tyrosine	0.14 ± 0.2	0.04 ± 0.25	✖	✖
Cystine	0.76 ± 0.22	3.28 ± 0.27	✔	✔
Valine	1.09 ± 0.28	0.87 ± 0.37	✔	✖
Methionine	0.26 ± 0.21	0.2 ± 0.26	✖	✖
Tryptophan	0.11 ± 0.14	0.28 ± 1.16	✖	✖
Phenylalanine	0.33 ± 0.18	0.2 ± 0.22	✖	✖
Isoleucine	1.89 ± 0.5	1.22 ± 0.71	✔	✖
Leucine	1.81 ± 0.51	1.34 ± 0.72	✔	✖
Lysine	0.8 ± 0.36	0.69 ± 0.49	✖	✖
	Secretion Fluxes			
Lactate	333 ± 15	423 ± 20	✔	✔
Glutamate	2.39 ± 0.47	7.39 ± 0.75	✔	✔
Asparagine	4.84 ± 2.23	-2.48 ± 1.99	✔	✔
Glycine	0.87 ± 0.41	0.91 ± 0.51	✔	✖
Alanine	3.02 ± 0.37	1.65 ± 0.34	✔	✖

5.3.3 Isotopically Nonstationary MFA – High and Low Myc Cells in a Normoxic Environment

Concurrently with the growth experiment, we conducted transient labeling experiments on the High and Low Myc cells under atmospheric oxygen tension. At the time points indicated in section 5.2, isotopomer data were collected resulting in 720 independent mass isotopomer measurements for High Myc and 732 for Low Myc. These measurements were combined with 13 extracellular fluxes (Table 5.1) to estimate metabolic fluxes and their 95% confidence intervals. The High Myc condition was overdetermined by 544 measurements and the fit was accepted based on a chi-square test with SSRES = 335.5. The accepted Low Myc estimation was also overdetermined by 555 measurements with SSRES=359.4. Figure 5.1 shows the High Myc dynamic labeling trajectories of several GC-MS fragments along with the INST-MFA model fits. Figure 5.2 shows the same results for the Low Myc experiment. The remaining ion fragments are shown in Appendix B, Figures 5.B.1 and 5.B.2

The flux maps determined by INST-MFA are shown in Figure 5.3. (Refer to Appendix B for full listings of net and exchange flux values, pool sizes, and all 95% confidence intervals.) The MFA results agree with the conclusion that glycolysis is upregulated in both conditions. The branch point at the pyruvate node indicates that in the High Myc condition 74% of the glucose was secreted as lactate as opposed to 85% in the Low Myc. Both conditions showed negligible pentose phosphate flux, with 3% or less of the incoming glucose carbon directed to this pathway. 24% of the pyruvate formed went to the TCA cycle in the High Myc condition as opposed to 14% in the Low Myc, corroborating the results we saw in chapter 4. Rates of glutamine conversion to α-ketoglutarate were higher in the High Myc condition (43% versus 32%), which supports the notion that High Myc cells are more reliant upon glutamine for growth. Cytosolic acetyl-CoA production was tied to growth rate in both cases. Similar activities of mitochondrial malic enzyme were measured in both conditions which, due to the Low Myc condition having an overall decreased TCA flux, means the cells relied upon this reaction more than in High Myc. Along with the nearly 3-fold increase in other TCA cycle enzymes such as succinate dehydrogenase and malate dehydrogenase, this indicates a clear shift toward oxidative phosphorylation, a conclusion reported previously in Chapter 4.

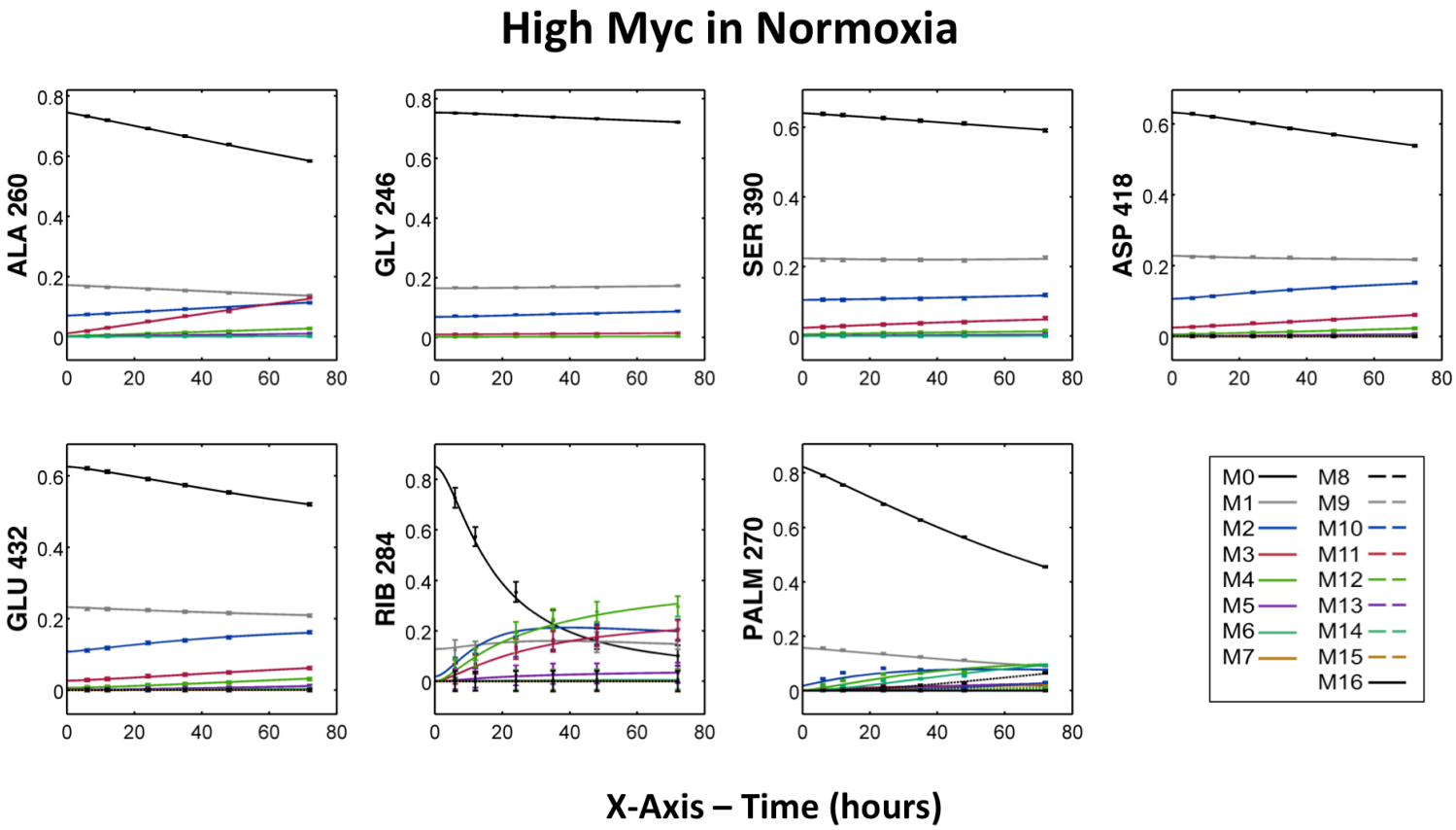

Figure 5.1 Labeling Dynamics of Selected GC-MS Fragment Ions for the High Myc Normoxic Condition. GC-MS ions are shown for alanine (ALA), glycine (GLY), aspartate (ASP), glutamate (GLU), ribose (RIB), and palmitate (PALM). Each panel shows the experimentally measured mass isotopomer abundances (data points) and INST-MFA model fits (solid lines) for a single fragment ion. Raw mass isotopomer data are shown without correction for natural isotope abundance.

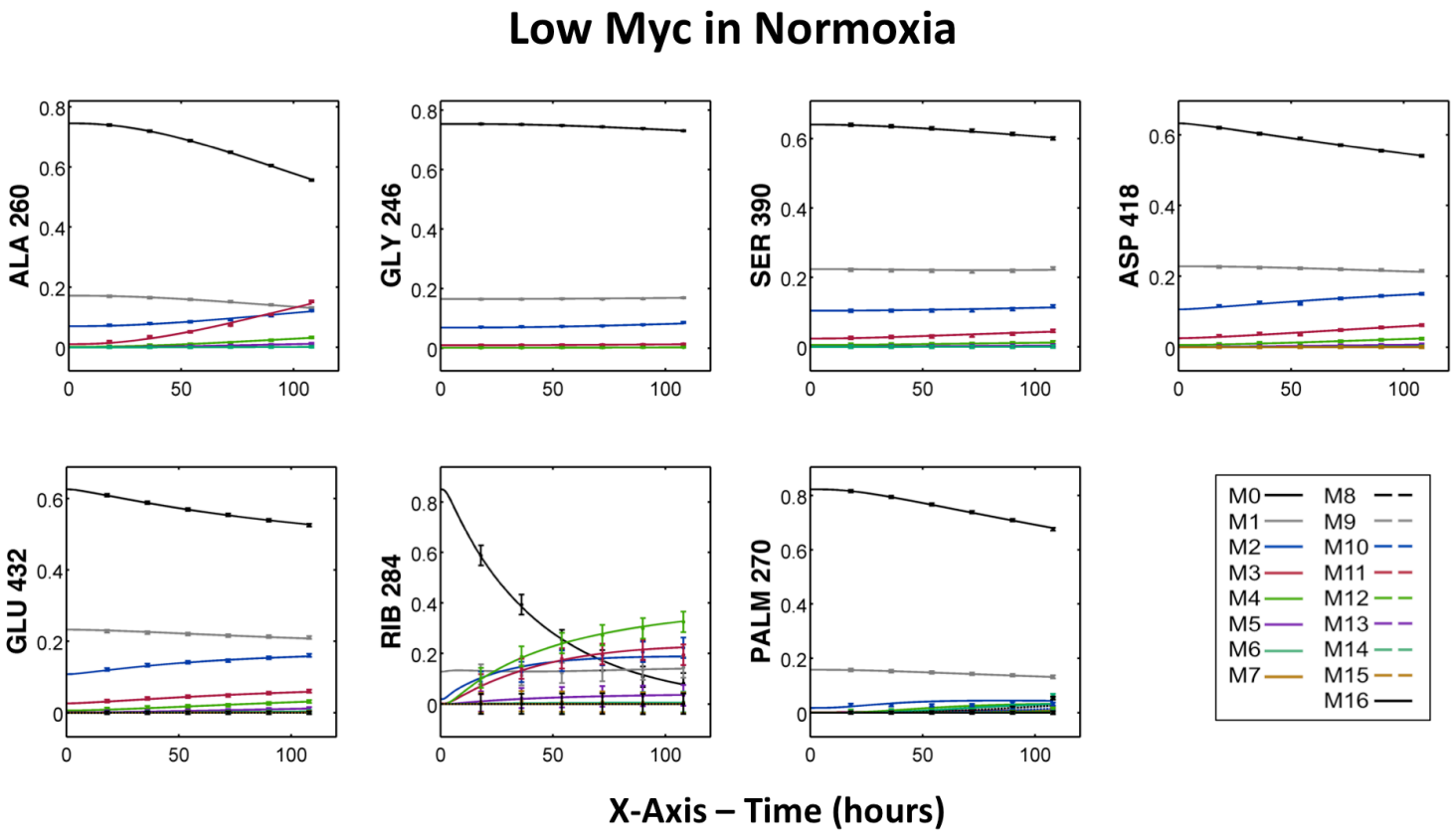

Figure 5.2 Labeling Dynamics of Selected GC-MS Fragment Ions for the Low Myc Normoxic Condition. GC-MS ions are shown for alanine (ALA), glycine (GLY), aspartate (ASP), glutamate (GLU), ribose (RIB), and palmitate (PALM). Each panel shows the experimentally measured mass isotopomer abundances (data points) and INST-MFA model fits (solid lines) for a single fragment ion. Raw mass isotopomer data are shown without correction for natural isotope abundance.

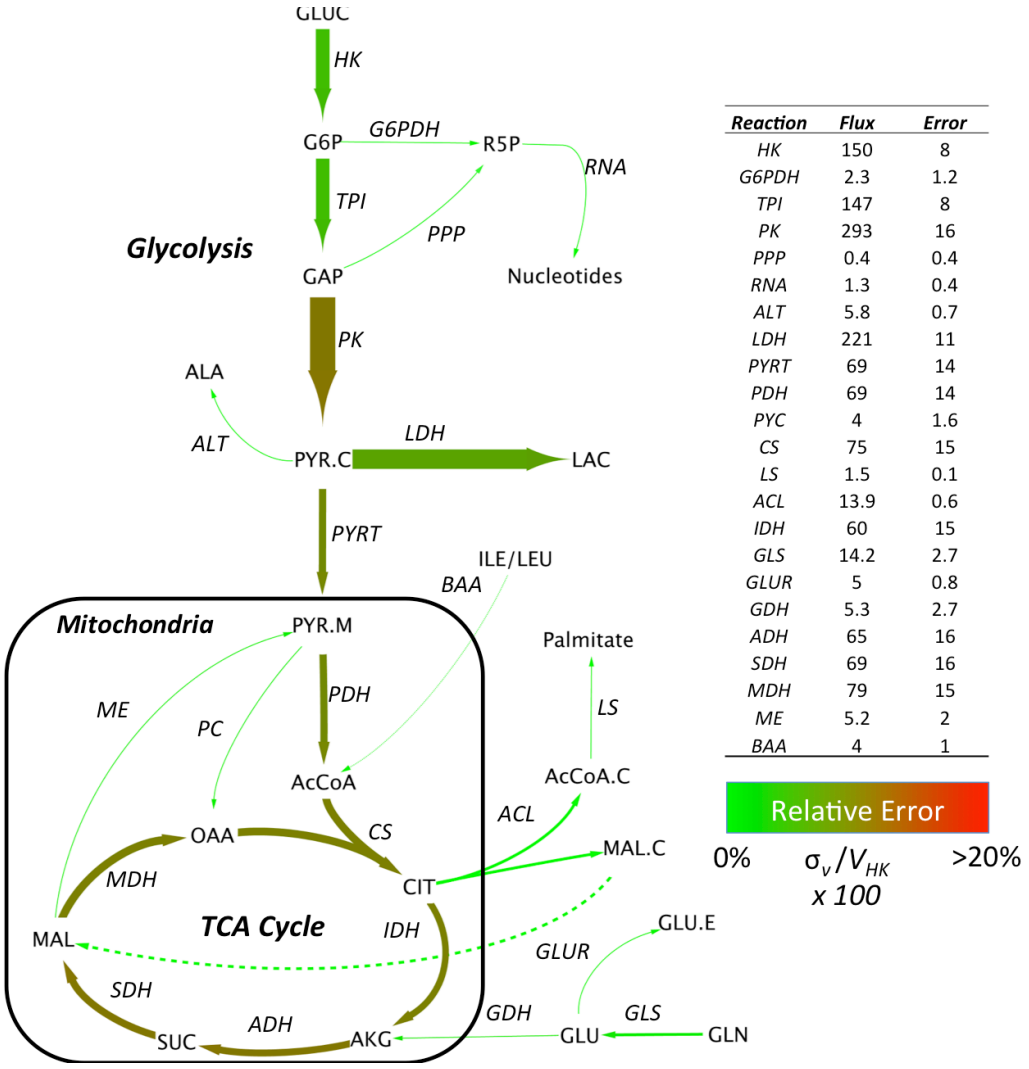

Reaction	Flux	Error
HK	150	8
G6PDH	2.3	1.2
TPI	147	8
PK	293	16
PPP	0.4	0.4
RNA	1.3	0.4
ALT	5.8	0.7
LDH	221	11
PYRT	69	14
PDH	69	14
PYC	4	1.6
CS	75	15
LS	1.5	0.1
ACL	13.9	0.6
IDH	60	15
GLS	14.2	2.7
GLUR	5	0.8
GDH	5.3	2.7
ADH	65	16
SDH	69	16
MDH	79	15
ME	5.2	2
BAA	4	1

Figure 5.3 High Myc Normoxic Flux Map Net fluxes are shown in units of nmol/10^6 cells/hour. Fluxes are represented as $M \pm SE$, where M is the median of the 95% flux confidence interval and SE is the estimated standard error of M calculated as (UB95-LB95)/3.92. UB95 and LB95 are the upper and lower bounds of the 95% confidence interval, respectively. Arrow thickness is scaled proportional to net fluxes included in the adjacent table. Arrow color is representative of the flux uncertainty relative to the hexokinase flux value and is scaled such that the fluxes with a relative error 20% of the HK flux or greater are bright red and the fluxes with the lowest relative error are bright green. Some fluxes included in the isotopomer model are not shown in the figure to enhance clarity.

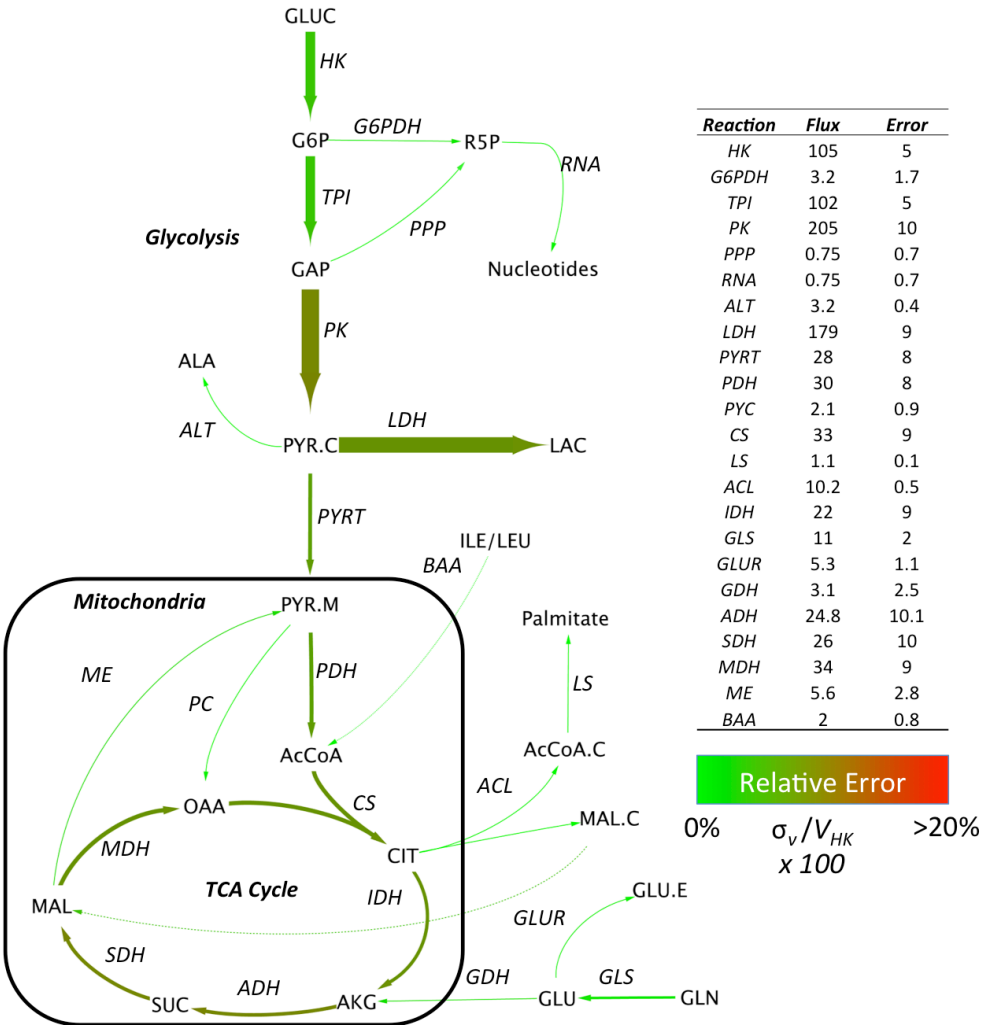

Reaction	Flux	Error
HK	105	5
G6PDH	3.2	1.7
TPI	102	5
PK	205	10
PPP	0.75	0.7
RNA	0.75	0.7
ALT	3.2	0.4
LDH	179	9
PYRT	28	8
PDH	30	8
PYC	2.1	0.9
CS	33	9
LS	1.1	0.1
ACL	10.2	0.5
IDH	22	9
GLS	11	2
GLUR	5.3	1.1
GDH	3.1	2.5
ADH	24.8	10.1
SDH	26	10
MDH	34	9
ME	5.6	2.8
BAA	2	0.8

Figure 5.4 Low Myc Normoxic Flux Map Net fluxes are shown in units of nmol/10^6 cells/hour. Fluxes are represented as $M \pm SE$, where M is the median of the 95% flux confidence interval and SE is the estimated standard error of M calculated as (UB95-LB95)/3.92. UB95 and LB95 are the upper and lower bounds of the 95% confidence interval, respectively. Arrow thickness is scaled proportional to net fluxes included in the adjacent table. Arrow color is representative of the flux uncertainty relative to the hexokinase flux value and is scaled such that the fluxes with a relative error 20% of the HK flux or greater are bright red and the fluxes with the lowest relative error are bright green. Some fluxes included in the isotopomer model are not shown in the figure to enhance clarity.

5.3.4 isotopically Nonstationary MFA – High and Low Myc Cells in a Hypoxic Environment

The transient labeling experiments done in the normoxic environment were repeated at a low oxygen tension (1%) to simulate the stressful conditions *in vivo* tumor cells would encounter when far from the body's vasculature. Six time points were taken for the High Myc condition while seven were taken for Low Myc. This resulted in 696 and 753 independent mass isotopomer measurements for High and Low Myc, respectively. The High Myc estimation included 13 extracellular fluxes while the Low Myc had 15. Each estimation was overdetermined by 514 and 551 measurements and accepted based on a chi-square test with SSRES equal to 294 and 165.2 for High and Low Myc, respectively. Figure 5.5 shows the High Myc dynamic labeling trajectories of several GC-MS fragments along with the INST-MFA model fits. Figure 5.6 shows the same results for the Low Myc experiment. The remaining ion fragments are shown in the Appendix Figures 5.B.3 and 5.B.4

Since these cells were in a hypoxic environment, we expected to see a decrease in mitochondrial flux and a significant increase in glycolytic activity. Under these conditions, Low Myc cells (Fig. 8) actually exhibited a larger glycolytic flux than High Myc cells (Fig. 7), but approximately 93% of the incoming glucose was converted to lactate in both conditions. (Refer to Appendix B for full listings of net and exchange flux values, pool sizes, and all 95% confidence intervals.) Only ~7% of the pyruvate synthesized from glucose entered the TCA cycle in either condition, with the remainder going to alanine synthesis. Both of these conditions had very low, though similar, TCA cycle rates compared to their glycolytic rates even though the Low Myc cells grew significantly slower than the High Myc cells. Due to limited OXPHOS capabilities under hypoxia, much of the isotopic labeling was diverted out of the cell prior to entry to the TCA cycle. This resulted in large confidence intervals because of the low level of labeling in TCA cycle-derived metabolites such as glutamate and aspartate. Figure 5.9 shows the different enrichment levels of selected GC-MS fragments between the four conditions. Due to the retrobiosynthetic approach, many of the fragments in the hypoxic condition had less than 2% isotopic enrichment. It is clear that in the hypoxic condition, the majority of the carbons in glutamate, aspartate, and palmitate fragments were from some unlabeled source other than glucose. The glycolytic metabolites (alanine, glycine, serine, and ribose) exhibited varying levels of enrichment. The high alanine enrichment corroborates the high glycolytic rates measured. Based on the rate of entry of carbon into the mitochondria, we can conclude that High and Low Myc cells had similar rates of mitochondrial activity, but slight differences in the metabolism are not detectable with this tracer mix.

5.3.5 Metabolic Alterations Due to a Switch to Hypoxia.

Dramatic differences in metabolism were seen when comparing High or Low Myc cells in hypoxia versus normoxia. The switch to a hypoxic environment activated numerous alternate pathways most likely via increase of the hypoxia-inducible transcription factors. In going from 21% to 1% O_2 we saw a significant decrease in the growth rates of High (62%) and Low Myc (44%) cells. In contrast to the growth rate, we saw the glycolytic flux increase dramatically: High Myc cells increased glucose uptake by 18% and lactate secretion by 50% in hypoxia while Low Myc cells increased glucose uptake by 110% and lactate secretion by 134%. Other fluxes, such as pyruvate dehydrogenase (PDH) decreased in the High Myc condition (63% decrease) while staying nearly the same in the Low Myc condition. In fact, the PDH flux was nearly identical in High Myc Hypoxic and both Low Myc conditions, highlighting how high levels of Myc, as well as oxygen, are necessary for significant TCA cycle activity in this cell model. With the decrease in oxidative phosphorylation we also saw an approximately 68% decrease in glutaminase activity in both conditions. Glutaminase activity was linked with anaplerotic malic enzyme (ME) activity, but due to the low level of labeling it is difficult to make specific claims about the differences between normoxic and hypoxic environments. Malic enzyme is important for regeneration of reducing equivalents in the form of NAD(P)H and for removal of excess anaplerotic carbon entering the TCA cycle (Moreadith and Lehninger, 1984). Glucose-6-phosphate dehydrogenase (G6PDH), the first enzyme in the pentose phosphate pathway, is also important for NADPH generation (Schwartz et al., 1986), but we saw almost no activity in all four conditions.

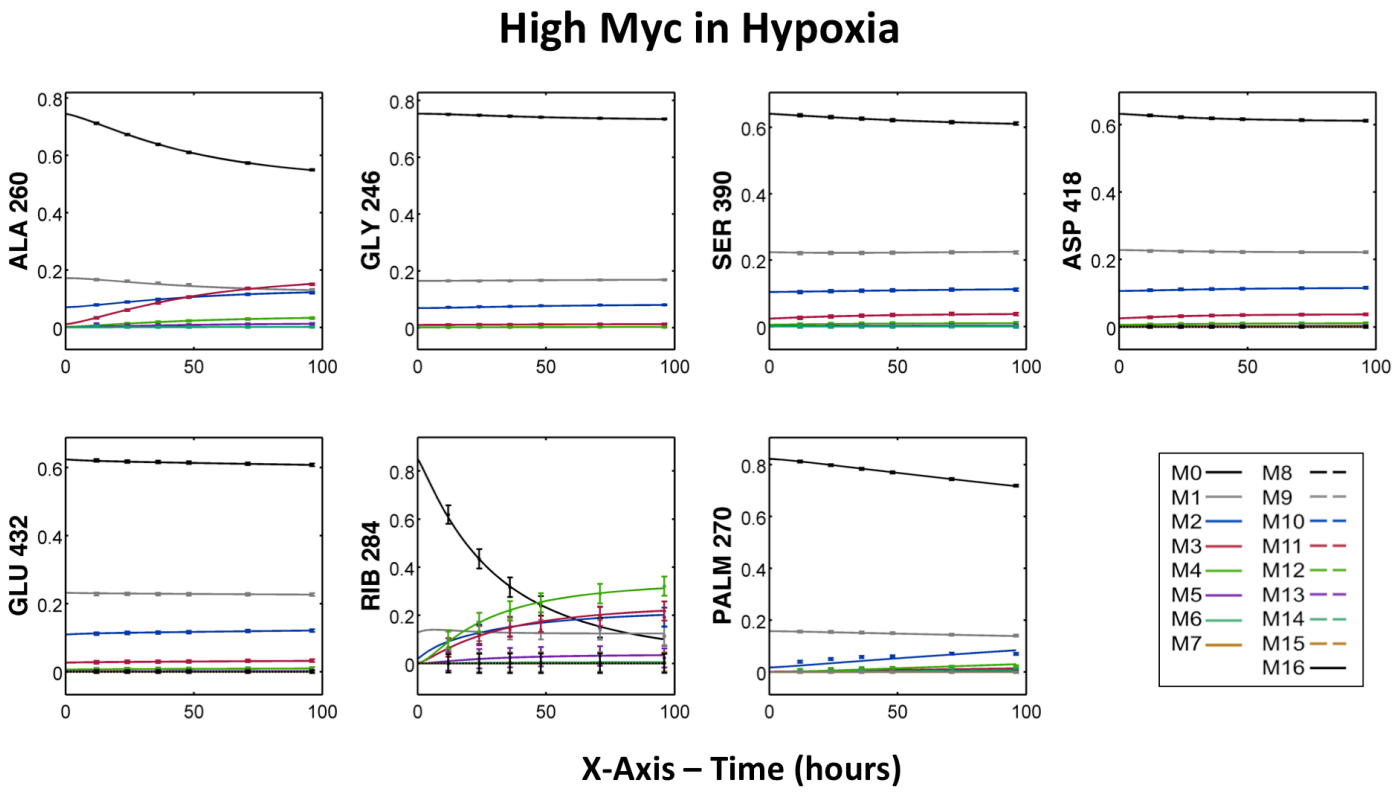

Figure 5.5 Labeling Dynamics of Selected GC-MS Fragment Ions for the High Myc Hypoxic Condition. GC-MS ions are shown for alanine (ALA), glycine (GLY), aspartate (ASP), glutamate (GLU), ribose (RIB), and palmitate (PALM). Each panel shows the experimentally measured mass isotopomer abundances (data points) and INST-MFA model fits (solid lines) for a single fragment ion. Raw mass isotopomer data are shown without correction for natural isotope abundance.

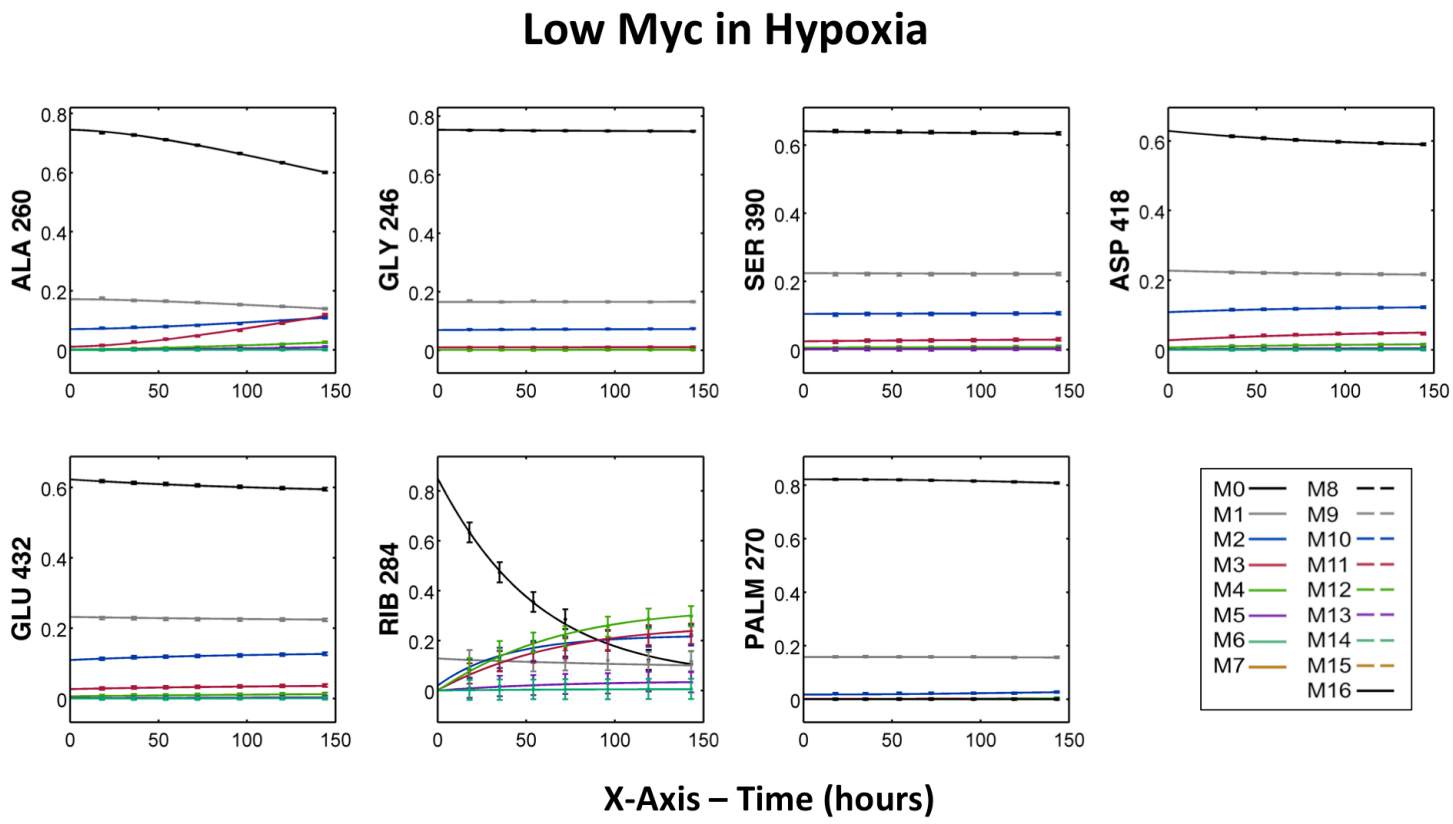

Figure 5.6 Labeling Dynamics of Selected GC-MS Fragment Ions for the Low Myc Hypoxic Condition. GC-MS ions are shown for alanine (ALA), glycine (GLY), aspartate (ASP), glutamate (GLU), ribose (RIB), and palmitate (PALM). Each panel shows the experimentally measured mass isotopomer abundances (data points) and INST-MFA model fits (solid lines) for a single fragment ion. Raw mass isotopomer data are shown without correction for natural isotope abundance.

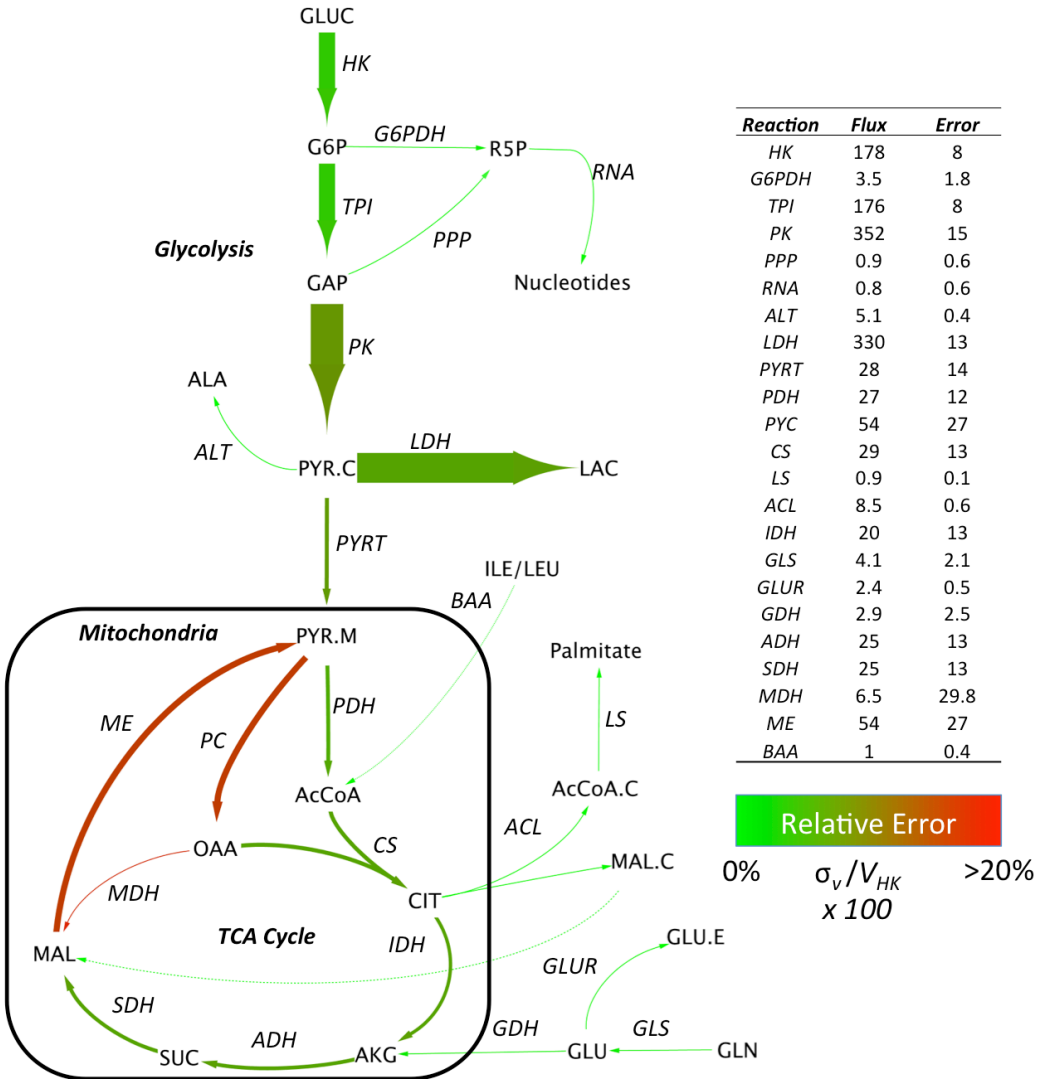

Reaction	Flux	Error
HK	178	8
G6PDH	3.5	1.8
TPI	176	8
PK	352	15
PPP	0.9	0.6
RNA	0.8	0.6
ALT	5.1	0.4
LDH	330	13
PYRT	28	14
PDH	27	12
PYC	54	27
CS	29	13
LS	0.9	0.1
ACL	8.5	0.6
IDH	20	13
GLS	4.1	2.1
GLUR	2.4	0.5
GDH	2.9	2.5
ADH	25	13
SDH	25	13
MDH	6.5	29.8
ME	54	27
BAA	1	0.4

Figure 5.7 High Myc Hypoxic Flux Map Net fluxes are shown in units of nmol/10^6 cells/hour. Fluxes are represented as $M \pm SE$, where M is the median of the 95% flux confidence interval and SE is the estimated standard error of M calculated as (UB95-LB95)/3.92. UB95 and LB95 are the upper and lower bounds of the 95% confidence interval, respectively. Arrow thickness is scaled proportional to net fluxes included in the adjacent table. Arrow color is representative of the flux uncertainty relative to the hexokinase flux value and is scaled such that the fluxes with a relative error 20% of the HK flux or greater are bright red and the fluxes with the lowest relative error are bright green. Some fluxes included in the isotopomer model are not shown in the figure to enhance clarity.

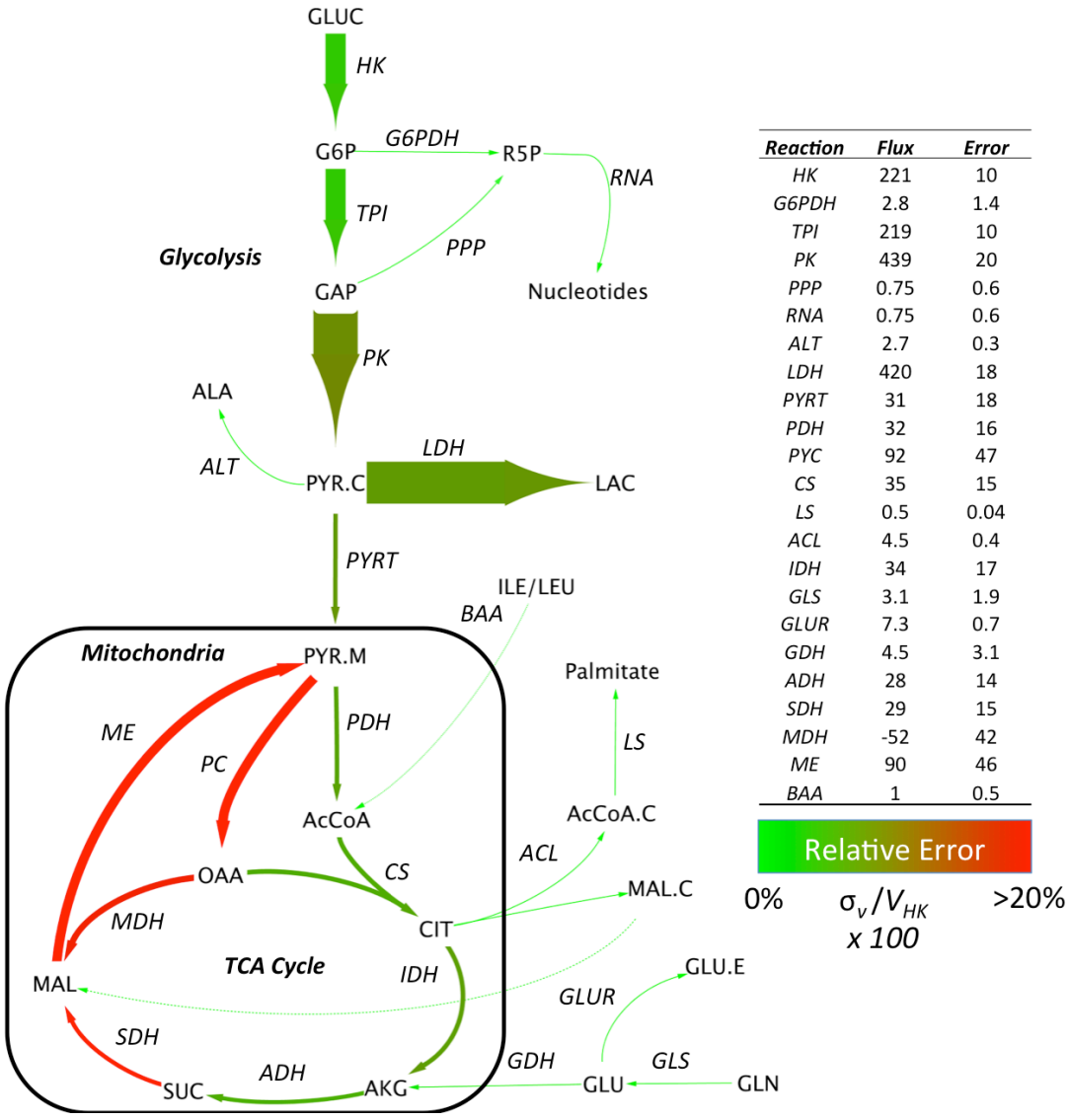

Reaction	Flux	Error
HK	221	10
G6PDH	2.8	1.4
TPI	219	10
PK	439	20
PPP	0.75	0.6
RNA	0.75	0.6
ALT	2.7	0.3
LDH	420	18
PYRT	31	18
PDH	32	16
PYC	92	47
CS	35	15
LS	0.5	0.04
ACL	4.5	0.4
IDH	34	17
GLS	3.1	1.9
GLUR	7.3	0.7
GDH	4.5	3.1
ADH	28	14
SDH	29	15
MDH	-52	42
ME	90	46
BAA	1	0.5

Figure 5.8 Low Myc Hypoxia Flux Map Net fluxes are shown in units of nmol/10^6 cells/hour. Fluxes are represented as $M \pm SE$, where M is the median of the 95% flux confidence interval and SE is the estimated standard error of M calculated as (UB95-LB95)/3.92. UB95 and LB95 are the upper and lower bounds of the 95% confidence interval, respectively. Arrow thickness is scaled proportional to net fluxes included in the adjacent table. Arrow color is representative of the flux uncertainty relative to the hexokinase flux value and is scaled such that the fluxes with a relative error 20% of the HK flux or greater are bright red and the fluxes with the lowest relative error are bright green. Some fluxes included in the isotopomer model are not shown in the figure to enhance clarity.

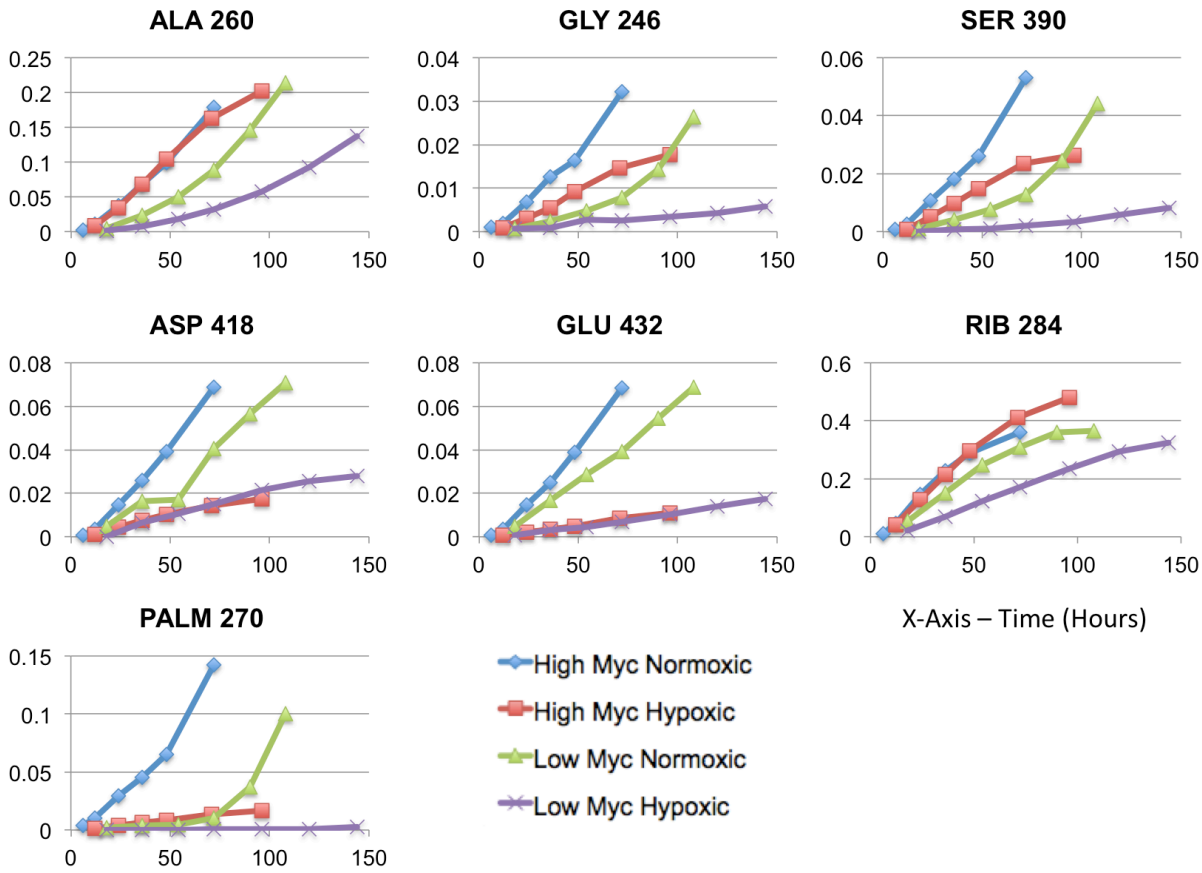

Figure 5.9 Atom Percent Enrichment (APE) of GC-MS Fragments Sampled. Fragments shown are for alanine (ALA), glycine (GLY), serine (SER), aspartate (ASP), glutamate (GLU), ribose (RIB), and palmitate (PALM). The atom percent enrichment represents the percentage of isotopically labeled carbons. The x-axis is time measured in hours. The remaining fragments are in Appendix B, Figures 5.B.5 and 5.B.6.

5.4 Discussion

Central to understanding cancer metabolism is determining differences in pathway flux between cancerous and normal cells as well as how cancerous cells adapt to altered growth environments (Vander Heiden, 2011; Vander Heiden et al., 2009). *In vivo*, a cancer cell has mutations that both remove anti-growth signals and increase pro-growth signals (Hanahan and Weinberg, 2011). Whether this is due to the loss of tumor suppressors or the expression of oncoproteins, the result is that cells adjust their physiology and metabolism to support rapid growth (Ward and Thompson, 2012). Not only are the signals inside the cell important but so are the external signals: factors such as nutrient availability, oxygen tension, and adjacent cells will greatly affect metabolic phenotypes. Quantitatively understanding how these changes specifically affect metabolism is key to finding new ways to exploit differences between normal and cancer cells (Koppenol et al., 2011).

In this study, we assessed P493-6 B-cells under four distinct conditions: High and Low Myc levels under normal (21%) and low (1%) oxygen levels. We previously stated that these cells are ideal for studying altered Myc expression levels due to their isogenic background as well as their well-documented use and success in other research groups (Le et al., 2010; Le et al., 2012; Murphy et al., 2013; Pajic et al., 2000; Pajic et al., 2001). Under all four conditions we measured the extracellular uptake and secretion rates of glucose, lactate, and 18 amino acids as well as the growth rate of the cells. Consistent with our previous report of High and Low Myc metabolism in normoxia (Chapter 4) we saw a decrease in growth in Low Myc and a decrease in the fluxes of glucose, lactate, and most amino acids. However, unlike the results in chapter 4, we find that the amino acid contribution is the same in both conditions (30%). It's possible that the improved methods employed in repeating the experiment yielded results that improved our accuracy but decreased precision slightly because we considered more sources of error in the analysis (see chapter 3). In hypoxia we measured an increase in glucose and lactate fluxes when compared to normoxia. However, Low Myc cells had a greater overall glycolytic flux than High Myc did.

Building on our work from the previous chapter, we decided to repeat the INST-MFA experiments in the normoxic condition and add the hypoxic condition. We also added more GC-MS fragments to our analysis and improved the method used for extracellular flux determination (Chapter 2). The addition of the palmitate 270 fragment was hypothesized to increase the accuracy of the flux estimation in the TCA cycle and lipid synthetic pathways. In

normoxic conditions, our MFA results confirmed the High Myc cells' shift towards mitochondrial metabolism measured in Chapter 4. Although not as dramatic as we previously reported, we did measure larger fluxes in the TCA cycle as well as a greater portion of the glucose-derived pyruvate entering the mitochondria. Fluxes controlled by isocitrate dehydrogenase and succinate dehydrogenase were increased approximately 2.5-fold in High Myc cells when compared to Low Myc. These results better align with our previously measured oxygen uptake rates (Figure 4.5 in Chapter 4). While the overall TCA cycle flux supports the previous OUR measurements, there are several differences between the two studies. We previously reported a dramatic increase in malic enzyme (ME) flux in High Myc cells. The difference measured in this study was not as great as previously observed. However, there is still significant flux through the pathway suggesting it is important for balancing the carbon flow through the TCA cycle and possibly for the maintenance of NAD(P)H. A recent study has highlighted how the tumor suppressor p53 can downregulate expression of ME1 and ME2 and that these proteins work in a positive-feedback loop to sustain p53 activation (Jiang et al., 2013). It is clear from this and other studies that malic enzyme has some role to play in supporting tumor growth (Moreadith and Lehninger, 1984; Vander Heiden et al., 2009). Whether it's solely through replenishment of cofactors or through feedback mechanisms like those seen with p53 is not wholly clear. Similar to our previous data we found that ATP-citrate lyase activity was tied to growth. This is primarily a byproduct of how the lipid synthetic reactions were modeled, but the flux results suggest this is an appropriate method of modeling the metabolism. Another important finding reconfirmed by this study is the low level of pentose phosphate pathway activity. We saw in all four conditions that less than 2 percent of the incoming glucose carbon entered the pentose phosphate pathway through glucose-6-phosphate dehydrogenase (G6PDH). This suggests that activity through this pathway is solely for nucleotide synthesis and not for cofactor balancing. It's possible that the larger flux through IDH and ME pathways meets the NADPH requirements of the cell.

In hypoxic conditions, HIF1α degradation is stabilized and dimerizes with HIF1β to form the HIF transcription factor that controls many similar aspects of central metabolism as Myc (Lum et al., 2007; Semenza, 2010b). At normal expression levels of Myc, HIF will act as an inhibitor of Myc and cause a decrease in the rate of growth and direct metabolism towards glycolysis (Dang et al., 2008). However, when Myc is ectopically expressed, the two transcription factors will cooperate to promote tumorigenesis via mechanisms that are not fully understood(Gordan et al., 2007). It's thought that Myc and HIF work to promote growth of the cell and glycolysis but it's not clear from

previous studies how this affects the cell specific fluxes. Our results show Myc and HIF can increase the growth rate, as seen in the High Myc cells, but the glycolytic fluxes are actually lower. Based on this result, it seems the cells are able to more efficiently use the nutrients to promote growth.

A new measurement we added to the MFA method was the labeling of palmitate. Labeled palmitate measurements have been used in previous studies to show the differences in carbon utilization from glucose and glutamine sources (Keibler et al., 2012). Work from Le et al. (2012) using the same P493-6 cell line showed that under hypoxic conditions, more of the carbons used for palmitate synthesis came from glutamine than from glucose. This suggests a way for cells to reconfigure their metabolism in a glucose-independent manner. Our MFA results support the conclusion that P493 cells can decouple glucose and glutamine metabolism, despite the presence of glucose in the culture media. These data, along with the low level of ^{13}C labeling in palmitate, show a significant rewiring of metabolism towards a glutamine-driven TCA cycle. However, in both High and Low Myc cells, glutamine uptake decreased and the overall rate of carbon through the TCA cycle was decreased when compared to the normoxic condition. Recent studies have suggested that the TCA cycle operates in a reductive manner when in a hypoxic environment, however our results still show a primarily oxidative directionality to the TCA cycle.

This study highlights with greater accuracy the differences between High and Low Myc conditions in both normoxic and hypoxic environments. The use of labeling from amino acids, RNA-bound ribose, and palmitate, along with the extracellular measurements, allowed us to peek inside the cell to quantitatively measure how cancerous cells alter their metabolism to support survival. Future work in hypoxic conditions will need to rely on alternate sources of labeled carbon, such as glutamine, due to the low level of glucose utilization in the TCA cycle. Flux results like these are the foundation for rational decision-making regarding new therapeutic targets such as those discussed in the next chapter (Keibler et al., 2012).

5.5 References

Antoniewicz MR, Kelleher JK, Stephanopoulos G. 2007. Accurate assessment of amino acid mass isotopomer distributions for metabolic flux analysis. *Anal. Chem* **79**:7554–7559.

Bonarius HP, Timmerarends B, de Gooijer CD, Tramper J. 1998. Metabolite-balancing techniques vs. 13C tracer experiments to determine metabolic fluxes in hybridoma cells. *Biotechnol. Bioeng.* **58**:258–262.

Dang CV, Kim J, Gao P, Yustein J. 2008. The interplay between MYC and HIF in cancer. *Nat. Rev. Cancer* **8**:51–56.

Gordan JD, Thompson CB, Simon MC. 2007. HIF and c-Myc: sibling rivals for control of cancer cell metabolism and proliferation. *Cancer Cell* **12**:108–113.

Hanahan D, Weinberg RA. 2011. Hallmarks of cancer: the next generation. *Cell* **144**:646–674.

Jiang P, Du W, Mancuso A, Wellen KE, Yang X. 2013. Reciprocal regulation of p53 and malic enzymes modulates metabolism and senescence. *Nature*.

Keibler MA, Fendt S-M, Stephanopoulos G. 2012. Expanding the concepts and tools of metabolic engineering to elucidate cancer metabolism. *Biotechnol. Prog.* **28**:1409–1418.

Koppenol WH, Bounds PL, Dang CV. 2011. Otto Warburg's contributions to current concepts of cancer metabolism. *Nat. Rev. Cancer* **11**:325–337.

Le A, Cooper CR, Gouw AM, Dinavahi R, Maitra A, Deck LM, Royer RE, Vander Jagt DL, Semenza GL, Dang CV. 2010. Inhibition of lactate dehydrogenase A induces oxidative stress and inhibits tumor progression. *Proc. Nat. Acad. Sci.* **107**:2037–2042.

Le A, Lane AN, Hamaker M, Bose S, Gouw A, Barbi J, Tsukamoto T, Rojas CJ, Slusher BS, Zhang H, Zimmerman LJ, Liebler DC, Slebos RJC, Lorkiewicz PK, Higashi RM, Fan TWM, Dang CV. 2012. Glucose-Independent Glutamine Metabolism via TCA Cycling for Proliferation and Survival in B Cells. *Cell Metab.* **15**:110–121.

Lum JJ, Bui T, Gruber M, Gordan JD, DeBerardinis RJ, Covello KL, Simon MC, Thompson CB. 2007. The transcription factor HIF-1alpha plays a critical role in the growth factor-dependent regulation of both aerobic and anaerobic glycolysis. *Genes Devel.* **21**:1037–1049.

Moreadith RW, Lehninger AL. 1984. Purification, kinetic behavior, and regulation of NAD(P)+ malic enzyme of tumor mitochondria. *J. Biol. Chem.* **259**:6222–6227.

Murphy TA, Dang CV, Young JD. 2013. Isotopically nonstationary 13C flux analysis of Myc-induced metabolic

reprogramming in B-cells. *Metab. Eng.* **15**:206–217.

Pajic A, Spitkovsky D, Christoph B, Kempkes B, Schuhmacher M, Staege MS, Brielmeier M, Ellwart J, Kohlhuber F, Bornkamm GW. 2000. Cell cycle activation by c-myc in a Burkitt lymphoma model cell line. *Int. J. Cancer* **87**:787–793.

Pajic A, Staege MS, Dudziak D, Schuhmacher M, Spitkovsky D, Eissner G, Brielmeier M, Polack A, Bornkamm GW. 2001. Antagonistic effects of c-myc and Epstein-Barr virus latent genes on the phenotype of human B cells. *Int. J. Cancer* **93**:810–816.

Schwartz AG, Pashko L, Whitcomb JM. 1986. Inhibition of tumor development by dehydroepiandrosterone and related steroids. *Toxicol. Path.* **14**:357–362.

Semenza GL. 2010a. Defining the role of hypoxia-inducible factor 1 in cancer biology and therapeutics. *Oncogene* **29**:625–634.

Semenza GL. 2010b. HIF-1: upstream and downstream of cancer metabolism. *Curr. Opin. Genet. Dev.* **20**:51–56.

Vander Heiden MG. 2011. Targeting cancer metabolism: a therapeutic window opens. *Nat. Rev. Drug Discov.* **10**:671–684.

Vander Heiden MG, Cantley LC, Thompson CB. 2009. Understanding the Warburg effect: the metabolic requirements of cell proliferation. *Science* **324**:1029–1033.

Ward PS, Thompson CB. 2012. Metabolic Reprogramming: A Cancer Hallmark Even Warburg Did Not Anticipate. *Cancer Cell* **21**:297–308.

Yoo H, Stephanopoulos G, Kelleher JK. 2004. Quantifying carbon sources for de novo lipogenesis in wild-type and IRS-1 knockout brown adipocytes. *J. Lipid. Res.* **45**:1324–1332.

APPENDIX 5.A - MFA Model Formulation

The metabolic network model includes the reactions listed in Table 5.B.3 in Appendix B and is based on the same assumptions as in Appendix 4A.

APPENDIX 5.B - Supplementary Tables and Figures

Table 5.B.1 Evaporation and Degradation Rates for High and Low Myc Cells in Normoxic and Hypoxic Conditions. Decay rates were determined in cell-free media control experiments using a first-order kinetic model. Negative values indicate accumulation due to evaporation and positive values indicate spontaneous degradation. Which rates to include were determined by whether the absolute value was greater than 0.001 and the uncertainty did not span zero. Abbreviations are as follows: HN – High Myc Normoxic, HH – High Myc Hypoxic, LN – Low Myc Normoxic, and LH – Low Myc Hypoxic. All values were input into ETA.

Metabolite	***Condition***	***Decay Rate (h^{-1})***
Aspartate	HN	-0.0048 ± 0.0025
Asparagine	HN	0.1075 ± 0.0038
Glutamine	HN	0.0042 ± 0.0011
Arginine	HN	0.0027 ± 0.0010
Alanine	HN	-0.0018 ± 0.0016
Tryptophan	HN	0.0064 ± 0.0030
Aspartate	HH	-0.0030 ± 0.0014
Asparagine	HH	0.0078 ± 0.0034
Glutamine	HH	0.0041 ± 0.0008
Arginine	HH	0.0026 ± 0.0008
Tryptophan	HH	-0.0015 ± 0.0007
Aspartate	LN	-0.0052 ± 0.0021
Glutamate	LN	-0.0017 ± 0.0011
Serine	LN	-0.0010 ± 0.0006
Glutamine	LN	0.0033 ± 0.0006
Arginine	LN	0.0020 ± 0.0007
Alanine	LN	-0.0017 ± 0.0008
Tyrosine	LN	-0.0017 ± 0.0010
Valine	LN	-0.0015 ± 0.0008
Tryptophan	LN	-0.0104 ± 0.0053
Phenylalanine	LN	-0.0018 ± 0.0010
Isoleucine	LN	-0.0012 ± 0.0006
Leucine	LN	-0.0011 ± 0.0006
Lysine	LN	-0.0012 ± 0.0009
Aspartate	LH	-0.0042 ± 0.0012
Glutamine	LH	0.0042 ± 0.0004
Arginine	LH	0.0026 ± 0.0003
Tryptophan	LH	-0.0062 ± 0.0037

Table 5.B.2 Isotope Labeling Measurements Used for Metabolic Flux Determination. GC-MS ions used to assess metabolite labeling. Standard errors of measurement (SEM) were determined based on the lack of agreement between measured and theoretically computed mass isotopomer distributions obtained from unlabeled cell extracts.

Metabolite	*Mass*	*Carbons*	*Composition*	*SEM (mol%)*
ALA	260	1-2-3	$C_{11}H_{26}O_2NSi_2$	0.3
ALA	232	2-3	$C_{10}H_{26}ONSi_2$	0.2
GLY	246	1-2	$C_{10}H_{24}O_2NSi_2$	0.2
GLY	218	2	$C_9H_{24}ONSi_2$	0.2
SER	390	1-2-3	$C_{17}H_{40}O_3NSi_3$	0.4
SER	362	2-3	$C_{16}H_{40}O_2NSi_3$	0.5
SER	288	2-3	$C_{14}H_{34}NOSi_2$	0.4
ASP	418	1-2-3-4	$C_{18}H_{40}O_4NSi_3$	0.3
ASP	390	2-3-4	$C_{17}H_{40}O_3NSi_3$	0.4
ASP	302	1-2	$C_{14}H_{32}O_2NSi_2$	0.3
GLU	432	1-2-3-4-5	$C_{19}H_{42}O_4NSi_3$	0.4
GLU	404	2-3-4-5	$C_{18}H_{42}O_3NSi_3$	0.5
GLU	330	2-3-4-5	$C_{16}H_{36}O_2NSi_2$	0.3
RIB	284	1-2-3-4	$C_{13}H_{18}O_6N_1$	0.5
RIB	259	3-4-5	$C_{12}H_{19}O_6$	0.5
GLUC	370	1-2-3-4-5	$C_{17}H_{24}O_8N$	0.5
GLUC	284	1-2-3-4	$C_{13}H_{18}O_6N$	0.5
GLUC	259	4-5-6	$C_{12}H_{19}O_6$	0.5
PALM	270	1-2-3-4-5-6-7-8-9-10-11-12-13-14-15-16	$C_{17}H_{34}O_2$	0.3

Table 5.B.3 Complete List of Reactions and Atom Transitions for the B-cell Metabolic Network. Refer to Appendix 5C for a list of metabolite abbreviations.

Glycolysis			
HK	GLC.c (abcdef)	→	G6P (abcdef)
PGI	G6P (abcdef)	↔	F6P (abcdef)
PFK	F6P (abcdef)	→	FBP (abcdef)
ALDO	FBP (abcdef)	↔	DHAP (cba) + GAP (def)
TPI	DHAP (abc)	↔	GAP (abc)
GAPDH	GAP (abc)	↔	3PG (abc)
ENO	3PG (abc)	↔	PEP (abc)
PK	PEP (abc)	→	PYR.c (abc)
LDH	PYR.c (abc)	↔	LAC (abc)
Pentose Phosphate Pathway			
G6PDH	G6P (abcdef)	→	RU5P (bcdef) + CO2 (a)
R5PE	RU5P (abcde)	↔	R5P (abcde)
R5PI	RU5P (abcde)	↔	X5P (abcde)
TK1	X5P (abcde)	↔	GAP (cde) + EC2 (ab)
TK2	F6P (abcdef)	↔	E4P (cdef) + EC2 (ab)
TK3	S7P (abcdefg)	↔	R5P (cdefg) + EC2 (ab)
TA1	F6P (abcdef)	↔	GAP (def) + EC3 (abc)
TA2	S7P (abcdefg)	↔	E4P (defg) + EC3 (abc)
TCA Cycle			
PYRT	PYR.c (abc)	↔	PYR.m (abc)
PDH	PYR.m (abc)	→	AcCoA (bc) + CO2 (a)
CS	OAA (abcd) + AcCoA (ef)	→	CIT (dcbfea)
IDH	CIT (abcdef)	↔	AKG (abcde) + CO2 (f)
ADH	AKG (abcde)	→	SUC (bcde) + CO2 (a)
SUDH	SUC (½ abcd + ½ dcba)	↔	FUM (½ abcd + ½ dcba)
FUMS	FUM (½ abcd + ½ dcba)	↔	MAL (abcd)
MDH	MAL (abcd)	↔	OAA (abcd)
Amphibolic reactions			
ME	MAL (abcd)	→	PYR.m (abc) + CO2 (d)
PYC	PYR.m (abc) + CO2 (d)	→	OAA (abcd)
ACL	CIT (abcdef)	→	AcCoA.c (ed) + MAL (fcba)

Table 5.B.3 Continued

Amino Acid Metabolism			
GDH	AKG (abcde)	↔	GLU (abcde)
ARGS	ARG (abcde)	→	GLU (abcde)
GLS	GLN (abcde)	↔	GLU (abcde)
AST	OAA (abcd)	↔	ASP (abcd)
ASNS	ASP (abcd)	↔	ASN (abcd)
PST	3PG (abc)	→	SER (abc)
SHT	SER (abc)	↔	GLY (ab) + MEETHF (c)
CYST	SER (abc)	↔	CYS (abc)
GLYS	CO2 (a) + MEETHF (b)	→	Gly (ab)
ALT	PYR.c (abc)	↔	ALA (abc)
BAA1	ILE (abcdef) + CO2 (g)	→	SUC (bcdg) +AcCoA (ef) + CO2 (a)
BAA2	LEU (abcdef) + CO2 (g)	→	AcCoA (bc) + AcCoA (de) + AcCoA (gf) + CO2 (a)
BAA3	VAL (abcde)	→	SUC (abcd) + CO2 (e)
ALAR	ALA (abc)	→	ALA.e (abc)
ARGR	ARG.e (abcde)	→	ARG (abcde)
ASNR	ASN.e (abcd)	→	ASN (abcd)
ASPR	ASP.e (abcd)	→	ASP (abcd)
CYSR	CYS.e (abcde)	→	CYS (abcde)
GLUR	GLU (abcde)	→	GLU.e (abcde)
GLNR	GLN.e (abcde)	→	GLN (abcde)
GLYR	GLY (ab)	→	GLY.e (ab)
ILER	ILE.e (abcdef)	→	ILE (abcdef)
LEUR	LEU.e (abcdef)	→	LEU (abcdef)
SERR	SER.e (abc)	→	SER (abc)
VALR	VAL.e (abcde)	→	VAL (abcde)
Transport			
UNLG	GLC.u (abcdef)	→	GLC.e (abcdef)
LABG	GLC.l (abcdef)	→	GLC.e (abcdef)
GLUT	GLC.e (abcdef)	→	GLC.c (abcdef)
LIPS	8*AcCoA.C	↔	PALM
MCT	LAC (abc)	→	LAC.e (abc)

Table 5.B.3 Continued

Biosynthesis			
BIOM	90 ALA + 56.55 ARG + 43.2 ASN + 70.8 ASP + 21.75 CYS + 48.3 GLN + 57.9 GLU + 98.7 GLY + 48.6 ILE + 84.6 LEU + 64.5 SER + 62.4 VAL + 43.28 G6P + 34.95 R5P + 38.25 MEETHF + 34.95 CO2 + 18.26 DHAP + 49.14 AcCoA.c + 40.26 PALM	→	BIOMASS

Table 5.B.4 Net Fluxes Determined by ^{13}C INST-MFA for High Myc Normoxic Cells. Values have units of nmol/10^6 cells/h. Estimated flux values and 95% confidence bounds are shown.

Reaction		*Value*	*LB95*	*UB95*
Glycolysis				
HK	GLC.C → G6P	148.86	134.49	166.19
PGI	G6P ↔ F6P	147.08	132.83	164.43
PFK	F6P → FBP	146.32	131.97	163.38
ALDO	FBP ↔ DHAP + GAP	146.32	131.97	163.38
TPI	DHAP ↔ GAP	145.64	131.26	162.99
GAPDH	GAP ↔ 3PG	291.58	263.03	326.48
ENO	3PG ↔ PEP	290.16	261.46	324.91
PK	PEP → PYR.C	290.16	261.46	324.91
LDH	PYR.C ↔ LAC	221.95	197.72	244.92
Pentose Phosphate Pathway				
G6PDH	G6P → RU5P + CO2	0.17	0.05	4.68
R5PE	RU5P ↔ R5P	-0.76	-0.86	2.28
R5PI	RU5P ↔ X5P	0.92	0.84	2.43
TK1	X5P ↔ GAP + EC2	-0.76	-0.86	2.28
TK2	F6P ↔ E4P + EC2	0.38	-1.14	0.43
TK3	S7P ↔ R5P + EC2	0.38	-1.14	0.43
TA1	F6P ↔ GAP + EC3	0.38	-1.14	0.43
TA2	S7P ↔ E4P + EC3	-0.38	-0.43	1.14
TCA Cycle				
PYRT	PYR.C ↔ PYR.M	62.46	40.93	97.85
PDH	PYR.M → AcCoA + CO2	62.57	40.26	97.62
CS	OAA + AcCoA → CIT	67.94	45.03	103.47
IDH	CIT ↔ AKG + CO2	54.11	30.87	89.80
ADH	AKG → SUC + CO2	58.96	33.97	95.86
SUDH	SUC ↔ FUM	63.10	38.04	100.30
FUMS	FUM ↔ MAL	63.10	38.04	100.30
MDH	MAL ↔ OAA	73.78	49.51	109.29
Amphibolic reactions				
ME	MAL → PYR.M + CO2	3.14	1.29	9.27
PYC	PYR.M + CO2 → OAA	3.03	0.93	7.22
ACL	CIT → AcCoA.C + MAL	13.83	12.69	15.06

Table 5.B.4 Continued

Reaction		*Value*	*LB95*	*UB95*
Amino Acid Metabolism				
GDH	AKG ↔ GLU	-4.85	-10.59	0.05
GLS	GLN ↔ GLU	11.98	6.82	17.73
AST	OAA ↔ ASP	8.87	5.29	12.57
ASNS	ASP ↔ ASN	8.87	5.29	12.57
PST	3PG → SER	1.42	0.85	2.31
SHT	SER ↔ GLY + MEETHF	3.43	2.79	4.06
CYST	SER ↔ CYS	0.01	0.00	0.74
GLYS	CO2 + MEETHF → GLY	2.00	1.39	2.62
ALT	PYR.C ↔ ALA	5.76	4.30	7.30
BAA1	ILE + CO2 → SUC + AcCoA + CO2	3.08	1.14	4.90
BAA2	LEU + CO2 → 3AcCoA + CO2	0.76	0.00	2.76
BAA3	VAL → SUC + CO2	1.05	0.10	1.92
ALAR	ALA → ALA.E	2.41	0.97	3.88
ASNR	ASN.E → ASN	7.26	3.66	10.90
CYSR	CYS.E → CYS	0.80	0.04	1.45
GLUR	GLU → GLU.E	4.97	3.34	6.77
GLNR	GLN.E → GLN	13.78	8.99	19.42
GLYR	GLY → GLY.E	1.76	0.53	2.98
ILER	ILE.E → ILE	4.89	2.93	6.70
LEUR	LEU.E → LEU	3.91	2.93	5.92
SERR	SER.E → SER	4.48	3.47	5.38
VALR	VAL.E → VAL	3.38	2.50	4.21
Transport				
GLUT	GLC.E → GLC.C	148.86	134.49	166.19
PALM	AcCoA.C → Palmitate	1.50	1.38	1.63
MCT	LAC → LAC.E	221.95	197.72	244.92
Biosynthesis				
BIOM	Biomass Synthesis	0.0373	0.0342	0.0406

Table 5.B.5 Exchange Fluxes Determined by ^{13}C INST-MFA for High Myc Normoxic Cells. Values have units of nmol/10^6 cells/h. Estimated flux values and 95% confidence bounds are shown.

Reaction		*Value*	*LB95*	*UB95*
Glycolysis				
PGI	G6P ↔ F6P	0.00	0.00	Inf
ALDO	FBP ↔ DHAP + GAP	14.87	0.00	Inf
TPI	DHAP ↔ GAP	29830.00	0.00	Inf
GAPDH	GAP ↔ 3PG	55.40	0.00	Inf
ENO	3PG ↔ PEP	210.76	0.00	Inf
LDH	PYR.C ↔ LAC	0.00	0.00	Inf
Pentose Phosphate Pathway				
R5PE	RU5P ↔ R5P	30425.00	0.00	Inf
R5PI	RU5P ↔ X5P	0.00	0.00	20.09
TK1	X5P ↔ GAP + EC2	0.00	0.00	23.40
TK2	F6P ↔ E4P + EC2	28.76	5.98	255.55
TK3	S7P ↔ R5P + EC2	0.06	0.00	4.26
TA1	F6P ↔ GAP + EC3	98.11	58.02	180.52
TA2	S7P ↔ E4P + EC3	683.52	0.00	Inf
TCA Cycle				
PYRT	PYR.C ↔ PYR.M	0.00	0.00	259.62
IDH	CIT ↔ AKG + CO2	91.96	47.21	168.00
SUDH	SUC ↔ FUM	346.19	0.00	Inf
FUMS	FUM ↔ MAL	2437.30	0.00	Inf
MDH	MAL ↔ OAA	190.97	0.00	Inf
Amino Acid Metabolism				
PALM	8*AcCoA.c ↔ PALM	0.00	0.00	0.17
GDH	AKG ↔ GLU	9.93	5.05	23.73
GLS	GLN ↔ GLU	31.16	4.80	117.68
AST	OAA ↔ ASP	0.00	0.00	26.34
ASNS	ASP ↔ ASN	29.30	13.74	Inf
SHT	SER ↔ GLY + MEETHF	11.54	6.27	21.33
CYST	SER ↔ CYS	0.00	0.00	Inf
ALT	PYR.C ↔ ALA	153.03	67.75	272.00

Table 5.B.6 Pool Sizes Determined by ^{13}C INST-MFA for High Myc Normoxic Cells. Values shown have units of nmol/10^6 cells. Estimated pool size and 95% confidence interval are shown. Only identifiable pool sizes are shown.

Pool	*Value*	*LB95*	*UB95*
3PG	0.00	0.00	59.71
AcCoA	0.00	0.00	12.05
AcCoA.c	0.00	0.00	2.27
Ala	18845.00	10057.00	27912.00
Asp	183.08	0.00	985.23
Cit	0.00	0.00	25.53
DHAP	0.00	0.00	46.40
E4P	0.00	0.00	1599.30
EC2	0.00	0.00	305.80
EC3	851.70	23.44	2285.00
F6P	0.00	0.00	32.03
FBP	0.00	0.00	24.46
Fum	0.00	0.00	312.12
G6P	0.00	0.00	25.33
GAP	0.00	0.00	48.63
Glc.c	0.00	0.00	24.29
Glc.e	5.94	3.13	7.81
Gln	816.94	211.22	2968.90
Glu	83.60	0.00	378.62
Gly	124.01	0.00	316.32
MEETHF	96.32	0.00	471.99
Mal	0.00	0.00	267.46
OAA	0.01	0.00	263.76
PEP	0.00	0.00	53.28
Palm	166.04	152.01	189.13
Pyr.c	0.00	0.00	78.42
Pyr.m	0.00	0.00	14.97
R5P	14.48	1.88	125.82
Ru5P	0.00	0.00	275.40
S7P	1004.60	314.37	1628.90
Ser	782.93	380.30	1447.50
Suc	0.00	0.00	249.29
X5P	3.13	1.01	283.74
aKG	1642.30	845.68	2945.90

Table 5.B.7 Net Fluxes Determined by ^{13}C INST-MFA for High Myc Hypoxic Cells. Values have units of nmol/10^6 cells/h. Estimated flux values and 95% confidence bounds are shown.

Reaction		*Value*	*LB95*	*UB95*
Glycolysis				
HK	GLC.C → G6P	176.26	163.21	194.61
PGI	G6P ↔ F6P	174.97	161.95	193.34
PFK	F6P → FBP	174.63	161.64	193.09
ALDO	FBP ↔ DHAP + GAP	174.63	161.64	193.09
TPI	DHAP ↔ GAP	174.21	161.23	192.65
GAPDH	GAP ↔ 3PG	348.67	322.74	384.23
ENO	3PG ↔ PEP	347.77	321.89	384.62
PK	PEP → PYR.C	347.77	321.89	384.62
LDH	PYR.C ↔ LAC	330.13	304.43	354.21
Pentose Phosphate Pathway				
G6PDH	G6P → RU5P + CO2	0.30	0.01	6.92
R5PE	RU5P ↔ R5P	-0.34	-0.55	4.03
R5PI	RU5P ↔ X5P	0.64	0.50	2.85
TK1	X5P ↔ GAP + EC2	-0.34	-0.55	4.03
TK2	F6P ↔ E4P + EC2	0.17	-2.02	0.28
TK3	S7P ↔ R5P + EC2	0.17	-2.02	0.28
TA1	F6P ↔ GAP + EC3	0.17	-2.02	0.28
TA2	S7P ↔ E4P + EC3	-0.17	-0.28	2.02
TCA Cycle				
PYRT	PYR.C ↔ PYR.M	12.55	0.27	54.89
PDH	PYR.M → AcCoA + CO2	10.26	3.25	51.05
CS	OAA + AcCoA → CIT	11.05	4.05	54.14
IDH	CIT ↔ AKG + CO2	2.50	-4.50	45.57
ADH	AKG → SUC + CO2	5.30	0.32	49.15
SUDH	SUC ↔ FUM	6.09	0.72	49.72
FUMS	FUM ↔ MAL	6.09	0.72	49.72
MDH	MAL ↔ OAA	14.51	-64.81	51.84
Amphibolic reactions				
ME	MAL → PYR.M + CO2	0.14	0.00	107.60
PYC	PYR.M + CO2 → OAA	2.42	0.21	108.72
ACL	CIT → AcCoA.C + MAL	8.55	7.38	9.71

Table 5.B.7 Continued

Reaction		*Value*	*LB95*	*UB95*
Amino Acid Metabolism				
GDH	AKG ↔ GLU	-2.80	-7.81	1.89
ARS	ARG → GLU	3.59	1.17	6.05
GLS	GLN ↔ GLU	2.92	-1.13	7.16
AST	OAA ↔ ASP	5.88	1.43	10.08
ASNS	ASP ↔ ASN	5.88	1.43	10.08
PST	3PG → SER	0.90	0.20	1.87
SHT	SER ↔ GLY + MEETHF	2.02	1.58	2.46
CYST	SER ↔ CYS	-0.21	-0.63	0.22
GLYS	CO2 + MEETHF → GLY	1.14	0.73	1.54
ALT	PYR.C ↔ ALA	5.09	4.31	5.87
BAA1	ILE + CO2 → SUC + AcCoA + CO2	0.79	0.00	1.78
BAA2	LEU + CO2 → 3AcCoA + CO2	0.00	0.00	1.01
ALAR	ALA → ALA.E	3.02	2.29	3.75
ARGR	ARG.E → ARG	3.59	1.17	6.05
ASNR	ASN.E → ASN	4.88	0.47	9.08
CYSR	CYS.E → CYS	0.71	0.29	1.14
GLUR	GLU → GLU.E	2.38	1.47	3.30
GLNR	GLN.E → GLN	4.04	0.00	8.28
GLYR	GLY → GLY.E	0.88	0.08	1.67
ILER	ILE.E → ILE	1.91	1.05	2.89
LEUR	LEU.E → LEU	1.95	1.69	2.90
SERR	SER.E → SER	2.43	1.72	3.14
Transport				
GLUT	GLC.E → GLC.C	176.26	163.21	194.61
PALM	AcCoA.C → Palmitate	0.93	0.80	1.05
MCT	LAC → LAC.E	330.13	304.43	354.21
Biosynthesis				
BIOM	Biomass Synthesis	0.023	0.0199	0.0262

Table 5.B.8 Exchange Fluxes Determined by ^{13}C INST-MFA for High Myc Hypoxic Cells. Values have units of nmol/10^6 cells/h. Estimated flux values and 95% confidence bounds are shown.

Reaction		*Value*	*LB95*	*UB95*
Glycolysis				
PGI	G6P ↔ F6P	270.92	0.00	Inf
ALDO	FBP ↔ DHAP + GAP	0.00	0.00	Inf
TPI	DHAP ↔ GAP	0.00	0.00	Inf
GAPDH	GAP ↔ 3PG	43.13	0.00	Inf
ENO	3PG ↔ PEP	369.98	0.00	Inf
LDH	PYR.C ↔ LAC	1384.90	445.68	29783.00
Pentose Phosphate Pathway				
R5PE	RU5P ↔ R5P	104.37	0.00	Inf
R5PI	RU5P ↔ X5P	426.95	0.00	Inf
TK1	X5P ↔ GAP + EC2	0.07	0.00	Inf
TK2	F6P ↔ E4P + EC2	377.63	37.92	Inf
TK3	S7P ↔ R5P + EC2	0.03	0.00	Inf
TA1	F6P ↔ GAP + EC3	2351.80	28.96	Inf
TA2	S7P ↔ E4P + EC3	0.00	0.00	14.42
TCA Cycle				
PYRT	PYR.C ↔ PYR.M	1444.80	0.00	Inf
IDH	CIT ↔ AKG + CO2	48.10	0.00	Inf
SUDH	SUC ↔ FUM	5.57	0.00	Inf
FUMS	FUM ↔ MAL	5622.00	1.88	Inf
MDH	MAL ↔ OAA	49.51	0.00	Inf
Amino Acid Metabolism				
PALM	8*AcCoA.c ↔ PALM	0.00	0.00	2.67
GDH	AKG ↔ GLU	33.10	0.41	Inf
GLS	GLN ↔ GLU	193.46	10.07	Inf
AST	OAA ↔ ASP	0.00	0.00	Inf
ASNS	ASP ↔ ASN	22.86	0.00	Inf
SHT	SER ↔ GLY + MEETHF	13.56	3.33	43.51
CYST	SER ↔ CYS	4.38	0.00	Inf
ALT	PYR.C ↔ ALA	0.00	0.00	145.62

Table 5.B.9 Pool Sizes Determined by ^{13}C INST-MFA for High Myc Hypoxic Cells. Values shown have units of nmol/10^6 cells. Estimated pool size and 95% confidence interval are shown. Only identifiable pool sizes are shown.

Pool	*Value*	*LB95*	*UB95*
3PG	0.09	0.00	1556.10
AcCoA	0.00	0.00	19.06
AcCoA.c	0.00	0.00	16.24
Ala	238.97	168.28	5958.40
Asp	1.78	0.00	17893.00
Cit	0.00	0.00	53.60
DHAP	0.10	0.00	854.45
E4P	0.01	0.00	908.76
EC2	421.10	8.88	844.51
EC3	0.17	0.00	1766.10
F6P	0.00	0.00	521.90
FBP	0.00	0.00	435.76
Fum	5.55	0.00	20007.00
G6P	0.02	0.00	532.51
GAP	0.03	0.00	869.38
Glc.c	0.03	0.00	450.97
Glc.e	6.02	0.00	8.95
Gln	10038.00	0.00	88824.00
Glu	0.33	0.00	8708.80
Gly	203.08	0.00	666.71
Lac	13152.00	2727.20	29330.00
MEETHF	53.91	0.00	8713.00
Mal	6.26	0.00	19981.00
OAA	167.79	0.00	17391.00
PEP	0.07	0.00	1557.80
Palm	360.77	298.51	1358.10
Pyr.c	0.44	0.00	3265.70
Pyr.m	0.07	0.00	3243.30
R5P	2.94	0.00	470.70
Ru5P	19.07	0.00	487.26
Ser	758.98	122.54	1841.10
Suc	184.33	0.00	45338.00
X5P	0.18	0.00	505.93
aKG	0.01	0.00	7213.80

Table 5.B.10 Net Fluxes Determined by ^{13}C INST-MFA for Low Myc Normoxic Cells. Values have units of nmol/10^6 cells/h. Estimated flux values and 95% confidence bounds are shown.

Reaction		*Value*	*LB95*	*UB95*
Glycolysis				
HK	GLC.C → G6P	104.01	94.94	115.02
PGI	G6P ↔ F6P	101.88	92.81	112.76
PFK	F6P → FBP	101.87	92.83	112.76
ALDO	FBP ↔ DHAP + GAP	101.87	92.83	112.76
TPI	DHAP ↔ GAP	101.37	92.18	112.23
GAPDH	GAP ↔ 3PG	203.23	185.08	225.03
ENO	3PG ↔ PEP	202.30	184.22	224.23
PK	PEP → PYR.C	202.30	184.22	224.23
LDH	PYR.C ↔ LAC	179.45	162.27	196.21
Pentose Phosphate Pathway				
G6PDH	G6P → RU5P + CO2	0.94	0.00	5.69
R5PE	RU5P ↔ R5P	-0.01	-0.68	3.33
R5PI	RU5P ↔ X5P	0.95	0.60	2.51
TK1	X5P ↔ GAP + EC2	-0.01	-0.68	3.33
TK2	F6P ↔ E4P + EC2	0.01	-1.67	0.34
TK3	S7P ↔ R5P + EC2	0.01	-1.67	0.34
TA1	F6P ↔ GAP + EC3	0.01	-1.67	0.34
TA2	S7P ↔ E4P + EC3	-0.01	-0.34	1.67
TCA Cycle				
PYRT	PYR.C ↔ PYR.M	19.64	11.95	42.10
PDH	PYR.M → AcCoA + CO2	22.82	14.08	45.29
CS	OAA + AcCoA → CIT	25.34	15.87	49.67
IDH	CIT ↔ AKG + CO2	15.15	5.48	39.60
ADH	AKG → SUC + CO2	17.81	4.97	42.90
SUDH	SUC ↔ FUM	19.48	6.25	44.97
FUMS	FUM ↔ MAL	19.48	6.25	44.97
MDH	MAL ↔ OAA	25.41	16.42	48.62
Amphibolic reactions				
ME	MAL → PYR.M + CO2	4.26	0.00	10.79
PYC	PYR.M + CO2 → OAA	1.08	0.31	3.90
ACL	CIT → AcCoA.C + MAL	10.19	9.29	11.13

Table 5.B.10 Continued

Reaction		*Value*	*LB95*	*UB95*
Amino Acid Metabolism				
GDH	AKG ⇔ GLU	-2.65	-7.88	1.52
ARS	ARG → GLU	0.12	0.00	3.50
GLS	GLN ⇔ GLU	9.47	5.76	13.39
AST	OAA ⇔ ASP	1.15	-2.18	1.26
ASNS	ASP ⇔ ASN	1.15	-2.18	1.26
PST	3PG → SER	0.93	0.55	1.55
SHT	SER ⇔ GLY + MEETHF	1.88	1.57	2.05
CYST	SER ⇔ CYS	-1.10	-1.48	-0.72
GLYS	CO2 + MEETHF → GLY	0.83	0.56	0.91
ALT	PYR.C ⇔ ALA	3.21	2.45	3.98
BAA1	ILE + CO2 → SUC + AcCoA + CO2	1.46	0.20	2.77
BAA2	LEU + CO2 → 3AcCoA + CO2	0.35	0.00	1.54
BAA3	VAL → SUC + CO2	0.21	0.00	0.96
ALAR	ALA → ALA.E	0.74	0.01	1.47
ARGR	ARG.E → ARG	1.67	1.45	5.03
ASNR	ASN.E → ASN	0.04	0.00	3.37
CYSR	CYS.E → CYS	1.70	1.31	2.08
GLUR	GLU → GLU.E	5.35	3.24	7.42
GLNR	GLN.E → GLN	10.79	7.06	14.84
GLYR	GLY → GLY.E	0.00	0.00	0.53
ILER	ILE.E → ILE	2.80	1.50	4.12
LEUR	LEU.E → LEU	2.67	2.13	3.88
SERR	SER.E → SER	1.66	0.99	2.26
VALR	VAL.E → VAL	1.93	1.57	2.64
Transport				
GLUT	GLC.E → GLC.C	104.01	94.94	115.02
PALM	AcCoA.C → Palmitate	1.10	1.01	1.21
MCT	LAC → LAC.E	179.45	162.27	196.21
Biosynthesis				
BIOM	Biomass Synthesis	0.0274	0.025	0.0300

Table 5.B.11 Exchange Fluxes Determined by ^{13}C INST-MFA for Low Myc Normoxic Cells. Values have units of nmol/10^6 cells/h. Estimated flux values and 95% confidence bounds are shown.

Reaction		*Value*	*LB95*	*UB95*
Glycolysis				
PGI	G6P ↔ F6P	3141.10	0.00	Inf
ALDO	FBP ↔ DHAP + GAP	0.00	0.00	Inf
TPI	DHAP ↔ GAP	277.91	0.00	Inf
GAPDH	GAP ↔ 3PG	18.71	0.00	67.64
ENO	3PG ↔ PEP	4349.40	0.00	Inf
LDH	PYR.C ↔ LAC	269.73	66.92	777.34
Pentose Phosphate Pathway				
R5PE	RU5P ↔ R5P	18.36	0.20	Inf
R5PI	RU5P ↔ X5P	0.14	0.00	Inf
TK1	X5P ↔ GAP + EC2	10.30	0.20	Inf
TK2	F6P ↔ E4P + EC2	1.42	0.00	13.30
TK3	S7P ↔ R5P + EC2	0.21	0.00	Inf
TA1	F6P ↔ GAP + EC3	0.00	0.00	371.04
TA2	S7P ↔ E4P + EC3	6.44	0.00	Inf
TCA Cycle				
PYRT	PYR.C ↔ PYR.M	3322.90	0.00	Inf
IDH	CIT ↔ AKG + CO2	0.00	0.00	10.41
SUDH	SUC ↔ FUM	0.00	0.00	Inf
FUMS	FUM ↔ MAL	2548.10	4.18	Inf
MDH	MAL ↔ OAA	1092.50	0.00	Inf
Amino Acid Metabolism				
PALM	8*AcCoA.c ↔ PALM	0.00	0.00	0.08
GDH	AKG ↔ GLU	21.06	3.60	70.42
GLS	GLN ↔ GLU	30.41	4.98	111.72
AST	OAA ↔ ASP	0.00	0.00	41.39
ASNS	ASP ↔ ASN	3.43	1.10	118.85
SHT	SER ↔ GLY + MEETHF	8.15	4.00	16.26
CYST	SER ↔ CYS	0.00	0.00	Inf
ALT	PYR.C ↔ ALA	0.00	0.00	20.37

Table 5.B.12 Pool Sizes Determined by ^{13}C INST-MFA for Low Myc Normoxic Cells. Values shown have units of nmol/10^6 cells. Estimated pool size and 95% confidence interval are shown. Only identifiable pool sizes are shown.

Pool	*Value*	*LB95*	*UB95*
3PG	10111.00	6470.00	14243.00
AcCoA	0.01	0.00	60.26
AcCoA.c	0.00	0.00	92.79
Ala	321.65	232.27	2249.90
Asn	262.93	49.90	8023.30
Asp	0.00	0.00	160.31
Cit	0.01	0.00	41.15
DHAP	295.19	0.00	1684.70
E4P	95.64	0.00	648.86
EC2	3.32	0.00	120.24
F6P	55.10	0.00	570.65
FBP	11.87	0.00	636.65
Fum	0.02	0.00	73.79
G6P	3.40	0.00	723.42
GAP	0.00	0.00	1284.70
Glc.c	90.06	0.00	501.57
Glc.e	4.19	2.25	5.52
Gln	3990.60	493.03	18049.00
Glu	0.01	0.00	143.10
Gly	337.30	188.68	640.94
Lac	6374.80	2959.60	10726.00
MEETHF	146.65	0.00	760.20
Mal	0.02	0.00	81.21
OAA	0.02	0.00	77.76
PEP	0.00	0.00	14246.00
Palm	511.86	445.66	587.02
Pyr.c	0.35	0.00	1834.40
Pyr.m	0.22	0.00	1770.10
R5P	41.92	23.54	248.39
Ru5P	0.00	0.00	92.32
S7P	3.97	0.00	719.19
Ser	589.60	266.17	1156.10
Suc	0.24	0.00	81.69
X5P	0.05	0.00	117.68
aKG	0.00	0.00	62.04

Table 5.B.13 Net Fluxes Determined by ^{13}C INST-MFA for Low Myc Hypoxic Cells. Values have units of nmol/10^6 cells/h. Estimated flux values and 95% confidence bounds are shown.

Reaction		*Value*	*LB95*	*UB95*
Glycolysis				
HK	GLC.C → G6P	217.72	201.27	240.08
PGI	G6P ↔ F6P	216.59	200.16	238.90
PFK	F6P → FBP	216.72	200.29	239.12
ALDO	FBP ↔ DHAP + GAP	216.72	200.29	239.12
TPI	DHAP ↔ GAP	216.50	200.09	238.88
GAPDH	GAP ↔ 3PG	433.28	400.42	478.02
ENO	3PG ↔ PEP	433.22	400.33	478.14
PK	PEP → PYR.C	433.22	400.33	478.14
LDH	PYR.C ↔ LAC	422.56	386.14	454.77
Pentose Phosphate Pathway				
G6PDH	G6P → RU5P + CO2	0.61	0.00	5.48
R5PE	RU5P ↔ R5P	0.13	-0.31	3.46
R5PI	RU5P ↔ X5P	0.48	0.25	2.10
TK1	X5P ↔ GAP + EC2	0.13	-0.31	3.46
TK2	F6P ↔ E4P + EC2	-0.06	-1.73	0.15
TK3	S7P ↔ R5P + EC2	-0.06	-1.73	0.15
TA1	F6P ↔ GAP + EC3	-0.06	-1.73	0.15
TA2	S7P ↔ E4P + EC3	0.06	-0.15	1.73
TCA Cycle				
PYRT	PYR.C ↔ PYR.M	7.93	-3.00	64.29
PDH	PYR.M → AcCoA + CO2	8.68	1.56	64.29
CS	OAA + AcCoA → CIT	10.96	5.50	66.34
IDH	CIT ↔ AKG + CO2	6.49	1.24	61.86
ADH	AKG → SUC + CO2	2.57	0.34	57.97
SUDH	SUC ↔ FUM	3.42	0.38	58.69
FUMS	FUM ↔ MAL	3.42	0.38	58.69
MDH	MAL ↔ OAA	-0.23	-135.17	22.10
Amphibolic reactions				
ME	MAL → PYR.M + CO2	8.11	0.00	175.72
PYC	PYR.M + CO2 → OAA	7.37	0.45	176.41
ACL	CIT → AcCoA.C + MAL	4.47	3.75	5.18

Table 5.B.13 Continued

Reaction		*Value*	*LB95*	*UB95*
Amino Acid Metabolism				
GDH	AKG ⇔ GLU	3.92	-1.60	10.68
ARS	ARG → GLU	2.11	-2.49	6.24
GLS	GLN ⇔ GLU	2.02	-0.66	6.54
AST	OAA ⇔ ASP	-3.82	-8.15	0.54
ASNS	ASP ⇔ ASN	-2.10	-5.88	0.58
PST	3PG → SER	0.07	0.03	0.30
SHT	SER ⇔ GLY + MEETHF	1.85	1.40	2.32
CYST	SER ⇔ CYS	-2.36	-2.82	-1.88
GLYS	CO2 + MEETHF → GLY	1.39	0.95	1.85
ALT	PYR.C ⇔ ALA	2.73	2.05	3.42
BAA1	ILE + CO2 → SUC + AcCoA + CO2	0.71	0.00	2.12
BAA2	LEU + CO2 → 3AcCoA + CO2	0.52	0.00	1.90
BAA3	VAL → SUC + CO2	0.13	0.00	0.87
ALAR	ALA → ALA.E	1.65	0.99	2.31
ARGR	ARG.E → ARG	2.79	-1.80	6.94
ASNR	ASN.E → ASN	2.62	0.00	6.40
ASPR	ASP.E → ASP	2.58	0.25	4.88
CYSR	CYS.E → CYS	2.62	2.14	3.09
GLUR	GLU → GLU.E	7.35	5.89	8.82
GLNR	GLN.E → GLN	2.60	0.00	7.14
GLYR	GLY → GLY.E	2.05	1.15	2.98
ILER	ILE.E → ILE	1.30	0.51	2.71
LEUR	LEU.E → LEU	1.54	0.87	2.91
SERR	SER.E → SER	0.22	0.00	0.85
VALR	VAL.E → VAL	0.88	0.64	1.61
Transport				
GLUT	GLC.E → GLC.C	217.72	201.27	240.08
PALM	AcCoA.C → Palmitate	0.48	0.41	0.56
MCT	LAC → LAC.E	422.56	386.14	454.77
Biosynthesis				
BIOM	Biomass Synthesis	0.0120	0.0101	0.0140

Table 5.B.14 Exchange Fluxes Determined by ^{13}C INST-MFA for Low Myc Hypoxic Cells. Values have units of nmol/10^6 cells/h. Estimated flux values and 95% confidence bounds are shown.

Reaction		*Value*	*LB95*	*UB95*
Glycolysis				
PGI	G6P ↔ F6P	127900.00	0.00	Inf
ALDO	FBP ↔ DHAP + GAP	0.00	0.00	Inf
TPI	DHAP ↔ GAP	15214.00	0.00	Inf
GAPDH	GAP ↔ 3PG	0.00	0.00	Inf
ENO	3PG ↔ PEP	294.22	0.00	Inf
LDH	PYR.C ↔ LAC	5926.80	0.00	20459.00
Pentose Phosphate Pathway				
R5PE	RU5P ↔ R5P	1.62	0.16	Inf
R5PI	RU5P ↔ X5P	2485.30	0.00	Inf
TK1	X5P ↔ GAP + EC2	17.49	0.16	Inf
TK2	F6P ↔ E4P + EC2	7.18	0.31	91.38
TK3	S7P ↔ R5P + EC2	0.28	0.04	Inf
TA1	F6P ↔ GAP + EC3	102260.00	776.11	Inf
TA2	S7P ↔ E4P + EC3	31.36	0.03	Inf
TCA Cycle				
PYRT	PYR.C ↔ PYR.M	0.00	0.00	61.00
IDH	CIT ↔ AKG + CO2	0.00	0.00	Inf
SUDH	SUC ↔ FUM	4.36	0.00	Inf
FUMS	FUM ↔ MAL	75.68	5.31	Inf
MDH	MAL ↔ OAA	13159.00	6.38	Inf
Amino Acid Metabolism				
PALM	8*AcCoA.c ↔ PALM	0.00	0.00	Inf
GDH	AKG ↔ GLU	0.00	0.00	349.16
GLS	GLN ↔ GLU	30.45	0.00	533.30
AST	OAA ↔ ASP	15.41	0.40	Inf
ASNS	ASP ↔ ASN	0.00	0.00	Inf
SHT	SER ↔ GLY + MEETHF	0.55	0.00	13.10
CYST	SER ↔ CYS	0.00	0.00	Inf
ALT	PYR.C ↔ ALA	0.00	0.00	65.85

Table 5.B.15 Pool Sizes Determined by ^{13}C INST-MFA for Low Myc Hypoxic Cells. Values shown have units of nmol/10^6 cells. Estimated pool size and 95% confidence interval are shown. Only identifiable pool sizes are shown.

Pool	*Value*	*LB95*	*UB95*
3PG	0.62	0.00	7074.90
AcCoA	0.01	0.00	330.34
AcCoA.c	78197.00	20184.00	174560.00
Ala	590.47	392.04	13264.00
Asp	0.01	0.00	621.03
DHAP	0.00	0.00	571.09
EC2	0.48	0.00	2910.00
EC3	0.36	0.00	458.67
F6P	0.15	0.00	1526.40
FBP	0.01	0.00	1340.40
Fum	0.00	0.00	371.36
G6P	8.92	0.00	1527.30
GAP	0.46	0.00	2875.70
Glc.c	0.40	0.00	1516.30
Glc.e	8.77	5.04	11.40
Glu	0.06	0.00	2566.10
Gly	0.02	0.00	631.16
Lac	42303.00	11773.00	63688.00
Mal	0.00	0.00	380.12
OAA	0.00	0.00	363.90
PEP	0.65	0.00	7182.40
Palm	0.00	0.00	21826.00
Pyr.c	7.64	0.00	31877.00
Pyr.m	0.00	0.00	171.11
R5P	118.20	10.93	502.92
Ru5P	0.03	0.00	494.40
S7P	633.34	0.00	2633.50
Ser	430.38	85.62	2638.10
Suc	0.00	0.00	367.74
X5P	0.00	0.00	445.40
aKG	0.00	0.00	614.62

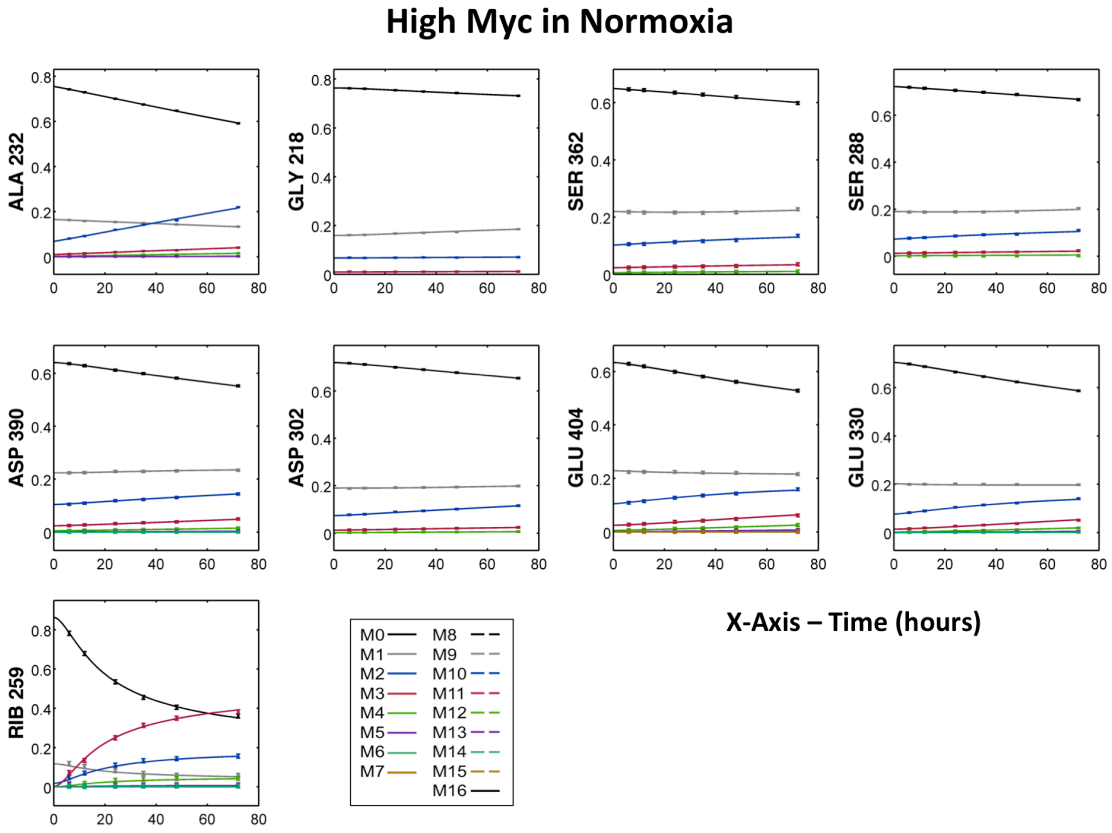

Figure 5.B.1 Dynamic Isotope Labeling Trajectories of Measured Metabolites in the High Myc Normoxic Condition. Experimentally determined (•) and INST-MFA fitted (−) mass isotopomer distributions for the **(A)** High Myc and **(B)** Low Myc conditions. Nominal masses of M0 mass isotopomers are shown next to the fragment abbreviation. Error bars represent standard measurement errors. Raw mass isotopomer data are shown without correction for natural isotope abundance.

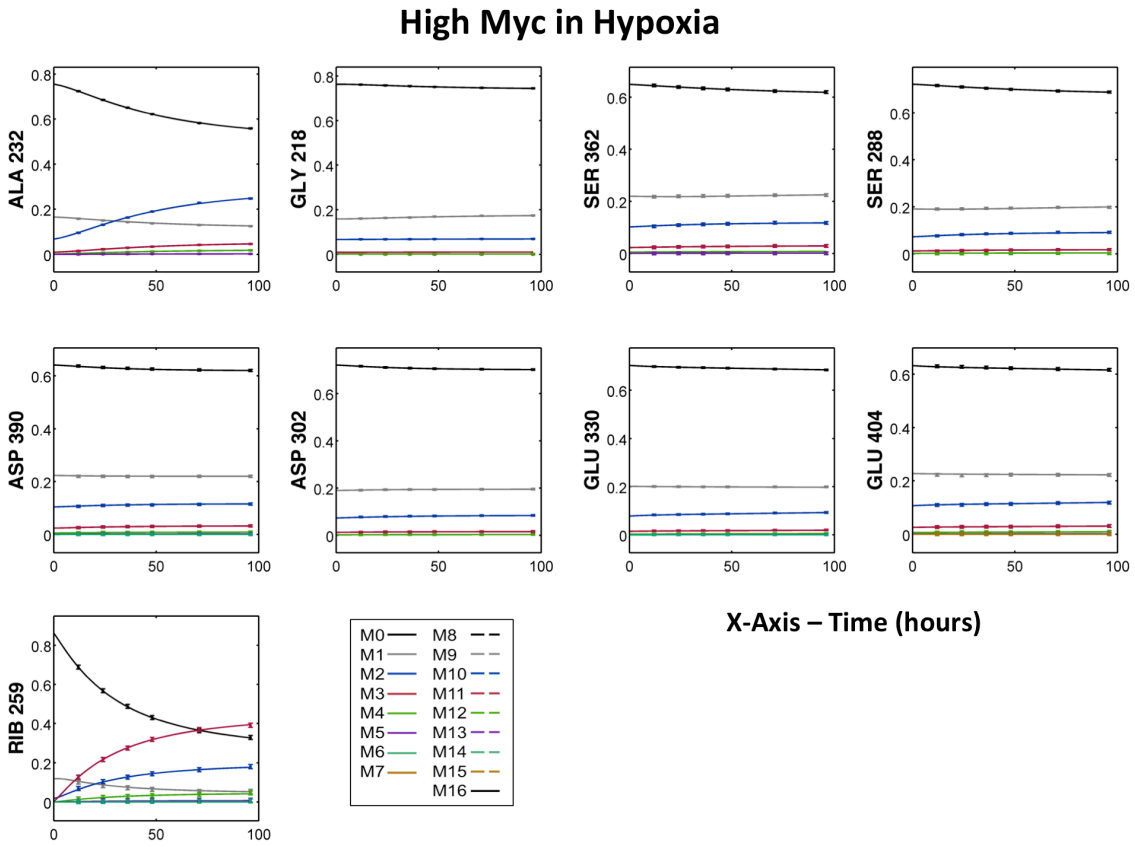

Figure 5.B.2 Dynamic Isotope Labeling Trajectories of Measured Metabolites in the High Myc Hypoxic Condition. Experimentally determined (•) and INST-MFA fitted (−) mass isotopomer distributions for the **(A)** High Myc and **(B)** Low Myc conditions. Nominal masses of M0 mass isotopomers are shown next to the fragment abbreviation. Error bars represent standard measurement errors. Raw mass isotopomer data are shown without correction for natural isotope abundance.

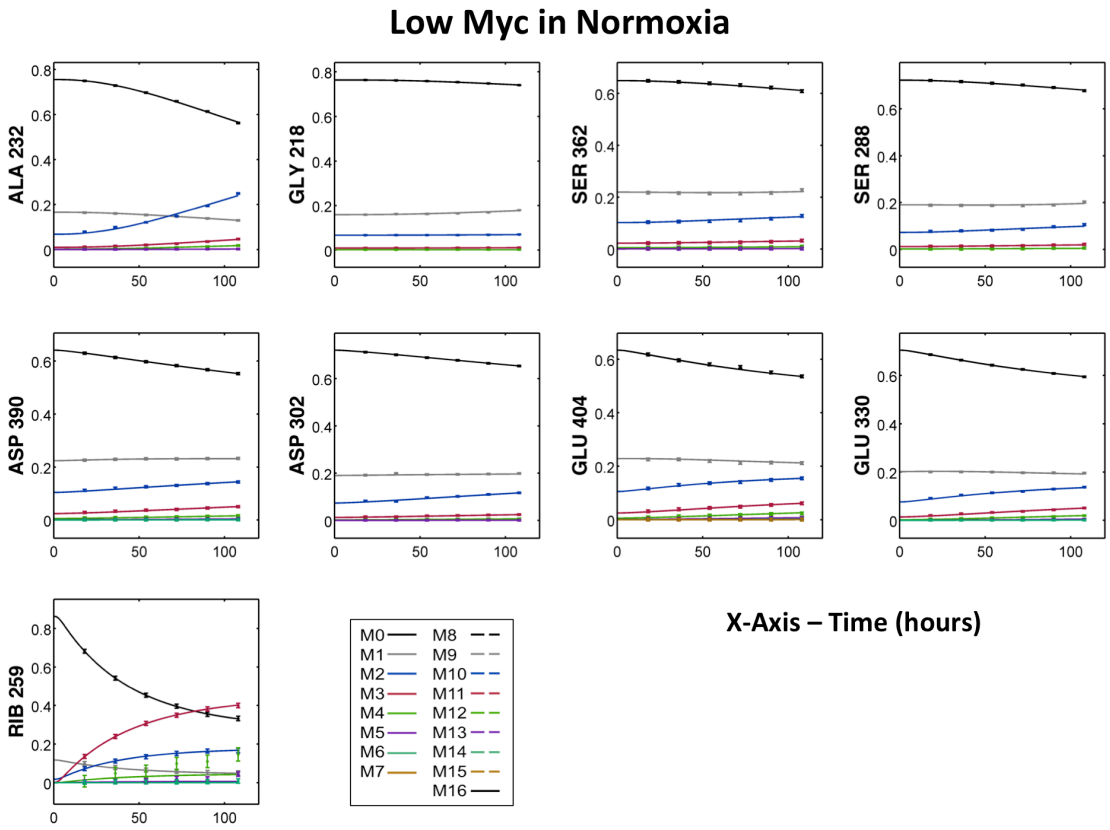

Figure 5.B.3 Dynamic Isotope Labeling Trajectories of Measured Metabolites in the Low Myc Normoxic Condition. Experimentally determined (•) and INST-MFA fitted (−) mass isotopomer distributions for the **(A)** High Myc and **(B)** Low Myc conditions. Nominal masses of M0 mass isotopomers are shown next to the fragment abbreviation. Error bars represent standard measurement errors. Raw mass isotopomer data are shown without correction for natural isotope abundance.

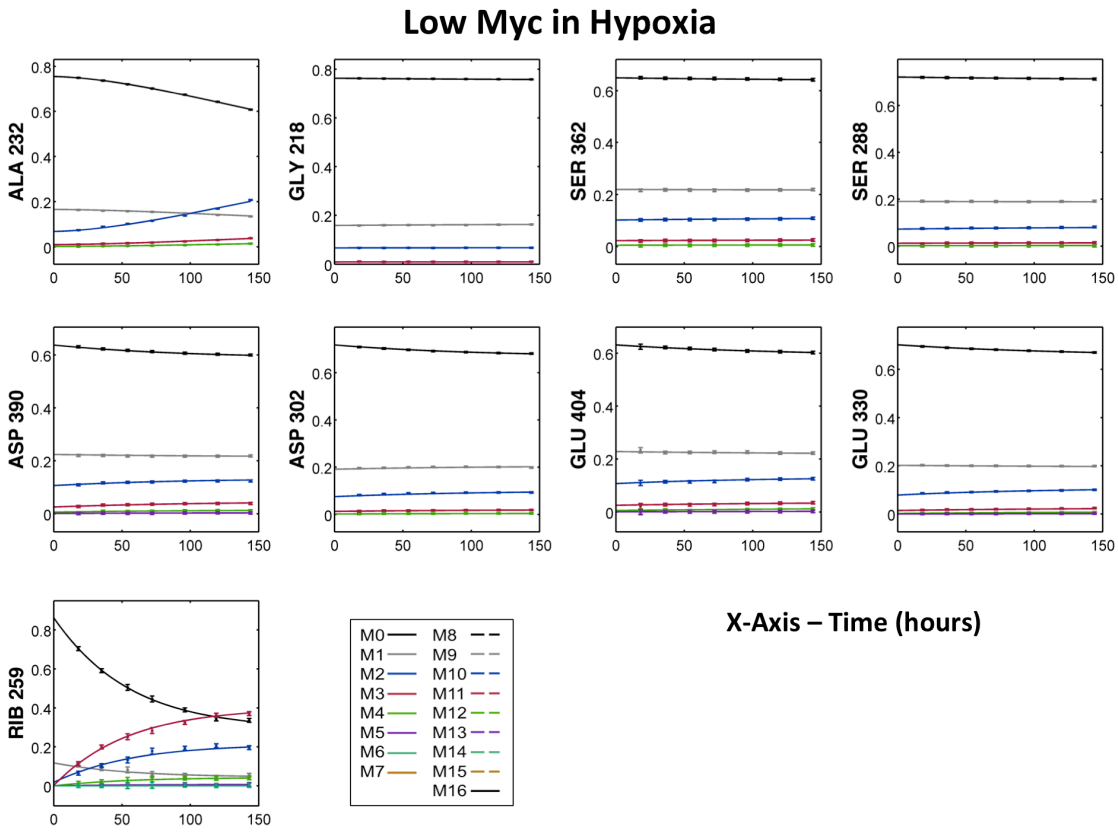

Figure 5.B.4 Dynamic Isotope Labeling Trajectories of Measured Metabolites in the Low Myc Hypoxic Condition. Experimentally determined (•) and INST-MFA fitted (−) mass isotopomer distributions for the **(A)** High Myc and **(B)** Low Myc conditions. Nominal masses of M0 mass isotopomers are shown next to the fragment abbreviation. Error bars represent standard measurement errors. Raw mass isotopomer data are shown without correction for natural isotope abundance.

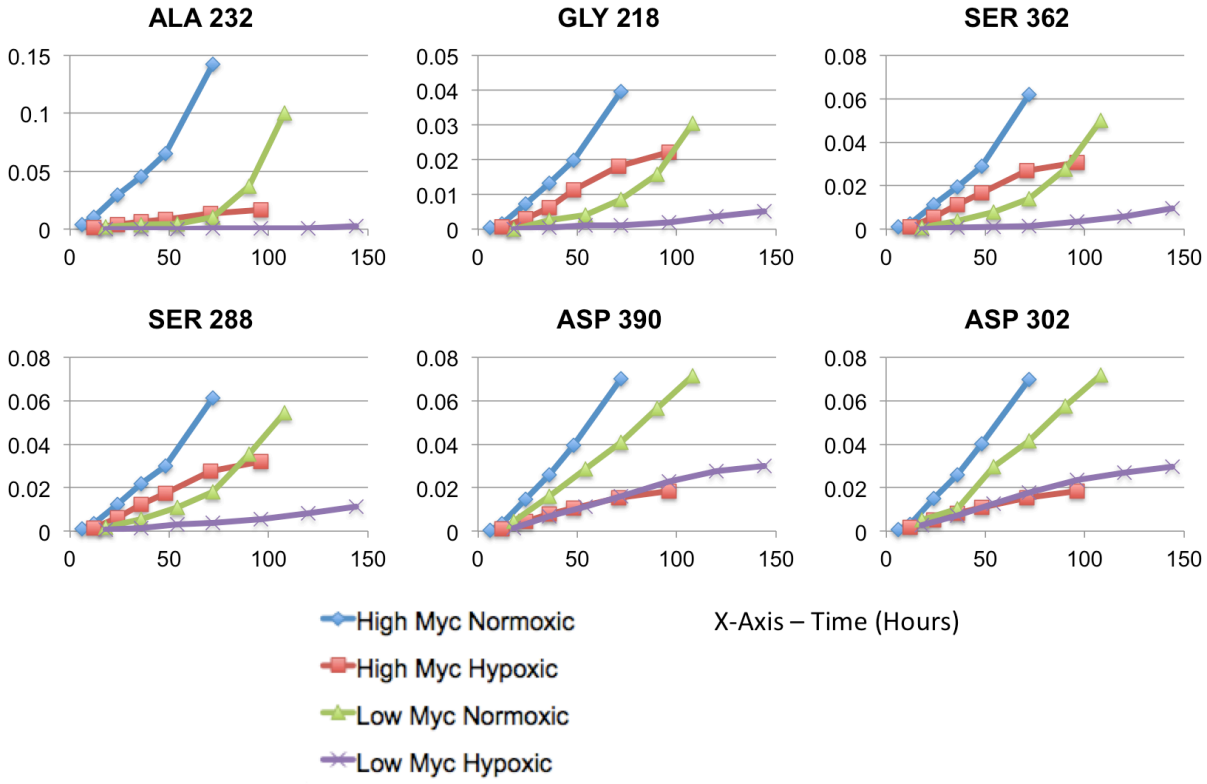

Figure 5.B.5 Atom Percent Enrichment (APE) of GC-MS Fragments Sampled. Fragments shown are for alanine (ALA), glycine (GLY), serine (SER), and aspartate (ASP). The atom percent enrichment represents the percentage of isotopically labeled carbons. The x-axis is time measured in hours.

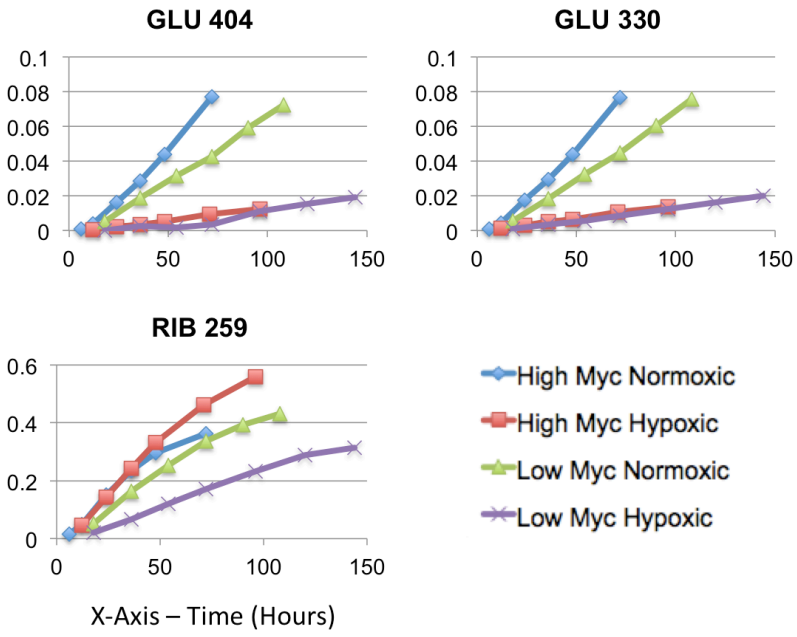

Figure 5.B.6 Atom Percent Enrichment (APE) of GC-MS Fragments Sampled. Fragments shown are for glutamate (GLU) and ribose (RIB). The atom percent enrichment represents the percentage of isotopically labeled carbons. The x-axis is time measured in hours.

APPENDIX 5.C - Abbreviations

3PG, 3-phosphoglycerate; **AcCoA**, Acetyl-Coenzyme A; **AcCoA.C**, cytosolic Acetyl-Coenzyme A; **ACL**, ATP-citrate lyase; **ADH**, α-ketoglutarate dehydrogenase; **AKG**, α-ketoglutarate; **ALA**, alanine; **ALA.E**, extracellular alanine; **ALAR**, alanine excretion rate; **ALDO**, aldolase; **ALT**, alanine transaminase; **ARG**, arginine; **ARG.E**, extracellular arginine; **ARGR**, arginine uptake rate; **ARGS**, arginase; **ASN.E**, extracellular asparagine; **ASNR**, asparagine uptake rate; **ASNS**, asparaginase; **ASP**, asparate; **AST**, aspartate transaminase; **BAA**, branched-chain amino acids; **BIOM**, biomass; **CIT**, citratre; **CO2,** carbon dioxide; **CS**, citrate synthase; **CYS**, cysteine; **CYS.E**, extracellular cysteine; **CYSR**, cysteine uptake rate; **CYST**, cystathionine synthase; **DHAP**, dihydroxyacetone phosphate; **E4P**, erythrose-4-phosphate; **EC2**, 2 enzyme-bound carbons; **EC3**, 3 enzyme-bound carbons; **ENO**, enolase; **F6P**, fructose-6-phosphate; **FBP**, fructose-1,6-bisphosphate; **FUM**, fumarate; **FUMS**, fumarase; **G6P**, glucose-6-phosphate; **G6PDH**, glucose-6-phosphate dehydrogenase;**GAP**, glyceraldehyde-3-phosphate; **GAPDH**, glyceraldehyde-3-phosphate dehydrogenase;**GDH**, glutamate dehydrogenase; **GLC.C**, cytosolic glucose; **GLC.E**, extracellular glucose; **GLN**, glutamine; **GLN.E**, extracellular glutamine; **GLNR**, glutamine uptake rate; **GLS**, glutaminase; **GLU**, glutamate; **GLU.E**, extracellular glutamate; **GLUR**, glutamate excretion rate; **GLUT**, glucose transport; **GLY**, glycine; **GLY.E**, extracellular glycine; **GLYR**, glycine excretion rate; **GLYS**, glycine synthase; **HK,** hexokinase; **IDH**, isocitrate dehydrogenase; **ILE**, isoleucine; **LABG**, labeled glucose; **LAC**, lactate; **LAC.E**, extracellular lactate; **LEU**, leucine; **LDH**, lactate dehydrogenase; **LIPS**, lipid sink; **MAL**, malate; **MCT**, monocarboxylate transporter; **MDH**, malate dehydrogenase; **ME**, malic enzyme; **MEETHF**, methylene tetrahydrofuran; **OAA**, oxaloacetate; **PALM**, palmitate; **PDH**, pyruvate dehydrogenase; **PEP**, phosphoenolpyruvate; **PFK**, phosphofructokinase; **PGI**, phosphoglucose isomerase; **PK**, pyruvate kinase;**PST**, serine transaminase;**PYC**, pyruvate carboxylase; **PYR.C**, cytosolic pyruvate; **PYR.M**, mitochondrial pyruvate; **PYRT**, pyruvate transport; **R5P**, ribose-5-phosphate; **R5PE**, ribulose-5-phosphate epimerase; **R5PI**, ribulose-5-phosphate isomerase; **RU5P**, ribulose-5-phosphate; **S7P**, sedoheptulose-7-phosphate; **SER**, serine; **SER.E**, extracellular serine; **SERR**, serine uptake rate; **SHT**, serine hydroxymethyl transferase; **SUC**, succinate; **SUDH**, succinate dehydrogenase; **TA1**, transaldolase 1; **TA2**, transaldolase 2; **TK1**, transketolase 1; **TK2**, transketolase 2; **TK3**, transketolase 3; **TPI**, triose phosphate isomerase; **UNLG**, unlabeled glucose; **VAL**, valine; **X5P**, xylulose-5-phosphate.

CHAPTER 6

TARGETED INHIBITION OF NORMOXIC HIGH AND LOW MYC CELLS USING SMALL-MOLECULE DRUGS

6.1 Introduction

Up to this point we have seen how metabolic flux analysis can be used to create quantitative maps of the intracellular flow of carbon through central metabolism. The true power of this analysis technique is in its ability to compare metabolic phenotypes with different genetic or environmental perturbations (Keibler et al., 2012). Because the fluxes are normalized to cell density, it is possible to compare disparate cell types for differences in metabolic activity (Niklas and Heinzle, 2012). In the previous chapters, the P493-6 B-cell line has served as a model of non-tumorigenic cell metabolism and Myc-driven cancer metabolism on an isogenic background. The only difference between the two states is the increased expression level of Myc, and any alterations can be directly (or indirectly) attributed to this increase (Pajic et al., 2000; Pajic et al., 2001).

In chapters 4 and 5, we saw how the different oncogenic and environmental states affect cell metabolism and discovered some key differences in metabolism that could potentially be exploited for therapeutic targeting. One of the big challenges in cancer therapeutics is specifically targeting cancerous cells versus normal cells (Kamb et al., 2007). Ideally, the chosen target would specifically inhibit the growth of the cancer while minimizing harm to normal tissue. What typically happens is some inhibition of the cancer with greater off-target side-effects (Kamb et al., 2007). Cancer is a subtle disease where normal processes are dysregulated, meaning it can be difficult to target specific pathways in the disease because many other cells in the body are using those same pathways, albeit in a more regulated manner. This altered regulation manifests in different metabolic phenotypes which can be revealed through flux analysis techniques.

The question then becomes, how do we go from flux maps to testing different therapeutic targets? Would it be better to target reactions that have a low flux because it can act as a pinch-point for the metabolism? Or does a larger flux magnitude indicate greater importance? A case could be made for targeting fluxes that have their rates either

increased or decreased, and there are no clear answers about which is the better option. Attempts at computational modeling of metabolism and drug effects have tried to answer this question but much is still unknown (Facchetti et al., 2012; Folger et al., 2011; Li et al., 2010).

Based on our previous flux data and prior research, we have chosen to target two aspects of cell metabolism: lactate formation and oxidative phosphorylation (OXPHOS). Previous studies on these cells have shown that inhibiting lactate dehydrogenase A (LDH-A) can be an effective method to target the High Myc phenotype (Dang, 2011; Le et al., 2010; Shim et al., 1997). We also observed an upregulation of lactate flux from Low to High Myc expression levels, meaning that High Myc cells could be more dependent on lactate secretion. Oxamate is a specific, competitive inhibitor of LDH-A, and we applied it to High and Low Myc cells at a variety of concentrations to understand its differential effects on growth and metabolism (Novoa et al., 1959; Pelicano et al., 2006; Ramanathan et al., 2005).

To target OXPHOS, we used phenformin, which is a more potent form of the anti-diabetic drug metformin (Caraci et al., 2003; Keibler et al., 2012). This drug was chosen for several reasons. First, several meta-analysis studies on diabetic patients taking metformin have shown a reduced incidence of cancer (Dowling et al., 2011; Evans et al., 2005; Niklas and Heinzle, 2012). Second, phenformin targets mitochondrial metabolism as a whole because it is an inhibitor of Complex I of the electron transport chain (Caraci et al., 2003; Pajic et al., 2000; Pajic et al., 2001). Since our data showed that High Myc cells have increased flux through the TCA cycle and a greater fraction of pyruvate going to mitochondrial oxidation, we chose to inhibit mitochondrial metabolism instead of a specific enzyme in the TCA cycle. Similar to oxamate, we applied varying concentrations of phenformin to understand its differential effects on High versus Low Myc cells.

Finally, we used both of these drugs in combination to test for synergistic effects of inhibiting two major bioenergetic pathways simultaneously. Metabolism has evolved to be robust in the face of perturbations, and in many cases cells are able to reroute metabolism to support growth when pathways become inhibited (Kamb et al., 2007; Vander Heiden et al., 2009). Understanding the interaction of drug combinations is an important aspect of research and shows promise in the clinic (Jia et al., 2009; Kamb et al., 2007). We hypothesized that the cells would

be able to overcome the inhibitory effect of a single drug by rerouting metabolism to alternate pathways. It would be logical to assume that in the presence of oxamate, a cell would shift its metabolism to a more oxidative phenotype while phenformin would force the cell to be more glycolytic. However, if both drugs were present simultaneously, they could potentially create a synergistic effect where the cell is unable to overcome the dual inhibition.

6.2 Methods

6.2.1 Cell Culture

Cells were maintained according to the method in section 3.2.7 of Chapter 3

6.2.2 Specific Rate Determination

Specific rates were determined according to the methods detailed in section 3.2 of Chapter 3.

6.2.3 Drug Treatment

Cells in culture were treated with sodium oxamate with the following concentrations: 1, 5, 10, 50, and 100 mM solutions. Treatment with phenformin hydrochloride was done at the following concentrations: 10, 25, 50, 100, 200, 400 μM. Drug combination treatments were done according to Figure 6.1. Concentrated stocks were made in RPMI 1640 medium, filtered in a 0.22 μm filter, and added to culture.

6.2.4 IC50 Estimation

IC50 values were determined by plotting the inhibition versus drug concentration, the latter on a logarithmic scale. A best-fit line was estimated using Microsoft Excel and the IC50 value was the point at which the line crossed the 50% inhibition mark.

6.2.5 Drug Combinatorial Effects

The combination index (i.e. synergy, antagonism, or additive) was calculated using the freely available CompuSyn software (ComboSyn Inc.). Briefly, this software uses equations derived from the mass-action law, which is based on models of enzyme kinetics and receptor binding theory (Chou and Talalay, 1984). The software fits the data to the median-effect principle and determines inhibition parameters (i.e., IC50) from the regression model.

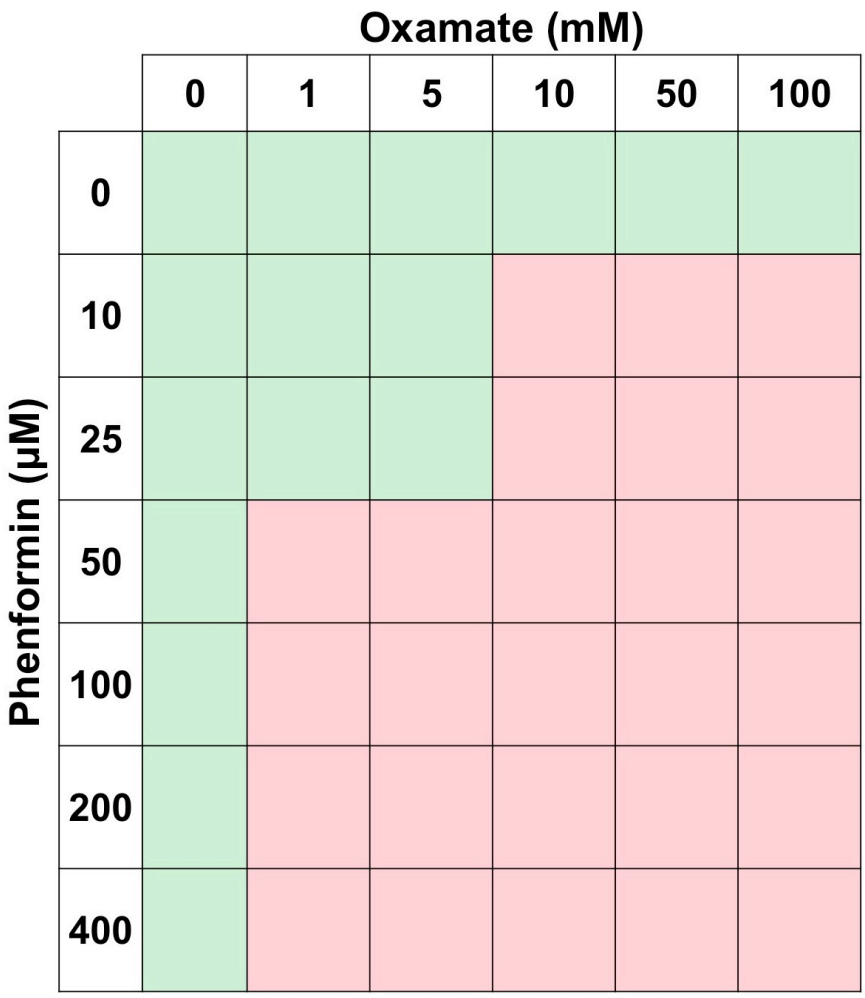

Figure 6.1 Design of Drug Inhibition Studies. P493-6 High and Low Myc cells were treated with varying concentrations of oxamate and phenformin. Green boxes indicate analyzed conditions while red indicates unanalyzed conditions.

6.3 Results

6.3.1 Treatment of High and Low Myc Cells with Oxamate

Oxamate is a potent inhibitor of the enzyme lactate dehydrogenase A (LDH-A) which converts pyruvate to lactate with concomitant conversion of NADH to NAD^+. Previous work has shown Myc to directly transactivate *LDHA*, and direct inhibition or knockdown of the enzyme has been shown to slow tumor growth (Facchetti et al., 2012; Folger et al., 2011; Le et al., 2010; Li et al., 2010; Shim et al., 1997). P493 cells treated with oxamate alone showed only slight growth inhibition up until 50 mM, at which point both High and Low Myc cells exhibited zero or negative growth (Figure 6.2). The IC50 concentration was estimated to be approximately 20 mM in High Myc cells and 24 mM in Low Myc cells. This indicates that High Myc cells were slightly more sensitive to the drug. However, only at the 50 mM concentration did we see a significant difference in growth rates with High Myc cells in a death phase while Low Myc were in a stationary phase. Normalized glucose and lactate fluxes responded similarly to oxamate treatments with no significant differences detected between High and Low Myc cells (Figure 6.2). We do see a dose-dependent decrease in lactate secretion, along with a commensurate decrease in glucose uptake, for both conditions indicating that oxamate is affecting LDH-A and there seems to be no difference in effectiveness. See figure 6.A.1 in Appendix A for absolute flux values.

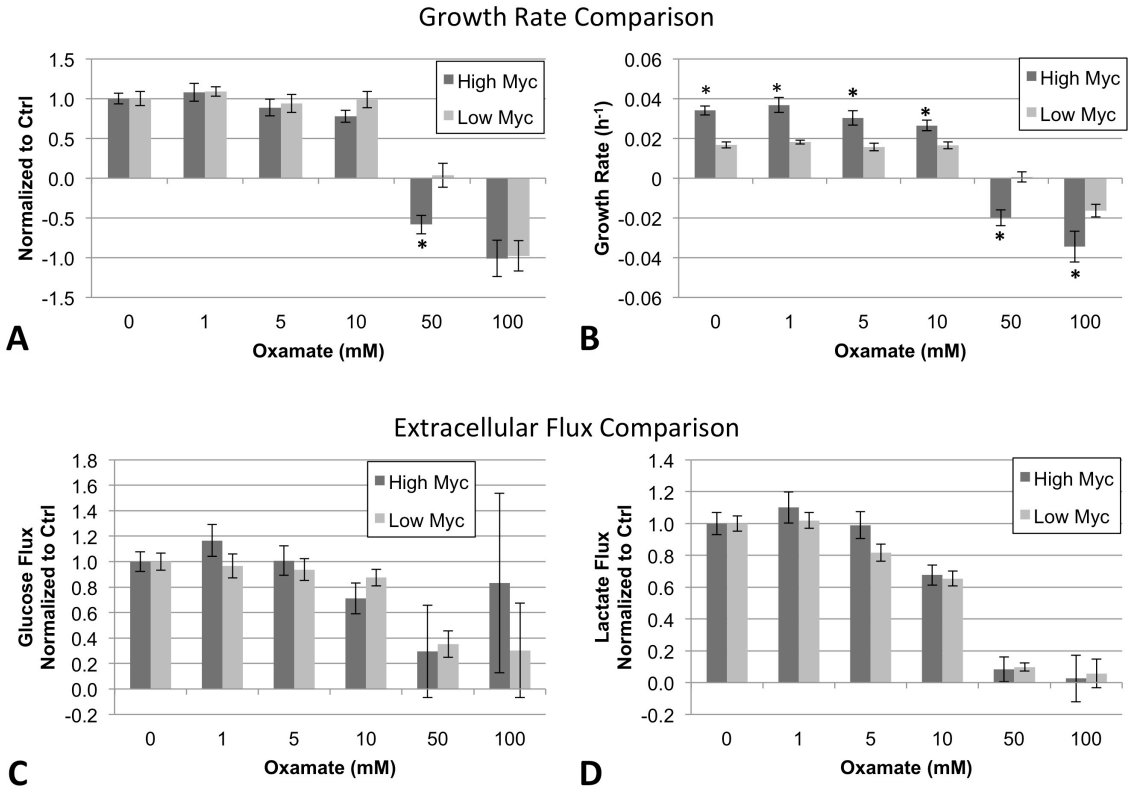

Figure 6.2 Effects of Treating High and Low Myc Cells with Oxamate. (A) Normalized growth rates are shown for High and Low Myc cells with oxamate inhibition alone. (B) Absolute growth rate values. (C) Normalized glucose uptake fluxes. (D) Normalized lactate secretion fluxes. * indicates significance with $p<0.05$. Rates were normalized to the untreated (0 mM) control.

6.3.2 Treatment of High and Low Myc Cells with Phenformin

Phenformin is a general inhibitor of oxidative phosphorylation and acts by inhibiting Complex I of the electron transport chain (Dang, 2011; Le et al., 2010; Owen et al., 2000; Shim et al., 1997). High and Low Myc cells treated with varying concentrations of phenformin showed significant differences in their response. Low Myc cells were more sensitive to a low concentration (10 μM) of the drug. However, increasing the concentration from 10 to 25 μM caused a more significant decrease in the High Myc cell growth rate than in Low Myc cells (Figure 6.3). Our previous data (Chapters 4 and 5) showed that High Myc cells rely more upon OXPHOS than Low Myc. It is reasonable to hypothesize that due to this difference the High Myc cells might be more sensitive to an inhibitor of OXPHOS. Indeed, we estimated IC50 concentrations of 90 μM for High Myc and 230 μM for Low Myc. Phenformin also had the effect of increasing the glycolytic flux, similar to the response seen when these cells were placed in a low oxygen environment (Figure 6.3). In particular, High Myc cells were able to increase their glycolytic flux magnitude greater than Low Myc cells indicating a higher capacity for metabolic alterations. However, the increase in flux magnitude did not improve the ability of the High Myc cells to survive at higher concentrations indicating that OXPHOS inhibition might be a viable therapeutic target that can more specifically target cancerous cells.

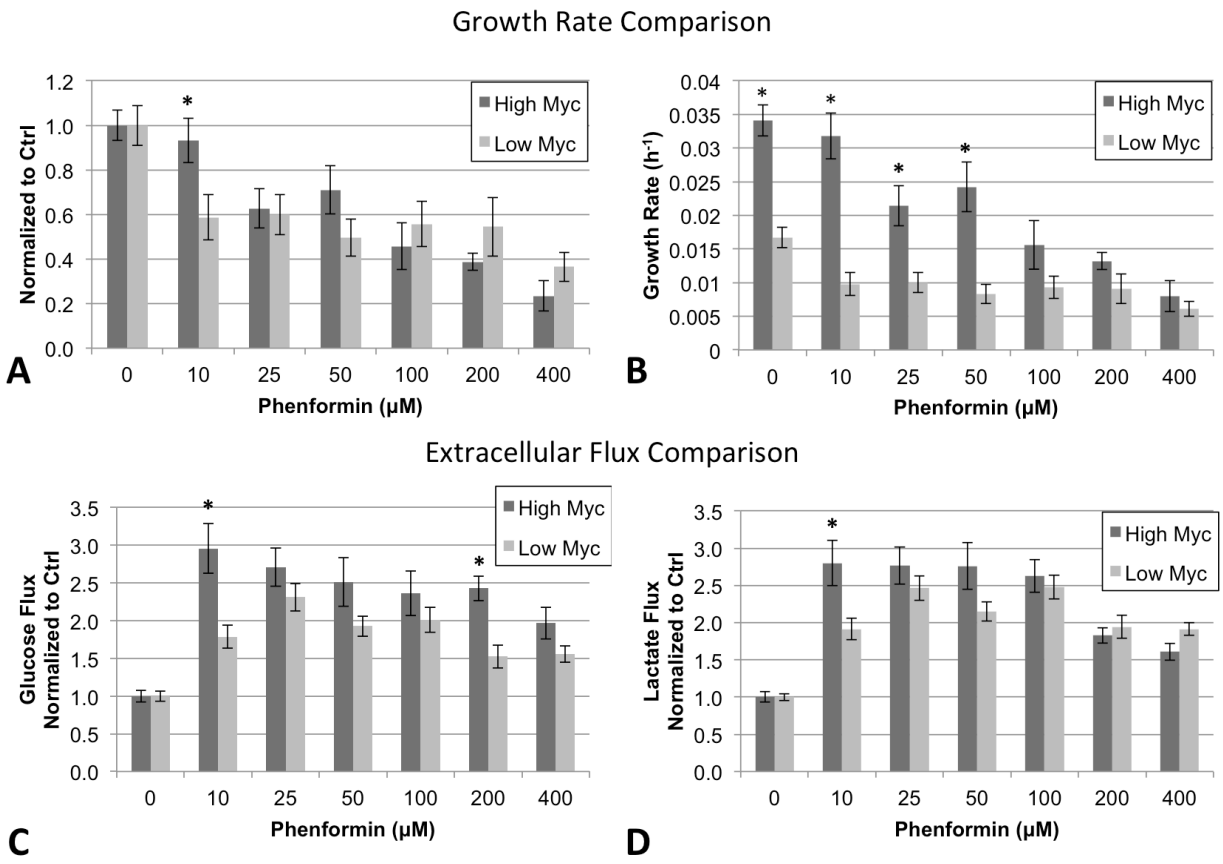

Figure 6.3 Effects of Treating High and Low Myc Cells with Phenformin. (A) Normalized growth rates are shown for High and Low Myc cells with phenformin inhibition alone. (B) Absolute growth rate values. (C) Normalized glucose uptake fluxes. (D) Normalized lactate secretion fluxes. * indicates significance with $p<0.05$. Rates were normalized to the untreated (0 mM) control.

6.3.3 Combinatorial Treatment of High and Low Myc Cells with Oxamate and Phenformin

We hypothesized that treating the cells with both drugs simultaneously would have a synergistic effect by potentially blocking the two main routes of ATP production in central metabolism. We treated High and Low Myc cells with oxamate and phenformin in combination at concentrations that, individually, had minimal effects on cell growth and metabolism (Fig. 6.1). Figure 6.4 describes the altered growth rates in response to dual treatments. At 1 mM oxamate and 10 μM phenformin (combination A), concentrations that are at least an order of magnitude below the IC50 of each individual drug, we measured a growth rate decrease of more than 20% in High and Low Myc cells. Estimated growth rate values for High and Low Myc cells were significantly different for increasing drug concentrations until the 5 mM oxamate and 10 μM phenformin (combination C) treatment, at which point both growth rates were almost identical. At the greatest concentration of both drugs (combination D), High and Low Myc cells both exhibited negative growth rates. Figure 6.5 compares the glucose and lactate fluxes for the combination drug treatments. At drug combinations A and B (1 mM oxamate and 25 μM phenformin), High Myc cells exhibited a significant increase in glucose and lactate fluxes, suggesting a possible mechanism by which these cells are able to overcome the metabolic insult. The point at which the High and Low Myc cells are growing at the same rate (combination C), we see a significant decrease in the glycolytic flux of the High Myc cells compared to combination B. It seems that up to a certain point, which is possibly related to energy or redox homeostasis, High Myc cells can upregulate glycolysis to stay alive until some imbalance inside the cell becomes too great and they start dying.

Based on analysis of growth rates using CompuSyn, combination index (CI) values were determined for the dual inhibition studies with High and Low Myc cells (Table 6.1). For all drug combinations, it was found that High Myc cells experienced drug synergism. Low Myc cells, however, exhibited synergism only for combinations B and C. Combination A showed an antagonistic effect in Low Myc cells, indicating the inhibition was lower than would be predicted based on the single inhibition curves. Low Myc cells were highly sensitive to the 10 μM dose of phenformin alone, but with the addition of oxamate there is a slight rescue in the growth rate. It's possible that the addition of a slight glycolytic insult via oxamate alters the redox (or ATP) homeostasis level to improve the growth rate. For combination C, where the growth rates were found to be identical, we see a greater sensitivity in High Myc cells than Low Myc. Synergy for the final combination where both phenotypes were dying was not assessed due to

the limitations of the CompuSyn software. However, based on visual inspection, it appears that there is a synergistic effect at this concentration as well.

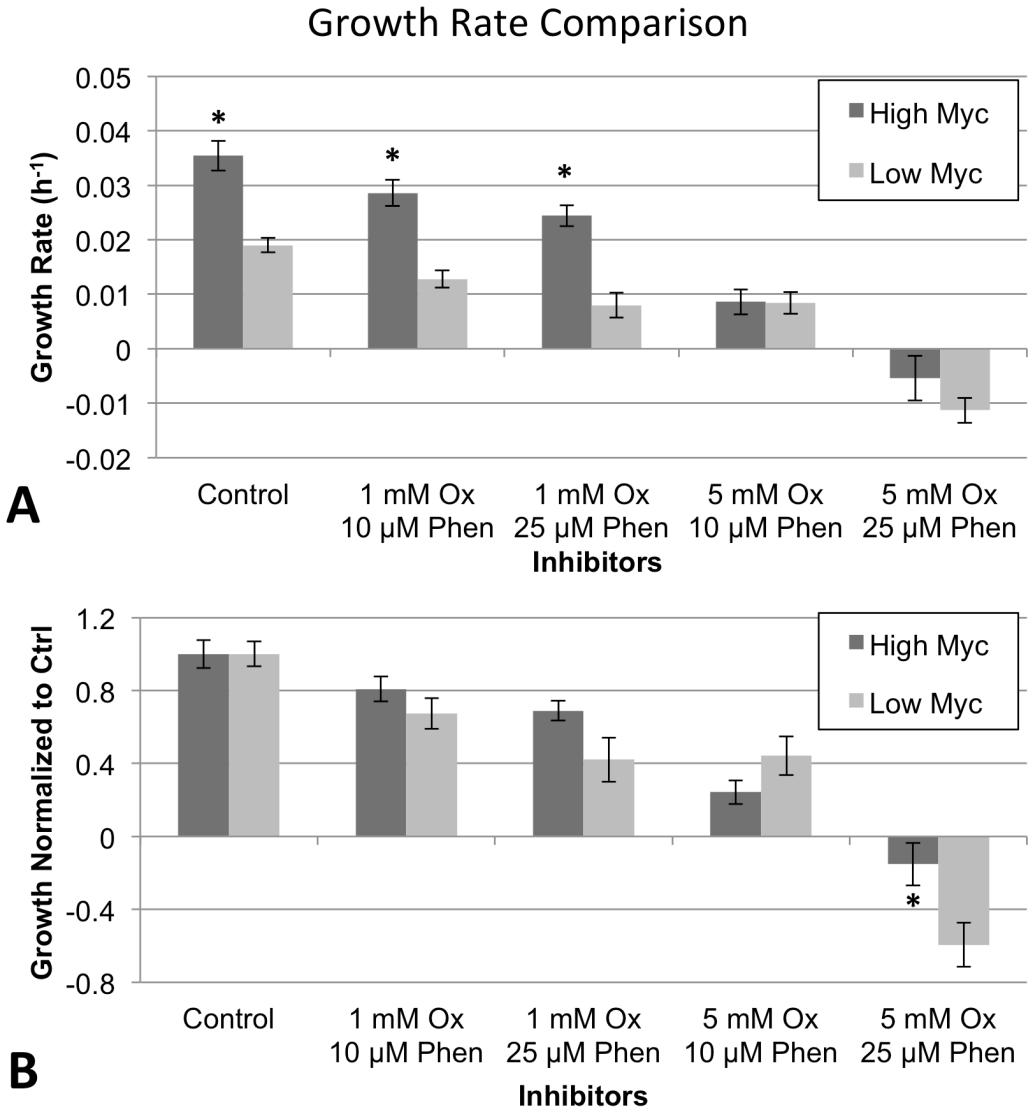

Figure 6.4 Comparison of High and Low Myc Growth Rates for Dual Inhibitor Treatments. High and Low Myc cells were treated with oxamate and phenformin simultaneously. Absolute growth rates (A) and normalized rates (B) are compared. * indicates significance with $p<0.05$. Rates were normalized to the untreated control.

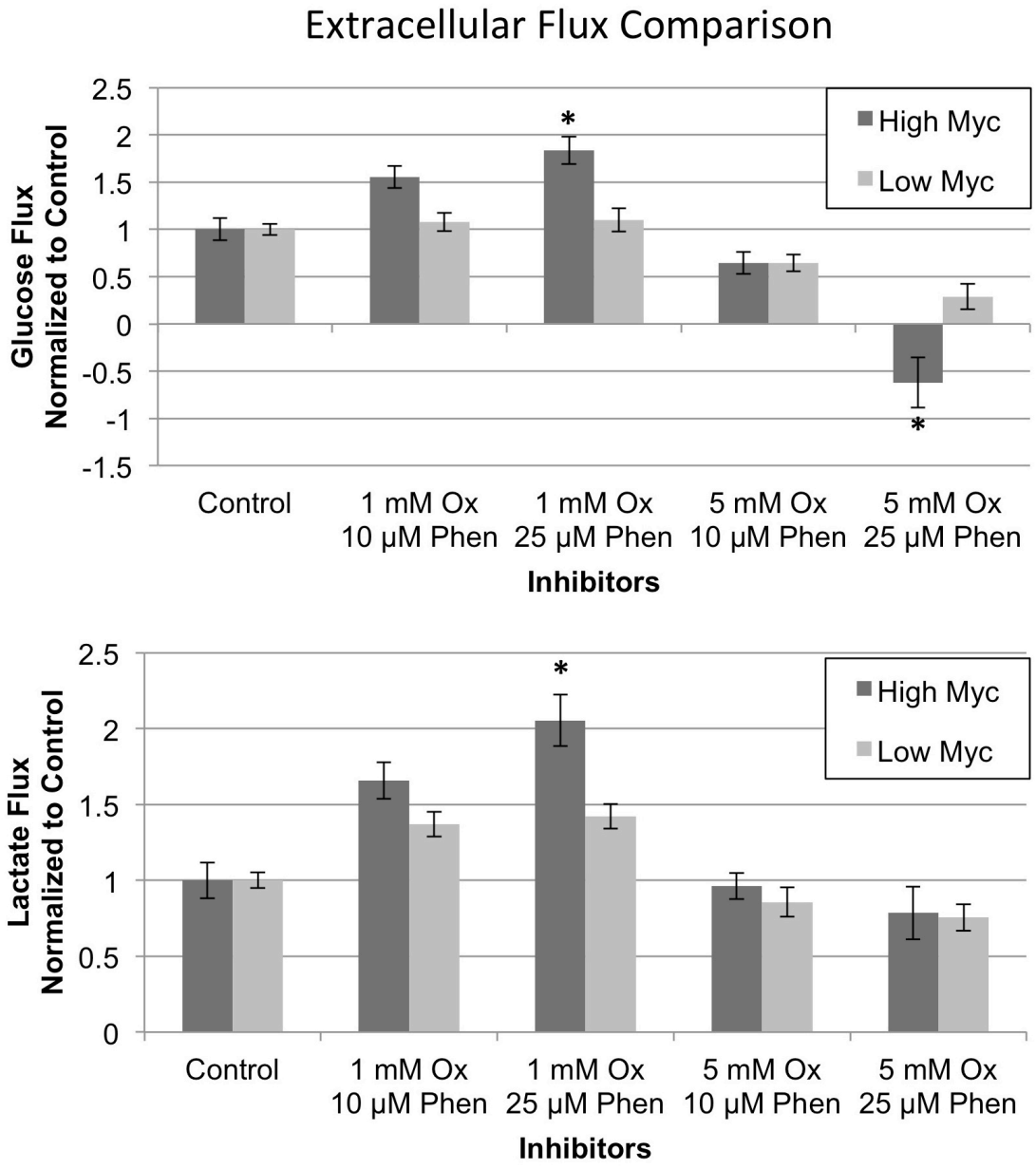

Figure 6.5 Comparison of Normalized Glycolytic Fluxes for High and Low Myc Cells for Dual Inhibition Treatments. Normalized glucose (A) and lactate (B) fluxes are shown for High and Low Myc cells in dual inhibition studies. * indicates significance with $p<0.05$. Rates were normalized to the untreated control.

Table 6.1 Combination Index (CI) Values for High and Low Myc Dual Inhibition Studies. Values were computed using CompuSyn. Values greater than 1 indicate antagonism while values lower than 1 indicate synergism. The lower or higher the number the greater the synergism or antagonism, respectively.

ID	Drug Combination	High Myc Combination Index (CI)	Low Myc Combination Index (CI)
A	*1 mM Oxamate* *10 μM Phenformin*	0.58	7.76
B	*1 mM Oxamate* *25 μM Phenformin*	0.61	0.06
C	*5 mM Oxamate* *10 μM Phenformin*	0.09	0.23

6.4 Discussion

One of the challenges of studying cancer metabolism is understanding and quantitating how cells adjust to perturbations. When a cell is in a hypoxic environment, experiences nutrient deprivation, or is inhibited by pharmacologic molecules, it adjusts its metabolism to meet the new demands and promote survival (Novoa et al., 1959; Pelicano et al., 2006; Ramanathan et al., 2005; Vander Heiden et al., 2009). Previous chapters have shown that ^{13}C-MFA can be used to map how these differences manifest themselves via altered intracellular fluxes.

Metabolic flux maps for High and Low Myc cells in normoxia highlighted alternate energy pathway utilization. High Myc cells were observed to shunt a greater portion of their glucose-derived pyruvate to the TCA cycle than Low Myc cells. Coupled with an increased glutamine flux, TCA cycle rates were elevated over 2-fold. Both cell types were still highly glycolytic, but mitochondrial OXPHOS contributed more to the energetic budget of High Myc cells than it did in Low Myc cells. Based on these flux results we chose to perturb the two key energy production pathways in central metabolism, glycolysis via lactate dehydrogenase and OXPHOS, using small-molecule inhibitors.

Lactate dehydrogenase A (*LDHA*) is one of the many direct gene targets of Myc transactivation. Previous work by Le et al. (2010) in P493-6 cells has shown that LDH-A is required for tumor growth and initiation. Using either a small-molecule drug-like inhibitor of LDH-A, called FX11, or siRNA on cultured cells, they were able to slow cell growth, decrease ATP stores, and induce high levels of reactive oxygen species and apoptosis. They also used FK866, an inhibitor of NAD^+ synthesis, and found that it had an antagonistic effect on the growth of cells and tumors. FX11 significantly inhibited the formation of tumors from P493-6 mouse xenografts, indicating a critical role for LDH-A activity *in vivo*. The combination of FX11 and FK866 actually induced tumor regression, suggesting that a dual hit approach could be a viable therapeutic option. Other studies have also highlighted the important role of LDH-A in tumor survival (Fantin et al., 2006; Xie et al., 2009). Interestingly, LDH-A is also a target of hypoxia inducible factor 1 (HIF1). HIF1 has increased expression in low oxygen environments, which is typical of *in vivo* tumors.

We first treated High and Low Myc cells with oxamate, a competitive inhibitor of LDH-A that interferes with pyruvate binding to the enzyme's active site. Oxamate is an effective and specific inhibitor and has been in use in research for over 50 years (Novoa et al., 1959). We hypothesized, based on our flux results, that High Myc cells would be more sensitive to oxamate due to their higher lactate flux. High Myc cells were in fact more sensitive, but the difference was slight (20 mM versus 24 mM). However, these are high doses of drug, and the large uncertainty estimates (not shown) make it difficult to assess the significance of the IC50 values. As expected, lactate fluxes were decreased in oxamate treated cells in a dose-dependent manner. This decrease possibly increased the concentration of NADH inside the cell, which can be compensated for by decreasing the glucose uptake rate. Indeed, we saw a concomitant decrease in glucose uptake as well, indicating the cells primarily adjusted to the perturbation by slowing glucose metabolism and growth.

We next treated cells with phenformin, an antagonist of Complex I in the electron transport chain. Phenformin is a more potent version of the anti-diabetic drug metformin which was found in a recent retrospective study of diabetic patients to reduce the incidence of cancer compared to patients not on the drug (Evans et al., 2005). Other studies have previously shown phenformin to be effective in reducing the growth rates of neuroblastoma and prostate adenocarcinoma cells (Caraci et al., 2003). This leads to the question of whether cancerous cells treated with phenformin are more sensitive than their normal counterparts. By disrupting Complex I, phenformin disrupts the proton gradient inside the mitochondria and increases the ratio of NADH to NAD+. This increase feeds back to the TCA cycle to decrease the flux, thereby making phenformin a general inhibitor of mitochondrial metabolism.

When High and Low Myc cells were treated with increasing concentrations of phenformin, we saw a dose-dependent decrease in growth rate. A comparison of normalized growth rates between High and Low Myc cells showed no statistical difference except at the lowest concentration tested (10 μM). However, estimated IC50 levels reveal that High Myc cells (90 μM) were more sensitive overall than Low Myc cells (230 μM). When compared to our flux maps these data seem to make sense: High Myc cells do rely more on the TCA cycle than Low Myc and they have an overall larger flux magnitude suggesting that they should be more susceptible to OXPHOS inhibition by phenformin. Myc is known to stimulate mitochondrial biogenesis and glutaminolysis, both of which play a role in enhancing TCA cycle flux and OXPHOS (Li et al., 2005; Wise et al., 2008). Extracellular flux measurements in the

presence of phenformin showed a marked increase in glycolysis. Glucose and lactate fluxes increased by nearly 3-fold in High Myc cells at a concentration of 10 μM. For the entire drug concentration range measured, High Myc cells had larger fluxes than Low Myc indicating the more cancerous phenotype has a greater capacity to alter its metabolism to overcome the insult. Even at the highest phenformin concentration tested (400 μM) the metabolism of both High and Low Myc cells were upregulated compared to the untreated controls. This shows that a cell, particularly a more cancerous one, can direct its metabolism to a more fermentative phenotype to survive. However, it is possible that, due to the High Myc cells' extra glycolytic capacity, the cell has a greater risk of dying when the concentration is high enough. High Myc cells typically have higher levels of ROS and oxygen uptake (see chapter 4) which, with the ectopic expression of Myc, could lead to a greater instability in the cells ability to handle chemical insults at high concentrations (Dang et al., 2005; Le et al., 2012).

When P493 cells were treated with single drugs they were able to adjust their metabolism to circumvent the perturbation. Growth rates slowed, but they were still able to survive and proliferate without dramatic differences in sensitivity between the two cell lines. Since cells treated with oxamate most likely shifted to OXPHOS under normoxic conditions to survive and cells treated with phenformin clearly upregulated glycolysis, we hypothesized that blocking both pathways simultaneously would leave the cells with no alternative routes to maintain ATP production and redox homeostasis, and they would succumb to the dual inhibition at lower doses. To test this, High and Low Myc cells were treated with both oxamate and phenformin at concentrations that, individually, had minimal effect on growth. At the lowest concentration combination tested (1 mM oxamate and 10 μM phenformin) there was a significant decrease in growth rate only for the Low Myc cells. However, based on the IC50 values, the drugs acted synergistically in High Myc cells and antagonistically in Low Myc. With a 10 μM dose of phenformin alone, Low Myc cells decreased their growth rate by almost 40%, but when co-treated with 1 mM oxamate, the growth rate was rescued slightly. This is a surprising result because it is not clear how small doses of two inhibitors acting with wholly different mechanisms and in different parts of the metabolic network would be less effective than the drugs individually. This result, however, is limited to a small range because as the dosage of each drug was increased the cells decreased their growth dramatically. At the final drug combination (5 mM oxamate and 25 μM phenformin) we measured a negative growth rate for both Myc expression levels. The most interesting part of this experiment was the combination of 5 mM oxamate and 10 μM phenformin. Both High and Low Myc cells had

identical growth rates when compared to their respective controls, meaning High Myc cells were more sensitive to this specific drug combination. Indeed, the combination index for the High Myc cells was much lower than Low Myc (0.09 vs. 0.23) indicating greater synergy.

When the intracellular fluxes of High and Low Myc cells were measured previously, there seemed to be several opportunities for targeted intervention. A straight comparison of the raw flux values indicated several differences. High Myc had many fluxes in glycolysis, TCA cycle, and anaplerotic pathways upregulated when compared to Low Myc. Intuitively, we hypothesized that the higher the flux the more sensitive the cell would be to targeted inhibition of that pathway. We did measure a slight increase in sensitivity in the High Myc cells but the difference is statistically insignificant. This line of thinking also held true when using phenformin: OXPHOS fluxes were larger in High Myc cells and they were also more sensitive to an inhibitor of OXPHOS. These conclusions indicate that perhaps MFA results on untreated cells can be used to predict drug responses in a straightforward manner. However, the drugs under study here are potent inhibitors of key enzymes in metabolism. It's not clear how the flux results would inform the drug response if enzymes such as malic enzyme, glucose-6-phosphate dehydrogenase, or any of the enzymes in the TCA (such as isocitrate dehydrogenase) were selectively targeted. Based on the data presented here, it may be logical to assume that an increased flux magnitude equates to a higher sensitivity, but that may not be the case in all instances. What is clear based on the data is that High Myc cells are able to adjust their metabolism more dramatically than their non-cancerous counterparts to overcome the chemical insult. This most likely extends to other cancer cell models as well. It would be beneficial to perform MFA studies on cells in the presence of drugs to gain a more complete picture of how metabolism adjusts. Based on simple extracellular measurements, it's not clear if other parts of metabolism (i.e. PPP, anaplerotic fluxes, lipid pathways) are changing in non-intuitive ways. Different mutations manifest in different phenotypes and it's possible they respond to drugs in slightly different manners too: Myc increases reliance on OXPHOS (Murphy et al., 2013) while K-Ras promotes the classic Warburg Effect (Gaglio et al., 2011) and these different cell types probably do not respond to inhibiting drugs in similar manners. A full understanding of how a cell's metabolism responds to different treatments is critical to rationally selecting new therapeutic strategies.

6.5 References

Caraci F, Chisari M, Frasca G, Chiechio S, Salomone S, Pinto A, Sortino MA, Bianchi A. 2003. Effects of phenformin on the proliferation of human tumor cell lines. *Life Sci.* **74**:643–650.

Chou TC, Talalay P. 1984. Quantitative analysis of dose-effect relationships: the combined effects of multiple drugs or enzyme inhibitors. *Adv. Enzym. Reg.* **22**:27–55.

Dang CV. 2011. Therapeutic targeting of Myc-reprogrammed cancer cell metabolism. *Cold Spring Harb. Symp. Quant. Biol.* **76**:369–374.

Dang CV, Li F, Lee LA. 2005. Could MYC induction of mitochondrial biogenesis be linked to ROS production and genomic instability? *Cell Cycle* **4**:1465–1466.

Dowling RJO, Goodwin PJ, Stambolic V. 2011. Understanding the benefit of metformin use in cancer treatment. *BMC Med.* **9**:33.

Evans JMM, Donnelly LA, Emslie-Smith AM, Alessi DR, Morris AD. 2005. Metformin and reduced risk of cancer in diabetic patients. *BMJ* **330**:1304–1305.

Facchetti G, Zampieri M, Altafini C. 2012. Predicting and characterizing selective multiple drug treatments for metabolic diseases and cancer. *BMC Sys. Biol.* **6**:115.

Fantin V, St-Pierre J, Leder P. 2006. Attenuation of LDH-A expression uncovers a link between glycolysis, mitochondrial physiology, and tumor maintenance. *Cancer Cell* **9**:425–434.

Folger O, Jerby L, Frezza C, Gottlieb E, Ruppin E, Shlomi T. 2011. Predicting selective drug targets in cancer through metabolic networks. *Mol. Sys. Biol.* **7**:501.

Gaglio D, Metallo CM, Gameiro PA, Hiller K, Danna LS, Balestrieri C, Alberghina L, Stephanopoulos G, Chiaradonna F. 2011. Oncogenic K-Ras decouples glucose and glutamine metabolism to support cancer cell growth. *Mol. Sys. Biol.* **7**:523.

Jia J, Zhu F, Ma X, Cao Z, Cao ZW, Li Y, Li YX, Chen YZ. 2009. Mechanisms of drug combinations: interaction and network perspectives. *Nat. Rev. Drug Discov.* **8**:111–128.

Kamb A, Wee S, Lengauer C. 2007. Why is cancer drug discovery so difficult? *Nat. Rev. Drug Discov.* **6**:115–120.

Keibler MA, Fendt S-M, Stephanopoulos G. 2012. Expanding the concepts and tools of metabolic engineering to elucidate cancer metabolism. *Biotechnol. Prog.* **28**:1409–1418.

Le A, Cooper CR, Gouw AM, Dinavahi R, Maitra A, Deck LM, Royer RE, Vander Jagt DL, Semenza GL, Dang

CV. 2010. Inhibition of lactate dehydrogenase A induces oxidative stress and inhibits tumor progression. *Proc. Nat. Acad. Sci.* **107**:2037–2042.

Le A, Lane AN, Hamaker M, Bose S, Gouw A, Barbi J, Tsukamoto T, Rojas CJ, Slusher BS, Zhang H, Zimmerman LJ, Liebler DC, Slebos RJC, Lorkiewicz PK, Higashi RM, Fan TWM, Dang CV. 2012. Glucose-Independent Glutamine Metabolism via TCA Cycling for Proliferation and Survival in B Cells. *Cell Metab.* **15**:110–121.

Li F, Wang Y, Zeller KI, Potter JJ, Wonsey DR, O'Donnell KA, Kim J-W, Yustein JT, Lee LA, Dang CV. 2005. Myc stimulates nuclearly encoded mitochondrial genes and mitochondrial biogenesis. *Mol. Cell. Biol.* **25**:6225–6234.

Li L, Zhou X, Ching W-K, Wang P. 2010. Predicting enzyme targets for cancer drugs by profiling human Metabolic reactions in NCI-60 cell lines. *BMC Bioinformatics* **11**:501.

Murphy TA, Dang CV, Young JD. 2013. Isotopically nonstationary 13C flux analysis of Myc-induced metabolic reprogramming in B-cells. *Metab. Eng.* **15**:206–217.

Niklas J, Heinzle E. 2012. Metabolic flux analysis in systems biology of Mammalian cells. *Adv. Biochem. Eng. Biotechnol.* **127**:109–132.

Novoa WB, Winer AD, Glaid AJ, SCHWERT GW. 1959. Lactic dehydrogenase. V. Inhibition by oxamate and by oxalate. *J. Biol. Chem.* **234**:1143–1148.

Owen MR, Doran E, Halestrap AP. 2000. Evidence that metformin exerts its anti-diabetic effects through inhibition of complex 1 of the mitochondrial respiratory chain. *Biochem. J.* **348 Pt 3**:607–614.

Pajic A, Spitkovsky D, Christoph B, Kempkes B, Schuhmacher M, Staege MS, Brielmeier M, Ellwart J, Kohlhuber F, Bornkamm GW. 2000. Cell cycle activation by c-myc in a Burkitt lymphoma model cell line. *Int. J. Cancer* **87**:787–793.

Pajic A, Staege MS, Dudziak D, Schuhmacher M, Spitkovsky D, Eissner G, Brielmeier M, Polack A, Bornkamm GW. 2001. Antagonistic effects of c-myc and Epstein-Barr virus latent genes on the phenotype of human B cells. *Int. J. Cancer* **93**:810–816.

Pelicano H, Martin DS, Xu R-H, Huang P. 2006. Glycolysis inhibition for anticancer treatment. *Oncogene* **25**:4633–4646.

Ramanathan A, Wang C, Schreiber SL. 2005. Perturbational profiling of a cell-line model of tumorigenesis by using metabolic measurements. *Proc. Nat. Acad. Sci.* **102**:5992–5997.

Shim H, Dolde C, Lewis B, Wu C, Dang CV, Jungmann R, Dalla-Favera R. 1997. c-Myc transactivation of LDH-A: implications for tumor metabolism and growth. *Proc. Nat. Acad. Sci.* **94**:6658.

Vander Heiden MG, Cantley LC, Thompson CB. 2009. Understanding the Warburg effect: the metabolic requirements of cell proliferation. *Science* **324**:1029–1033.

Wise D, DeBerardinis RJ, Mancuso A, Sayed N, Zhang X, Pfeiffer H, Nissim I, Daikhin E, Yudkoff M, McMahon S. 2008. Myc regulates a transcriptional program that stimulates mitochondrial glutaminolysis and leads to glutamine addiction. *Proc. Nat. Acad. Sci.* **105**:18782.

Xie H, Valera VA, Merino MJ, Amato AM, Signoretti S, Linehan WM, Sukhatme VP, Seth P. 2009. LDH-A inhibition, a therapeutic strategy for treatment of hereditary leiomyomatosis and renal cell cancer. *Mol. Cancer Therap.* **8**:626–635.

APPENDIX 6.A - Supplementary Figures

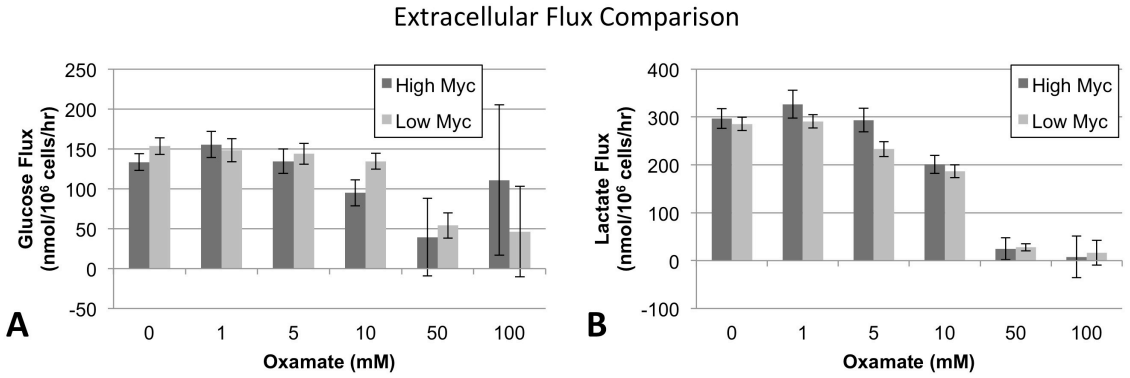

Figure 6.A.1 Glucose and Lactate Fluxes of Oxamate-treated High and Low Myc Cells. (A) Glucose uptake fluxes are shown for High and Low Myc cells with oxamate inhibition alone. (B) Lactate secretion fluxes. * indicates significance with $p<0.05$.

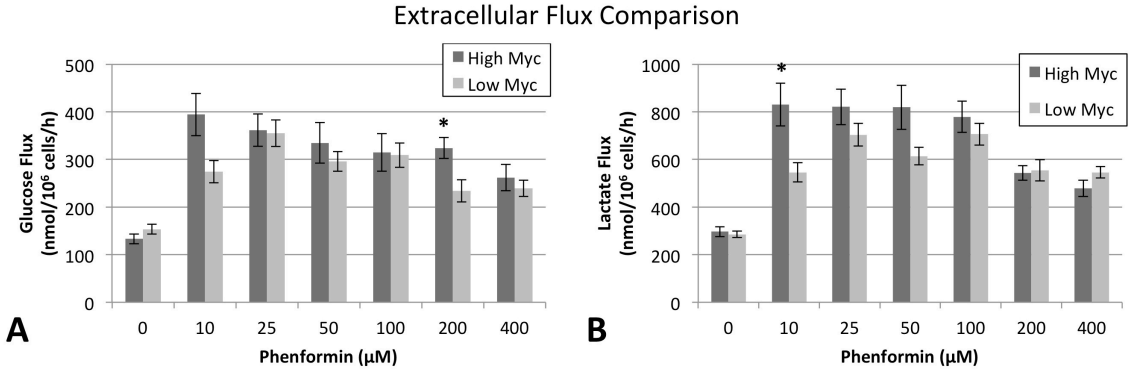

Figure 6.A.2 Glucose and Lactate Fluxes of Phenformin-treated High and Low Myc Cells. (A) Glucose uptake fluxes are shown for High and Low Myc cells with phenformin inhibition alone. (B) Lactate secretion fluxes. * indicates significance with $p<0.05$.

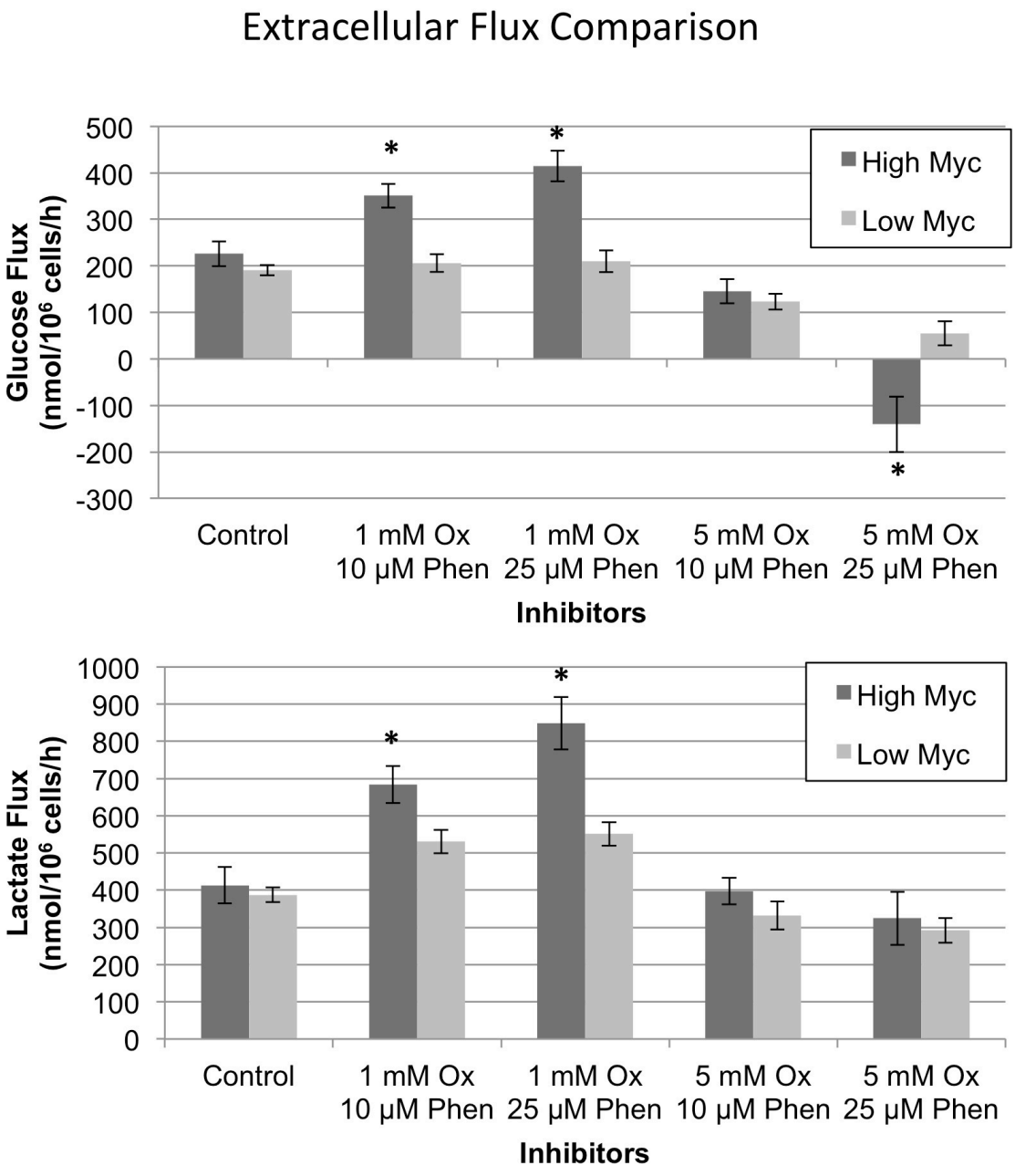

Figure 6.A.3 Comparison of Fluxes for High and Low Myc Cells in Dual Inhibition Cultures. Glucose (A) and lactate (B) fluxes are shown for High and Low Myc cells in dual inhibition studies. * indicates significance with $p<0.05$.

CHAPTER 7

APPLICATION OF METABOLIC FLUX ANALYSIS TO AN *IN VIVO* MODEL OF MYC-DRIVEN LYMPHOMAGENESIS

7.1 Introduction

The utility of metabolic flux analysis (MFA) in cancer research has grown rapidly over the past several years (Keibler et al., 2012). Numerous studies, including those discussed in chapters 4 and 5, have shown surprising alterations in cancer metabolism that were only evidenced using isotope tracers (Gaglio et al., 2011; Kim and Forbes, 2007; Le et al., 2012; Metallo et al., 2012). The majority of these studies have been conducted using *in vitro* models of cancer. These studies are very useful but there is a fundamental disconnect between cancerous cell growth in a flask versus in a human body. Unlike a cell culture flask, the tumor microenvironment is complex, three-dimensional, and subject to variations in nutrient and oxygen availability (Vander Heiden, 2011). Various aspects of the *in vivo* environment can be emulated *in vitro*, but it is only a simulacrum of a true *in vivo* environment.

The next step with MFA is to expand it to more complicated culture systems such as 3-D culture and *in vivo* tissue. Animals studies, and mice in particular, are highly relevant for clinical applications, and their use in research is well-established (Frese and Tuveson, 2007; Shultz et al., 2007). Isotope tracers have been used in mice for many years (Fan et al., 2012) but their application to *in vivo* cancer metabolism is relatively nascent. ^{13}C tracers have been used to study mouse models of *MET* and *MYC*-induced liver tumors (Yuneva et al., 2012), glioblastoma (Marin-Valencia et al., 2012), and lung cancer (Fan et al., 2011). One study by Fan et al. (2009) used ^{13}C-labeled glucose to study cancerous and non-cancerous lung tissue resected from a patient. These studies are on the cutting edge of *in vivo* metabolomics research, but much still remains unknown and very few labs are able to do this kind of work.

One of the primary assumptions of MFA *in vitro* is the homogeneity of the cell culture (Zamboni, 2011). When the metabolites in an experiment are pooled, the assumption is that a very large portion of the cell population is in a similar metabolic state: their nutrient availability and environment are the same. This assumption is not necessarily true *in vivo* (Ward and Thompson, 2012). Cells that are closer to the host's vasculature will have an increased supply

of oxygen and substrates while those farther away will experience more nutrient deprivation and stress (Jones and Thompson, 2009). This heterogeneity complicates the analysis.

Another aspect of *in vitro* MFA is the relative ease with which extracellular uptake and secretion fluxes can be measured (see Chapter 3). Simply by measuring the concentration of metabolites from the culture medium along with the growth rate of the culture, cell specific fluxes can be readily estimated. Inside an animal, this is very difficult, if not impossible. There are some techniques available for estimating the growth rate of an *in vivo* tumor, but the pool of nutrients is shared throughout the entire body, making determination of specific fluxes between the tumor and its surroundings difficult. As such, it may only be possible to determine relative flux ratios between different pathways (e.g., glycolysis versus pentose phosphate or TCA cycle) rather than absolute rates.

Also limiting the analysis is the cost of the isotopic tracer. Cell cultures consume a miniscule amount of carbon compared to whole animals. When a significant portion of the incoming carbon needs to be isotopically labeled, the cost can be prohibitive. Optimization can be done to minimize the amount needed, but the requirement is still going to be greater than an equivalent *in vitro* experiment.

Finally, tumor resection and cell isolation can affect the analysis by altering the mass isotopomer distributions (MID) of intracellular metabolites. The labeling of some intracellular metabolites can change on the time scale of a few seconds, due to rapid turnover in highly active pathways of central metabolism. To avoid these unwanted sampling artifacts, the metabolism has to be rapidly quenched upon sample collection. This is relatively simple *in vitro,* and there are established protocols for cold quenching cultured cells (Nöh et al., 2007). However, the time required to sacrifice an animal, harvest the tissue, and quench the metabolism can be on the order of minutes instead of seconds (Fan et al., 2011). While it is theoretically more ideal to measure the labeling of free intracellular metabolites directly, it may be practically better to measure the labeling of macromolecules that provide a stable proxy of the metabolite building blocks from which they were biosynthetically derived (see Chapter 4 for details). True *in vivo* isotopomer analysis can be done using NMR with a small surface coil, but the uses are limited due to the shallow depth of measurements that can be achieved (Fan et al., 2012). Measuring the isotopic enrichment of

macromolecule pools (protein, RNA, lipids) offers an alternative approach that could enable isotopomer analysis of *in vivo* tumor samples while avoiding the introduction of sampling artifacts.

Here, we describe a proposed method for extending the INST-MFA approach applied in chapters 4 and 5 to an *in vivo* tumor model, including recommended procedures for sample collection and analysis. We propose to use an Eμ-*myc* transgenic mouse model that develops fatal lymphoma within a few months of birth (Adams et al., 1985). We have performed computational simulations to determine the minimum required tracer amount that should be fed to precisely estimate flux ratios using INST-MFA while minimizing the tracer cost. We assumed a metabolic phenotype similar to the High Myc normoxic flux map described in Chapter 5 and predicted isotope labeling trajectories for a variety of tracer and measurement combinations. The information from these simulations was then used to develop a recommended protocol for performing an *in vivo* isotope labeling experiment that would enable relative flux estimation of early-stage lymphoma based on INST-MFA. This protocol will be tested in a future pilot study to establish proof of concept of our approach.

7.2 Methods

7.2.1 Metabolic Network

Based on previous experience and conversations with collaborators, it was determined that the only *in vivo* measurements we would be able to make are the labeling of the cell macromolecules and possibly the growth rate based on BrdU incorporation and ribose isotopic enrichment. As such, the model was adjusted to best describe the available data: glucose and glutamine were assumed to be the major carbon sources and lactate and biomass were the primary carbon sinks. Dilution of labeling was allowed via alanine, aspartate, glutamate, glycine, and serine. The growth rate was the only rate input to the estimation and was used primarily to aid in the estimation of the relative uptake rate. As it's not possible to know the actual glucose or glutamine uptake in the system, the growth rate is used to roughly estimate the range of possible uptake fluxes. Once that range is determined, the growth rate is removed from the estimation and the split ratios are determined. Two separate flux estimations were performed: first, glucose uptake was fixed to 100 and the split ratio between glycolysis and pentose phosphate (PP) pathway was calculated; and second, pyruvate dehydrogenase (PDH) was fixed to 100 and relative TCA cycle fluxes were calculated. The reaction networks and atom transitions used for MFA are listed in Table 7.A.1 in the Appendix.

7.2.2 Tracer Formula Optimization

To identify the best combination of naturally labeled glucose, [U-$^{13}C_6$]glucose, and [1,2-$^{13}C_2$]glucose for an *in vivo* flux study we utilized the High Myc normoxic flux map from chapter 5 as the basis for our estimation. Using these finalized flux values, the amount of each tracer was adjusted to multiple set points. At each combination, the MIDs were simulated (the "forward" MFA simulation) based on the flux values and tracer fed. Three time points were simulated: 24, 48, and 72 hours. We then used these simulated measurements to solve the "inverse" MFA calculation and estimate flux confidence intervals. The optimum combination was defined as the least expensive mixture that allowed the G6PDH flux to be estimated to within +/-10% of the glucose uptake flux.

7.2.3 Determination of Growth Rate from Ribose Labeling

Since glucose is the primary carbon source for RNA synthesis, the atom percent enrichment (APE) (see chapter 5) of ribose derived from RNA follows close with the theoretical maximum APE. Because of this fact, the growth rate can be estimated via a least-squares optimization by comparing the lack of fit between the measured and theoretical maximum APEs at each time point and adjusting the growth rate until the fit is minimized. It will be important to accurately determine the actual amount of labeled carbon being fed to the mice to get a good estimate of the maximum theoretical APE.

The APE was calculated for the Ribose 284 fragment from the High Myc normoxic labeling experiment in Chapter 5. Based on the tracer used in the experiment (1:1 - [U-^{13}C]glucose : [1,2-^{13}C]glucose) we calculated the maximum theoretical APE which is 0.66. Using this as the maximum, we then used the following expression to estimate the APE at each time point based on a given growth rate:

$$\left(1 - \frac{1}{e^{\mu t}}\right) \text{x } \text{APE}_{\text{Max}} \tag{7.1}$$

where μ is the growth rate, t is the time, and APE_{Max} is the maximum APE given the tracer input. For each time point, the estimated and measured APE is subtracted from each other and the result squared. The squares are then

summed and square-rooted. This value is then minimized by adjusting the growth rate using Microsoft Excel's 'Goal Seek' feature.

7.3 Results

7.3.1 *In Vivo* Tracer Optimization

If the cost of the *in vivo* tracers was not a concern then all of the glucose consumed by the mice should be isotopically labeled. However, to decrease expenses we attempted to estimate the minimum required amount of tracer needed to precisely estimate flux ratios in upper glycolysis. [1,2-$^{13}C_2$]glucose is the most expensive tracer we typically use, but it is necessary to fully resolve PP pathway flux relative to glycolysis (see chapters 4 and 5). Without this tracer the precision of our PP pathway estimates decreases dramatically. Ten different tracer combinations were tested and the 95% confidence intervals of the G6PDH flux were compared. Figure 7.1 shows the flux magnitude and confidence intervals for each tracer combination. 30% [1,2-$^{13}C_2$]glucose was found to be the minimum amount required to give a confidence interval that was less than 10% of the magnitude of the glucose uptake flux (set to 100 in these simulations). Increasing concentrations of [U-$^{13}C_6$] and [1,2-$^{13}C_2$] did seem to improve the estimation, but the cost increases would not justify the marginal improvements in sensitivity. Keeping the two tracers at a 1:1 ratio, as done in chapter 5, with a minimum of 30% [1,2-$^{13}C_2$]glucose and the remainder as unlabeled glucose seems to be the best compromise.

7.3.2 Comparison of Growth Rate Estimation

The measured growth rate of the High Myc normoxic cells in chapter 5 was 0.0363 hours^{-1} +/- 0.0016. The MFA results returned a value of 0.0373 hours^{-1} with a 95% confidence range of 0.0342 to 0.0406. By comparing the theoretical APE to the measured APE for each of the six Ribose 284 time points, we estimated the growth rate to be 0.0357 hours^{-1}. This value is well within the 95% confidence interval and within the standard error of our original estimation.

7.4 Proposed Methods

7.4.1 Tracer Feed

Due to the high cost of the isotopic tracer and long times necessary to reach isotopic steady-state within the macromolecular pools to be sampled, we decided to conduct an isotopically nonstationary experiment. Previous data have shown that the B-cells inside the Eμ-*myc* mouse double approximately every 16-24 hours, meaning that 3-4 doubling periods could be achieved within 3 days (conversations with Christine Eischen, PhD). Based on the data presented in section 7.3, the tracer combination of 40% naturally labeled glucose, 30% [U-$^{13}C_6$]glucose, and 30% [1,2-$^{13}C_2$]glucose will be optimal for data precision and cost. Due to the complicated nature of the animal feed we determined that it would be best to use the glucose available in the original formula, in the form of cornstarch, as the naturally labeled fraction. The isotopically labeled glucose tracer mix will then be mixed with the custom formulation of the AIN-93G Growth Diet (Purina Animal Nutrition). Sucrose, maltodextrin, and soybean oil will be completely removed with the cornstarch lowered to 25.18% of the original formulation. Sucrose and maltrodextrin will be removed because they enter the cell as glucose and would dilute the labeled pool. Soybean oil was removed to enhance the mixing process. This affects the formula by increasing the fraction of the other feed components (See Table 7.1). Depending on the final amount of feed needed, the glucose tracer will first be mixed with the powdered chow. Once the powders have been thoroughly mixed, the soybean oil will be slowly added to the powder in the blender to create a homogenous mixture. Beginning on day 1 of the labeling experiment, 3 grams of custom isotopically labeled chow will be given to the mice once in the morning and once in the evening for up to three days.

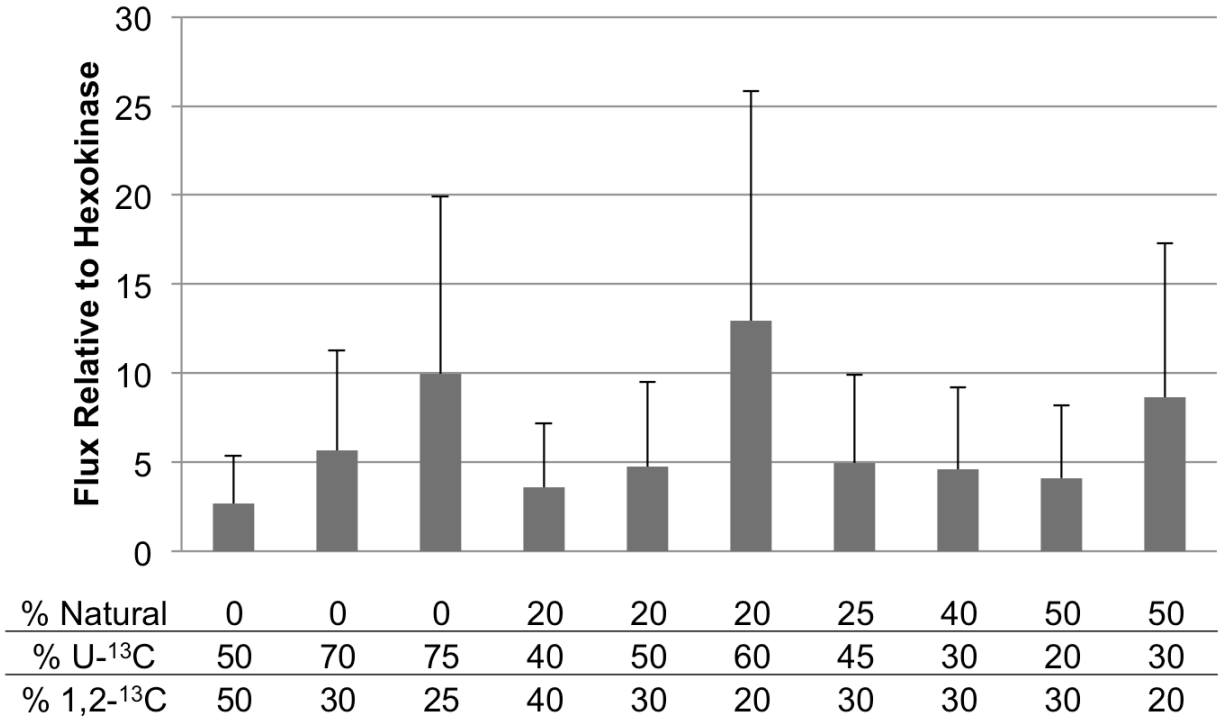

Figure 7.1 Comparison of G6PDH Flux Resolution Provided by Different Glucose Tracer Combinations. 10 different combinations of naturally labeled, [U-$^{13}C_6$], and [1,2-$^{13}C_2$]glucose were compared for differences in predicted G6PDH flux resolution. Glucose uptake was fixed to 100. Values represent the median of the 95% confidence interval. Error bars are the upper bound of the 95% confidence interval.

Table 7.1 *In Vivo* Flux Analysis Feed Formulation. The AIN-93G feed formulation was adjusted by removing soybean oil, maltodextrin, sucrose, and 14.57% of the cornstarch. The tracer will be added to the powdered chow and mixed thoroughly. The soybean oil will be added last and mixed in. The total fraction of carbohydrates from starch and the glucose tracer will be the same as prior to adjustment. Soybean oil will be added in the same ratio as the original formula.

Ingredient	*Original (%)*	*Adjusted (%)*	*w/ Tracer (%)*	*w/ Soybean Oil (%)*
Tracer Mix	0	0	40.61	37.77
Corn Starch	39.7486	45.59	27.07	25.18
Casein	20	36.21	21.51	20
Maltodextrin	13.2	0	0	0
Sucrose	10	0	0	0
Soybean Oil	7	0	0	7
Powdered Cellulose	5	9.05	5.38	5
Mineral Mix	3.5	6.34	3.76	3.5
Vitamin Mix	1	1.81	1.08	1
L-Cystine	0.3	0.54	0.32	0.3
Choline Bitartrate	0.25	0.45	0.27	0.25
t-Butylhydroquinone	0.0014	0.0025	0.0015	0.0014
Total Amount	100	100	100	100

7.4.2 Experimental Outline

Animals

Three Eμ-*myc* transgenic mice that are 5 to 7 weeks old (Adams et al., 1985) will be fed the custom diet discussed in section 7.4.1. Mice will be fed 3g of chow twice daily, once in the morning and once in the evening. One mouse will be sacrificed after one day on the tracer diet, one mouse after two days, and one mouse after three days. Each animal will be injected intraperitoneally with 100 μL of 10mg/mL bromodeoxyuridine (BrdU) in sterile PBS 12-16 hours prior to sacrifice (O'Donnell et al., 2005). Tissues (spleen, bone marrow, liver, and kidney) samples will be harvested and processed according to the following methods. See Figure 7.2 for a description of the proposed workflow.

Spleen

The spleen will be minced and red blood cells lysed using a hypotonic solution (Gey's solution). The remaining splenocytes will be partitioned for three different analyses. First, approximately 10-15 million cells will be removed to analyze the isotopic enrichment present in the heterogeneous population. Second, B-cell lymphocytes will be separated from the remaining splenocytes via negative selection on a BD IMag enrichment set (BD Biosciences), and the remaining cells will be discarded. BrdU incorporation of 1-2 million extracted B lymphocytes will be analyzed by flow cytometry. The remaining B lymphocytes will be either lysed in TRIzol or frozen at -80°C or flash frozen in liquid nitrogen for future lipid analysis.

Bone marrow

Once bone marrow cells have been extracted, the red blood cells will be lysed using a hypotonic solution (Gey's solution). The cells will be split into multiple microcentrifuge tubes with at least 5 million cells and either lysed in TRIzol and frozen at -80°C or flash frozen in liquid nitrogen for future lipid analysis.

Liver and kidney

Tissues from the liver and kidney will be analyzed as non-proliferative control samples. Cells in the kidney are not known to exhibit a high degree of metabolic activity, making it an ideal negative control sample. Conversely, cells in the liver, chiefly hepatocytes, are known to be highly metabolically active. However, neither tissue should exhibit proliferation during the experiment. Therefore, labeling of macromolecular pools are not expected to be significantly altered in either tissue. Homogenized tissues will either be lysed in TRIzol or stored at -80°C or flash frozen in liquid nitrogen for future lipid analysis.

7.4.3 Sample Analysis

Labeling of amino acids, RNA, and palmitate will be done according to the protocols in chapter 5. BrdU labeling corresponds with the fraction of cells that are in S-phase. This labeling will be used to measure variations among the three mice based on differences in labeling. Theoretically, a similar fraction of the cells should be labeled if the metabolism of each mouse is similar. Using the ribose labeling it is possible to estimate the growth rate of cells based on the maximum theoretical labeling (see section 7.2.3). Two fluxes will be individually fixed to 100 in order to estimate split ratios in glycolysis/PP pathway (relative to glucose uptake) and TCA cycle activity (relative to

PDH) (see section 7.2.1). All labeling and growth data will be input into the INCA software and analyzed in a similar manner to data in chapters 4 and 5.

7.5 Discussion

This chapter proposes a method for conducting an *in vivo* flux analysis study of cancer metabolism. Many of the methods needed for this study have been already optimized but have yet to be brought together. We've previously described optimized methods for measuring isotopic labeling in protein, RNA, and lipid samples, and we've shown how the isotopically nonstationary approach can be effectively applied to estimate fluxes in cultured cells (see chapters 4 and 5). Our collaborators in the Eischen lab have extensive experience with *in vivo* studies including tissue resection, B-cell purification, and BrdU analysis. Therefore, we now have brought together the necessary expertise to perform a pilot study.

Prior to conducting the experiment it was necessary to optimize the amount of ^{13}C-glucose tracer used in the study. Typical costs for [U-$^{13}C_6$]glucose and [1,2-$^{13}C_2$]glucose are approximately \$100/gram and \$400/gram, respectively. Any efforts at reducing the amount of tracer will be beneficial as long as the reduction does not increase the uncertainty in the flux estimation dramatically. Based on the work presented here it seems that keeping a 1:1 ratio of uniformly labeled glucose to 1,2-labeled glucose is ideal, the same combination used in chapter 5, but with the total fraction of labeled glucose reduced to roughly half of the total carbohydrate fed. We found that a minimum of 30% [1,2-$^{13}C_2$] glucose is the best compromise between cost and data precision and, in keeping with the 1:1 ratio, we also propose using 30% [U-$^{13}C_6$]glucose. The remaining naturally labeled carbohydrate will come from the cornstarch already present in the mouse chow.

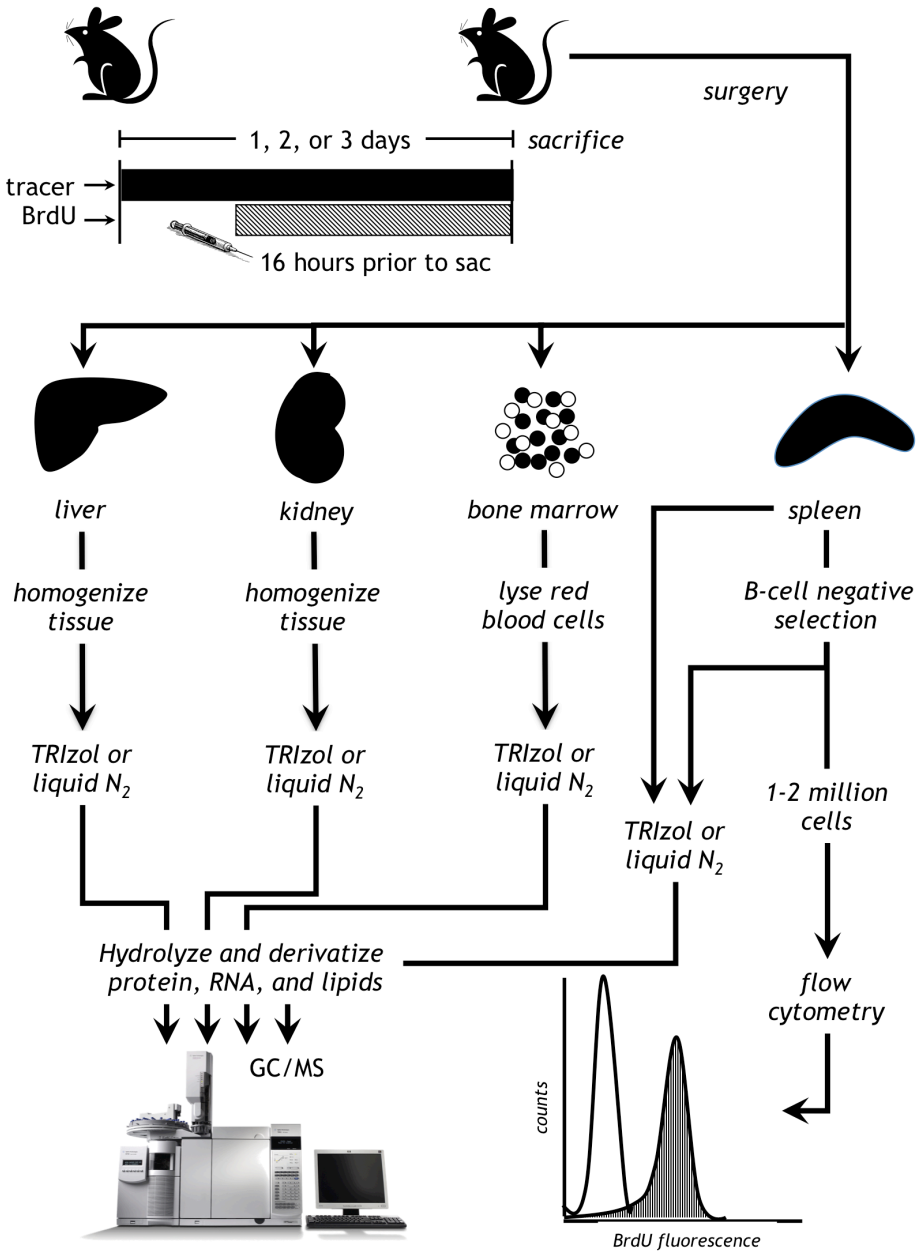

Figure 7.2 Proposed Workflow for *In Vivo* INST-MFA Study. Each mouse is treated exactly the same after sacrifice with four different tissues being resected. The liver and kidney will serve as negative controls because their macromolecule labeling is presumed not to change significantly. Bone marrow will have the red blood cells lysed prior to analysis. A small slice of the spleen will be analyzed for heterogeneous labeling and the remaining portion will be negatively selected for B-cells. The B-cells will be split and either measured for BrdU incorporation or analyzed via GC/MS.

This study is built upon the work presented in this dissertation in a way that is unique to the previous literature (Fan et al., 2011; Marin-Valencia et al., 2012; Yuneva et al., 2012). To the best of our knowledge, nobody has applied MFA techniques to the study of *in vivo* lymphoma mouse models. Our proteinogenic MFA method was designed specifically with this application in mind, and the isotopically nonstationary approach was found to be superior because it provides increased flux resolution relative to steady-state MFA and can also be applied to systems where isotopic labeling does not have time to fully equilibrate. We specifically chose to work with the Eμ-myc transgenic mouse model for the proposed pilot study because it overexpresses Myc, similar to the P493-6 cells studied previously, and develops fatal B-cell lymphoma, making it an excellent model for studying Myc-driven cancer (Adams et al., 1985). Our expectation in working with this mouse model is that it will give more information about when the metabolic transition occurs in pre-cancerous cells. It's understood that cells alter their metabolism to support cancerous growth. What's not well understood is when this alteration occurs in the development of cancer and determining when this transition happens will guide the search for new therapeutics. This also has the potential to inform about the differences between cancerous cells *in vivo* and *in vitro*. We expect this experiment will be rich in data and will enable us to advance understanding of cancer metabolism as well as the application of metabolic engineering techniques to complex systems.

7.6 References

Adams JM, Harris AW, Pinkert CA, Corcoran LM, Alexander WS, Cory S, Palmiter RD, Brinster RL. 1985. The c-myc oncogene driven by immunoglobulin enhancers induces lymphoid malignancy in transgenic mice. *Nature* **318**:533–538.

Fan TWM, Lane AN, Higashi RM, Farag MA, Gao H, Bousamra M, Miller DM. 2009. Altered regulation of metabolic pathways in human lung cancer discerned by (13)C stable isotope-resolved metabolomics (SIRM). *Mol. Cancer* **8**:41.

Fan TWM, Lane AN, Higashi RM, Yan J. 2011. Stable isotope resolved metabolomics of lung cancer in a SCID mouse model. *Metabolomics* **7**:257–269.

Fan TWM, Lorkiewicz PK, Sellers K, Moseley HNB, Higashi RM, Lane AN. 2012. Stable isotope-resolved metabolomics and applications for drug development. *Pharmacol. Ther.* **133**:366–391.

Frese KK, Tuveson DA. 2007. Maximizing mouse cancer models. *Nat. Rev. Cancer* **7**:654–658.

Gaglio D, Metallo CM, Gameiro PA, Hiller K, Danna LS, Balestrieri C, Alberghina L, Stephanopoulos G, Chiaradonna F. 2011. Oncogenic K-Ras decouples glucose and glutamine metabolism to support cancer cell growth. *Mol. Sys. Biol.* **7**:523.

Jones RG, Thompson CB. 2009. Tumor suppressors and cell metabolism: a recipe for cancer growth. *Genes Devel.* **23**:537–548.

Keibler MA, Fendt S-M, Stephanopoulos G. 2012. Expanding the concepts and tools of metabolic engineering to elucidate cancer metabolism. *Biotechnol. Prog.* **28**:1409–1418.

Kim B-J, Forbes NS. 2007. Flux analysis shows that hypoxia-inducible-factor-1-alpha minimally affects intracellular metabolism in tumor spheroids. *Biotechnol. Bioeng.* **96**:1167–1182.

Le A, Lane AN, Hamaker M, Bose S, Gouw A, Barbi J, Tsukamoto T, Rojas CJ, Slusher BS, Zhang H, Zimmerman LJ, Liebler DC, Slebos RJC, Lorkiewicz PK, Higashi RM, Fan TWM, Dang CV. 2012. Glucose-Independent Glutamine Metabolism via TCA Cycling for Proliferation and Survival in B Cells. *Cell Metab.* **15**:110–121.

Marin-Valencia I, Yang C, Mashimo T, Cho S, Baek H, Yang X-L, Rajagopalan KN, Maddie M, Vemireddy V, Zhao Z, Cai L, Good L, Tu BP, Hatanpaa KJ, Mickey BE, Matés JM, Pascual JM, Maher EA, Malloy CR, DeBerardinis RJ, Bachoo RM. 2012. Analysis of tumor metabolism reveals mitochondrial glucose oxidation in genetically diverse human glioblastomas in the mouse brain in vivo. *Cell Metab.* **15**:827–837.

Metallo CM, Gameiro PA, Bell EL, Mattaini KR, Yang J, Hiller K, Jewell CM, Johnson ZR, Irvine DJ, Guarente L, Kelleher JK, Vander Heiden MG, Iliopoulos O, Stephanopoulos G. 2012. Reductive glutamine metabolism by IDH1 mediates lipogenesis under hypoxia. *Nature* **481**:380–384.

Nöh K, Grönke K, Luo B, Takors R, Oldiges M, Wiechert W. 2007. Metabolic flux analysis at ultra short time scale: Isotopically non-stationary 13C labeling experiments. *J. Biotech.* **129**:249–267.

O'Donnell K, Wentzel E, Zeller K, Dang CV, Mendell J. 2005. c-Myc-regulated microRNAs modulate E2F1 expression. *Nature* **435**:839–843.

Shultz LD, Ishikawa F, Greiner DL. 2007. Humanized mice in translational biomedical research. *Nat. Rev. Immunol.* **7**:118–130.

Vander Heiden MG. 2011. Targeting cancer metabolism: a therapeutic window opens. *Nat. Rev. Drug Discov.* **10**:671–684.

Ward PS, Thompson CB. 2012. Metabolic Reprogramming: A Cancer Hallmark Even Warburg Did Not Anticipate.

Cancer Cell **21**:297–308.

Yuneva MO, Fan TWM, Allen TD, Higashi RM, Ferraris DV, Tsukamoto T, Matés JM, Alonso FJ, Wang C, Seo Y, Chen X, Bishop JM. 2012. The metabolic profile of tumors depends on both the responsible genetic lesion and tissue type. *Cell Metab.* **15**:157–170.

Zamboni N. 2011. 13C metabolic flux analysis in complex systems. *Curr. Opin. Biotechnol.* **22**:103–108.

Appendix 7.A - Supplementary Table

Table 7.A.1 Complete List of Reactions and Atom Transitions for the *In Vivo* B-cell Metabolic Network. Refer to Appendix 5C for a list of metabolite abbreviations.

Glycolysis			
HK	GLC.c (abcdef)	→	G6P (abcdef)
PGI	G6P (abcdef)	↔	F6P (abcdef)
PFK	F6P (abcdef)	→	FBP (abcdef)
ALDO	FBP (abcdef)	↔	DHAP (cba) + GAP (def)
TPI	DHAP (abc)	↔	GAP (abc)
GAPDH	GAP (abc)	↔	3PG (abc)
ENO	3PG (abc)	↔	PEP (abc)
PK	PEP (abc)	→	PYR.c (abc)
LDH	PYR.c (abc)	↔	LAC (abc)
Pentose Phosphate Pathway			
G6PDH	G6P (abcdef)	→	RU5P (bcdef) + CO2 (a)
R5PE	RU5P (abcde)	↔	R5P (abcde)
R5PI	RU5P (abcde)	↔	X5P (abcde)
TK1	X5P (abcde)	↔	GAP (cde) + EC2 (ab)
TK2	F6P (abcdef)	↔	E4P (cdef) + EC2 (ab)
TK3	S7P (abcdefg)	↔	R5P (cdefg) + EC2 (ab)
TA1	F6P (abcdef)	↔	GAP (def) + EC3 (abc)
TA2	S7P (abcdefg)	↔	E4P (defg) + EC3 (abc)
TCA Cycle			
PYRT	PYR.c (abc)	↔	PYR.m (abc)
PDH	PYR.m (abc)	→	AcCoA (bc) + CO2 (a)
CS	OAA (abcd) + AcCoA (ef)	→	CIT (dcbfea)
IDH	CIT (abcdef)	↔	AKG (abcde) + CO2 (f)
ADH	AKG (abcde)	→	SUC (bcde) + CO2 (a)
SUDH	SUC (½ abcd + ½ dcba)	↔	FUM (½ abcd + ½ dcba)
FUMS	FUM (½ abcd + ½ dcba)	↔	MAL (abcd)
MDH	MAL (abcd)	↔	OAA (abcd)

Table 7.A.1 Continued

Amphibolic reactions			
ME	MAL (abcd)	→	PYR.m (abc) + CO2 (d)
PYC	PYR.m (abc) + CO2 (d)	→	OAA (abcd)
ACL	CIT (abcdef)	→	AcCoA.c (ed) + MAL (fcba)
Amino Acids			
GDH	AKG (abcde)	↔	GLU (abcde)
GLS	GLN (abcde)	↔	GLU (abcde)
AST	OAA (abcd)	↔	ASP (abcd)
PST	3PG (abc)	→	SER (abc)
SHT	SER (abc)	↔	GLY (ab) + MEETHF (c)
CYST	SER (abc)	↔	CYS (abc)
GLYS	CO2 (a) + MEETHF (b)	→	Gly (ab)
ALT	PYR.c (abc)	↔	ALA (abc)
GLNR	GLN.E (abcde)	→	GLN (abcde)
Transport			
UNLG	GLC.U (abcdef)	→	GLC.E (abcdef)
LABG	GLC.L (abcdef)	→	GLC.E (abcdef)
GLUT	GLC.E (abcdef)	→	GLC.C (abcdef)
LIPS	8*(1/8*AcCoA.C)	→	PALM
MCT	LAC (abc)	→	LAC.E (abc)
Biosynthesis			
BIOM	90 ALA + 70.8 ASP + 48.3 GLN + 57.9 GLU + 98.7 GLY + 64.5 SER + 43.28 G6P + 34.95 R5P + 38.25 MEETHF + 34.95 CO2 + 18.26 DHAP+ 49.14 AcCoA.C + 40.26 PALM	→	BIOMASS

CHAPTER 8

CONCLUSIONS AND FUTURE WORK

8.1 Conclusions

The work presented in this dissertation provides new knowledge and understanding in the fields of metabolic engineering and cancer biology. The combination of these fields is a relatively nascent application and much is unknown about what the data will reveal. We have contributed to the knowledge base by testing and optimizing flux analysis methods on a Myc-driven model of cancer, attempting to predict drug effects based on our flux results, and extending these methods to *in vivo* systems. Since a metabolic flux is the functional endpoint of a host of cellular processes, accurately quantifying these reaction rates is critical to properly interpreting other experimental results such as gene expression and protein levels (Sauer, 2006).

Over the past several years the metabolism of cancer has been accepted as an important aspect of the disease and its alteration is now recognized as a bona fide hallmark (Ward and Thompson, 2012). Several recent studies have examined cancer using isotopic tracers while only a handful have used full-scale MFA (DeBerardinis et al., 2007; Gaglio et al., 2011; Grassian et al., 2011; Jain et al., 2012; Kim and Forbes, 2007; Le et al., 2012; Marin-Valencia et al., 2012; Metallo et al., 2012; Scott et al., 2011; Wise et al., 2011). Our work, along with the existing literature detailed in chapter 2, attests to the power of flux quantification in cancer research.

In chapter 3, we presented a robust method for accurately quantifying the growth rate and extracellular fluxes of a cell. The new method combined improvements in sampling, measurement, and error analysis into a software package called ETA that is now freely available to the scientific community.

Chapter 4 incorporated the improved techniques from the previous chapter into a novel ^{13}C MFA method that relies on samples collected during the nonstationary labeling period. Steady-state and ISA methods were compared with the new INST-MFA method, with the latter returning the best results. The P493-6 B-cell cancer model at High and

Low Myc expression levels was used as the test bed, and we found Myc to be a strong driver of amino acid metabolism and oxidative phosphorylation.

In chapter 5, we used the same cell model and improved the INST-MFA methodology to include lipid-labeling analysis. In addition to a normoxic flux analysis study at High and Low Myc levels, we also examined the P493-6 cells under a hypoxic environment. The normoxic results confirmed our previous studies while the hypoxic data confirmed the highly glycolytic phenotype seen in other studies (Semenza, 2010). We also saw evidence for interaction between Myc and HIF. High Myc cells in hypoxic conditions had decreased glycolytic flux magnitude but an increased growth rate whereas Low Myc cells had a slower growth rate but greater glycolytic flux. This suggests Myc levels strongly affect the growth and fluxes of cells, particularly in relation to HIF.

Next, in chapter 6, we looked at how we could use the normoxic MFA results to predict potential therapeutic targets. Little is known about how differences in flux data correspond to inhibitory effects. Using an inhibitor of lactate formation and another inhibitor of OXPHOS we found that a cancer cells' increased reliance on a pathway, as indicated by a larger fraction of carbon flowing through that pathway than in a more normal phenotype, suggested a greater sensitivity than increased flux magnitude alone. In the context of High and Low Myc cells, the High Myc cells had more carbon flowing through glycolysis but a greater fraction of the pyruvate generated was going to the TCA cycle than to lactate formation. In Low Myc cells, a larger portion of the pyruvate was going to lactate secretion than to mitochondrial metabolism. Each cell line was also able to dramatically alter its metabolism to overcome the inhibition. In the case of the High Myc cells, flux magnitudes could be increased 2- to 3-fold suggesting they are better able to withstand the inhibition than Low Myc cells. The drugs were also used in combination, and again the High Myc cells were able to adjust their metabolism more dramatically than Low Myc. We also found that combining the drugs at doses that, individually, had no effect on the growth, significantly inhibited the cells.

Finally, in chapter 7 we detailed some preliminary work and proposed methods to extend the INST-MFA technique to an *in vivo* mouse model of Myc-driven cancer. This work has great potential in bringing metabolic engineering techniques closer to the clinic.

8.2 Recommendations for Future Work

While the methods and studies detailed in this dissertation are complete, there is room for more work to be done. Our INST-MFA methodology is applicable to a wide variety of cells and cell types, not just the P493-6 B-cell model discussed. Within the realm of cancer metabolism, there are numerous oncogenes whose expression is dysregulated and it's unknown how those alterations functionally affect metabolism. Applying this method to more cell lines and models of cancer is essential to gaining a better understanding of the link between oncogenes, metabolism, and tumorigenesis.

While our INST-MFA method is robust and we've shown it to be accurate and efficacious, it can still be improved and optimized further. One comparison we did not make is between flux maps generated from intracellular metabolite labeling versus our proteinogenic method. While we expect no significant differences to be found it would still be valuable to conduct this study. It would also be beneficial to examine different tracer combinations and different labeled substrates. Particularly in the hypoxic condition where we saw low levels of labeling in TCA cycle metabolites, it would be good to either repeat the study with ^{13}C-labeled glutamine or allow the cells to grow longer in the labeled glucose. Several other research groups are working to analyze the use of different tracers individually and in combination (Ahn and Antoniewicz, 2013; Leighty and Antoniewicz, 2012; Metallo et al., 2009). Future flux studies with the B-cells studied here, or other cancer cell models with different tracers, could improve the quality of flux estimates and reveal new insights about metabolic rewiring.

MFA is new to the study of cancer biology and, as such, the understanding of how flux results predict drug effects is limited. The drug studies done in chapter 6 helped answer this question but more studies are needed. In particular, repeating these studies in hypoxia would help relate the hypoxic MFA results to drug inhibition data. A larger panel of drugs targeting specific enzymes, metabolically related pathways, and signaling networks will enable a better understanding of the relation between flux results and drugs effects. Additionally, combinatorial studies are essential to treating cancer (Dang et al., 2011). There is no doubt that cancerous cells are able to dramatically alter their metabolism to compensate for a perturbation. Limiting the available alternatives in a targeted manner with multiple drugs and correlating it with flux data will be essential to the next generation of drug treatments. Also important to

the future of cancer research is conducting experiments in more clinically relevant models (Johnson, 2012). Our work to extend the INST-MFA methodology to mice is just one example of a larger push to generate more clinically meaningful results. INST-MFA and *in vivo* flux analysis techniques are on the cutting edge of both cancer research and metabolic engineering and much remains to be discovered in both fields.

8.3 References

Ahn WS, Antoniewicz MR. 2013. Parallel labeling experiments with [1,2-(13)C]glucose and [U-(13)C]glutamine provide new insights into CHO cell metabolism. *Metab. Eng.* **15**:34–47.

Dang CV, Hamaker M, Sun P, Le A, Gao P. 2011. Therapeutic targeting of cancer cell metabolism. *J. Mol. Med.* **89**:205–212.

DeBerardinis RJ, Mancuso A, Daikhin E, Nissim I, Yudkoff M, Wehrli S, Thompson C. 2007. Beyond aerobic glycolysis: transformed cells can engage in glutamine metabolism that exceeds the requirement for protein and nucleotide synthesis. *Proc. Nat. Acad. Sci.* **104**:19345.

Gaglio D, Metallo CM, Gameiro PA, Hiller K, Danna LS, Balestrieri C, Alberghina L, Stephanopoulos G, Chiaradonna F. 2011. Oncogenic K-Ras decouples glucose and glutamine metabolism to support cancer cell growth. *Mol. Sys. Biol.* **7**:523.

Grassian AR, Metallo CM, Coloff JL, Stephanopoulos G, Brugge JS. 2011. Erk regulation of pyruvate dehydrogenase flux through PDK4 modulates cell proliferation. *Genes Devel.* **25**:1716–1733.

Jain M, Nilsson R, Sharma S, Madhusudhan N, Kitami T, Souza AL, Kafri R, Kirschner MW, Clish CB, Mootha VK. 2012. Metabolite profiling identifies a key role for glycine in rapid cancer cell proliferation. *Science* **336**:1040–1044.

Johnson L. 2012. Cancer: Clinical trials unite mice and humans. *Nature* **483**:546–548.

Kim B-J, Forbes NS. 2007. Flux analysis shows that hypoxia-inducible-factor-1-alpha minimally affects intracellular metabolism in tumor spheroids. *Biotechnol. Bioeng.* **96**:1167–1182.

Le A, Lane AN, Hamaker M, Bose S, Gouw A, Barbi J, Tsukamoto T, Rojas CJ, Slusher BS, Zhang H, Zimmerman LJ, Liebler DC, Slebos RJC, Lorkiewicz PK, Higashi RM, Fan TWM, Dang CV. 2012. Glucose-Independent Glutamine Metabolism via TCA Cycling for Proliferation and Survival in B Cells. *Cell Metab.* **15**:110–121.

Leighty RW, Antoniewicz MR. 2012. Parallel labeling experiments with [U-(13)C]glucose validate E. coli metabolic network model for (13)C metabolic flux analysis. *Metab. Eng.* **14**:533–541.

Marin-Valencia I, Yang C, Mashimo T, Cho S, Baek H, Yang X-L, Rajagopalan KN, Maddie M, Vemireddy V, Zhao Z, Cai L, Good L, Tu BP, Hatanpaa KJ, Mickey BE, Matés JM, Pascual JM, Maher EA, Malloy CR, DeBerardinis RJ, Bachoo RM. 2012. Analysis of tumor metabolism reveals mitochondrial glucose oxidation in genetically diverse human glioblastomas in the mouse brain in vivo. *Cell Metab.* **15**:827–837.

Metallo CM, Gameiro PA, Bell EL, Mattaini KR, Yang J, Hiller K, Jewell CM, Johnson ZR, Irvine DJ, Guarente L, Kelleher JK, Vander Heiden MG, Iliopoulos O, Stephanopoulos G. 2012. Reductive glutamine metabolism by IDH1 mediates lipogenesis under hypoxia. *Nature* **481**:380–384.

Metallo CM, Walther JL, Stephanopoulos G. 2009. Evaluation of 13C isotopic tracers for metabolic flux analysis in mammalian cells. *J. Biotech.* **144**:167–174.

Sauer U. 2006. Metabolic networks in motion: 13C-based flux analysis. *Mol. Sys. Biol.* **2**:62.

Scott DA, Richardson AD, Filipp FV, Knutzen CA, Chiang GG, Ronai ZA, Osterman AL, Smith JW. 2011. Comparative metabolic flux profiling of melanoma cell lines: beyond the Warburg effect. *J. Biol. Chem.* **286**:42626–42634.

Semenza GL. 2010. HIF-1: upstream and downstream of cancer metabolism. *Curr. Opin. Genet. Dev.* **20**:51–56.

Ward PS, Thompson CB. 2012. Metabolic Reprogramming: A Cancer Hallmark Even Warburg Did Not Anticipate. *Cancer Cell* **21**:297–308.

Wise DR, Ward PS, Shay JES, Cross JR, Gruber JJ, Sachdeva UM, Platt JM, Dematteo RG, Simon MC, Thompson CB. 2011. Hypoxia promotes isocitrate dehydrogenase-dependent carboxylation of α-ketoglutarate to citrate to support cell growth and viability. *Proc. Nat. Acad. Sci.* **108**:19611–19616.

APPENDIX A

DETAILED PROTOCOLS

A.1 - ^{13}C INST-MFA

The purpose of this protocol is to guide the user in starting an isotopically nonstationary metabolic flux analysis experiment. At the end of the experiment, the user will have frozen samples ready to be analyzed further.

Supplies

- 50 mL centrifuge tubes
- 10 mL centrifuge tubes
- 2 mL microcentrifuge tubes
- Isotopically labeled cell culture medium
- Unlabeled cell culture medium
- T-75 Flasks / 15 cm Plates
- TRIzol
- Liquid N_2
- Centrifuge

Planning - MFA

1. Choose appropriately spaced time points for the cell line. In the first doubling period, 3 samples need to be taken. For example, if the doubling time is 24 hours, samples should be taken at 6, 12, and 24 hours. The early time points are when the most rapid change is occurring in labeling patterns. Time points can be spaced further apart after the first doubling. The final 3 time points for this example would be 36, 48 and 72 hours.
2. Determine the total number of flasks / plates that are needed. Every time point needs 3 biological replicates and a minimum of 4 time points are needed. A typical experiment is 6-10 time points.

3. Calculate the total volume of media needed. Typical volume is 30 mL for a T-75 flask and 40 mL for a 15-cm dish.
4. Determine the initial seeding concentration for each time point. The final cell number for each point needs to be around 10^7 cells. Use the growth rate to back-calculate for the seeding density based on the time points. Do not seed below the minimum density used for normal growth conditions. It is essential to keep the cells in the exponential growth phase. Seeding them too low will create a long lag phase and alter the data.
5. Make enough media with the isotopically labeled substrate for the entire experiment.

Planning – Control Experiment

1. Along with the MFA experiment, a control growth experiment is conducted to measure the rates of cell lines under study. Growth, uptake and secretion fluxes, as well as evaporation rates are measured in this experiment. Refer to the protocol on setting up time-course growth experiments for the protocol.
2. Include this data in the calculations for how many cells are needed. This experiment needs to be run concurrently with the MFA experiment so that conditions are identical.

MFA Setup – Suspension Cells

1. Count all cells being used for the growth experiment in unlabeled medium
2. Remove unlabeled medium and add labeled medium in the appropriate amount.
3. Seed each T-75 flask with the appropriate volume and bring the final volume to 30 mL.
4. Place in the incubator at 37°C, 5% CO_2
5. Control experiment is set up at the same time as well

MFA Setup – Attached Cells

1. Count all cells being used for the growth experiment in unlabeled medium
2. Use unlabeled medium and dilute to the appropriate density.
3. Seed each 15 mL dish with the appropriate volume and bring the final volume to 40 mL.
4. Place in the incubator at 37°C

5. Control experiment is set up at the same time as well
6. After 3 to 4 hours, remove all plates from incubator. Ensure that cells are attached to the plate
7. Remove unlabeled medium and add labeled tracer medium. The clock starts when the cells are placed in labeled medium.
8. Place back into incubator.

MFA Sampling – Suspension Cells

1. Remove flasks for the specific time point from the incubator.
2. Remove cells from flask and split 50:50 into two separate 50 mL centrifuge tubes.
3. Centrifuge at 1500 rpm for 5 minutes.
4. Take 500 μL of medium (from either flask) and store at -80°C for future analysis
5. Aspirate remaining medium
6. Wash with 5 mL PBS
7. Centrifuge at 1500 rpm for 5 minutes.
8. Aspirate PBS
9. To one flask add 1 mL of TRIzol and homogenize with pipette tip. Incubate 5 min at room temp
10. To the other flasks, add 1 mL of PBS. Transfer to 2 mL microcentrifuge tube. Spin tube, aspirate PBS
11. Using tweezers, dip the tube in liquid nitrogen for 30 seconds. Store at -80°C. These samples will be stored for lipid analysis.
12. After 5 minutes has passed for TRIzol extraction, transfer the liquid to a new 2 mL centrifuge tubes
13. Freeze at -80°C
14. Take appropriate samples from the control experiment after all MFA samples have been placed in freezer.

MFA Sampling – Attached Cells

1. Remove plate for the specific time point from the incubator.
2. Take 500 μL of medium and store at -80°C for future analysis
3. Aspirate remaining medium
4. Trypsinize cells according to preferred protocol

5. Add FBS to stop the activity of the trypsin
6. Transfer cells to 10 mL tube
7. Centrifuge cells at 1500 rpm for 5 minutes and aspirate FBS
8. Wash with 5 mL PBS
9. Split cells into two separate 10 mL tubes 50:50
10. Centrifuge at 1500 rpm for 5 minutes.
11. Aspirate PBS
12. To one flask add 1 mL of TRIzol and homogenize with pipette tip. Incubate 5 min at room temp
13. To the other flasks, add 1 mL of PBS. Transfer to 2 mL microcentrifuge tube. Spin tube, aspirate PBS
14. Using tweezers, dip the tube in liquid nitrogen for 30 seconds. Store at -80°C. These samples will be stored for lipid analysis.
15. After 5 minutes has passed for TRIzol extraction, transfer the liquid to a new 2 mL centrifuge tubes
16. Freeze at -80°C
17. Take appropriate samples from the control experiment after all MFA samples have been placed in freezer.

A.2 - Aldonitrile Pentapropionate Derivatization of Glucose

This protocol details the derivatization of glucose for analysis using GC/MS.

Supplies

- Acetone (refrigerated)
- 2 wt% hydroxylamine hydrochloride in pyridine solution (may be refrigerated up to a year)
- Propionic anhydride
- Ethyl acetate
- Heating block

Sample preparation

1. Transfer 10-100 μL glucose solution (0.1 – 10 mM) to Eppendorf tube (1.5 mL)
2. Add 300 μL cold acetone
3. Vortex vigorously for 10 sec
4. Centrifuge for 5 min at 14,000 rpm to remove proteins
5. Decant fluid into Eppendorf
6. Evaporate to dryness under air flow at 60°C – approx. 20 min

Derivatization

1. Add 50 μL hydroxylamine / pyridine solution to the sample
2. Incubate for 60 min at 90°C on the heating block
3. Centrifuge for 10 sec at 14,000 rpm
4. Add 100 μL propionic anhydride
5. Incubate for 30 min at 60°C on the heating block
6. Centrifuge for 10 sec at 14,000 rpm
7. Evaporate to dryness under air flow at 60°C – approx. 30 min
8. Dissolve sample in 100 μL ethyl acetate, some precipitation may form

9. Centrifuge for 10 min at 14,000 rpm to remove solids

10. Transfer liquid to GC injection vial containing a 150 μL insert

A.3 - Aldonitrile Pentapropionate Derivatization of RNA-Derived Ribose

This protocol details the hydrolysis of RNA to ribose and the derivatization of the ribose for analysis using GC/MS.

Supplies

- Acetone (refrigerated)
- 2 wt% hydroxylamine hydrochloride in pyridine solution (may be refrigerated up to a year)
- Propionic anhydride
- Ethyl acetate
- Heating block
- Evaporator
- Vacuum Hydrolysis Tube
- Microcentrifuge tubes
- Liquid Sonicator
- Pasteur Pipettes

Sample preparation

1. Decant ethanol from RNA pellet
2. Dry under airflow at RT for <5 min.
3. Add 400 μL ddH_2O per tube
4. Sonicate briefly to dissolve RNA
5. Use Pasteur pipette to transfer solution to vacuum hydrolysis tube
6. Add 200 μL of 6N HCl on top in hydrolysis tube
7. Apply vacuum to the tube
8. Heat at 100°C for 2 hours
9. Transfer to microcentrifuge tube
10. Evaporate to dryness under air flow at 60°C – approx. 120 min

Derivatization

1. Add 50 μL hydroxylamine / pyridine solution to the sample
2. Centrifuge for 30 sec at 14,000 rpm
3. Sonicate in water sonicator for 5 minutes
4. Incubate for 60 min at 90°C on the heating block. Ensure centrifuge tube lid stays secure
    a. Periodically check to make sure solution is in contact with pellet and hasn't condensed on the lid of the tube. Shake liquid down if it has.
5. Centrifuge for 30 sec at 14,000 rpm
6. Add 100 μL propionic anhydride
7. Sonicate in water sonicator for 5 minutes
8. Incubate for 30 min at 60°C on the heating block
9. Centrifuge for 30 sec at 14,000 rpm
10. Transfer supernatant to new microcentrifuge tube
11. Evaporate to dryness under air flow at 60°C – approx. 30 min
12. Add 100 μL of ethyl acetate
13. Sonicate in water sonicator for 5 minutes
14. Leave overnight to fully dissolve (may not be fully necessary. Use best judgment)
15. Centrifuge for 10 min at 14,000 rpm to remove solids
16. Transfer liquid to GC injection vial containing a 150 μL insert

A.4 - CyQuant

The purpose of this protocol is to measure the DNA content of cells in a 96-well plate format and generate standard curves to convert DNA levels to cell number.

Supplies

- Multichannel pipette capable of going up to 200μL.
- Several conical tubes for holding lysis buffer and dye. Use plastic ware for holding the dye because the dye can adsorb to glass.
- CyQuant Lysis Buffer 20X, CyQuant GR Dye 400X
- DI Water
- Pipettes for transferring lysis buffer and dye
- Cell DNA Standards prepared before hand (1e6 cells/mL in Lysis Buffer)

Preparation of Reagents

1. Remove plates, dye, lysis buffer, and DNA Standard (or Cell # Standard) from freezer and thaw for at least 1 hour before analysis
2. Determine desired number of wells to be analyzed, including standards.
    a. 2X Dye Needed = ((#Samples x 100) + (#Cell Lines x 300)) / 1000 This will be in mL
        i. Round up to next 5 or 10 mL.
    b. 1X Dye Needed = ((#Cell Lines x #Std. Curve Replicates x 11 x 250)) / 1000 This will be in mL
        i. Round up to next 5 or 10 mL
    c. Lysis Buffer Needed = Amt of 2X Dye + Amt of 1X Dye + (# Samples x 300)/1000 This will be in mL
        i. Be generous… don't want to run out.
3. *To make 10 mL of 2X Dye: 50 μL of GR Dye in 10 mL of 1X Lysis Buffer*
4. *To make 10 mL of 1X Dye: 25 μL of GR Dye in 10 mL of 1X Lysis Buffer*
5. *To Make 20 mL of Lysis Buffer: 1 mL of Buffer in 19 mL of DI Water*

Procedure for Samples

1. Add 200 μL of Lysis Buffer to each sample well. Incubate at RT for 30 min.
2. Gently mix solution in wells and transfer either 10μL or 20μL to new well.
    a. **Note**: Choice of amount depends on expected number of cells. This just dilutes the amount of DNA analyzed to get it within the range of the standard curve.
3. Add 80 μL or 90 μL of Lysis Buffer to each well depending on original dilution factor. (Total volume should be 100 μL at this point)
4. Add 100 μL of 2X Dye to each well. This makes the final concentration of dye in the well 1X. (Final volume should be 200 μL)
5. Incubate in the dark at room temperature for 5-10 minutes.
6. Read plate in the plate reader using the following settings.

Procedure for Standard Curve Preparation

Standard curve concentrations : 50000, 25000, 12500, 6250, 3125, 1563, 781, 391, 195, 98, 49, 0.

1. Cells should already be in lysis buffer at a concentration of 1 million cells / mL.
2. Add 300μL of cell lysate to 300μL of 2x dye in Eppendorf tube.
3. Add 150μL of 1X Dye to wells 2-12 for each standard curve.
4. Add 200μL of the Cell Lysate mixture to well 1 for each standard curve.
5. Add 100μL of 1X Dye to well 1 for each standard curve.
6. Remove 150μL from well 1 and transfer to well 2.
7. Remove 150μL from well 2 and transfer to well 3.
8. Repeat for each well except for well 11. Discard 150μL of sample from well 11.
7. Add 50μL of 1X dye to each well (Final volume should be 200 μL in each well)
8. Incubate in the dark at room temperature for 5-10 minutes.
9. Read plate in the plate reader using the following settings.

A.5 - Determination of Cellular Rates

The purpose of this protocol is to determine the specific growth rate and specific uptake and secretion rates of extracellular metabolites. This is accomplished by taking multiple time points over the course of several cell doublings and measuring cell number as well as metabolite concentration levels. This protocol is for cell cultures that are believed to be growing exponentially. It is not suitable for quiescent cells or cells with non-exponential growth phenotypes. This is a general protocol that allows for multiple methods of assessing cell number or cell density and metabolite concentrations.

Supplies

All the materials below are not necessary all the time.

- Eight 96-well plates
- Multi-channel pipette capable of handling 200μL
- Microcentrifuge tubes (or 200 μL PCR tubes)
- Fluorescence Plate Reader
- CyQuant Cell Proliferation Assay Kit (Invitrogen C7026)
- Glucose Assay Kit (Biovision K606-100)
- Lactate Assay Kit (Biovision K607-100)
- Materials specified by kits
- T-75 Flasks or 6-well plates
- Hemacytometer
- Trypan Blue
- Other cell number, glucose, lactate, and amino acid measuring methods

Notes

No matter the culture condition, it is recommended that 8 time points are taken for the time-course experiment. When done in normoxic conditions, it is possible to take samples from the same flask, e.g. a T-75 flask. In hypoxic conditions, however, it is recommended to avoid re-oxygenating the culture. To do this, it is necessary to seed 8

separate plates or flasks at the beginning of the experiment and completely harvest it. Re-oxygenation has the potential to alter the growth and affect the analysis.

It is absolutely necessary to control for evaporation in every experiment. The best way to do this is to seed an identical number of wells, plates, or flasks with the same volume of media sans cells. When a time point is taken, take a sample of the media and freeze it along with the media taken from the cell sample.

Time points should be spaced so that every sample is taken at approximately every half-doubling period. For example, if the doubling time of the cell line is 24 hours, then samples should be taken approximately every 12 hours.

At every time point, 3 samples should be captured: the media in which the cells were cultured, the control media that does not have cells, and the cell number/cell density. If the cell number is not immediately measured, the plates or sample should be frozen for later analysis (e.g. CyQuant analysis).

Protocol

Hypoxic Method

1. Choose a seeding density that is appropriate for the cells, but that is also detectable by the chosen measurement method. For example, the P493-6 B-cell culture requires about 150,000 - 200,000 cells/mL. For adherent cells, 10% seeding density would be appropriate.
2. Seed a minimum of 3 wells on each plate, or have 3 separate flask with cells and the appropriate volume of media.
3. Seed a minimum of 3 wells on each plate, or have 3 separate flask with cell-free media to control for evaporation.
4. Place into the hypoxic chamber and allow them to culture. Every ½ doubling period (so every 12 hours for a 24 hour doubling culture) take out one plate as rapidly as possible to avoid re-oxygenation.
5. **Suspension Cells**: Mix the culture well before taking a sample. Take 500 μL from each well and put into separate microfuge tubes. Spin these down, transfer the media to a new tube and freeze at -80°C until ready

for analysis. Use the cells in the old tube for hemacytometer counting. (Use according to desired method, trypan blue or not.) Record the cell number in a notebook as # cells/mL (back calculate for the original volume of media). If done on a plate (i.e. 96-well plate), spin the plate and carefully remove cell media. Either count cells manually or freeze for later analysis by chosen protocol.

6. **Adherent Cells**: Take 500 μL from each well and put into separate microfuge tubes. Freeze these at -80°C. Add Trypsin or other agent to detach the cells if manually counting. Count according to preferred method and record the value as # cells/well. Record the initial volume along with the cell number.

Normoxic Protocol for Suspension Cultures

1. Choose a seeding density that is appropriate for the cells, but that is also detectable by the chosen measurement method. For example, the P493-6 B-cell culture requires about 150,000 - 200,000 cells/mL. For adherent cells, 10% seeding density would be appropriate.
2. Seed 3 separate T75 Flasks with 30 mL of media with the cells at the appropriate density. Or seed 96- or 6-well plates at the nominal volume and cell density.
3. Every ½ doubling period mix the media repeatedly. Remove 500 μL from each flask, spin down, transfer media to new tube and freeze at -80°C.
4. Use cells in tube for counting in hemocytometer. Record values as # cells/mL.
5. For experiments done in well plates, spin the plates, remove the media and freeze, and count cells according to chosen method.

Normoxia Protocol for Adherent Cultures

The hypoxic protocol for adherent cells is appropriate for cultures of this type. Seeding separate plates for each time point makes the analysis easier and more efficient.

A.6 - Methylation of Fatty Acids to Measure Palmitate 270

The purpose of this protocol is to describe the steps necessary to *trans*-methylate palmitate from a cell pellet.

Protocol

1. Make fresh solution of 5% sulfuric acid:methanol (0.1 mL H_2SO_4:1.9 mL CH_3OH)
2. Add 1 mL of sulfuric acid and methanol solution to cell pellet. Homogenize pellet.
3. Transfer solution to 6 mL glass tube. Add 1 mL of sulfuric acid and methanol solution.
4. Add 0.5 mL of Toluene
5. Add 25 uL 0.2% BHT in MeOH solution (3.168 mg BHT for 2 mL MeOH). This inhibits lipid peroxidation.
6. Heat at 95°C for 2 hours. Vortex occasionally.
7. Add 3 mL of DI-H_2O and shake to quench reaction.
8. Extract with 2 mL of Hexane. Shake vigorously.
9. Centrifuge tubes at 2500 rpm for 2 minutes.
10. Remove hexane (top portion) and dry under N_2 and heat.
11. Resuspend in 200 uL hexane and thoroughly vortex to clean walls
12. Add to GC/MS vial with glass insert.
13. Analyze on GC/MS with the following settings
    a. DB-23 capillary column (30 m × 0.25 mm i.d. × 0.25 μm; Agilent J&W Scientific) I
    b. Injection volume of 1 μL, split mode, inlet temperature of 270°C, split ratio of 10:1.
    c. Helium flow at 1 mL/min.
    d. Mass spectrometer (MS) in electron impact mode with temperatures of 230°C for the ion source and 150°C for the quadrupole.
    e. GC temperature program: inject sample at 100°C, ramp at 40°C/min to 150°C, ramp at 10°C/min to 190°C, ramp at 40°C to 250°C, hold for 3 minutes.
    f. Obtained mass spectra in scan mode over the range 269-290 m/z

A.7 – Polymerase Chain Reaction (PCR)

The purpose of this protocol is to extract mRNA from cells, synthesize cDNA, and amplify the chosen cDNA via the polymerase chain reaction.

Cell harvesting (from a 24 well plate – adjust quantities as needed)

1. Transfer samples to an empty well and aspirate old media
2. Wash with 1 ml PBS, 2 min
3. Add 250 uL trypsin, wait until cells detach

a. Plate can be incubated at 37°C for 2 min to favor cell detachment

4. Add 250 uL media with FBS to inactivate the trypsin
5. Pipette up and down the trypsin/media with cells on top of the material (do this at least 3 times).
6. Transfer cells/trypsin/media to 1.5 mL tube
7. Centrifuge at 5000 rpm for 5 min
8. Aspirate supernatant
9. Wash with 500 uL PBS
10. Centrifuge at 5000 rpm for 5 min
11. Aspirate supernatant as much as possible without aspirating the cell pellet

RNA isolation (Using RNeasy mini kit)

Before beginning:

β-mercaptoethanol (β-ME) must be added to Buffer RLT before use. β-ME is toxic; dispense in a fume hood and wear appropriate protective cloting. Add 10 ml of β-ME per 1 ml Buffer RLT. RLT buffer is stable for 1 month after addition of β-ME.

1. Disrupt the cells by addition of Buffer RLT
    i. 350 ml if number of pelleted cells< $5x10^6$ or
    ii. 600 ml if number of pelleted cells is between $5x10^6$ and $1x10^7$
2. Loosen the pellet thoroughly and vortex or pipet to mix

3. Homogenize the sample: Pipet the lysate directly onto a QIAshredder (Cat No. 79656) spin column placed in a 2 ml collection tube, and centrifuge for 2 min at full speed (13200 rpm)
4. Add 70% ethanol and mix thoroughly

a. 350 ml if number of pelleted cells< $5x10^6$ or

b. 600 ml if number of pelleted cells is between $5x10^6$ and $1x10^7$)

5. Transfer up to 700 ml of the sample, including any precipitate that might have formed, to an RNeasy mini column placed in a 2 mL collection tube
6. Close the tube gently and centrifuge for 15 s at ≥ 8000xg (≥10,000 rpm)
7. Discard the flow through and re-locate the RNeasy mini column on the same 2 mL collection tube

a. Repeat steps 5 to 7 if there is more than 700 ml of the sample

8. Add 350 ml of Buffer RW1 to the RNeasy mini column
9. Close the tube gently and centrifuge for 15 s at ≥ 8000xg (≥10,000 rpm)
10. Discard the flow through and collection tube
11. Prepare DNAse solution (Components Cat. No. 79254)

a. Buffer RDD → 70 ml / sample

b. DNAse → 10 ml / sample

12. Add the DNAse solution (80 ml / sample) to the RNeasy spin column membrane and place on the benchtop (@20-30ºC) for 15 min
13. Add 350 ml of Buffer RW1 to the RNeasy spin column
14. Close the tube gently and centrifuge for 15 s at ≥ 8000xg (≥10,000 rpm)
15. Transfer the RNeasy column into a new 2 ml collection tube
16. Pipet 500 ml buffer RPE onto the RNeasy column
17. Close the tube gently and centrifuge for 15 s at ≥ 8000xg (≥10,000 rpm)
18. Discard the flow through and re-locate the RNeasy mini column on the same 2 mL collection tube
19. Add another 500 ml Buffer RPE to the RNeasy column
20. Close the tube gently and centrifuge for 2 min at ≥ 8000xg (≥10,000 rpm) (make sure the column is dry. If this is not the case, place the column in a new 2 ml collection tube and centrifuge at full speed for 1 min)
21. Centrifuge for an extra minute at 13200 rpm

22. Transfer the RNeasy column to a new 1.5 ml collection tube.
23. Pipet 30 ml of RNease-free water directly onto the RNeasy column
24. Close the tube gently and let it sit for 1 min. Then centrifuge for 1 min at ≥ 8000xg (≥10,000 rpm)
25. Remove and discard the RNeasy column, and close the 1.5 ml collection tube
    i. **RNA is not stable!** Keep it in ice while working with it in downstream steps
26. Measure the RNA concentration using an Eppendorf BioPhotometer Plus
    i. Eppendorf BioPhotometer Plus
    ii. Blank: 100 ml of RNase-free water
    iii. In an UVette dilute 2 ml of the sample in 98 ml of RNase-free water and mix well by pipetting
    iv. Feed the dilution information to the equipment and read the RNA concentration
    v. "Purity ratio" = Abs260nm/Abs280nm a good value is ~1.7

NOTE: If the RNA needs to be stored, this should be done at -80°C. This should be avoided; the cDNA should be prepared as soon as possible.

cDNA synthesis (Using iScript cDNA synthesis kit)

1. After measuring the RNA content in all the samples, determine the amount of RNA template to be used in the cDNA synthesis (it should be as close to 1mg as possible)

NOTE: The initial RNA amount to use as a template should be the same for all of the samples; it will be limited by the sample with less total isolated RNA.

CONTINUED ON NEXT PAGE

2. For each sample:
    a. In a nuclease-free 1ml tube add the following reagents:

Components	Volume per reaction
5x iScript reaction mix	4 ml
iScript reverse transcriptase	1 ml
Nuclease-free water	X ml
RNA template	Y ml
Total volume	20 ml

X and Y depend on the amount of RNA quantified in the sample

3. Transfer the tubes to a thermocycler and use the following protocol (40 min):
    a. 5 minutes at 25°C
    b. 30 minutes at 42°C
    c. 5 minutes at 85°C
    d. Hold at 4°C
4. Store the cDNA at -20°C

PCR

1. Obtaining the PCR product
    a. Set up reaction tubes on ice
    b. Add the following components to the reaction tube to obtain 20 ml total:
        i. RNAse free water
        ii. PCR Supermix
        iii. Primer solution
            1. The forward and reverse primer come together in a concentration of 100 mM. This solution needs to be diluted according to the parameters of the test. For example, to

prepare a 2.5 mM primer solution: mix 5 ml of the original primer with 195 ml of RNAse free water.

iv. cDNA

v. The amounts of each component will vary according to the concentrations determined for each experiment. An example is shown here:

Components	Final desired concentration	Amount added
Water		5.55 ml
Supermix		11.25 ml
Primer (initial conc.=2.5 mM)	250 nM	2 ml
cDNA	30 ng/ml	1.2 ml

c. Transfer the tube to a thermocycler and use the following protocol (1h30min):

i. Lid 100°C Vol 20 ml

ii. 5 min at 95°C

iii. 30 sec at 95°C

iv. 30 sec at 55°C

v. 30 sec at 72°C

vi. Go back to step 2-4 x35 times

vii. 7 min at 72°C

viii. End

d. Keep the PCR product at -20°C until loading onto the gel

Agarose gel electrophoresis of PCR products

The following procedure can be followed to prepare a 1.5 mass% agarose gel to use with an 8 well comb.

NOTE: lower concentration of agarose works better for larger molecules. 0.7% is good for DNA fragments with length between 5 and 10 kb. 2% works for DNA fragments with 0.2-1 kb.

1. Place casting gates and combs in gel casting tray on a level surface. Looking at the tray from the top, it should look like:

2. Prepare a 1.5% mass Agarose solution in 1XTAE (Tris Base/Acetate/EDTA)
    a. In a beaker, mix 35 ml of 1XTAE with 0.525g of Agarose

NOTE: To dilute 10xTAE: 50 ml of 10xTAE + 450 ml dH2O = 500 ml of 1xTAE

    b. Cover the beaker with plastic foil and poke small holes on the plastic
    c. Warm up the mixture ~1 min in the microwave
    d. Remove carefully from the microwave using a heat protection glove
    e. Add 1 ml Ethidium Bromide and mix

3. Load the gel onto the gel casting tray, cover the tool with plastic wrap and let it solidify. Do not cover with the lid because it can move the comb and damage the gel.

NOTE: To clean the beaker where the gel was prepared, let it stand at room temperature and after the gel has solidified detach it from the surface of the glass. Discard the excess gel in a biowaste container.

4. Remove the comb and add 1X TAE at the sides of the gel casting tray until the gel is covered by the buffer

NOTE: To clean the electrophoresis tool only use water, NO ETHANOL

5. Load the PCR product/dye mixture onto the gel
    a. Locate a strip of paraffin paper on the table and combine 10 ml of the PCR product and 2 ml of the dye (Promega) for each sample
    b. Use the pipette to mix the samples
    c. Use a pipette to carefully load each sample into a well in the gel
    d. Load 3-4 ml of the pre-mixed DNA ladder (Biolabs- 1kb N32325-can be found at The Core) into at least one well
    e. Cover the electrophoresis tool with the appropriate lid

NOTE: Promega supplies only the dye (6x). Biolabs sells the DNA ladder with a vial of dye. To load the sample, dye needs to be added to the proper amount. To load the DNA ladder, the DNA ladder, the dye and water need to be mixed according to the manufacturer's instructions.

6. Set the electrophoresis tool to run at 100V, 400mA, for 40 min
7. Remove the gel and keep moist
8. Read the gel
    a. Bio-rad quantity one
    b. Basic select scanner- Gel DocxR, UV-push button "TRANS UV" – Auto expose
    c. Save-export JPEG

A.8 - Protein and RNA Extraction from Cultured Cells

This protocol is for the extraction of RNA and proteins from cells. This is a triphasic extraction protocol with the total RNA in the aqueous phase, the DNA in the interphase and the protein and other organelles in the organic phase.

Supplies

- Cells in a flask or dish
- Cell Scraper (for adherent cells)
- 1X PBS
- TRIzol (Invitrogen 15596-26)
- 2 mL microcentrifuge tubes (Eppendorf 022363352)
- Chloroform
- 100% Ethanol
- Isopropanol
- Acetone
- Refrigerated centrifuge for microcentrifuge tubes and for 15 mL tubes
- 75% Ethanol

Protocol

A. Pellet Formation

1. Remove the growth media and wash cells one to three times with 5 ml 1x PBS.
2. Add 2 mL of Trizol for a 10 cm dish (10^6-10^7 cells) and use cell scraper to break cells open.
3. Transfer in 1ml aliquots to two microcentrifuge tubes. 2 mL has been best in my experience.
4. Leave at RT, 5mins (samples may be frozen at this stage)
5. Add 0.2ml chloroform / 1ml homogenates
6. Shake vigorously for 15secs. (Should have a “pepto-bismol” look)
7. Incubate at RT for 2-3mins. The mixture should separate by now.

8. Spin at 12k rpm, 4°C, 15min this will separate cell homogenate to three phases: a clear aqueous supernatant (total RNA), a white interphase (DNA), and a pink organic phase containing the other cellular fraction including proteins, membranes etc.
9. Continue with DNA Precipitation

B. DNA Precipitation

1. Transfer the clear aqueous phase from the previous step to clean microcentrifuge tubes (larger 2 mL preferable). Be sure not to take up any of the DNA interphase! Take the aqueous phase and extract according to the RNA Precipitation (Step D) protocol.
2. Add to the tube with the remaining organic phase 0.3 ml of 100% ethanol per 1 ml of TRIzol Reagent used for the initial homogenization.
3. Mix samples by inversion. Incubate at room temperature for 2-3 minutes.
    a. While these are incubating, the first two steps of the RNA Precipitation can be done so that when the next centrifugation step is complete, the RNA will be ready to be centrifuged.
4. Sediment DNA by centrifugation at 5k rpm (2000 g) for 10 minutes at 4ºC.
5. Continue with Protein Precipitation.

C. **Protein Precipitation**

1. Transfer the supernatant to a single clean 15 mL centrifuge tube. In my experience, it's been best to take about 500 μL off the top of the pink supernatant.
2. Add several volumes of acetone to precipitate protein. Exact amount of acetone is not necessary.
3. Mix by inversion for 10-15 sec to obtain a homogeneous solution.
4. Store samples for 10 min at room temperature.
5. Centrifuge at top speed for 10 min at 4ºC**.** Protein pellet sediments. If 4ºC is not available for larger tubes, they can be stored in -20ºC for about 15 minutes and then centrifuged at RT.
6. Store in -20ºC freezer until ready to analyze.

D. **RNA Precipitation**

1. Add 0.5ml Isopropanol/1 mL homogenates.
2. Mix by inversion.
3. Incubate at Room Temperature for 10 minutes then centrifuge for 15 minutes at 12k RPM and 4°C
4. Decant the supernatant, gently mix pellet in 1 mL of 75% or 100% EtOH. (This is a wash step.) The RNA pellet will adhere to the side of the tube quite well, so pouring out any solution into a waste container works very well.
5. Centrifuge for 5 minutes at 12k RPM at 4°C
6. Store in -20ºC freezer until ready to analyze.

A.9 – *tert*-butyldimethylsilyl (TBDMS) Derivatization of Amino Acids

This protocol describes the derivatization of (proteinogenic) amino acids for subsequent GC/MS analysis.

Supplies

- 6 N Hydrochloric Acid, HCl (J.T. Baker)
- Pyridine (Sigma)
- MTBSTFA + 1% TBDMCS, 1 mL ampules (Pierce Biotechnology, product# 48927)
- 13 mm Acrodisc Syringe Filter with PVDF Membrane, 0.2 um pore size (Pall, product# 4450)
- 1 mL Syringe (VWR)
- Syringe Needle (VWR)
- 9" Pasteur Pipettes (VWR)
- 1 mL Vacuum Hydrolysis Tube (Pierce Biotechnology, product# 29550)
- 1.5 mL Eppendorf Tubes
- 2 mL Amber Glass Injection Vial (Varian, product# 392611547)
- 150 uL Insert for injection vial (Waters, product# WAT094171)
- Drying oven
- Analytical Nitrogen Evaporator (Organomation N-Evap, model# 112)
- Heating block

Biomass Hydrolysis and Sample Preparation

1. Centrifuge fermentation sample for 1 min at 3000 rpm (suitable to pull pellet to bottom)
2. Aspirate liquid
3. Transfer small amount of biomass pellet to Vacuum Hydrolysis tube using Pasteur pipette
4. Add 700 uL of 6 N HCl to hydrolysis tube
5. Apply vacuum to hydrolysis tube
6. Place sample on heating block for 20 hours at 110°C
7. Let the hydrolysis tube cool down for several minutes
8. Transfer sample to Eppendorf tube using a Pasteur pipette

9. Centrifuge for 10 min at 14,000 rpm to remove cell debris
10. Transfer liquid layer into a new Eppendorf tube (Pasteur Pipette may be better. Avoid particles)
11. Evaporate sample to dryness under air flow at 60°C
12. Dissolve in 150 uL ddH_2O. May be necessary to centrifuge and sonicate to have sample contact H_2O and fully dissolve
13. Transfer sample using a Pasteur Pipette and using a syringe, filter the sample through the Acrodisc 0.2 um pore size filter
14. Evaporate sample to dryness under air flow at 60°C

Derivatization

1. Dissolve dried sample in 50 uL pyridine (in a fume hood)
2. Add 70 uL of MTBSTFA +1 % TBDMCS
3. Centrifuge and sonicate sample to fully contact sample and liquid
4. Incubate for 30 min at 60°C on a heating block
5. Centrifuge for 5 min at 14,000 rpm to remove solid debris
6. Transfer liquid to injection vial containing a 150 uL glass insert